THÈSE

Pour obtenir le grade de

DOCTEUR DE L'UNIVERSITÉ GRENOBLE ALPES

École doctorale : STEP - Sciences de la Terre de l'Environnement et des Planètes
Spécialité : Sciences de la Terre et de l'Environnement
Unité de recherche : Institut des Géosciences de l'Environnement (IGE)

Mélange océanique en rotation : entraînement turbulent, oscillations inertielles et validation de modèles de fermeture turbulentes

Oceanic mixing in rotation: turbulent entrainment, inertial oscillations and validation of turbulent closure models

Présentée par :

Max COPPIN

Direction de thèse :

Joël SOMMERIA Directeur de Recherche, CNRS	Directeur de thèse
Bruno DEREMBLE CHARGE DE RECHERCHE, CNRS	Co-directeur de thèse

Rapporteurs :

Benjamin FAVIER
CHARGE DE RECHERCHE, CNRS Délégation Provence et Corse
Marie-Noelle BOUIN
Chercheuse, Centre National de Recherches Météorologiques

Thèse soutenue publiquement le **24 septembre 2026**, devant le jury composé de :

Joël SOMMERIA, DIRECTEUR DE RECHERCHE, CNRS Délégation Alpes	Directeur de thèse
Benjamin FAVIER, CHARGE DE RECHERCHE, CNRS Délégation Provence et Corse	Rapporteur
Marie-Noelle BOUIN, Chercheuse, Centre National de Recherches Météorologiques	Rapporteure
Maria-Eletta NEGRETTI, DIRECTRICE DE RECHERCHE, CNRS Délégation Alpes	Examinatrice
Yves MOREL, SENIOR SCIENTIST, CNRS Délégation Occitanie Ouest	Examinateur
Thomas DUBOS, PROFESSEUR DES UNIVERSITES, École Polytechnique Palaiseau	Examinateur

Invités :

Bruno DEREMBLE
CHARGE DE RECHERCHE, Institut des Géosciences de l'Environnement (IGE) - UMR 5001- CNRS -

UNIVERSITÉ DE GRENOBLE ALPES

ÉCOLE DOCTORALE STEP

Sciences de la Terre, de l'environnement et des planètes.

T H È S E

pour obtenir le titre de

Docteur en sciences

de l'Université Grenoble Alpes

Mention : Sciences de la Terre et de l'Environnement

Présentée et soutenue par

Max COPPIN

Mélange océanique en rotation : entraînement turbulent, oscillations inertielles et validation de modèles de fermeture turbulentes

Thèse dirigée par Joël SOMMERIA et
co-encadrée par Bruno DEREMBLE préparée au sein des
laboratoires IGE et LEGI

Jury :

Rapporteurs :	Benjamin FAVIER	-	IRPHE
	Marie-Noelle BOUIN	-	CNRM
Examinateur :	Yves MOREL	-	LEGOS
Examinateur :	Thomas DUBOS	-	LMD
Examinatrice :	Maria Eletta NEGRETTI	-	LEGI
Directeur :	Joël SOMMERIA	-	LEGI
Co-encadrant :	Bruno DEREMBLE	-	IGE

If one had to pick an animal
whose character most resembled turbulence,
my choice would be an irritable,
unpredictable old goat, liable to react violently when prodded

Launder

Contents

———Article published in Geophysical and Astrophysical Fluid Dynamics———

Résumé en Français

Chapitre 1: Introduction

Le vent est l'une des principales sources d'énergie de l'océan. Sur une moyenne annuelle, il transfère à la surface de l'océan une puissance de l'ordre de 20 TW. Cette énergie ne se répartit pas de façon uniforme selon les échelles de la dynamique océanique. En effet, une très grande part de cette énergie ($\approx 90\%$) est dissipée au sein des premiers mètres sous la surface, à travers l'action des vagues et de la turbulence à la surface. La partie restante est transférée d'une part à la circulation générale océanique de grande échelle, et d'autre part aux tourbillons dits de méso-échelle (dont la taille correspond au rayon de déformation de Rossby) et aux ondes d'inertio-gravité. La part d'énergie associée à la circulation moyenne de grande échelle se trouve être approximativement la même que celle responsable des écoulements transitoires plus petits.

Dans le cadre de cette thèse, nous nous intéressons à la manière dont le vent agit sur la partie superficielle de l'océan. En effet, la couche de mélange joue un rôle climatique majeur en modulant les interactions entre l'atmosphère et l'océan profond. C'est à travers elle que l'océan échange chaleur et gaz avec l'atmosphère, et notamment qu'il absorbe une part importante du dioxyde de carbone émis chaque année. La turbulence générée en surface homogénéise la température et la salinité sur une profondeur allant de quelques mètres à quelques centaines de mètres.

Si l'on considère la couche de mélange forcée par le vent, trois facteurs contrôlent la profondeur de la couche de mélange (MLD) : l'intensité du vent, la stratification de la colonne de fluide sous la couche de mélange et la rotation de la Terre. Selon leur importance relative, l'écoulement change de nature. En l'absence de rotation, la turbulence érode la stratification et la couche de mélange s'approfondit proportionnellement à la racine carrée du temps, ie $h(t) \propto \sqrt{t}$. En l'absence de stratification, la rotation organise l'écoulement en une spirale d'Ekman. Par ailleurs, dans un océan en rotation, une impulsion de vent met en mouvement les particules de fluide dont la trajectoire suit naturellement des cercles en raison de la déviation des vitesses par la force de Coriolis ; ce sont les oscillations inertielles. Ces trajectoires se ferment sur une période caractéristique qu'est la période inertielle $T_f = 2\pi/f$.

Ce travail s'inscrit dans un projet plus large, le projet PLUME, qui vise à mieux représenter la convection océanique dans les modèles de climat. En effet, les paramétrisations utilisées aujourd'hui ont été calibrées sur des écoulements stationnaires et sans rotation ; leur validité en rotation reste donc à vérifier. Pour cela, l'approche qui est adoptée combine : modélisation numérique, analyse théorique et expérience en laboratoire. Au sein de ce projet, cette thèse vise (i) à mettre en place une partie des campagnes expérimentales de convection forcée et de convection libre, (ii) à décrire la dynamique de la convection forcée par le vent, (iii) à confronter

un modèle de turbulence avec les données expérimentales dans des expériences d'écoulement cisaillé en rotation. Trois questions sont adressées dans ce manuscrit.

1. Quel est le régime d'approfondissement de la couche de mélange en rotation, et quel y est le rôle des oscillations inertielles ?

2. Quelle est la dynamique transitoire de la couche d'Ekman turbulente, et comment ces oscillations s'amortissent-elles ?

3. Les modèles de fermeture turbulente, en particulier le modèle k-ε , restent-ils valables en rotation ?

Chapitre 2: Approche Expérimentale et numérique

Pour répondre à ces questions, ce travail combine des expériences de laboratoire et des simulations numériques idéalisées 1D. Les expériences ont été réalisées sur la plateforme tournante Coriolis (voir Figure1), au LEGI à Grenoble. Avec ses treize mètres de diamètre, c'est la plus grande plateforme au monde dédiée à l'étude des écoulements géophysiques. Sa taille permet d'atteindre des régimes de turbulence pleinement développée, plus proches des conditions réelles de l'océan.

Deux campagnes expérimentales ont été menées, l'une pour la convection forcée (causé par cisaillement), l'autre pour la convection libre (causé par une anomalie de flottabilité). Lorsque les deux effets sont couplés, on parle de convection mixte. Pour la convection forcée, la stratification est créée par un gradient vertical de température dans la cuve. Le forçage est appliqué au fond, par une accélération impulsionnelle de la vitesse de rotation de la plateforme : c'est la procédure dite de "spin-up". Dans le cadre des approximations habituelles (Boussinesq), cette configuration inversée, forcée par le bas, est équivalente à un vent appliqué à la surface de l'océan, aux effets de surface libre près. Son grand avantage est de permettre de contrôler séparément la rotation, la stratification et l'intensité du forçage. Plusieurs techniques de mesure sont employées. La principale est la vélocimétrie par image de particules (PIV), en configuration stéréoscopique. Des particules sont dispersées dans l'eau et éclairées par une nappe laser ; deux caméras filment le même plan sous des angles différents, ce qui permet de reconstruire les trois composantes de la vitesse. Des sondes mesurent par ailleurs les profils verticaux de température, et pour certaines expériences un colorant fluorescent permet de visualiser directement la turbulence au sein de la couche limite (voir aussi la Figure 3).

La seconde campagne, dédiée à la convection libre, utilise un plancher chauffant d'environ 100 m^2 installé au fond de la cuve. Elle permet d'étudier la convection thermique en rotation, c'est-à-dire la formation de panaches de fluide chaud qui érodent la stratification. Une caméra infrarouge complète les mesures en visualisant la signature de ces panaches à la surface.

En complément des expériences, la dynamique verticale est modélisée à l'aide d'un modèle dit 1D. Ce modèle décrit uniquement la structure verticale de l'écoulement, ce qui permet d'isoler les

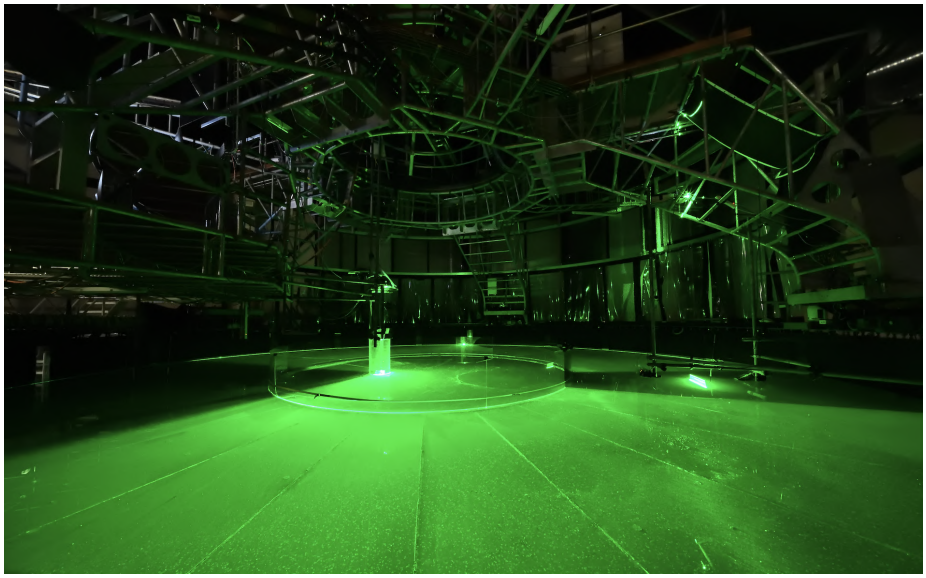

Figure 1: Photographie de l'intérieur de la plateforme Coriolis pendant une expérience. La couleur verte provient du laser servant à illuminer des particules dans le fluide pour la méthode PIV. Deux régions d'observation sont ici visibles, une large zone horizontale pour observer les écoulements à un niveau donné et une tranche verticale qui permet d'observer l'évolution de l'écoulement à une position donnée sur toute la hauteur de la colonne de fluide.

processus responsables du mélange et d'évaluer les paramétrisations turbulentes dans un cadre idéalisé. La turbulence y est représentée par une viscosité turbulente, qui traduit le transport de quantité de mouvement par les tourbillons. Le manuscrit s'appuie principalement sur le modèle k-ε , qui calcule cette viscosité à partir de deux équations de transport : l'une pour l'énergie cinétique turbulente (TKE, aussi notée k), l'autre pour la dissipation (ε).

Chapitre 3: Couche de surface océanique forcée par le vent

Dans ce chapitre, nous reproduisons une étude publiée dans la revue *Geophysical and Astrophysical Fluid Dynamics*. Dans cette dernière, nous étudions l'approfondissement de la couche de mélange sous l'effet d'un vent constant. Le modèle théorique canonique Pollard et al. (1973) démontre que l'approfondissement de la couche de mélange obéit à la loi $h \propto \sqrt{t}$. Dans un référentiel en rotation, cette théorie prédit que les oscillations inertielles, provoquées par l'impulsion du vent, dévient les vitesses dans la couche de mélange et bloquent l'injection d'énergie au-delà de la moitié d'une période inertielle, ce qui arrête complètement l'approfondissement de la couche. Cette hypothèse d'arrêt s'est révélée incorrecte d'apres des simulations LES (Ushijima and Yoshikawa, 2020) (représenté sur la Figure 2), mais aucune loi analytique n'a été dérivée pour caractériser ce régime d'approfondissement forcé par le vent à long terme.
Dans ce chapitre, nous proposons la loi d'évolution

$$h \propto \frac{u_*}{\sqrt{N_0 f}} (ft)^{1/4}.$$

Cette loi a été testée à l'aide de simulations numériques à colonne unique avec une fermeture turbulente de la forme k-ε et s'est révélée cohérente et indépendante du paramètre $S = \sqrt{N_0/f}$.

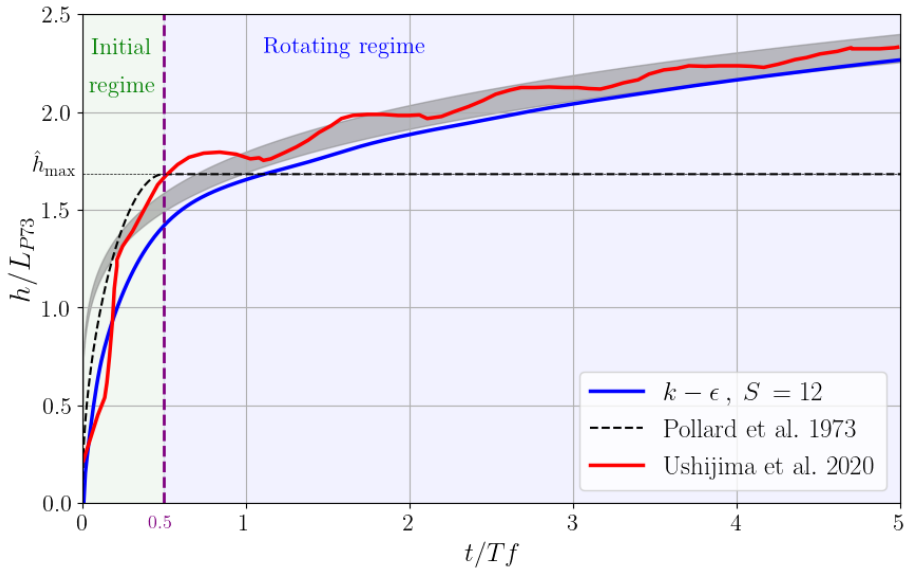

Figure 2: Evolution temporelle de la hauteur de la couche de mélange normalisé par la hauteur caractéristique $L_{P73} = u_*/\sqrt{N_0 f}$. Le temps est normalisé par la période inertielle $T_f = 2\pi/f$. La courbe rouge correspond à la valeur moyenne de toutes les expériences LES réalisées par Ushijima and Yoshikawa (2020) et représentées dans leur figure 3. La zone ombrée illustre la dispersion des estimations de la profondeur de la couche de mélange obtenues à partir de leur modèles pour $S = \sqrt{N/f}$ compris entre 7 et 27. La ligne pointillée noire représente la loi d'échelle de Pollard et al. (1973). Selon leur théorie, l'approfondissement s'arrête à $t/T_f = 0,5$, et $\hat{h}_{max} = h_{max}/L_{P73} = 8^{1/4}$. La ligne bleue correspond à une simulation numérique utilisant le schéma k-ϵ avec $S = 12$.

De plus, une dérivation plus précise, basée sur un profil quadratique de la viscosité turbulente raccordé à une décroissance exponentielle dans la couche d'entraînement, permet : (i) une description de la structure de la couche de mélange et de la couche d'entraînement (ii) une décomposition du champ de vitesse en une composante quasi-stationnaire et une composante oscillante (à la fréquence f, attribuée aux oscillations inertielles), et enfin (iii) une évaluation de la contribution de chaque composante à l'érosion de la couche stratifiée. La contribution des oscillations inertielles s'avère négligeable, et il est démontré que c'est la composante quasi-stationnaire qui contrôle majoritairement le mélange. Cette deuxième dérivation a confirmé la loi d'échelle pour les régimes rotatifs pour $S \sim 3 - 24$, c'est-à-dire les régimes modérément à fortement dominés par les effets de stratification.

Chapitre 4: Régime transitoire et oscillant de la couche d'Ekman Turbulente

Le chapitre précédent se focalise sur l'approfondissement de la couche de mélange pour un forçage constant. Or le vent est intermittent : la couche de surface est donc rarement à l'équilibre, et le plus souvent en processus d'ajustement. Dans ce chapitre, nous reproduisons une étude soumise à la revue *Geophysical and Astrophysical Fluid Dynamics*. Nous y étudions ce régime transitoire à partir d'expériences de spin-up réalisées sur la plateforme Coriolis.

Ces expériences permettent d'observer la mise en place de la couche d'Ekman turbulente (équilibre entre le forçage frictionnel et la rotation). Trois configurations sont comparées : sans rotation ni stratification, sans rotation stratifiée, puis en rotation et stratifiée. Dans les trois cas, les profils verticaux de vitesse, d'énergie cinétique turbulente et de température sont consistants avec les simulations 1D utilisant la fermeture turbulente $k - \varepsilon$.

L'épaisseur de la couche limite se stabilise rapidement, et les vitesses horizontales s'organisent sous forme de spirale d'Ekman : le vecteur vitesse est dévié progressivement avec la profondeur. Cette structure moyenne s'établit en une demi-période inertielle. En parallèle, des oscillations inertielles sont excitées et persistent plus longtemps, pendant environ cinq périodes, avant de s'amortir. Le fait que la structure moyenne s'établisse avant que les oscillations ne disparaissent montre qu'en régime turbulent, la spirale d'Ekman stationnaire et les oscillations inertielles évoluent de façon largement indépendante : elles se superposent linéairement. Ce résultat, exact dans le cas laminaire, n'avait jamais été vérifié en régime turbulent.

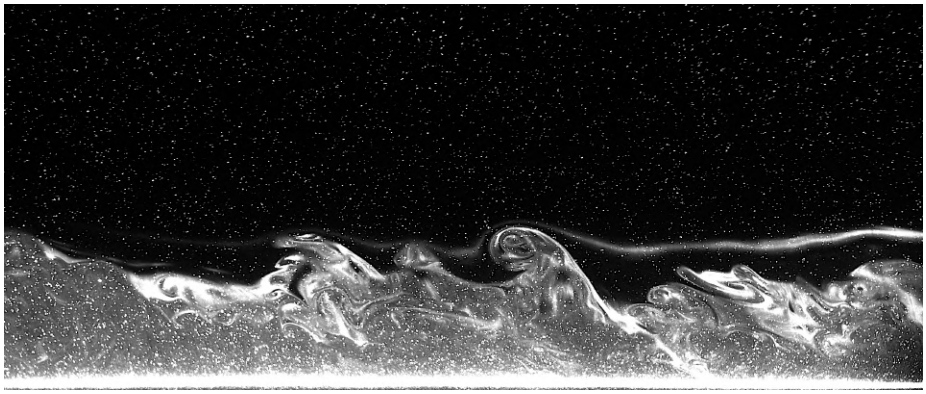

Figure 3: Visualisation sur un plan vertical d'une couche limite cisaillée dans laquelle a été injecté un colorant fluorescent (partie lumineuse). Cette couche cisaillée est forcée par une rotation impulsive de la plateforme Coriolis (transmise par le fond). La région sombre est stratifié en température et initialement au repos. Les points lumineux representent les particules pour la PIV illuminées par laser.

L'amortissement des oscillations inertielles est contrôlé par la formulation de la contrainte de fond : un coefficient de frottement quadratique C_f contrôle la dissipation d'énergie et détermine la durée de vie des oscillations. Cette formulation se situe entre les limites laminaires de glissement libre (pratiquement aucun amortissement) et de non-glissement (fort taux d'amortissement). Une valeur de $C_f = 5 \times 10^{-3}$, calibrée indépendamment avec l'angle isobare obtenu dans les

simulations DNS de Marlatt et al. (2012), reproduit fidèlement le taux d'amortissement observé expérimentalement. Ces résultats soulignent l'importance de la paramétrisation du frottement de fond dans la description de la dynamique transitoire des couches limites turbulentes d'Ekman et confirment la capacité de la fermeture k-ε à reproduire la dynamique dans de tels régimes.

Chapitre 5: Expériences de Convection Horizontale

Dans ce dernier chapitre, nous présentons un travail exploratoire mené lors d'un séjour de deux mois au laboratoire de physique de l'université d'Oxford en collaboration avec P. Read. Nous avons mis en place un dispositif expérimental constitué d'une cuve cylindrique reposant sur une plaque de cuivre refroidie en son centre et chauffée sur sa périphérie. Ce dispositif nous permet d'étudier le processus de convection horizontale et les effets de la rotation sur sa dynamique.

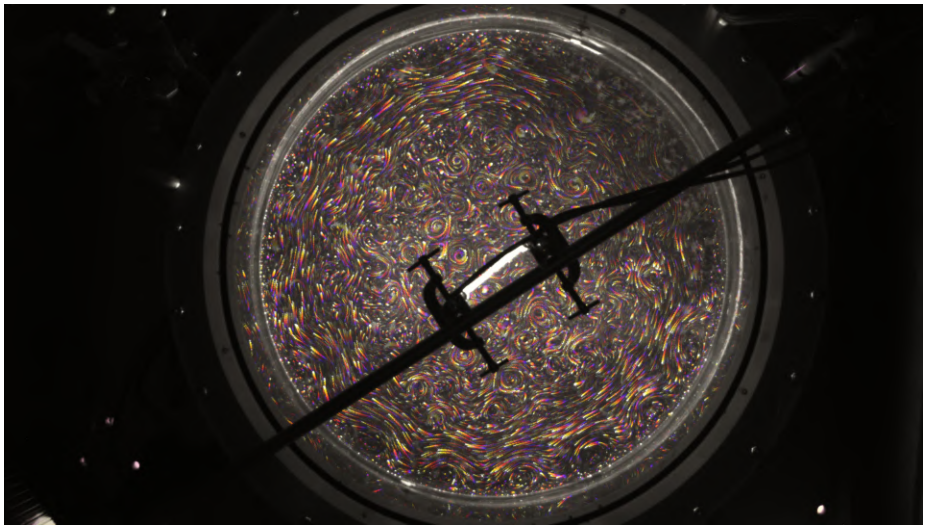

Figure 4: Composition d'une series de 30 images lors d'une experience de convection horizontales. Chaque image (Initialement en noir et blanc) est coloré progressivement du bleu vers le jaune ce qui permet de suivre la trajectoire des particules. Cette configuration expérimentale correspond à un chauffage sur le centre du fond de la cuve et un refroidissement sur le même fond en périphérie.

La convection horizontale désigne l'écoulement produit lorsqu'on chauffe et refroidit un fluide à une même altitude (plus précisément sur un même niveau géopotentiel). Cette configuration a une propriété, connue sous le nom de postulat de Sandström : comme la source et le puits de chaleur sont au même niveau, la circulation engendrée est fondamentalement limitée et devient même très faible lorsque la viscosité du fluide tend vers zéro.

Sans rotation, l'écoulement moyen est stationnaire et reproduit la solution laminaire classique décrite par Rossby (1965). Avec rotation, la dynamique change de nature. L'écoulement devient géostrophique : il s'organise en un équilibre entre la force de Coriolis et les gradients de pression, appelé vent thermique. L'inclinaison des surfaces de densité constitue alors un réservoir d'énergie potentielle. Au-delà d'un certain seuil, cette énergie est libérée par une instabilité barocline,

qui engendre un champ de tourbillons de méso-échelle et rend l'écoulement instationnaire. Les mesures effectuées par PIV montrent que l'énergie cinétique de l'écoulement augmente avec la différence de température imposée au fond et qu'elle est redistribuée par la rotation. À rotation modérée, l'énergie est plus élevée que sans rotation : la contrainte de rotation, qui inhibe les mouvements verticaux, réoriente l'énergie vers les mouvements horizontaux. À rotation plus forte, en revanche, l'énergie diminue et devient du même ordre que celle observée sans rotation.

La conclusion principale est que la rotation est le facteur principal contrôlant la transition de la convection horizontale d'un état laminaire, au sens de Paparella and Young (2002), à un état instationnaire et tourbillonnaire. Ce travail reste préliminaire, mais constitue un premier pas vers une quantification précise de la redistribution énergétique de la convection horizontale en présence de rotation. Par ailleurs, ce travail a également permis de tester avec succès un nouveau système de mesure de température par sondes, ensuite déployé dans les expériences de convection sur la plateforme Coriolis.

Chapter I

Introduction: Wind-Driven Ocean Dynamics

Summary of the Chapter

In this chapter, we introduce the field of wind-driven ocean dynamics and provide a general overview of the processes governing the interaction between the atmosphere and the upper ocean. We describe the energy budget associated with wind forcing and its partition among the different components of ocean dynamics. By doing so, we recall that a fraction of energy comparable to that sustaining the large-scale general circulation is transferred into mesoscale eddies and inertia–gravity wave motions. We then focus on the mixed-layer dynamics and on the key physical processes acting in the surface ocean, which will be extensively used throughout this manuscript. Finally, we position this work by formulating the main scientific questions addressed in this thesis and by outlining the structure of the manuscript.

Contents

I.1 The mixed layer

The upper-ocean forms the dynamic interface through which the atmosphere exchanges heat, water, dissolved gases, in particular CO_2, and momentum with the deep ocean. This layer also interacts directly with the oceanic cryosphere, including sea ice, ice shelves and marginal ice zones, regulating their melting and extent. This interface is characterised by a layer, typically between a few tens and a few hundred metres thick, within which turbulence effectively homogenises water properties. Its role in the climate is significant: the ocean absorbs approximately 25–30% of the anthropogenic CO_2 emitted each year (Wanninkhof et al., 2013; Le Quéré et al., 2015; Watson et al., 2020), and the top two metres of the water column alone contain a quantity of heat comparable to that of the entire atmosphere (Johnson et al., 2012).

The mixed layer depth (MLD) is therefore a key metric for evaluating and comparing numerical ocean circulation models. Note that there is no consensus on the precise definition of this depth (de Boyer Montégut et al., 2004), with several criteria coexisting in the literature, such as density or temperature thresholds (Monterey and Levitus, 1997; Kara et al., 2000) or maximum vertical gradients (Brainerd and Gregg, 1995). The vertical structure of this layer depends heavily on surface boundary conditions, notably wind, heat fluxes, and freshwater fluxes, as well as on the underlying stratification and latitude (rotation). In the idealised case of a steady wind with no buoyancy flux, the dynamics reduce to the classical Ekman layer, whose vertical profile reflects a balance between the Coriolis force and the turbulent diffusion of momentum. In the idealised case of surface cooling without mechanical forcing, the dynamics are dominated by

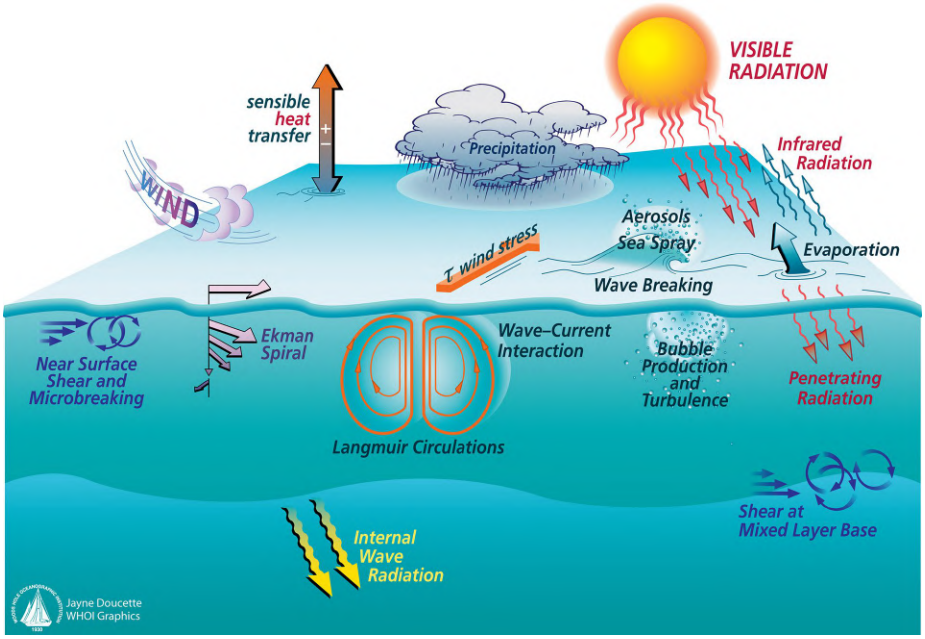

Figure I.1: Scheme of the key physical processes linking the atmosphere, the oceanic mixed layer and the deep ocean. From: Jayne Doucette, Woods Hole Oceanographic Institution, 2013

characteristic coherent convective structures (e.g., plumes (Marshall and Schott, 1999)) which drive heat fluxes and lead to a deepening of the mixed layer.

There are several processes contributing to the formation and maintenance of this layer, as illustrated in Fig. I.1, such as turbulence generated by wind shear, wave breaking, Langmuir circulation, nocturnal or winter cooling, evaporation, freshwater inflow, and brine discharge beneath the ice. The impact of each of these processes on surface dynamics is an active field of research; here we are primarily interested in vertical dynamics and structure of the flow. The origin of convective motion in the mixed layer can be divided into two categories depending on the forcing. We refer to **free convection** when the fluid motion is driven by buoyancy anomalies relative to its surroundings. If the advection is driven by an external mechanical force, for example due to wind stress, we refer to **forced convection**. If both types of forcing are applied simultaneously, we refer to it as **mixed convection**.

While the oceanic mixed layer is generally influenced by a combination of these processes, the present manuscript focuses on idealised configurations in which the forcing mechanisms can be studied separately. In the first part (Chap. III and IV), which is the core of this thesis, is devoted to purely mechanical wind forcing, in the absence of waves, Langmuir circulation and surface buoyancy fluxes. The second part (Chap. V) is devoted to horizontal convection experiments, solely forced by heat flux.

Within this framework, the first step is to understand how wind forces the ocean and how this momentum is redistributed within the mixed layer.

I.2 Wind forcing over the ocean

Wind is one of ocean's main sources of energy. It is partly responsible for its global circulation and it generates turbulence at the air-sea interface. It plays a key role in climate regulation: decadal wind variations, in the context of climate change, directly affect ocean's uptake of heat (McMonigal et al., 2023; Duan et al., 2025) and carbon (Keppler and Landschützer, 2019).

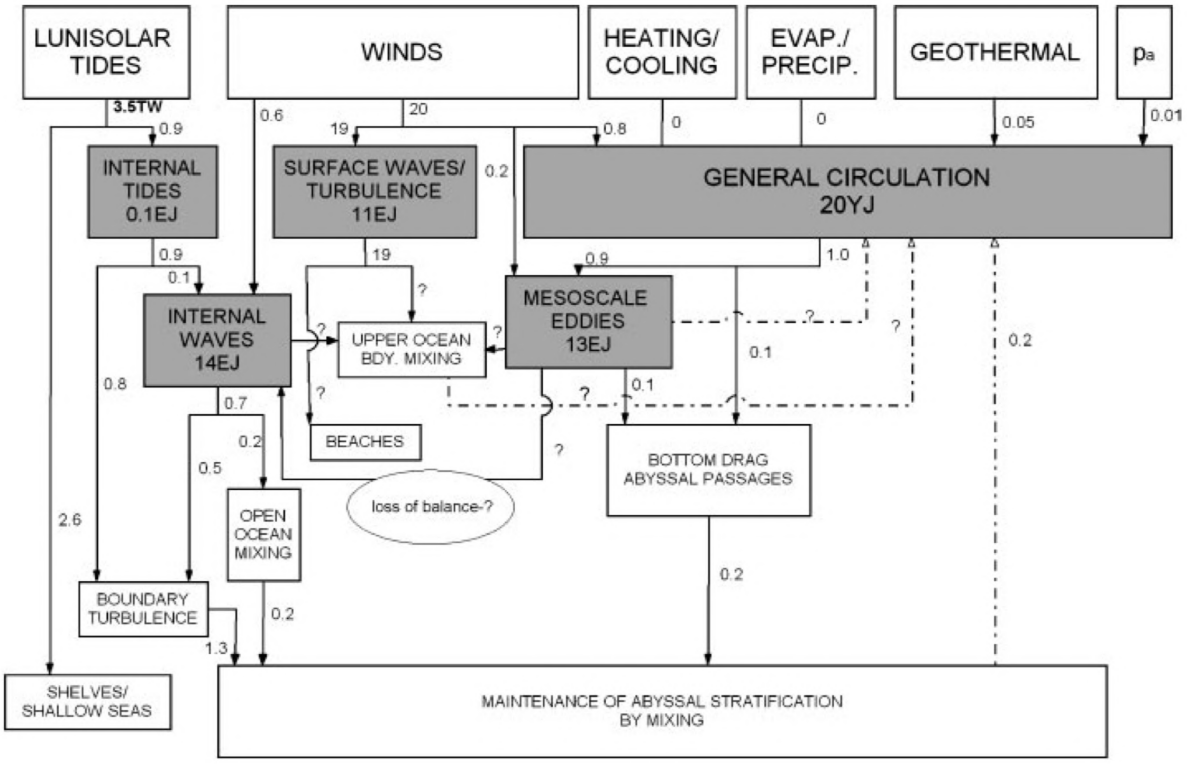

Figure I.2: Diagram showing the distribution of ocean energy across different sources of forcing. The grey boxes represent the various energy reservoirs (in exajoules – EJ 10^{18} J, and yottajoules – YJ 10^{24} J). Fluxes to and from the reservoirs are in terawatts (TWs). The associated uncertainties are estimated to be of the order of 2 at a minimum, up to a factor of 10. Diagram from Wunsch and Ferrari (2004)

In annual average, wind injects approximately 20 TW of kinetic energy into the ocean[1]. This energy injection is not evenly distributed across scales but instead feeds independently several dynamical mechanisms (see Fig. I.3). Wunsch and Ferrari (2004) —building on the estimates of Lueck and Reid (1984)— suggest the following partition:

- **Surface gravity waves and shear driven turbulence:** $\simeq$ 19 **TW:** This is the main outcome of the wind energy injection. Almost all that energy is dissipated within the upper 3 m and on the coastal boundaries.
- **General Circulation:** $\simeq$ 0.8 **TW:** On a large scale, wind forcing imposes a vorticity constraint that controls ocean circulation via the Sverdrup balance (Sverdrup, 1947) in

[1]The estimation of the kinetic energy input from the wind remains debated; values as high as 64 TW have also been proposed (Huang, 2004).

the ocean basins, linking the integrated meridional transport to the curl of wind stress (Pedlosky, 1996; Vallis, 2017; Cushman-Roisin and Beckers, 2011).

- **Mesoscale eddies :** $\simeq 0.2$ **TW:** Fluctuations in the wind forcing lead to the formation of geostrophic vortices (Müller and Frankignoul, 1981; Stammer et al., 2001). These coherent structures are among the most prominent features of the ocean circulation. Their characteristic horizontal scale is set by the Rossby deformation radius,

$$R_d = NH/f \tag{I.1}$$

with f the Coriolis parameter and $N = \sqrt{-\frac{g}{\rho_0}\frac{\partial \rho}{\partial z}}$ the Brunt-Väisälä frequency. Typical values of R_d are in the range 10 - 100 km (Chelton et al., 1998).

- **Inertia-gravity waves :** $\simeq 0.6$ **TW:** For more localized and high frequency fluctuations near-inertial motions and inertia-gravity waves are generated (Liu et al., 2019; Watanabe and Hibiya, 2002).

This distribution suggests that approximately half of the energy that the wind injects beyond the immediate surface layer goes into a steady, large-scale response. The other half can be linked to the intermittent nature of the wind which drives a variety of more localized and transient motions.

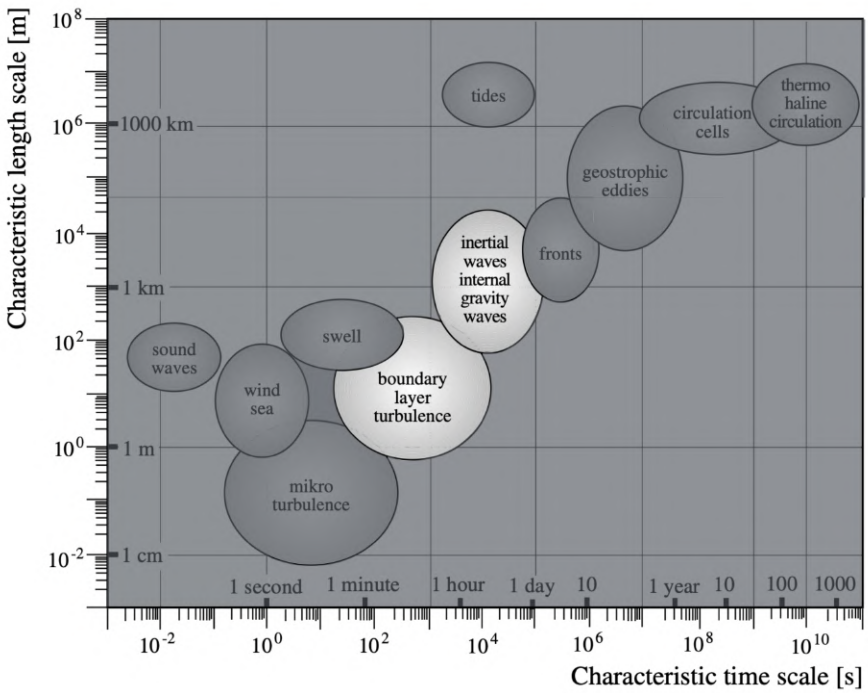

Figure I.3: Scale of process in oceanography, Figure from Von Storch and Zwiers (2002). The light area highlights the range of processes that are considered in this work.

I.2.1 Intermittency of the wind forcing

The inertial period

$$T_f = 2\pi/|f| \tag{I.2}$$

corresponds to the natural period of oscillation of a fluid parcel that has received an impulse in a rotating reference frame. The trajectory of this particle will be circles advected by the mean current (see Fig. I.4). This period depends only on latitude and is typically of the order of one day at mid-latitude. This timescale provides a natural separation within the spectrum of wind fluctuations. Wind variations with timescales longer than T_f primarily contribute to the mesoscale response of the ocean, whereas higher-frequency fluctuations preferentially excite inertia-gravity waves and near-inertial motions.

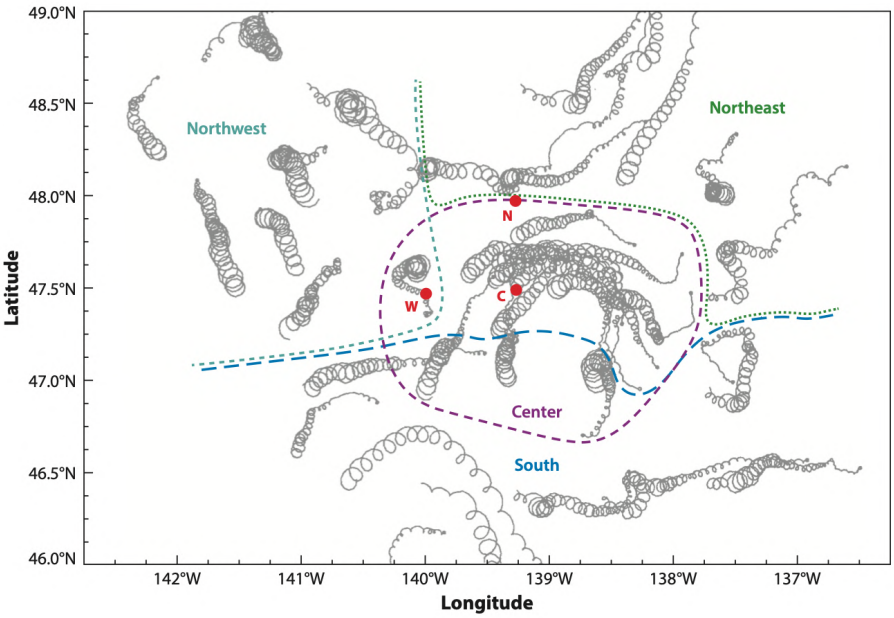

Figure I.4: Drifters' trajectory on the ocean surface during an atmospheric storm at mid-latitude. Figure from Alford et al. (2016) adapted from D'Asaro (1985).

Turbulent wind stress entrains surface momentum and drives boundary-layer turbulence (Thorpe, 2005), which homogenises the first few metres of the water column.

I.3 Turbulent stress and mixing

I.3.1 Wind stress and momentum injection

Standard parametrerization of the surface wind stress (Fairall et al., 2003) are given by

$$\boldsymbol{\tau} = \rho_0\, C_d\, |\mathbf{U}_{10} - \mathbf{u_s}|\, (\mathbf{U}_{10} - \mathbf{u_s}), \qquad |\tau| = \rho_0 u_*^2, \tag{I.3}$$

where U_{10} is the wind velocity, u_s the ocean velocity at its surface[2], C_d a drag coefficient and u_* is the friction velocity. Because the stress is a quadratic function of the wind, fluctuations do not average out linearly but instead contribute positively to the total stress at the interface (Large and Pond, 1981). Zhai et al. (2012) showed that the stress computed from 6-hourly winds significantly exceeds that obtained from the same winds averaged monthly (see Fig. I.5). At a fixed location, the instantaneous friction is therefore dominated by energetic wind events (fronts, storms and wind bursts) rather than by the mean wind itself.

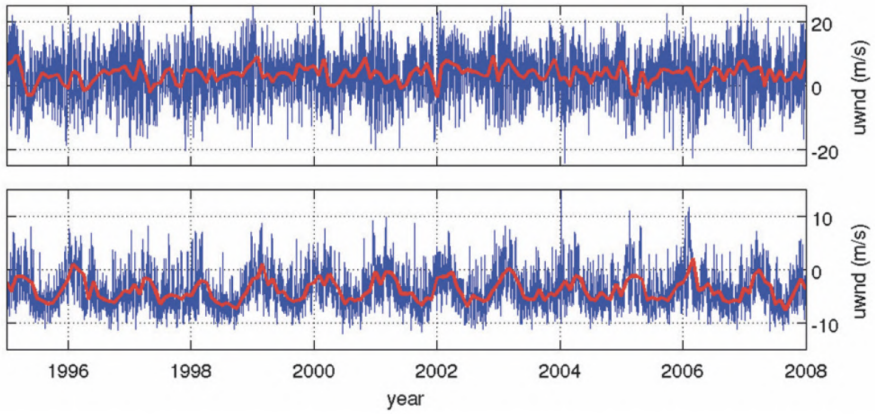

Figure I.5: Time series of the zonal component of the 10-m wind (upper panel: at 50°N, 326°E; lower panel: at 14°S, 184°E). For both, the blue line shows the 6-hourly average wind and the red line represents the monthly averaged wind. Figure from Zhai et al. (2012).

The wind stress affects the momentum equation and as a consequence, is a forcing term of the kinetic energy (KE) equation as

$$\frac{d}{dt}(KE) = \underbrace{\boldsymbol{\tau} \cdot \mathbf{u_s}}_{\text{Injection term}} + \quad \text{Other.} \tag{I.4}$$

I.3.2 Structure of the wind-driven surface layer

The wind-driven surface layer exhibits a vertical organisation resulting from the downward transfer of momentum injected at the air-sea interface (Fig. I.6). This structure can be described in three layers.

Just below the air-sea interface, the wind stress maintains a thin logarithmic layer in which the mean velocity follows a law of the wall profile, analogous to the classical turbulent boundary layers in fluid mechanics (Pope, 2000)

$$\frac{u}{u_*} = \frac{1}{\kappa} \ln\left(\frac{z}{z_0}\right) \tag{I.5}$$

where κ is the Von Karman constant and z_0 is the roughness length.

[2]By convention $\mathbf{U}_{10}$ is measured at 10 m above the sea surface. The $-u_s$ permits the feedback of the ocean current over the wind (Dewar and Flierl, 1987).

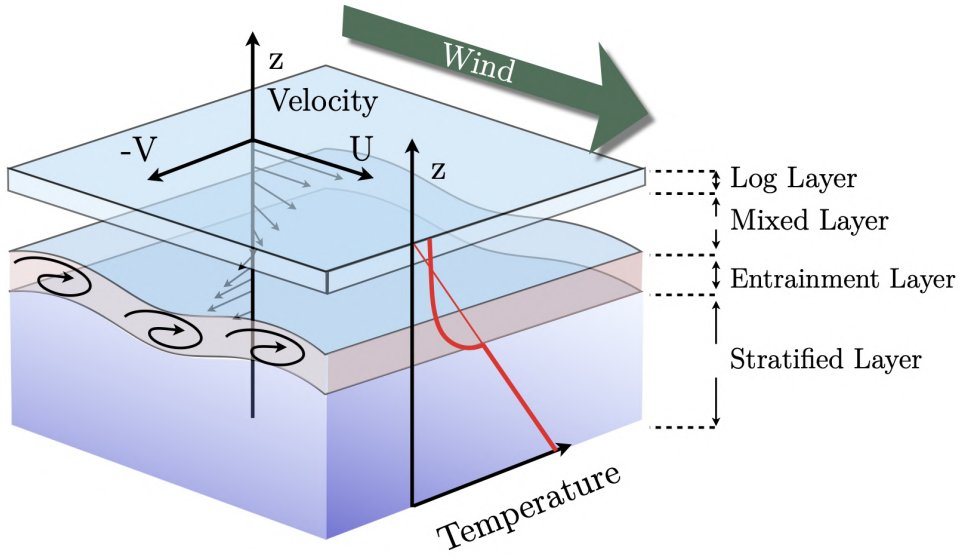

Figure I.6: Scheme of the influence of the wind over a stratified ocean. The upper layer, where the gradient of density represented by the temperature (the salt is not represented on this scheme) is fairly uniform, is the mixed layer. Below, the circular arrows highlight the intermediate layer where most entrainment takes places.

Below this layer lies the core of the mixed layer, where turbulence generated by shear redistributes momentum vertically and maintains an approximately homogenised region (see Sec. I.1). In the absence of stratification and over sufficiently long times, the turbulent stress drives a shear flow that takes the form of an Ekman spiral (Ekman, 1905), characterised by a progressive twist and decay of the velocity vector with depth.

Then, at the lower boundary reached by turbulence, at the bottom of the mixed layer, we find the entrainment layer. There, vertical gradients are maximal and the state of this region is often considered to be in marginal stability. This implies that this layer has a structure such that the density gradient is proportional to the square of the velocity shear and that any disturbance creates mixing. This is formalized by the Richardson $Ri = \frac{N^2}{(\partial u/\partial z)^2}$ reaching a critical value (see Sec.I.4.1). It is through this mechanism that the surface mixed layer progressively erodes the stratification leading to the deepening of the mixed layer.

The vertical extent of the mixed layer results from the competition between turbulence, rotation, and stratification. The thickness h of the mixed layer is therefore controlled by three external parameters: the wind forcing u_*, the underlying stratification N_0 and the Earth's rotation f.

In the limit of a rotating unstratified fluid, an Ekman layer develops over a time scale of the inertial period (Blumen and Lundquist, 2001). (i) The turbulent diffusion spreads the momentum injected at the surface vertically over a distance $\sqrt{\nu_t\, t_i}$ in a time t_i with ν_t the turbulent viscosity (ii) The rotation inhibits the diffusion after half an inertial period. The Ekman layer thickness therefore corresponds to the length $\delta_{Ek} \sim \sqrt{\nu_t\, T_f}$ that diffusion manages to cover over an inertial period (Zilitinkevich et al., 1979).

In the limit of a non-rotating stratified fluid, the mixed layer depth h evolves in time as turbulence erodes the stratification under the competing effect of shear stress and stratification (see Fig. I.7). Pollard et al. (1973) showed that the thickness of the mixed layer h is deepening following

$$h(t) = 2^{1/4} u_* \left(\frac{t}{N_0} \right)^{1/2}. \tag{I.6}$$

For an intermediate regime, the mixed layer experiences the influence of inertial oscillations and the inhibition of vertical penetration from rotational effect. For Pollard et al. (1973) the presence of inertial oscillation halts the deepening. Because they consider a bulk model of the ML the surface velocity is assumed to be uniform throughout the mixed layer and thus deflected by the Coriolis force (following the inertial oscillations) until it becomes exactly opposite to the wind stress at time $t = \pi/f$. At this moment, the work exerted by the wind at the surface drops to zero in average

$$\langle \boldsymbol{\tau} \cdot \mathbf{u_s} \rangle = 0, \tag{I.7}$$

and the transfer of kinetic energy from the atmosphere to the ocean ceases.

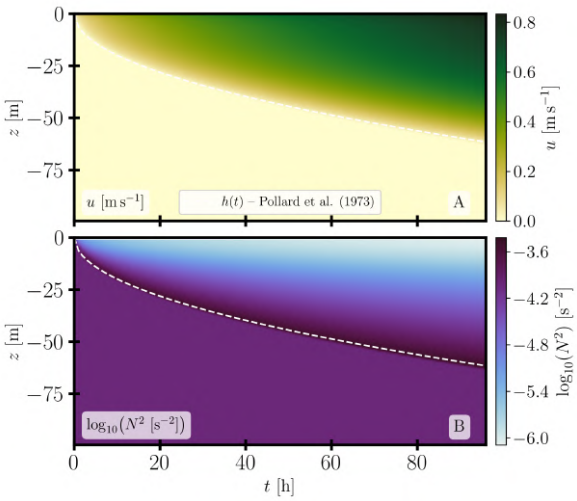

Figure I.7: Evolution of (a) the zonal velocity u and (b) the squared buoyancy frequency N^2 in a wind-stress-driven mixed layer, simulated with a one-dimensional numerical model for $N_0^2 = 10^{-4}\,\mathrm{s}^{-2}$, $u_*^2 = 10^{-4}\,\mathrm{m}^2\,\mathrm{s}^{-2}$, and $f = 0$. Dashed lines show the mixed layer depth predicted by Pollard et al. (1973) (Eq. I.6).

In a model that resolves the vertical structure of the mixed layer, the surface velocity may remain aligned with the wind direction and this intermediate regime is either blocked by stratification or by rotation effect. The ratio N/f provides a natural measure of this competition. In Chap. III, we present an analytical description of the mixing process in a case of wind forcing in the presence of rotation.

Finally, the validity of dynamics is limited by the intermittency of the wind forcing. As emphasized in Sec. I.2, the wind stress fluctuates on timescales comparable to T_f and therefore the boundary layer rarely reaches a steady Ekman configuration. Instead, it remains in a continuously adjusting transient state, in which a significant fraction of the energy input is transferred into near-inertial motions (Watanabe and Hibiya, 2002). Observations confirm that the instantaneous surface current is often dominated by these oscillations rather than by a steady Ekman spiral (Pollard and Millard, 1970; Alford, 2001; Villas Bôas et al., 2019). In Chap. IV, we present an experimental description of the transient turbulent Ekman layer.

I.4 Regime and similitude

I.4.1 Key non-dimensional parameters

As mentioned above, wind-driven dynamics involve several distinct physical processes which vary in intensity: advection by the mean current, planetary rotation, stratification within the water column, vertical shear, molecular and turbulent diffusion of momentum and heat, each operating on their own characteristic timescales. One way of assessing the relative importance of different processes, and thus of characterising the flow regime, is to define dimensionless numbers by comparing these different time scales (Aurnou, 2025)[3].

For a flow with characteristic velocity U and dimension L, advection by the mean flow, i.e. the transport of a quantity by the (mean) flow, is characterised by the advection time $T_{adv} = L/U$. Viscous diffusion propagates the momentum (or heat) over the scale L in a time $T_\nu = L^2/\nu$ (or $T_\kappa = L^2/\kappa$, where κ is the thermal diffusivity). Rotation imposes an inertial frequency on the motion $T_f = 1/f$, and the natural period of oscillation of a fluid particle of different density compared to its surroundings is characterised by the Brunt–Väisälä frequency $T_N = 1/N$. Finally, the vertical shear of the velocity $M = \partial_z U$ also defines its own time scale $T_M = 1/M$.

Comparing these different time scales allows us to determine which process dominates the flow dynamics with non-dimensional numbers. We can organise them around three primary balances, each pitting a destabilising process (advection, or shear) against a process that tends to stabilise or constrain the flow (viscosity, stratification, or rotation, respectively).

Reynolds number The balance between non-linear acceleration terms and viscosity effects is characterised by the dimensionless Reynolds number

$$Re = \frac{T_\nu}{T_{adv}} = \frac{UL}{\nu} \sim \frac{\text{Advection}}{\text{Viscous diffusion}}, \tag{I.8}$$

At high Reynolds numbers, non-linearities dominate and the flow is turbulent in the absence of other stabilising effects.

Richardson number The Richardson number Ri compares the destabilising effect of velocity shear to the stabilising effect of density stratification, which tends to restore displaced fluid parcels to their equilibrium position. This competition is quantified by

$$Ri = \left(\frac{T_M}{T_N}\right)^2 = \frac{N^2}{(\partial U/\partial z)^2} \sim \frac{\text{Buoyancy}}{\text{Shear}}. \tag{I.9}$$

Small values ($Ri \ll 1$) indicate that shear dominates over buoyancy, allowing mixing through the overturning of fluid parcels; large values ($Ri \gg 1$) correspond to strongly stratified conditions

[3]The reader is referred to an elegant presentation of these dimensionless numbers in the context of rotating (free) convection, given by Jonathan Aurnou.

in which vertical motions, and hence mixing, are halted. If a single characteristic velocity and length scale are used in place of the local shear, $\partial U/\partial z \sim U/L$, the Richardson number reduces to the square of the inverse Froude number Fr,

$$Fr = \frac{T_{adv}}{T_N} = \frac{U}{LN} \sim Ri^{-1/2} \sim \frac{\text{Advection}}{\text{Stratification}}.$$

The Froude number can therefore be viewed as a bulk analogue of the Richardson number: $Fr \ll 1$ and $Fr \gg 1$ correspond respectively to strongly and weakly stratified regimes.

Rossby number The Rossby number compares the effect of advection to the Coriolis force,

$$Ro = \frac{T_f}{T_{adv}} = \frac{U}{fL} \sim \frac{\text{Advection}}{\text{Rotation}}. \tag{I.10}$$

Small values ($Ro \ll 1$) indicate that the Coriolis force dominates over advective effects, so that the flow is strongly constrained by rotation; large values ($Ro \gg 1$) correspond to a regime where rotation has a negligible influence on the dynamics, as in many small-scale or rapidly evolving flows. Another number can be directly related to the Rossby and Reynolds number: The Ekman number

$$Ek = \frac{T_f}{T_\nu} = \frac{\nu}{fL^2} = \frac{Ro}{Re} \sim \frac{\text{Viscous diffusion}}{\text{Rotation}}.$$

A small Ekman number means that rotation acts on a much shorter timescale than viscous diffusion over L: friction is then confined to a thin boundary layer, the Ekman layer, of thickness $\delta_E \sim \sqrt{\nu/f}$, consistent with $Ek \sim (\delta_E/L)^2$.

In the context of a fully turbulent frictional boundary layer, U is no longer the relevant velocity scale: it is the friction velocity u_* that determines the amplitude of the turbulent fluctuations, and the characteristic length L is replaced by a length intrinsic to the layer, typically the turbulent Ekman depth $\delta_E \sim u_*/f$ or the roughness length z_0. Thus, we can provide two variations of the above dimensionless number.

Turbulent Reynolds (or frictional Rossby number)

$$Re_* = \frac{u_* \delta_E}{\nu} = \frac{u_*^2}{f\nu}. \tag{I.11}$$

As with the classical Reynolds number, high values of Re_* indicate that the boundary layer (Ekman layer) is in a turbulent state rather than laminar.

Bulk (frictional) Richardson Number

$$Ri_b = \frac{N^2 h^2}{u_*^2} \sim \frac{\text{Potential Energy}}{\text{(Frictional) TKE}}. \tag{I.12}$$

	u_* (m. s^{-1})	f (s^{-1})	N (s^{-1})	B_0 (m^2. s^{-3})	h (m)	Ri_b	Re_*
Ocean	0–$3{\cdot}10^{-2}$	10^{-4}	$0 - 10^{-2}$	10^{-7}	$0 - 2000$	$0 - 10^3$	$10^7 - 10^8$
Coriolis (lab)	$0 - 10^{-2}$	$0 - 0{,}2$	$0 - 0{,}2$	$3 \cdot 10^{-7}$	$0 - 1$	$0 - 500$	$10^4 - 10^5$

Table I.1: Ranges of physical and dimensionless parameters observed in the ocean and in experiments on the Coriolis platform. $Re_* = u_*^2/(f\nu)$ is the turbulent Reynolds number associated with the Ekman depth.

This number is widely used in so-called 'bulk' studies of the mixed layer, as it provides an overall picture of the stability of the mixed layer rather than local stability (Pollard et al., 1973; Niiler, 1975).

Table I.1 shows the different correspondences and similarities between the parameters involved in the convection process in the ocean and in the laboratory experiments carried out during this thesis (see Chap. II).

I.5 Position of the present work

The work presented in this manuscript lies at the interface of three scientific communities. The first is physical oceanography, which provides the conceptual framework for the study through the challenges of modelling the oceanic mixed layer and the associated theoretical approaches. This thesis also has a strong experimental fluid mechanics component, offering an experimental translation of these issues as well as a detailed study of boundary layer turbulence in stratified and rotating fluids. Finally, this work is part of an ocean modelling perspective, providing new experimental constraints for the evaluation and improvement of turbulent closure schemes used oceans models.

I.5.1 The PLUME project:

This thesis is part of the ANR PLUME project (*Observation and Parameterisation of Oceanic Convection*), which aims at improving the representation of oceanic convection in the numerical models. Despite their importance, free and forced convection remain imperfectly understood and are still poorly represented in current ocean and climate models. One of the main difficulties lies in the fact that the turbulent structures responsible for vertical transport, in particular convective plumes, are smaller than the grid resolution of models. These processes therefore must be parameterized. However, the parametrisations currently used in ocean models, such as Enhanced Vertical Diffusivity (EVD), K-Profile Parameterizations (KPP) (Large et al., 1994) or Generic Length Scale (GLS) closures (Umlauf and Burchard, 2003; Burchard, 2002), have significant limitations. Indeed, these closure schemes were historically calibrated on canonical, stationary and non-rotating flows, and their ability to represent rotating and transient oceanic convection remains largely unconstrained by direct observation.

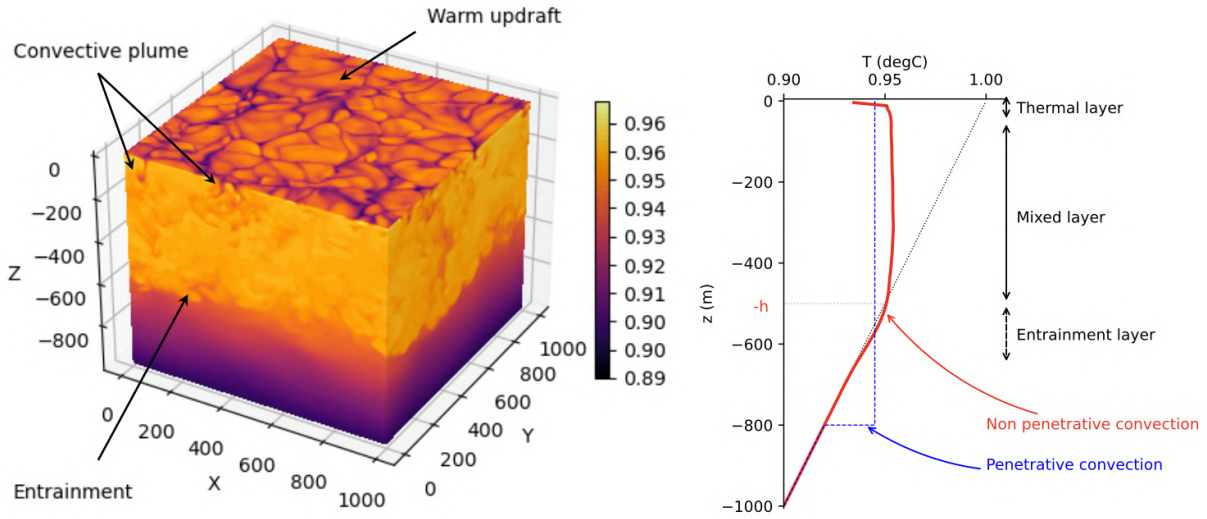

Figure I.8: Left: Numerical model of oceanic convection. The model is initialized with a uniform stratification $N^2 = 2 \times 10^{-7}$ s^{-2} and heat is removed at a rate of $Q = -500$ W .m^{-2}. The snapshot of temperature field (in color, unit of °C) is after one day of simulation. The domain is a cube of 1000 m×1000 m×1000 m. The right panel is the mean vertical profile of temperature averaged over the whole domain (solid red line), the initial profile (dotted black line) and a hypothetical penetrative convection profile (dashed blue).

The PLUME project is based on several scientific assumptions. The first is that a more accurate representation of convective processes would help to reduces the uncertainties associated with heat absorption and redistribution in climate models. The second is that the structure of convection, in particular the distinction between penetrating and non-penetrating regimes (see Fig. I.8), differs significantly between canonical thermal convection and forced convection in the presence of rotation and wind. A third hypothesis is that the parameterisations currently in use do not capture the full range of physical mechanisms governing vertical exchanges within the mixed layer.

In order to test these hypotheses, four main objectives have been defined:

1. Build a consistent database of convective events based on laboratory experiments and LES numerical simulations in order to constrain and calibrate turbulence parameterisations.
2. Characterise the structure of thermal plumes and turbulent shear layers across a parameter space covering the effects of rotation and stratification.
3. Develop a data-driven approach to formulate a model of convection without any preconceived bias about the mathematical formulation.
4. Perform a sensitivity analysis of the oceanic heat uptake in global circulation models as a function of parameterisation of convection.

The experiments enable the convective dynamics to be reproduced in a controlled environment and provide direct insight into the physical mechanisms underlying turbulent transport.

Numerical simulations, meanwhile, provide a better spatial and temporal coverage of the dynamical variables and allow for the exploration of a wider range of parameters. The combined use of these two approaches thus enables experimental observations to be compared with numerical results and a coherent understanding of the various convective regimes to be developed.

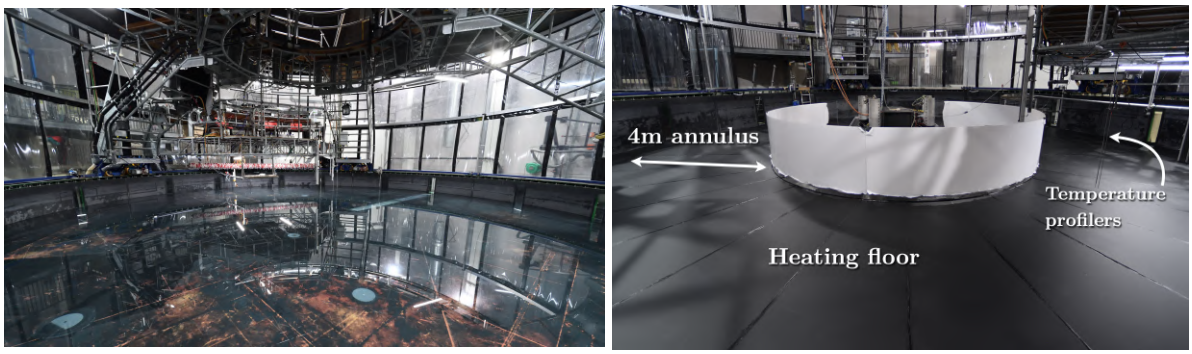

Figure I.9: Left: Picture from inside the Coriolis platform. The gray discs at the bottom are the filling nozzles. The structure at the back is the place where the measurements are monitored (inside the platform). Right: Picture of the Coriolis Platform equipped with a heating floor. Credit: S. Viboud).

This strategy is relevant in the context of convective problems, where the representation of boundary conditions is one of the main challenges in numerical modelling. Experiments therefore provide a realistic framework for evaluating the assumptions and approximations made in the simulations.

In this context, the Coriolis platform plays a central role within the project. With a diameter of 13 m, it is currently the largest rotating platform dedicated to the study of geophysical flows. Its dimensions allow fully developed turbulence regimes to be achieved whilst independently controlling rotation, stratification and the mechanical forcings applied to the surface. It thus provides a unique experimental setting for studying convection regimes relevant to the ocean, observing the large-scale organisation of convection, and quantitatively assessing the validity of the turbulence parameterisations used in ocean circulation models.

I.5.2 Contribution and scientific positioning

This thesis is primarily involved in the experimental component of the PLUME project. The experiments carried out cover all the configurations: free convection (via bottom heating), forced convection (via spin-up), as well as regimes combining thermal and mechanical forcing. My contribution included the experimental implementation of these different regimes, the conduct of data acquisition, and part of the data post-processing. This work notably led to the development of new methods for temperature measurement. As part of this, a research visit to the University of Oxford (AOPP) was dedicated to the development and evaluation of a new method for local temperature measurement, aimed at estimating turbulent heat fluxes.

The scientific section of this manuscript focuses primarily on forced convection and the dynamics of the rotating ocean surface boundary layer under the influence of wind.

The fundamentally transient nature of the rotating boundary-layer dynamics has important consequences for ocean modelling. Firstly, the classical theoretical framework describing the deepening of the wind-driven mixed layer, inherited from Pollard et al. (1973), stated that, in a condition of a constant wind, the generation of inertial oscillations causes the surface velocity $\mathbf{u_s}$ to be deviated and to be at $t = \pi/f$ opposed to the wind stress. The consequence is that the injected energy $\boldsymbol{\tau} \cdot u_s$ is zero in average. Therefore the development/deepening of the surface layer is stopped. However, this conclusion is based on a bulk vision of the mixed layer, whereas in reality, the vertical structure of the velocity is such that erosion can still occur at the base of the mixed layer even if $\langle \boldsymbol{\tau} \cdot \mathbf{u_s} \rangle = 0$. This leads to a first set of questions:

WHAT IS THE INFLUENCE OF INERTIAL OSCILLATIONS ON THE DYNAMICS OF THE OCEAN SURFACE BOUNDARY LAYER? WHAT IS THE DEEPENING REGIME OF THE WIND-DRIVEN MIXED LAYER IN ROTATION?

Secondly, the existing models of inertial oscillations remain poorly constrained by observation (Alford, 2020). The damping rate is often modelled by linear Rayleigh damping term $-r\mathbf{u}$ proportional to the velocity $\mathbf{u}$ (Csanady and Shaw (1980), Ashkenazy et al. (2015) Kim et al. (2014)). The coefficient r being an empirical parameter that aggregates unresolved mechanisms such as surface wave breaking and turbulent dissipation. The transient regime of the Ekman layer has, to our knowledge, never been explored experimentally and remains poorly explored numerically. This leads to a second set of questions:

WHAT IS THE TRANSIENT DYNAMICS OF THE TURBULENT EKMAN LAYER? TO WHAT EXTENT DO THE OSCILLATIONS GENERATED BY WIND FORCING INTERACT WITH THE STEADY-STATE SOLUTION OF THE EKMAN LAYER?

Besides, most turbulent closure schemes used in ocean circulation models (k-ε , KPP, GLS) were primarily calibrated using stationary and non-rotating flows (Large et al., 1994; Umlauf and Burchard, 2003; Burchard, 2002). Their ability to reproduce the transient response of a turbulent rotating flow remains largely unconstrained and needs to be verified in such conditions.

TO WHAT EXTENT DO TURBULENCE CLOSURE MODELS – IN PARTICULAR THE k-ε MODEL – REMAIN VALID IN ROTATING FLOWS? DO THE UNDERLYING ASSUMPTIONS OF ISOTROPIC EDDY VISCOSITY APPLY TO THE STUDY OF ROTATING BOUNDARY LAYERS?

Characterizing experimentally and numerically these three issues constitute the main objectives of the present thesis.

I.5.3 Organisation of the manuscript

The specific contribution of this manuscript concerns: (i) The derivation of an analytical model of a wind-driven mixed layer in rotation. (ii) The acquisition and processing of experimental data for both forced and free convection configurations. (iii) The interpretation of data in forced convection configurations with a characterisation of the transient regime of forced

convection. (iv) The comparison of experimental data with one-dimensional simulations using the k-ε closure scheme. (v) A preliminary investigation on turbulence onset in a horizontal thermal convection experiment. The manuscript is organized as follows.

- Chapter II describes the forced convection experimental setup along with related numerical modelling aspects. It also includes a description of the apparatus for the free convection experiments forced by a heat flux.

The following two chapters form the scientific core of the manuscript which is focused on the frictional effect on a rotating and stratified boundary layer; each addresses a distinct physical question and each forms the content of a publication.

- Chapter III examines the deepening of the forced mixed layer induced by wind in a rotating frame. In this chapter, we develop an analytical framework that predicts the long-term deepening rate and the vertical structure. This chapter is extended by a study of the asymptotic regime investigated using the single-column framework.
- Chapter IV exploits experimental data to characterise the damping of inertial oscillations under realistic turbulent conditions and the transient nature of the Ekman layer; it also provides elements for validating the k-ε closure against experimental data obtained under conditions of rotation.

The following chapter offers an insight into the effect of thermal forcing.

- Chapter V presents a rotating horizontal convection experiment conducted during a research visit to the University of Oxford at the AOPP laboratory, which focuses on the onset of turbulence and the influence of rotation on this onset.

Chapter II

Experimental and numerical Approach

Summary of the Chapter

In this chapter, we present the methods and the models used in this thesis. We begin by presenting the Coriolis platform (LEGI, France), then we explain in detail how forced convection is simulated within it by applying an impulsive acceleration to the angular velocity. The various measurement methods, in particular stereoscopic PIV, are described. Then we detail the turbulent models closures used for one-dimensional simulations carried out using the GOTM[a] (General Ocean Turbulence Model) to study vertical dynamics and evaluate turbulent parametrisations in an idealised framework. A description of the free convection set up is also given

Highlights

- The Coriolis platform (13 m) enables large turbulent regime and reach turbulent Reynolds numbers several orders of magnitude higher than in the historical experiments of Kato and Phillips (1969a).
- Experimental implementation of a turbulent boundary layer allows us to observe realistic boundary conditions that are notoriously complex to reproduce numerically.
- Spin-up experiments accurately replicates a rotational boundary layer driven by friction in the laboratory reference frame, allowing independent control of the rotation rate, stratification and the magnitude of the forcing.
- Free convection experiments were carried out at an unprecedented aspect ratio.
- The k-ε implementation in GOTM is presented.

[a] https://gotm.net/portfolio/

Contents

II.1 The Coriolis Rotating platform

The experimental approach enables convection processes to be reproduced across a fairly wide range of parameters whilst approximating realistic dynamics. With a diameter of 13 m and a maximum depth of 1 m, the LEGI Coriolis platform in Grenoble, shown in Figure II.1, is the world's largest rotating platform dedicated to the study of geophysical flows. The major benefit of conducting research on this instrument is that it allows observation of flows in turbulent regimes, whilst providing a quasi-reproducible framework under similarity conditions of rotation and initial stratification. Moreover, its modularity allows it to be fitted with various equipments to reproduce a large range of geophysical processes, such as gravity flows (Rétif et al., 2024; Tassigny et al., 2024), bottom bathymetry and tidal currents (Tassigny et al., 2026), discharge of a river into a lake (Shi et al., 2022) or the formation of jets in large-scale flow (Read et al., 2015).

During this work, two separate experimental campaigns were carried out: one for forced convection and one for free convection experiments. In the following two sections, we describe the experimental configurations developed as part of the project to which this thesis relates. Each configuration has specific characteristics related to the type of forcing under consideration, namely mechanical or thermal forcing.

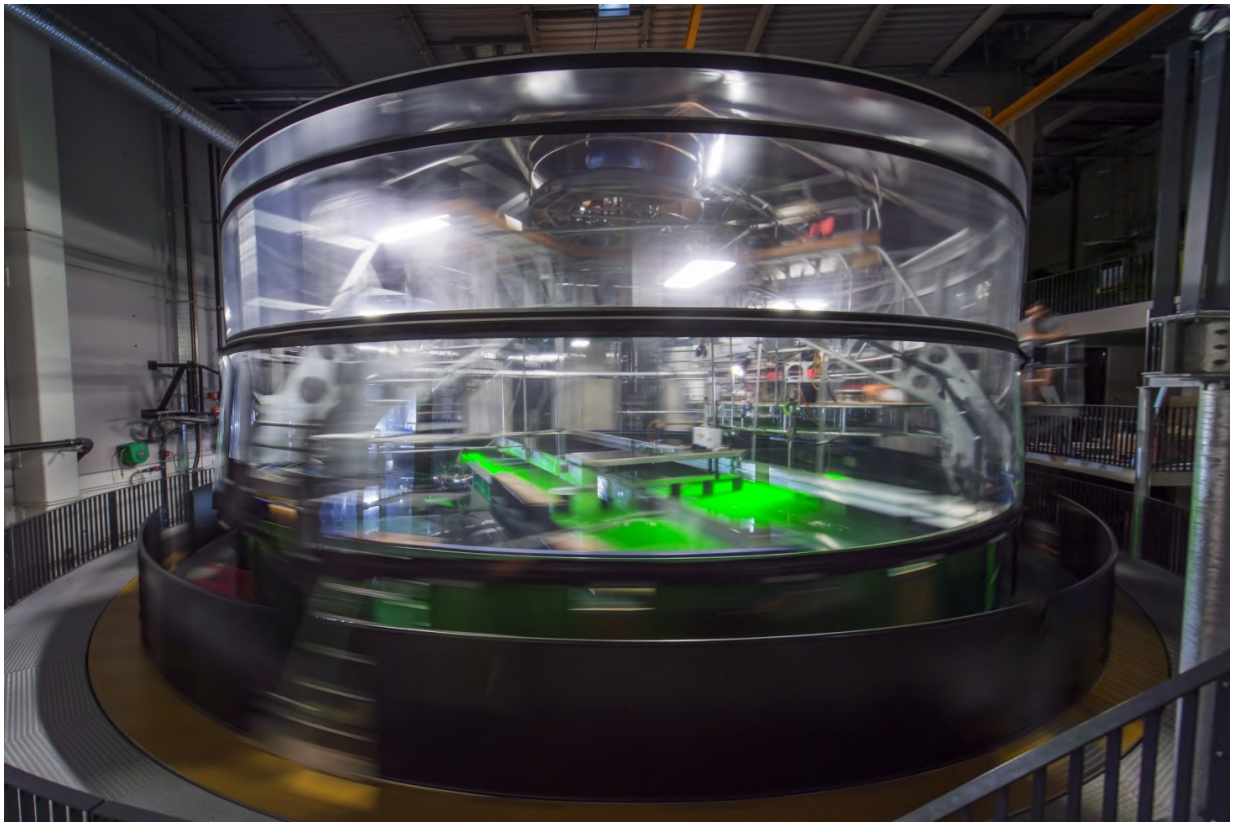

Figure II.1: Coriolis Platform. Credit: Cyril Fresillon

II.2 Forced convection experiments

The experimental configuration described in this section aims to work on the canonical turbulent entrainment experiments conducted by Kato and Phillips (1969b) and later by Kantha et al. (1977) (hereinafter referred to as KP and KPA respectively). These experiments laid the foundations for the study of entrainment in a stratified layer (linear for KP, two-layer for KPA) initially at rest, subjected to a surface shear stress, by tracking the vertical penetration of the interface between the stationary fluid and the entrained fluid. And thus, the evolution of the mixed layer.

The Coriolis platform allows this canonical configuration to be extended: first, the size of the tank provides access to turbulent Reynolds numbers Re_* higher than those of the historical implementations of KP and KPA, and second, the platform allows for the implementation of an impulsive acceleration (spin-up) on a fluid already in rotation, thereby extending the study of turbulent entrainment to rotating boundaries layers and covering the competition between rotational and stratification effects on the development of the mixed layer.

Note however that, whilst we are able to control the platform's rotation rate, it is not possible to maintain a constant torque throughout an experiment, something that KP and KPA have achieved. This implies that the value of the friction induced at the wall in our experiment is not constant over time.

II.2.1 Apparatus

The working area in this configuration is the entire cylindrical basin of the platform (132 m^2), filled with water to a depth of $H = 50$ cm. The stratification consists in a vertical temperature gradient (see procedure in Sec. II.2.2). The mechanical forcing is applied at the bottom of the tank by an impulsive variation in the platform's rotational speed; within the framework of the Boussinesq approximation, this upside-down configuration is equivalent to a wind stress applied to the ocean surface (Sous et al., 2013). All instruments are fixed to the rotating frame of reference and is organised around two types of measurement. The first consists in cameras observing a vertical laser sheet (see Sec. II.2.1.1) illuminating the water column in a plane tangent to a radius of $r_0 = 4.5$ m. The second type of measurement consists in a single-point Acoustic Doppler Velocimeter (ADV) probe positioned on the same radius as the laser sheet, which provides a velocity measurement at a fixed altitude (not shown in Fig. II.2) and three temperature/conductivity probes mounted on a motorised vertical shaft, which allows vertical profiles to be taken; the three profilers are positioned at 2.5 m, 4 m and 5 m from the centre of the tank, respectively.

Moreover, for certain experiments, dye is injected into the bottom layer of fluid (at the bottom of the tank), providing a qualitative visualisation of boundary layer turbulence (Fig. II.8). These components are described successively below.

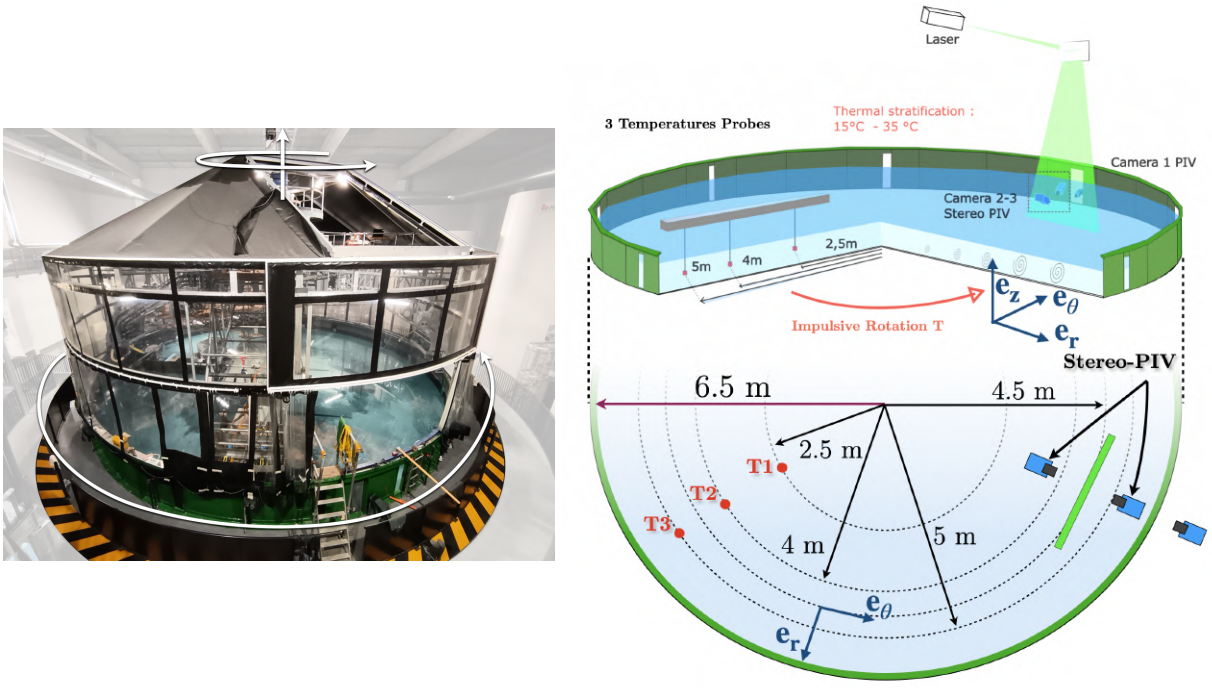

Figure II.2: Illustration of the experimental apparatus. Left: Picture of the 13 m wide rotating Coriolis Platform. Right: Schematic side and top view of the experimental set-up. The water height in the tank is 50 cm.

II.2.1.1 Vertical laser

The laser beam is generated by a continuous YAG laser (5 W, $\lambda = 532$ nm) attached to the platform structure (fixed to the tank), the beam is then spread into a flat sheet by a Powell lens and reflected downwards along a vertical axis by a mirror (see the detailed setup in Figure II.3). The sheet enters the water column from above with a thickness of approximately 0.5 cm, extends vertically throughout the water column, and covers a width at the bottom of approximately $L_{\text{laser}} \approx 50$ cm at the measurement radius r_0. The light emitted by the laser is then reflected by polyamide particles (Orgasol, 60 µm in diameter, close to neutrally buoyant) which have been seeded throughout the water column. A particular feature of these experiments is that the seeding must be as homogeneous as possible across the water since we move along the periphery by the mean motion of the platform.

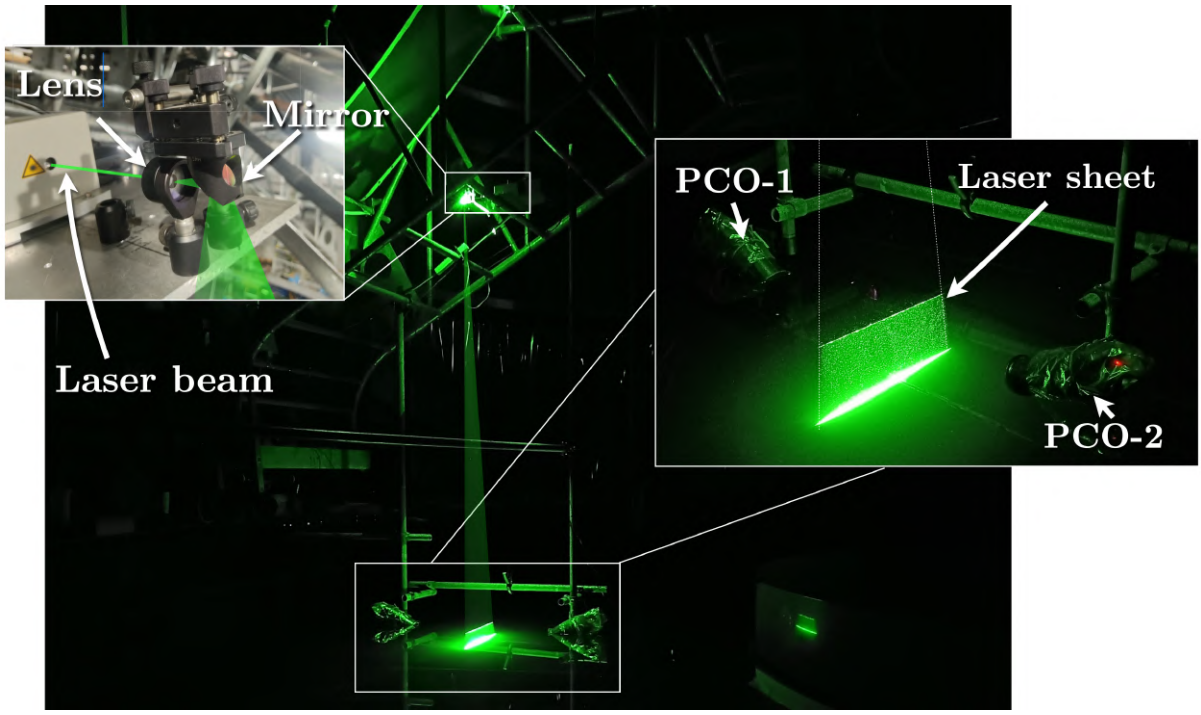

Figure II.3: Photograph of experimental setup depicting the device forming the laser sheet (Laser + lens + mirror) illuminating the Orgasol particles suspended in the fluid, and the apparatus supporting the two cameras above the surface. In the upper right box, the illuminated region is in the water.

II.2.1.2 Camera

This laser sheet is visualised by a set of cameras. In this experimental setup, two types of camera were used. The first are PCO[1] cameras, which offer large dynamic range in greyscale but have limited acquisition speed and spatial resolution. The second type is a JAI[2] camera, which is more limited in number of grey levels but possess

[1] sCMOS PCO EDGE 5.5 - B&W 16bit 2560×2160 pixels (5.5 MPix)
[2] sCMOS SP-12000M-CXP4 - B&W 10bit 4096×3072 pixels (12 MPix)

a much higher spatial resolution than the PCO, making them particularly suitable for large fields of view, especially horizontal ones, such as those described in section II.3.2. The first experimental setup involved observing the laser beam using a camera positioned behind a window and another positioned just above the free surface (see Fig. II.4). Both of these configurations proved to be problematic, each for different reasons. The camera positioned above the surface was affected by slight deformations of the free surface, making the images unusable. For the second camera, situated behind the viewing window, problems arose mainly during stratified experiments. In this case, the optical path was aligned with the isopycns, and the slightest variations in density altered the refractive index along the light's path. This effect was all the more pronounced as the camera was situated two metres from the laser sheet, these disturbances resulting in a "blurry" effect. This is particularly true in spin-up experiments, in which centrifugal acceleration forces the water masses towards the outer edge of the platform. The regions near the outer walls, which also correspond to the areas most affected by mixing, are therefore particularly prone to these optical disturbances (see Flór and Bush (2002)). In the case of saline stratification, an alternative method to avoid these effects is to add ethanol (Tassigny et al., 2026), but this proves to be quite costly in the quantities required given the scale of the Coriolis platform.

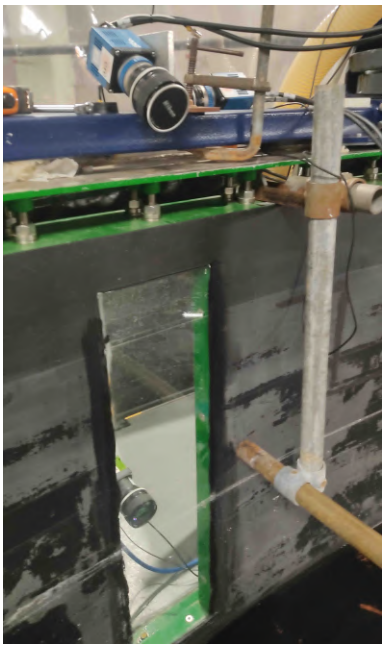

Figure II.4: Camera set-up for the observation of the vertical sheet. The JAI (in green) is positioned behind a window and the PCO (in blue) observes across the free surface.

The method ultimately adopted therefore consisted of two PCO cameras positioned face to face, both inserted into PVC tubes with one end submerged and sealed by a Plexiglas window as illustrated in Fig: II.5. This setup both bypasses disturbances that distort the free surface and allows for the most direct possible observation through the water column. PCO cameras were chosen due to their grey-scale dynamics, which are essential for the quality of the measurements. However, the required acquisition frequency, in the order of 100 Hz, necessitated an adjustment to the acquisition mode. Initially, the maximum frequency was increased by reducing the region of interest (ROI) of the image. For the second experimental campaign, the use of new-generation PCO cameras enabled the acquisition rate to be increased through the use of a rolling shutter. This method involves not acquiring all pixels simultaneously, but scanning the image progressively (for example, from right to left), which allows the acquisition rate to be increased without reducing the field of view.

II.2.1.3 ADV - Probes T/C

The Acoustic Doppler Velocimeter (ADV) is positioned on the same radius as the laser sheet, opposite the tank, in order to avoid any disturbances in the PIV field. This ADV is used to validate, at a given altitude, the PIV data and, more specifically, the transverse component obtained by stereoscopic PIV.

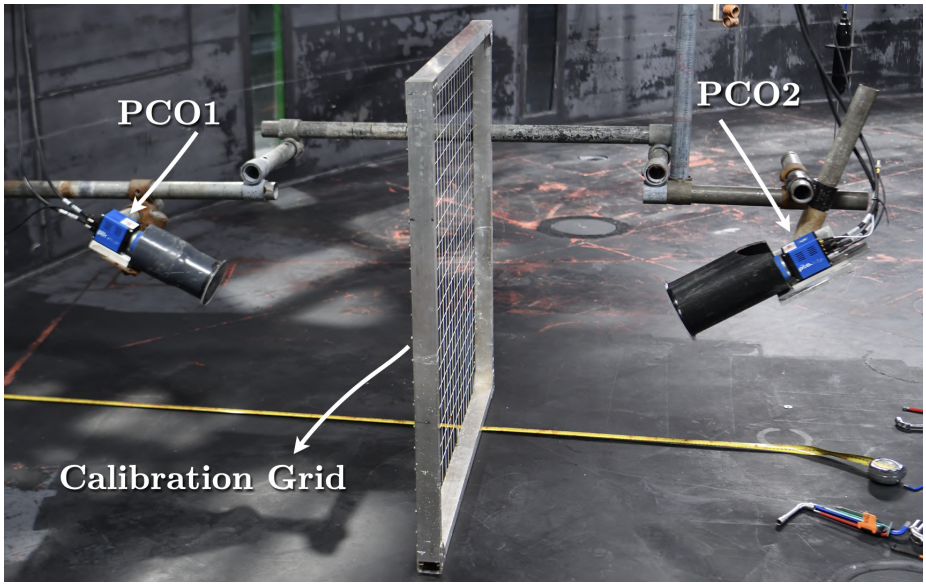

Figure II.5: Picture of the S-PIV setup: the two (PCO) cameras are positioned in such a way that their fields of view are the same but with different angles of incidence. A frame supporting a wire grid, spaced at regular intervals of 5 cm, is positioned at the PIV slice location and is used to calibrate the geometric distortion caused by the lenses.

Temperature and salinity measurements are carried out by three vertically profiling temperature/conductivity probes (hereinafter referred to as T/C probes), mounted on a motorised carriage positioned along a radius of the tank. The probes sample at radial distances of $1{,}5$ m, $2{,}5$ m and 4 m from the outer wall. As for the ADV, these probes are placed at the azimuthal position diametrically opposite the S-PIV measurement plane, in order to minimise the hydrodynamic disturbance they induce on the velocity field. Each probe traverses the water column at a vertical velocity of 3 cm.s^{-1} with an acquisition frequency of 240 Hz; the raw profiles are then interpolated onto a regular time–vertical grid with a resolution of $\Delta t_{\mathrm{Temp}} = 0.01$ s and $\Delta z_{\mathrm{Temp}} = 1$ mm. Only the descending profiles are retained.

II.2.2 Experimental procedure

The procedure for each experiment is divided into two steps. The first involves the preparation of a stable stratification in temperature. The second step involves the application of a frictional forcing that drives the turbulent boundary layer by means of an impulsive acceleration of the platform. For all the experiments, filling is carried out from below via a filling nozzle covered by a disc with a diameter of 1 m. The positioning of this disc reduces vertical velocity that might be introduced by the filling nozzle (see Fig. II.6)

II.2.2.1 Initial stratification

Thermal stratification As mentioned above, the tank is filled from the bottom using several filling nozzles shown in Figure II.6, and the water is supplied from two separate tanks, A and B.

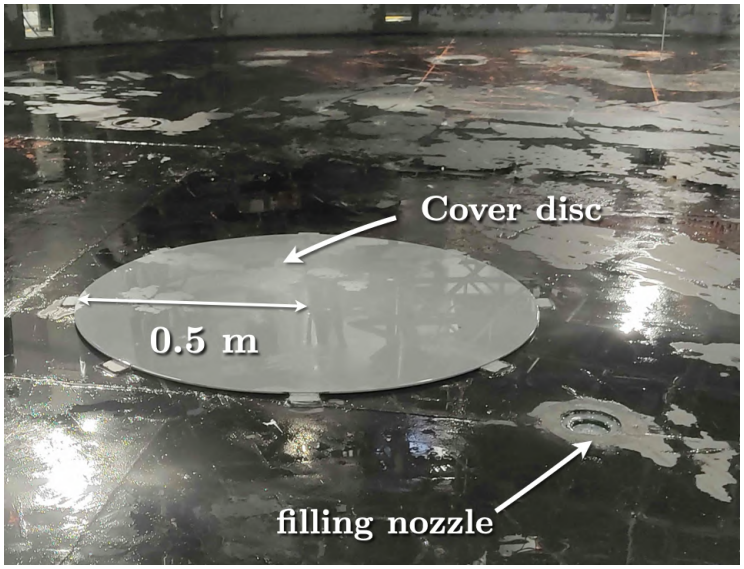

Figure II.6: Filling nozzle and its removed cover disc, which enables filling from below with the smoothest possible flow and removing the vorticity injected in the rotating case. The flow rate for one ensemble is ≈ 15 m^3/h.

Tank A is filled with tap water at $15°$C, whilst tank B allows the water to be heated up to $37.5°$C. Filling begins using only water from tank B. Note that, as we start with hot water, the water temperature spreads partly through the pipes, resulting in an outlet temperature (in the tank) of around $35°$C. Then, as filling continues, the proportion of cold water supplied from tank A increases, reaching 100% by the end of the filling process. In practice, the water being injected, which is denser than that already present in the tank, 'pushes' the lighter layers and inserts itself underneath, thus creating a 'layered' structure of increasingly dense (colder) layers. The resulting profile is close to a constant vertical temperature gradient, characterised by the buoyancy frequency

$$N^2 = -\frac{g}{\rho_0}\frac{\partial \rho}{\partial z} = g\,\alpha_T\,\frac{\partial T}{\partial z}\,, \tag{II.1}$$

where α_T is the thermal expansion coefficient and ρ_0 is a reference density (conventionally taken as $20°$C). The temperature of the laboratory where the platform is located is controlled but cannot be set to the surface temperature of the tank (corresponding to the hottest temperature) for obvious reasons.

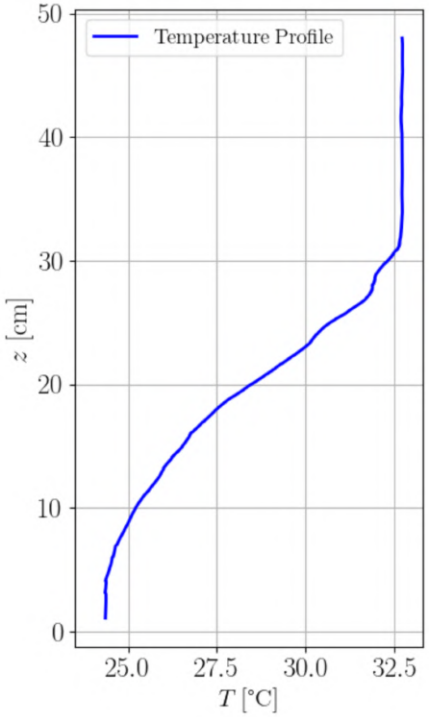

Figure II.7: Example of a vertical profile of the temperature.

Thus, although the tank is more or less hermetically sealed, heat loss occurs at the surface in the upper layers, and this loss is all the greater the longer the filling takes. To address this issue, we tested the use of tarpaulins – bubble wrap – to limit heat loss during the filling phase, but these proved difficult to remove without causing significant surface disturbance.

A compromise was therefore made on the filling speed, which was set at 4 hours for a water depth of 50 cm, corresponding to a flow rate of ≈ 15 m^3/h.

With this method, the resulting thermal stratification (see Fig II.7 for example) was practically linear over the first 30 centimetres (from the bottom) with a difference in temperature between the top and the bottom of the stratified layer $\Delta T \approx [10 - 15]^\circ$C; the temperature became homogeneous over the 20 centimetres above. Given that our study focuses on the bottom boundary layer, this homogeneous portion is of little significance. In experiments involving rotation, the filling process takes place in the initial rotating frame of reference. We use a thermal rather than a haline stratification because these experiments also provide a preliminary test of the experimental methodology required for the free-convection campaign on the Coriolis platform (see Sec. II.3.2).

Dye injection For experiments involving the visualisation of a tracer and its evolution within the boundary layer (Sec. II.2.1.2), a fluorescent dye (Rhodamine 6G) is injected into the densest layer at the end of filling (corresponding to a concentration of 0.2 g per 4 m^3) prior to the application of the forcing. A settling time is required to allow the dye to flow across the entire surface of the platform. Given the dimensions of the platform, it is unrealistic to expect a homogeneous distribution of dye. Nevertheless, this allows us to qualitatively monitor the development of boundary layer turbulence and the entrainment of the stratified fluid (Fig. II.8).

Figure II.8: Picture of a coloured layer with dye. The experiment is a spin-up in a rotating frame. The bottom is the Coriolis floor. The observed field is 35 cm in the x-axis and 26cm in the y-axis

Several elements must be taken into account when defining the initial conditions for the experiments. Firstly, as mentioned above, filling is always carried out (for rotational experiments) in the rotating frame; it is therefore common for vortex structures to form during this process. The dissipation of these structures is slow compared to the rotation period in the presence of stratification. Secondly, the formed stratification diffuses over time; whilst a salinity stratification may persist for days or even weeks, this is not at all the case for temperature, which has a higher diffusivity. Consequently, we cannot generally expect a perfect steady state, as this would take too long given the persistence of the temperature stratification. Thus, the characterization of the initial state as 'at rest' must take these considerations into account.

II.2.2.2 Mechanical forcing

Let Ω_i be the initial rotation (solid rotation of the fluid column) of the platform ($\Omega_i = 0$ in the case of no rotation). The flow is forced by an impulsive change in the platform's rotation rate $\Delta\Omega = \Omega_f - \Omega_i$. We refer to this procedure as *spin-up* when the rate is increased ($\Delta\Omega > 0$) and *spin-down* when it is decreased. In all the experiments presented here (unless stated otherwise), the same increment $\Delta\Omega = 0.053$ rad.s^{-1} is applied. Given the platform's inertia, this impulse does not result in an instantaneous change but rather in an acceleration ramp. Figure II.9 shows the velocity measured at $r_0 = 4$m by PIV and the platform's azimuthal acceleration measured by an accelerometer. We can see that the nominal target speed is reached in ≈ 20 s and that the velocity ramp is relatively linear; furthermore, no overshoot is measured. This ramp also allows us to define the time $t = 0$ of the experiment, which is set when the observed velocity corresponds to half the nominal velocity; this also allows us to synchronise the various instrumentation channels (PIV-Probes).

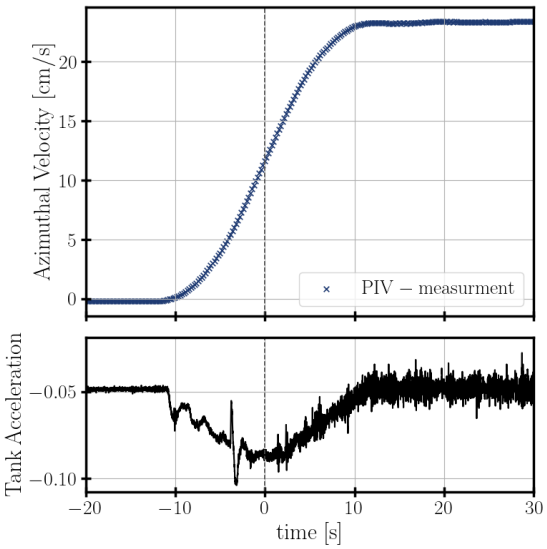

Figure II.9: Time series comparing the PIV-measurement versus the azimuthal acceleration of the platform measured from the accelerometer during an impulsive acceleration (Spin-up procedure).

In the platform's reference frame, this impulse is equivalent to suddenly setting the bottom of the tank in motion at an azimuthal velocity $v_0 = r_0\,\Delta\Omega \simeq 23.5$ cm/s at the measurement radius r_0, whilst the interior of the fluid remains momentarily at rest due to inertia. The resulting shear stress at the bottom, $\tau = \rho\, u_*^2$ where u_* is the friction velocity, leads to the growth of a turbulent boundary layer which gradually sets the column into solid rotation at the new rate.

II.2.3 Measurement techniques

II.2.3.1 Stereoscopic PIV

The principle of stereoscopic PIV (S-PIV) is based on the redundancy of observational data. The basic idea is to use two cameras with the same field of view but different angles of view. The set-up used for all our experiments, shown in Figure II.5, illustrates the placement of our two cameras facing each other and positioned in such a way as to minimise the optical path for the reasons outlined in Sec. II.2.1.2. Each camera measures a velocity field using conventional PIV within the laser slice (2D); the two velocity fields obtained are then combined, using geometric arguments, to obtain a third velocity component (the component transverse to the laser slice) within the 2D field. This is referred to as a 3C2D field, denoting three components within a 2D field.

In detail, for each observation point, the camera measures the displacement (as in conventional PIV) of the particles in the plane perpendicular to the line of view. This principle, illustrated by the schematic diagram II.10, is based on the fact that the laser sheet has a finite thickness d_l. Thus, each point on the laser slice is observed twice, but the displacement is observed in two different planes and therefore depends on its position, the position of the cameras, and the geometric deformations induced by the objective lenses.

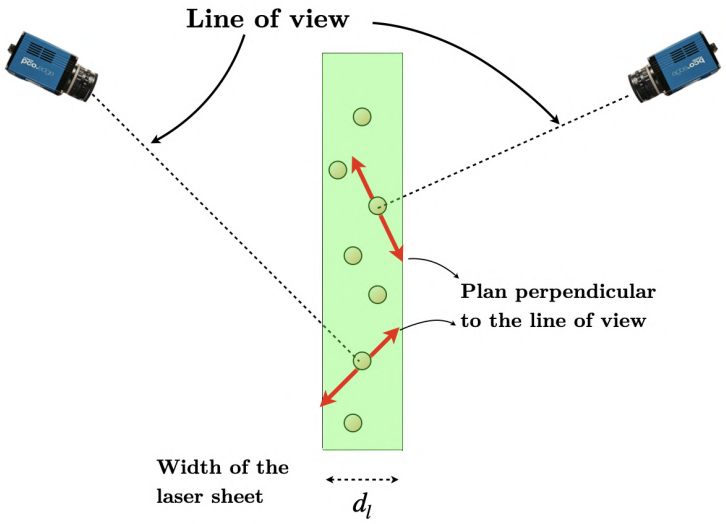

Figure II.10: Schematic illustration of the S-PIV method using two cameras.

Finally, this shows that, despite the relative thinness of d_l compared to the length and height of the laser sheet, the accuracy of the S-PIV method in the transverse component is no less than in the other two components.

For a more detailed description of the S-PIV technique and the details of the geometric matrices used to reconstruct the third component, the reader is directed to Sous and Sommeria (2012). All the post-processing are performed using the UVMAT[3] software.

II.2.3.2 Dye-visualisation

The classical LIF (Laser Induced Fluorescence) method consists in injecting a fluorescent dye into a fluid. Once illuminated by a laser, the chemical species re-emits light in the form of fluorescence. There is a bijective relationship between the concentration of the dye chemical species and the intensity of the light it re-emits. Thus, for short times (shorter than diffusive times), it is possible to correlate the concentration of the dye with a quantity that would otherwise be difficult to measure (such as temperature or salinity). However, using this method requires rigorous calibration and a good knowledge of the initial state of the field. Indeed, if we want to correlate a temperature field with a dye concentration field, this requires the state to be perfectly stable. For an experiment on the scale of the Coriolis platform, the LIF method[4] for a

[3] https://gricad-gitlab.univ-grenoble-alpes.fr/legi/soft/uvmat-doc

[4] Note this is different from the T-LIF method (described in Appendix: A.1.1) which is based on an homogeneous distribution of a thermo-reactive fluorescent dye (Rhodamine-B).

temperature measurement is too imprecise because the setting of a temperature stratification is particularly delicate due to its very limited lifespan (unlike salt) of around ten hours. It is therefore impossible to expect a sufficiently horizontally uniform concentration for this method.

II.3 Free convection experiments

The experiments described in this section aim to observe thermal convection in rotation. These experiments lead to a submitted article which is not included in this manuscript:

> Marchand, O., Negretti, E., **Coppin, M.**, Valran, T., Viboud, S., Deremble, B., Sommeria, J. (submitted). "Laboratory experiments on rotating convection in a stratified fluid at high Rayleigh number." *Journal of Fluid Mechanics*.

This experimental campaign, comprising 31 distinct experiments, covers a range of flux Rayleigh numbers $10^7 \leq Ra_f \leq 10^{11}$, with $Ra_f = B_0 H^4/(\kappa^2 \nu)$, where B_0 is the buoyancy flux, H the water depth, κ the thermal diffusivity and ν the viscosity. Rotation is investigated over a wide range, from the non-rotating case up to a period of 40 s ($f = 0.3$ s^{-1}). The effects of stratification are also addressed through the set-up of linear thermal stratification (similarly to forced convection experiments).

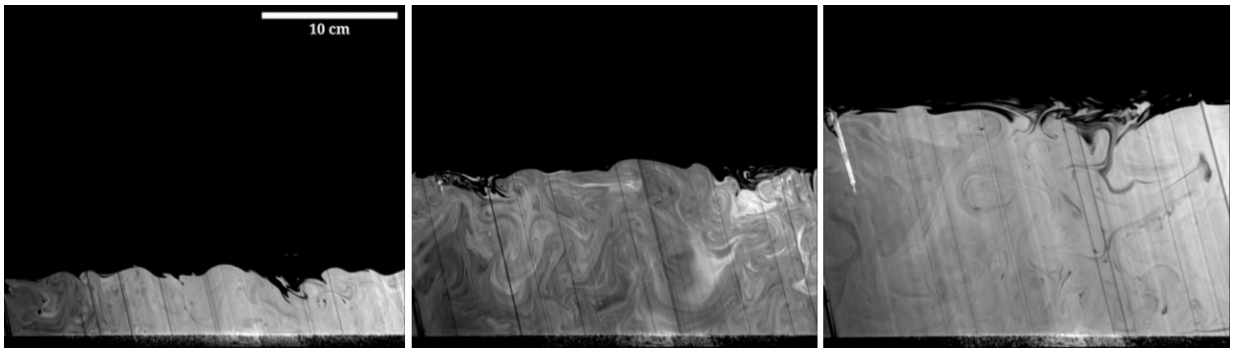

Figure II.11: Sequence of flow visualizations in a vertical plane from stratified experiment in free convection experiment without rotation. The light region is dyed with Rhodamine G. Three moments are shown: $t = 780$ s, $t = 2780$ s, $t = 4780$ s. Courtesy of Olivier Marchand

II.3.1 Apparatus

This configuration is dictated by two constraints: firstly, the presence of the heated floor blocks the usual filling outlets of the tank; secondly, a laser has been installed at the centre of the tank to illuminate a horizontal plane. Despite this reduction in the working volume, this configuration provides a heating area of nearly 100 m^2, making it the largest rotating convection experiment (with the exception of previous experiments carried out on the Coriolis platform). Furthermore, the small aspect ration allows for (i) a very broad sampling of convective structures,

providing good statistical representativeness, and (ii) large-scale observation of the organisation of convection. For the last four experiments, the water depth was increased to approximately 1 m, compared with 50 cm for the others, in order to increase the Rayleigh numbers achieved.

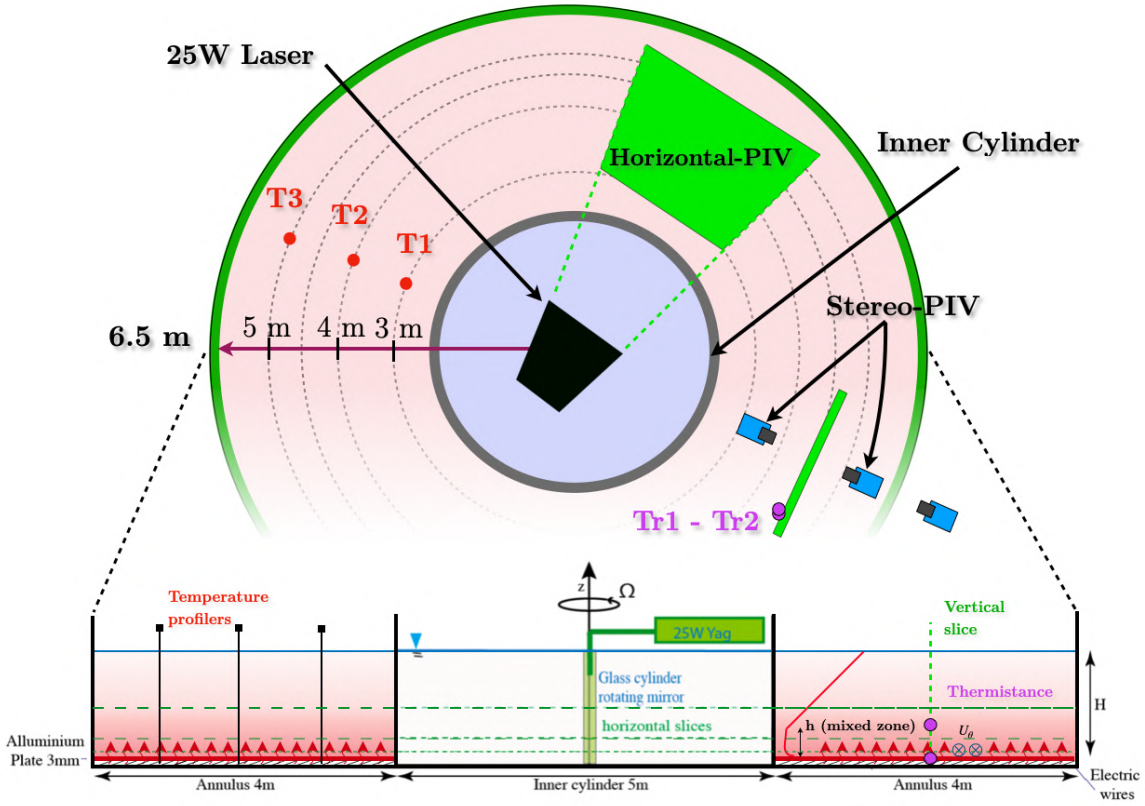

Figure II.12: Schematic top and side view of the experimental apparatus for the free convection configuration.

The instrumentation for this configuration incorporates many elements described in the previous section II.2.1; we present here only the new elements.

II.3.1.1 Heating device

The annulus is uniformly heated from below by a grill-work of electrical wires (see Fig. II.12) embedded in a shallow water layer (3 cm thick) separated from the main working volume by a 3 mm thick aluminium sheet. The wires are disposed in a spiral from the outer edges to the inner edge of an annulus domain of width $R = 4$ m (see Fig. II.13b)). The heating power is about 45 ± 0.2 kW, providing at the bottom a heat flux $Q = 381 \pm 8$ W m^{-2}. The resulting buoyancy flux can therefore be estimated to $B = \alpha g Q/(\rho_0 c_p) \approx 2.5 \times 10^{-7}$ m^{2}s^{-3}. A layer of sand is poured above the wires, beneath the aluminium sheet in order to prevent bubbles from being generated during the heating and to maximize the homogeneity of the flux. Furthermore, this homogeneity of the flow, as well as lateral leakage, was verified using an infrared camera (see Sec. II.3.3.3).

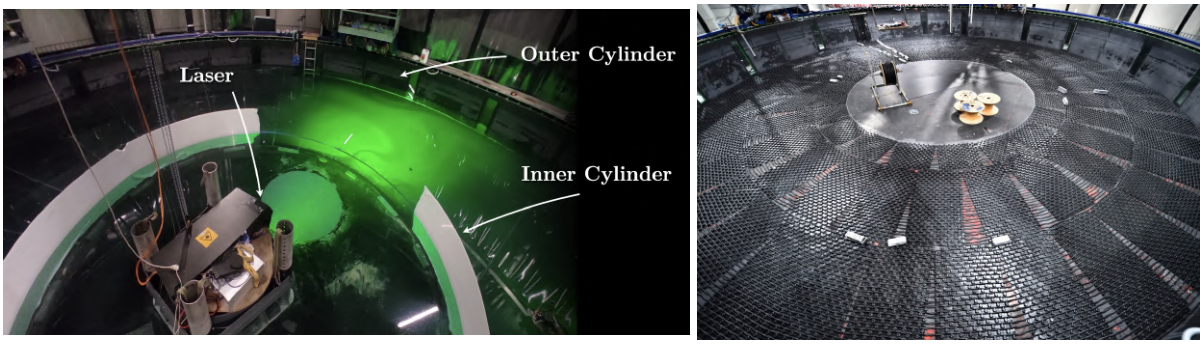

Figure II.13: Photograph of the 13 m wide rotating Coriolis Platform. Left: Picture of the inside of the platform with at the center the 25 W Yag laser. Right: Electrical wires network

II.3.2 Experimental procedure

The reason for using thermal stratification throughout the experiments presented in this manuscript is that the heat flux originates from the bottom of the water column. However, stable salinity stratification in such a configuration would tend to introduce double-diffusive regimes and would interfere with the processes we want to study[5].

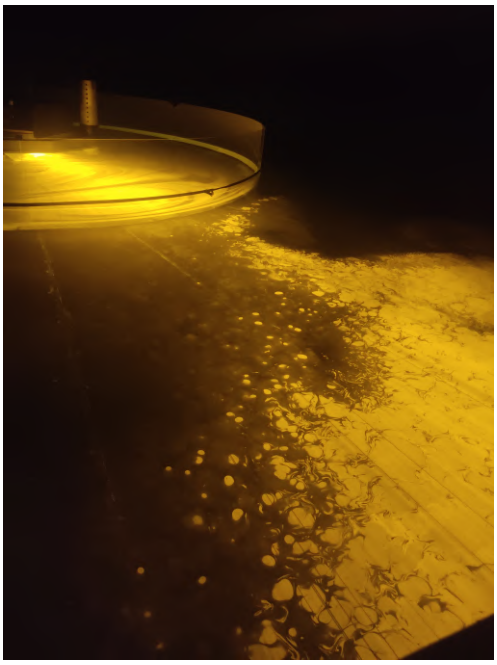

Figure II.14: Photograph of the horizontal laser sheet during a free convection experiment. The photograph was taken using a filter and highlights the convective plumes containing dye (rhodamine). The laser section was not perfectly horizontal due to the stratification present in this experiment.

For most experiments, the filling procedure is identical to that used for forced convection. However, there is one significant difference between the two protocols: the presence of the central ring delimiting the heated zone. As the filling nozzle is positioned at the centre of the tank, it was necessary to create an opening in the separating boundary. As this wall consists of six panels held together by a rope, one of them was removed during the filling phase and then replaced once this was complete. Although this method was successful in the majority of cases, it sometimes caused vortices to form when filling was carried out in rotation.

To preserve as much of the heat energy injected into the water as possible and to reuse the same water between experiments, a second procedure was employed to create a thermal stratification for certain runs. At the end of an experiment, part of the tank was drained and the heating system was switched on overnight. The following day, cooler water was injected in

[5]A few exploratory experiments using salinity stratification were also carried out with the present apparatus to investigate double-diffusive effects. These preliminary results helped motivate the STAIRWAY project, which is now underway on the Coriolis platform using the same experimental facility to characterise double-diffusive processes. Its scientific perspectives are discussed in the conclusion of this manuscript.

the same manner as previously described. This method allowed us to minimize water consumption between successive stratified experiments while achieving satisfactory stratification profiles. The experiment start when we turn on the heating device. Fig. II.15 shows the evolution of the temperature at fixed location (at the bottom and at $z = 12$ cm above the plate). It shows there is some inertia of the heating device since we observe an initial regime of the order of 800 s.

II.3.3 Measurement techniques

The acquisition system for the temperature profiles is identical to the one used for the forced convection experiment (see Sec. II.2.3 for its full description). The thermal probe profilers were positioned at intervals of 1 m from one another and from the side edges. For the S-PIV measurements, the principle and positioning are identical, the difference lying in the observed field of view to be increased.

II.3.3.1 Horizontal PIV

A horizontal laser sheet with a large field of view (4 m $\times$ 3 m) is used. The laser beam is sent vertically by a 25 W Yag laser and reflected by a $45°$ mirror mounted on a horizontal direction motor. This system enables to precisely adjust the vertical position of the sheet and scan the water depth from 4cm from bottom to 10cm from the surface. This laser sheet is then observed by a JAI camera (256 grey levels, pixel size 5.5 μm, with a resolution of 4096×3072). Its thickness varies with the radius but does not exceed 1 cm.

II.3.3.2 Thermal measurements

Three vertically oriented, motor-driven thermistor probes were mounted on a gantry positioned along a tank radius. The probes were regularly spaced at one meter intervals, allowing temperature measurements at radial distances of 1 m, 2 m, and 3 m from the inner cylinder. The vertical velocity of the profiler is (10cm.s^{-1}). Two other stationary thermistors (Tr1, Tr2) are fixed in the platform frame. One is placed in contact to the heated plate to measure its temperature and the other is placed within the vertical sheet at 12cm above the plate. The acquisition is driven by the same Labview software as the camera trigger and therefore the camera and thermistors can be synchronized in order to compute the turbulent heat fluxes. Measuring a turbulent heat flux requires the simultaneous resolution of velocity and temperature fluctuations. Whilst PIV presents no particular difficulty for velocity fluctuations, the same is not as easy for temperature. It requires a fixed measurement and the acquisition time must be fast enough to resolve the turbulent fluctuations. Thermocouples, whilst suitable for measuring average temperatures over long periods, cannot be used here: on the Coriolis platform, the length of the cables necessary attenuates the tension variations associated with temperature fluctuations which become indistinguishable from noise. The fixed thermistors used in this configuration have thermal inertia that limits their ability to resolve the fastest fluctuations. It

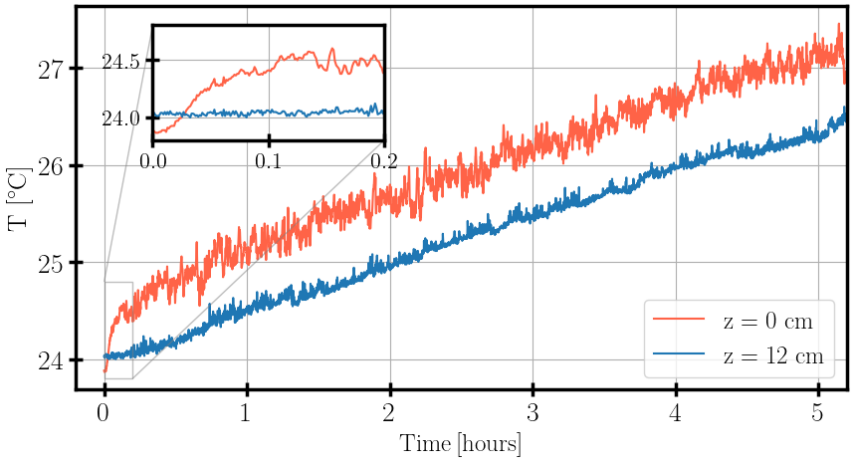

Figure II.15: Time series of the temperature for an experiment heated from below without stratification nor rotation. The temperature is measured at 12 cm from the bottom and in contact to it. The insert shows the initial stage of the experiment.

was this instrumental challenge that motivated a new temperature measurement method tested during the research visit to Oxford (see Chap. V).

II.3.3.3 Infrared- acquisition

For these experiments, an infrared camera (IR Telops M-350) was installed alongside the camera capturing the horizontal plane. This enabled us, on the one hand, to test the homogeneity of the heat flux in test cases with no, or with a few cm of water. On the other hand, to identify the signature of plumes on the surface of the water column during the experiments.

Using this method, observation is restricted to the surface temperature anomaly, thus plumes are only visible if the convective zone reaches the surface, i.e. in the absence of stratification. With rotation, this method also allows the horizontal size of the plumes to be characterised, as illustrated in Fig. II.16. It can be seen that the characteristic size of the positive temperature anomalies decreases as the rotation increases.

It should also be noted that, assuming the structures evolve adiabatically over short periods, it is possible to perform image correlation (similar to PIV processing) using the infrared images. However, this approach did not prove particularly successful in our case, as part of the dynamics visible on the surface is due to convection at the air–water interface, which makes the signal too noisy to analyse the convective dynamics driven by the heated floor.

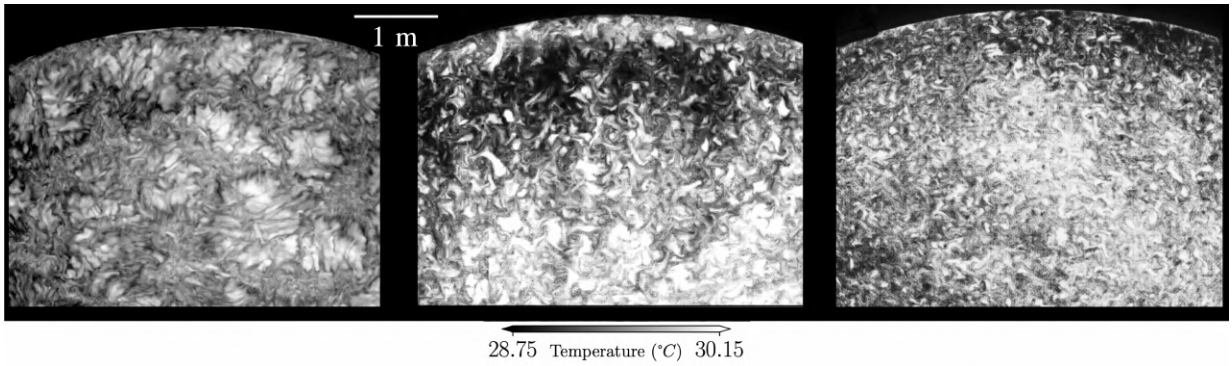

Figure II.16: Surface temperature viewed from above, captured by an infrared camera for three different experiments. Left panel: without initial rotation $f = 0\ \mathrm{s}^{-1}$, middle: $f = 0.1\ \mathrm{s}^{-1}$ and right: $f = 0.3\ \mathrm{s}^{-1}$. The upper boundary of the plot represents the outer edge of the annulus (outer edge of the platform) and the lower boundary is closer to the centre.

II.4 Turbulence modelling — single column framework

In complement to the experimental approach, we model convective dynamics using a single-column model. This framework allows us to isolate the processes responsible for the deepening of the mixing layer, and it provides an idealised test benchmark for evaluating turbulent closures independently of the three-dimensional and lateral effects present on the platform. The simulations are carried out using the open-source GOTM (*General Ocean Turbulence Model*) model, either in idealized oceanic conditions (see Chap. III), or configured to reproduce the experimental conditions (see Chap. IV) at the PIV measurement radius $r_0 = 4.5$ m (see Fig. II.2).

II.4.1 Single column framework

We consider a one-dimensional model of the vertical structure of the boundary layer, where turbulence and mixing processes are captured as an ensemble average of vertical fluxes. In this context, dynamics are governed by the turbulent vertical transport of momentum and heat, which we model using an eddy viscosity ν_t, and an eddy diffusivity ν_t'.

$$\frac{\partial u}{\partial t} - fv = \frac{\partial}{\partial z}\left(\nu_t \frac{\partial u}{\partial z}\right) \tag{II.2a}$$

$$\frac{\partial v}{\partial t} + fu = \frac{\partial}{\partial z}\left(\nu_t \frac{\partial v}{\partial z}\right), \tag{II.2b}$$

$$\frac{\partial T}{\partial t} = \frac{\partial}{\partial z}\left(\nu_t' \frac{\partial T}{\partial z}\right), \tag{II.2c}$$

where u and v are the horizontal (x and y) components of the mean flow, $b = -g\alpha(T - T_0)$ the buoyancy, which depend only on depth (z) and time (t). The incompressibility condition implies that the vertical velocity w is zero, as $\partial w/\partial z = 0$, and $w = 0$ at the surface (with

a rigid lid blocking vertical motion). In this one-dimensional model, the nonlinear advective terms vanish without further approximation. Additionally, we assume that the mean horizontal velocity is zero, so there are no geostrophic pressure gradients. The boundary conditions depend on the configuration used —idealized ocean or laboratory twin— and are detailed in Sec. (III.3.1) and Sec. (IV.7.2) respectively. Unlike molecular viscosity, the turbulent coefficients ν_t and ν'_t are not intrinsic properties of the fluid: they depend on the state of the flow and must be parameterised using a turbulent closure model.

II.4.2 TKE Equation

The equation for the turbulent kinetic energy (TKE) $k \equiv \overline{\mathbf{u}'^2}/2$ can be written in the form

$$\frac{\partial k}{\partial t} + \frac{\partial T_k}{\partial z} = P + B - \varepsilon \tag{II.3}$$

where the eddy flux T_k, the production rate P, the conversion rate to potential energy B, and the dissipation rate ε can be expressed from correlations of turbulent fluctuations (the notation $\bar{\cdot}$ and $\cdot'$ denote the standard ensemble averaging and deviation from the ensemble mean respectively).

Within the eddy viscosity model, the production P is modelled from the shear as

$$P = -\overline{u'w'}\frac{\partial u}{\partial z} - \overline{v'w'}\frac{\partial v}{\partial z} = \nu_t \left|\frac{\partial \mathbf{u}}{\partial z}\right|^2 \tag{II.4}$$

The conversion rate to potential energy B also represents the vertical flux of buoyancy. Within the eddy diffusivity hypothesis, it is expressed as

$$B = \overline{w'b'} = -\nu'_t \frac{\partial b}{\partial z} \equiv -\nu'_t N^2. \tag{II.5}$$

II.4.3 $k - \varepsilon$ model formulation

The eddy-viscosity hypothesis introduced above does not specify the turbulent viscosity itself. A second variable is therefore required to relate $\nu_t,\ \nu'_t$ to the turbulent state of the flow. The classical approach is the mixing-length theory proposed by Prandtl (1925). It assumes that turbulent transport is carried by fluid parcels travelling over a characteristic distance, the mixing length l_m, before "forgetting" their initial properties. Within this framework, from an analogy with the kinetic theory, the eddy viscosity can be written as

$$\nu_t \sim u'\, l_m \tag{II.6}$$

where u' is an estimate of the velocity fluctuations and l_m is the mixing length. This formulation therefore needs a constraint on the two quantities in order to express the eddy viscosity.

In two-equation turbulence closures, the characteristic velocity is naturally estimated from the TKE: $u' \sim k^{1/2}$. The problem then remains to determine a characteristic length l_m. From the

equation (II.3) the dissipation scale as $-\varepsilon = dk/dt = -u'^3/l_m$ which expresses the turbulent cascade: large eddies of size l_m transfer kinetic energy towards progressively smaller scales, where it is ultimately dissipated by viscosity.
Which yields

$$l_m \sim \frac{u'^3}{\varepsilon} \sim \frac{k^{3/2}}{\varepsilon} \tag{II.7}$$

Finally, the eddy viscosity ν_t and the eddy diffusivity are parametrised by

$$\nu_t = c_\mu \frac{k^2}{\varepsilon} \qquad \nu'_t = c'_\mu \frac{k^2}{\varepsilon}\,, \tag{II.8}$$

with c_μ and c'_μ non-dimensional constants.

The k-ε approach therefore considers ε as the additional variable instead of the prescribing l_m, and a diffusion equation is introduced for ε to close the system. It takes a similar form as the TKE equation (II.3),

$$\frac{\partial \varepsilon}{\partial t} + \frac{\partial}{\partial z}\left(\frac{\nu_t}{\sigma_\varepsilon}\frac{\partial \varepsilon}{\partial z}\right) = \frac{\varepsilon}{k}\left(c_{\varepsilon 1}\, P + c_{\varepsilon 3}\, \overline{w'b'} - c_{\varepsilon 2}\, \varepsilon\right)\,. \tag{II.9}$$

The values chosen for the coefficients are $\sigma_\varepsilon = 1.3$, $c_{\varepsilon 1} = 1.44$ and $c_{\varepsilon 2} = 1.92$. Those are the classical choices for neutrally buoyant fluids, resulting from fits to simple turbulent flow configurations (Rodi, 1987). The parameter $c_{\varepsilon 3}$ is less consensual. We use here $c_{\varepsilon 3} = -0.621$, which has been adjusted to provide reasonable results in the case of 'sustainable uniform shear' (Burchard and Bolding, 2001). In this case, the left-hand side of (II.3) and (IV.42) are set to 0, so we are left with a pair of algebraic equations. This balance yields by linear combination of the two equations,

$$-\overline{w'b'} = \frac{c_{\varepsilon 2} - c_{\varepsilon 1}}{c_{\varepsilon 2} - c_{\varepsilon 3}} P = 0.189\, P \tag{II.10}$$

This is the model representation of the steady state Richardson criterion (see section. I.4.1). Indeed, expressing B by (II.5) and P by (II.4), this condition (II.10) takes the form of the marginal stability condition, with $Ri \equiv Ri_{st} = 0.189\, \nu_t/\nu'_t$.

Note that there are other two-equation turbulence closures, for example the $k-\omega$ is based on the transport equation for the turbulence frequency $\omega = k/\varepsilon$ instead of the dissipation. This provides the advantages to be integrated into the viscous sub-layer down to the boundaries without need of wall function (Speziale et al., 1992).[6]

II.4.3.1 Stability Function

For homogeneous fluids, the standard values $c_\mu \simeq c'_\mu \simeq 0.09$ are used to reproduce data from simple shear flows. In the stratified case, they are assumed to depend on the local shear and stratification, expressed as functions of the respective non-dimensional parameters $\alpha_M = k^2 \left|\partial \mathbf{u}/\partial z\right|^2 / \varepsilon^2$ and $\alpha_N = k^2 N^2/\varepsilon^2$. These so-called 'stability functions' fulfil appropriate

[6] Comparisons between the two models in the same configuration have shown no difference near the boundary, but a slight departure in the interior. This is why we did not extend the validation to the $k-\omega$ model.

physical and mathematical constraints, as discussed by Burchard and Bolding (2001) and Umlauf and Burchard (2005). Note that $\sqrt{\alpha_N}$ can be viewed as the inverse of a turbulent Froude number from the scaling $\varepsilon \sim k^{3/2}/l$, which yields $\sqrt{\alpha_N} = Nl/k^{1/2}$. Moreover, the Richardson number is the ratio $Ri = \alpha_N/\alpha_M$. Particular cases of interest are the 'quasi-equilibrium states', for which Eq. (II.3) reduce to the local balance $P = -B + \varepsilon$. Expressing P and $-B$ respectively by the expressions (II.4) and (II.5), and using (IV.38), this local balance writes $c_\mu \alpha_M - c'_\mu \alpha_N = 1$. This expression defines a relation between α_M and α_N, or equivalently between the turbulent Froude number $\alpha_N^{-1/2}$ and the Richardson number $Ri = \alpha_N/\alpha_M$. In these quasi-equilibrium relations, the Froude number, as well as the functions c_μ and c'_μ, decrease with increasing Richardson number. They reach zero at a critical Richardson number, denoted Ri_c, beyond which turbulence cannot be locally maintained by the shear. This threshold differs from Ri_{st}, representing the 'sustainable uniform shear'. In the latter case, the flux of ε also vanishes.

In the present manuscript, we use Canuto et al. (2001)'s formulation of the stability functions c_μ and c'_μ. It corresponds to the case denoted 'CA' by Burchard and Bolding (2001), and 'CHCD01A' by Umlauf and Burchard (2005). The reference Richardson numbers are $Ri_{st} = 0.25$ and $Ri_c = 0.843$.

II.4.4 KPP closure

Another model closure we test in this thesis is the K-Profile Parameterisation (KPP) of Large et al. (1994). It is a diagnostic turbulence closure originally developed for oceanic surface boundary layers. Unlike the k-ε model, KPP does not solve prognostic transport equations for turbulent quantities; instead, it diagnoses the boundary layer depth h from a bulk Richardson number criterion. In its original formulation, the bulk Richardson number compares the stabilising effect of buoyancy to the destabilising effect of velocity shear, and the boundary layer base is identified where Ri_b exceeds a critical value Ri_c.

Within the diagnosed boundary layer, the eddy viscosity is prescribed as the product of a turbulent velocity scale w_m and a cubic polynomial shape function $G(\sigma)$,

$$\nu_t(z) = h\, w_m(\sigma)\, G(\sigma), \qquad \sigma = z/h \in [0, 1], \tag{II.11}$$

where σ is the normalised distance from the wall. The shape function $G(\sigma) = \sigma(1-\sigma)^2$ satisfies $G(0) = 0$, $G(1) = 0$, and $G'(1) = 0$, ensuring a smooth transition to the interior at the boundary layer base. The turbulent velocity scale w_m depends on the friction velocity u_* and the local stability. Beyond the mixed layer, only a weak background diffusivity is active.

We use the CVMix implementation (Van Roekel et al., 2018) within GOTM, with a critical Richardson number $Ri_c = 0.3$ and quadratic interpolation for the bulk Richardson number profile. No Langmuir parameterisation is activated, and no clipping at the Ekman or Monin-Obukhov scales is applied.

Chapter III

Wind-Mixed layer deepening

Summary of the Chapter

We study the deepening of the mixed layer forced solely by winds The canonical theoretical model Pollard et al. (1973) demonstrates that the deepening of the mixed layer follows a law of $h \propto \sqrt{t}$. In a rotating frame, this theory predicts that inertial oscillations, caused by wind impulse, deflect the surface layer and block the injection of energy beyond half an inertial period and thus completely halts the deepening of the layer in rotation. This hypothesis of arrest has been shown to be incorrect by large eddy simulations (Ushijima and Yoshikawa, 2020), but no analytical law has been derived to characterise this regime of wind-forced deepening in the long term.
In this chapter, we propose the long term evolution law

$$h \propto \frac{u_*}{\sqrt{N_0 f}} (ft)^{1/4}.$$

This law has been tested using single-column numerical simulations with the k-ε turbulent closure and has been found to be consistent and independent of the parameter $S = \sqrt{N_0/f}$. Furthermore, a more precise derivation, based on a quadratic profile of turbulent viscosity with an exponential decay within the entrainment layer, has provided: a description of the structure of the mixing layer and the entrainment layer, a decomposition of the velocity field into a quasi-stationary component and an oscillating component (at frequency f, attributed to inertial oscillations), and finally an evaluation of the contribution of each component to the erosion of the stratified layer. The contribution of the inertial oscillations proves to be negligible, and it is shown that it is the quasi-stationary component that controls the mixing. This second derivation confirmed the scaling law for rotating regimes for $S \sim 3 - 24$, i.e, regimes moderately to strongly dominated by stratification effects.

The results of this chapter are reproduced from :
Coppin, M., Deremble, B., & Sommeria, J. (2025). "Wind-mixed layer deepening in a rotating frame". *Geophysical & Astrophysical Fluid Dynamics*, 119(5), 646-684. DOI: 10.1080/03091929.2025.2609460

Contents

———Article published in Geophysical and Astrophysical Fluid Dynamics———

In the introduction chapter (I), we outlined the research topics that underpin this thesis: how does wind-driven turbulence shape the vertical structure and transient dynamics of the rotating, stratified ocean surface layer? To answer this, we have identified several questions, the first of which addresses the ocean's response to wind stress.

Schematically, a wind stress applied to the surface of a rotating ocean triggers two processes. On the one hand, it generates mixing through turbulent entrainment, which forms a layer with relatively homogeneous properties, the thickness of which increases over time: this is the deepening of the mixing layer. On the other hand, the wind impulse excites inertial oscillations, which constitute a considerable reservoir of kinetic energy but which, in classical theories, inhibit this deepening. **This chapter aims specifically to characterise the mixing regime of a wind-driven stratified fluid in the presence of these inertial oscillations, describe its long-term deepening rate and its dynamics.**

To isolate this mechanism, we adopt in this chapter the simplest possible framework: a wind applying a constant, uniform and unidirectional stress to a 1D, linearly stratified fluid column, without considering the effect of gravity waves or Langmuir circulations. In this chapter, we draw on a theoretical analytical derivation and an idealised 1D model; then, in the following chapter, we shall specify the nature of the forcing by explicitly defining the frictional boundary conditions, and then compare these dynamics with experimental data obtained on the Coriolis rotating platform.

Article published in *Geophysical and Astrophysical Fluid Dynamics*

Wind-Mixed layer deepening in a rotating frame

Abstract: Under wind forcing, the oceanic mixed layer deepens over time. Scaling laws exist to predict the deepening rate, but either neglect Earth's rotation or do not take into account the vertical structure of the mixed layer. This study aims to address these limitations by investigating the long-term dynamics of a wind-driven mixed layer in a rotating, linearly stratified fluid. We derive an analytical scaling law for the mixed layer depth h as a function of time t,

$$h \propto \frac{u*}{\sqrt{N_0 f}}(tf)^{1/4}$$

where N_0 the initial stratification, f the rotation parameter and u_* the friction velocity. This law extends classical theories by considering rotational effects and is consistent with recent Large Eddy Simulations. Building upon the work of Kundu (1980), with analytical solutions for the vertical structure of the mixed layer. We show that mixing, mostly concentrated within the entrainment layer, is primarily controlled by the stationary component of the velocity and that inertial oscillations have little effect on entrainment.

III.1 Introduction

Wind action on the ocean's surface induces turbulence primarily through surface waves and shear stresses. This turbulence erodes local stratification, creating a mixed layer where temperature and salinity are roughly uniform over the vertical. The accurate representation of mixed layer depth in climate models is essential, as it influences ocean heat uptake (Senapati et al., 2024; Kataoka et al., 2019), vertical mixing, and the carbon cycle (Gardner et al., 1999). Errors in mixed layer depth representation can introduce significant uncertainties in climate predictions and ocean circulation (Sallée et al., 2021; Treguier et al., 2023).

The vertical structure of the oceanic mixed layer depends strongly on surface boundary conditions (wind, heat, freshwater fluxes, wave state) and the underlying stratification of the ocean (Legay et al., 2024). In the idealized case of constant wind, no buoyancy forcing, stationary flow, and constant diffusivity the dynamics of an Ekman layer (Ekman, 1905) can be described by an analytical solution which corresponds to a balance between the Coriolis force and (turbulent) diffusion of momentum. The velocity field exhibits an Ekman spiral, characterized by vertical shear in the surface currents. The characteristic depth of the turbulent Ekman layer in a neutrally buoyant fluid is given by

$$d_E \simeq 0.3\frac{u_*}{f}\,, \tag{III.1}$$

where $u_* = \sqrt{\tau/\rho}$ is the friction velocity (square root of wind stress τ divided by the density of water ρ) and f the vertical component of the Coriolis parameter (Weatherly and Martin, 1978; Zilitinkevich and Esau, 2003; Caldwell et al., 1972). Although Ekman layer theory is well-established, the Ekman spiral has not been directly observed in the ocean (Lenn and Chereskin, 2009; Sun and Sun, 2020), as assumptions of stationarity and absence of buoyancy effects often do not hold in realistic conditions. Moreover, stratification below the mixed layer typically constrains the Ekman layer dynamics to a depth shallower than d_E.

In a pioneering study, Pollard et al. (1973) (denoted P73) extended this framework to describe the non-stationary evolution of the mixed layer under wind and heat fluxes, accounting for rotation. They assumed a uniform vertical profile for velocity and fluid density in the mixed layer, allowing them to predict the mixed layer depth evolution, $h(t)$, when a constant wind stress is applied to a uniformly stratified fluid with buoyancy frequency N_0. For wind forcing alone (no heat flux), they obtained

$$h(t) = \frac{u_*}{\sqrt{N_0 f}} \left[4(1 - \cos\ ft)\right]^{1/4} . \tag{III.2}$$

For $ft \ll 1$ this simplifies in

$$h(t) = 2^{1/4} u_* \sqrt{\frac{t}{N_0}} , \tag{III.3}$$

which represents the deepening law in the absence of Coriolis effects. This scaling law can be easily understood by noting that the momentum of the mixed layer increases as $uh \propto u_*^2 t$, while the condition of marginal stability for a stratified shear flow imposes a constant Richardson number $Ri \simeq h^2 N_0^2 / 2u^2 = const$. This initial scaling law $h \sim t^{1/2}$ and $u \sim t^{1/2}$ has been verified by several studies, notably with high resolution Direct Numerical Simulations (DNS) by Jonker et al. (2013), and is consistent with laboratory results obtained by Kato and Phillips (1969b), although these were originally misinterpreted as $h \sim t^{1/3}$ (see also the discussion in Price et al., 1978a).

P73 predicted that mixed layer deepening arrests when the oceanic current opposes the wind forcing, at half the inertial period ($t = \pi/f$). At this time, the mixed layer depth expression (III.2) yields

$$h_{max} = 8^{1/4} \frac{u_*}{\sqrt{N_0 f}} , \tag{III.4}$$

which is proportional to the characteristic length

$$L_{P73} = \frac{u_*}{\sqrt{N_0 f}} . \tag{III.5}$$

In this scenario, the terminal depth is typically smaller than the Ekman depth d_E due to the limiting effect of interior stratification. Zilitinkevich and Esau (2003) proposed an empirical law to determine the terminal mixed layer depth based on the ratio

$$S^2 = \frac{N_0}{f} . \tag{III.6}$$

When S is small, the mixed layer depth is limited by the Coriolis effect to the value d_E, while for large S, stratification limits the depth to the P73 scale $L_{P73} \simeq 3.3\ d_E/S$.

In the idealized scenario of uniform stratification eroded by constant wind stress, the evolution of the mixed layer depth h (dependent variable) is a function of four independent variables: u_*, f, N_0, and t. Using f^{-1} as a characteristic time and L_{P73} as a characteristic length, the evolution of the (non-dimensional) mixed layer depth is thus a function of two non-dimensional variables: the non-dimensional time, and $S = \sqrt{N_0/f}$, a stratification parameter.

P73 assumed that shear at the bottom of the mixed layer is stabilized by strong stratification, preventing further deepening after half an inertial period. They acknowledged, however, that slow deepening could still occur through turbulent entrainment. While P73 described this entrainment using a bulk mixed layer approach with uniform velocity profiles, we argue that accurate representation of long-term entrainment requires resolving the detailed vertical structure within the mixed layer.

To explore this possibility, we now focus on the interface layer between the mixed layer and the stratified interior, referred to as the entrainment layer. This layer corresponds to the thermocline in Cushman-Roisin (1981)'s model and to the perturbation energy production zone in Niiler (1975)'s framework. Observations of this layer (Davis et al., 1981; Johnston and Rudnick, 2009; Dohan and Davis, 2011) reveal strong velocity gradients in both the along- and across-wind velocity components. These profiles suggest that the mean flow dynamics result from the interaction between directly wind-driven behavior, dominant in the along-wind component, and inertial oscillations (D'Asaro, 1985).

In modeling the entrainment process, Niiler (1975) expanded on P73 by incorporating turbulent erosion of stratification (Kraus and Turner, 1967). They proposed a turbulent energy balance equation that describes both early and late stages of deepening (de Szoeke and Rhines, 1976), with subsequent reviews supporting the continuation of deepening and suggesting a long-term scaling law of $h \propto t^{1/3}$ (Kraus, 1977; Zilitinkevich et al., 1979; Moen, 1981). Kundu (1980) proposed a thorough description of entrainment processes, using the k-ϵ turbulent closure to describe the vertical structure of turbulent flows and demonstrates long-term deepening slower than $h \propto t^{1/3}$ without providing a precise scaling. Using large eddy simulation (LES), Ushijima and Yoshikawa (2020) (U20) found a different scaling law

$$h = 1.5 L_{P73} \left(\frac{N_0}{f}\right)^{0.022} \left(\frac{t}{T_f}\right)^{0.18}, \tag{III.7}$$

for a range of $S = \sqrt{N_0/f} \in [7, 27]$, and with $T_f = 2\pi/f$. Figure III.1 reproduces the evolution of the mixed layer depth based on U20's scaling law. In this figure, we highlight the two regimes: initial deepening, described by Eq. (III.3), and the rotating regime with U20's scaling law. Although U20 provided an empirical fit, they did not explain the physical mechanisms behind this scaling, and other studies (Niiler, 1975; Kundu, 1980; Cushman-Roisin, 1981) are not entirely consistent with this deepening rate. In the present study, our aim is to address key gaps in the current understanding of mixed layer deepening, particularly regarding the vertical structure of the mixed layer and the role of turbulent dynamics. While previous studies have provided important insights into the evolution of the mixed layer depth, several critical aspects remain underexplored. These include the separation of inertial oscillations from the logarithmic layer, which is crucial for understanding how the vertical structure of the mixed

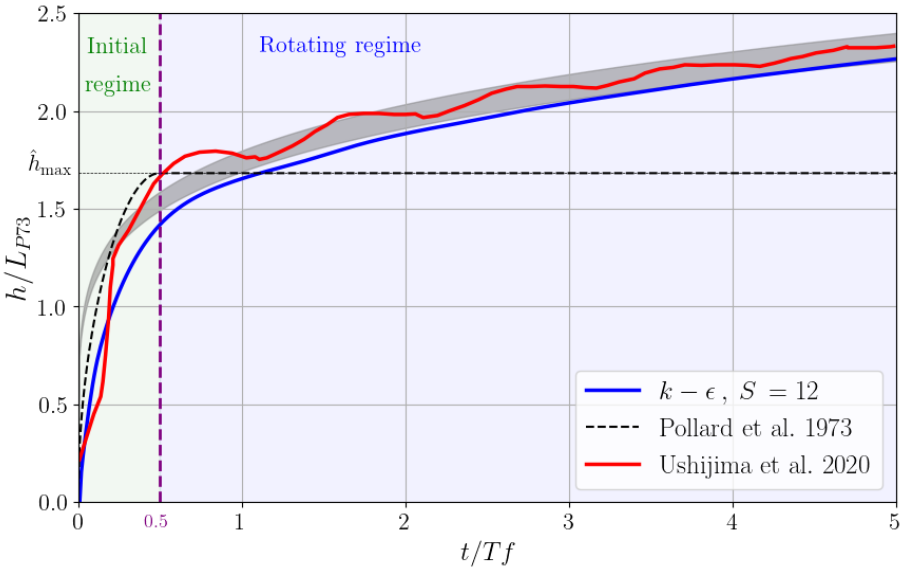

Figure III.1: Temporal variation of the mixed layer depth normalized by L_{P73}. Time is normalized by the inertial period T_f. The red curve is the averaged value of all LES experiments performed by Ushijima and Yoshikawa (2020) represented in their Fig. 3. Shading shows the spread of the estimate of the mixed layer depth from Eq. III.7 for $S = \sqrt{N/f}$ ranging from 7 to 27 (note that we used a prefactor of 1.55 instead of 1.5 in Eq. III.7 to reproduce Fig. 3 of U20). The black dashed line shows Pollard et al. (1973)'s scaling law. According to their theory, the deepening stops at $t/T_f = 0.5$, and $\hat{h}_{max} = h_{max}/L_{P73} = 8^{1/4}$. The blue line is a numerical simulation using the k-ϵ scheme with $S = 12$ that will be introduced later in this article.

layer evolves over time. This distinction is key to understanding the physical processes that govern mixed layer deepening beyond the initial inertial period and the complex interactions between turbulence and stratification. One other key point we want to address here is the effect of the self-similarity breaking due to the effect of rotation (Kundu, 1981). To address these gaps, following Kundu (1980)'s approach, we will first analyse the mixed layer dynamics in a single column model with the k-ϵ closure for the turbulent fluxes (Umlauf and Burchard, 2005). We chose this parameterization for two reasons: (i) it captures well the deepening rate of the LES as briefly illustrated in Fig. III.1, and (ii) this parameterization is energetically consistent so that we can rely on it to do energy budgets. We will use these energy budgets to derive an idealized model of the mixed layer and propose a scaling law for the long-term evolution of the mixed layer depth.

The paper is organized as follows: in Section III.2, we describe our modelling approach and the theoretical background. We build on P73 to propose an extension of their scaling law for long times. Section III.3 presents the k-ϵ results where we describe the vertical structure of the mixed layer. In Section III.4, we introduce an idealized eddy viscosity model that reproduces the main features of the k-ϵ model. With this model, we can confirm the scaling law derived in Section III.2 although more firmly grounded with the vertical structure of the mixed layer. We conclude in Section III.8.

III.2 Review and amplification of Pollard et al. (1973)

III.2.1 Momentum equations

We consider a one-dimensional model of the ocean to represent the vertical structure of the oceanic mixed layer, where turbulence and mixing processes are captured as an ensemble average of vertical fluxes. This representation is justified because the horizontal scale of atmospheric perturbations producing surface winds is much larger than the vertical scale of the mixed layer depth. In this context, dynamics are governed by the turbulent vertical transport of momentum, which we model using an eddy viscosity ν_t,

$$\frac{\partial u}{\partial t} - fv = \frac{\partial}{\partial z}\left(\nu_t \frac{\partial u}{\partial z}\right) \tag{III.8a}$$

$$\frac{\partial v}{\partial t} + fu = \frac{\partial}{\partial z}\left(\nu_t \frac{\partial v}{\partial z}\right), \tag{III.8b}$$

where u and v are the horizontal (x and y) components of the mean flow, which depend only on depth (z) and time (t). The incompressibility condition implies that the vertical velocity w is zero, as $\partial w/\partial z = 0$, and $w = 0$ at the surface (with a rigid lid blocking vertical motion). In this one-dimensional model, the nonlinear advective terms vanish without further approximation. Additionally, we assume that velocity is zero in the deep interior, so there are no geostrophic pressure gradients.

The boundary conditions at the air-sea interface ($z = 0$) are given by

$$\nu_t \frac{\partial u}{\partial z} = u_*^2 \tag{III.9a}$$

$$\nu_t \frac{\partial v}{\partial z} = 0. \tag{III.9b}$$

The dynamics in the mixed layer are constrained by the vertical integration of (III.8), which gives equations for the integrals $\langle u\rangle \equiv \int_{-H}^{0} u\, dz$ and $\langle v\rangle \equiv \int_{-H}^{0} v\, dz$ (throughout the rest of the article, $\langle\cdot\rangle$ will denote the vertical integral). Considering the boundary condition (III.9) and the assumption that momentum flux vanishes at large depth ($z = -H$), we obtain

$$\frac{d\langle u\rangle}{dt} - f\langle v\rangle = u_*^2 \tag{III.10a}$$

$$\frac{d\langle v\rangle}{dt} + f\langle u\rangle = 0\,. \tag{III.10b}$$

The solution describes inertial oscillations starting from $\langle u\rangle = \langle v\rangle = 0$ at $t = 0$,

$$\langle u\rangle = \frac{u_*^2}{f}\sin(ft) \tag{III.11a}$$

$$\langle v\rangle = -\frac{u_*^2}{f}(1 - \cos(ft)) \tag{III.11b}$$

III.2.2 Buoyancy and potential energy

The buoyancy b is defined in terms of the fluid density ρ and a reference density ρ_0 as $b = -g(\rho - \rho_0)/\rho_0$. In this study, we consider an initial condition corresponding to a linear stratification, $b(t = 0, z) = N_0^2 z$, where N_0 is the constant Brunt-Väisälä frequency. Buoyancy is assumed to follow a diffusion equation with an eddy diffusivity ν_t', which is expected to be close to ν_t, to model the turbulent buoyancy flux

$$\frac{\partial b}{\partial t} = \frac{\partial}{\partial z}\left(\nu_t' \frac{\partial b}{\partial z}\right) . \tag{III.12}$$

We consider the case with no buoyancy flux at the surface, so that $\nu_t' \partial b/\partial z = 0$, and the

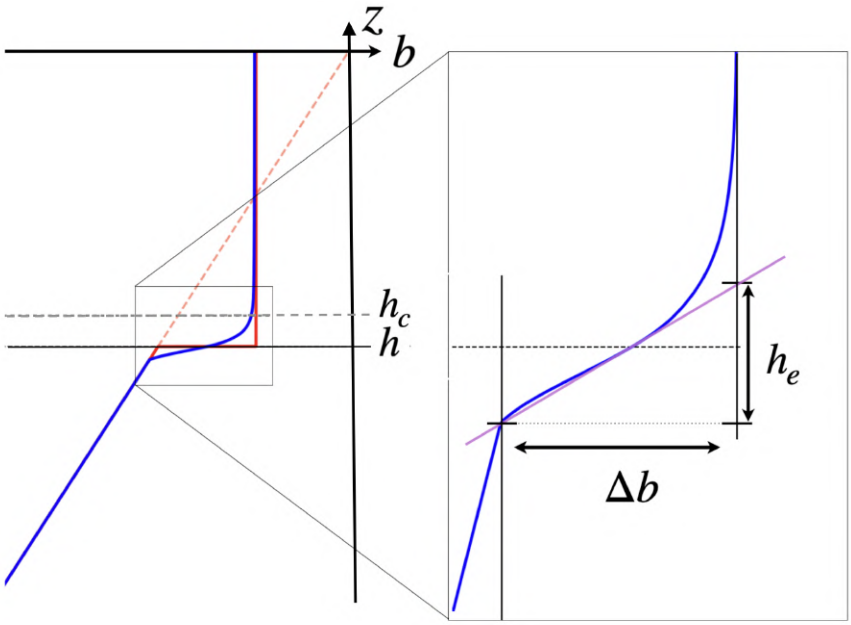

Figure III.2: Vertical buoyancy profiles of the mixed layer: red dashed line is the initial buoyancy profile, solid lines are the idealised (red), and realistic (blue) buoyancy profiles after the wind has turned on. The zoom shows the definition of the entrainment layer of thickness $h_e = \Delta b/N_e^2$, with N_e, the buoyancy frequency of the entrainment layer.

diffusivity vanishes at large depth, ensuring that $\nu_t' \partial b/\partial z \to 0$. As a result, the integral is preserved over time:

$$\frac{d}{dt}\int_{-H}^{0} b dz = \left[\nu_t' \frac{\partial b}{\partial z}\right]_{-H}^{0} = 0 . \tag{III.13}$$

At time t, assuming perfect mixing down to the depth $z = -h$, the uniform value $b = -N_0^2 h/2$ is obtained for $z > -h$, while the initial profile $b = N_0^2 z$ is preserved below. This configuration is plotted with the red curve in Fig. III.2. Thus, the relation $\partial b/\partial t = -(N_0^2/2)\, dh/dt$ holds everywhere in the mixed layer, and Eq. (III.12) integrates as

$$-\frac{N_0^2}{2}\frac{dh}{dt} z = \nu_t' \frac{\partial b}{\partial z} . \tag{III.14}$$

Mixing of buoyancy corresponds to an increase of potential energy $E_{pot} = -\langle bz \rangle$. In the state of a perfectly mixed layer down to $z = -h$, the potential energy is

$$E_{pot} = -\int_{-H}^{0} bz dz = -\int_{-H}^{-h} N_0^2 z^2 dz + N_0^2 \frac{h}{2} \int_{-h}^{0} z dz = N_0^2 \left(\frac{h^3 - H^3}{3} - \frac{h^3}{4} \right) . \tag{III.15}$$

The increase of potential energy due to mixing is therefore

$$E_{pot} - E_0 = N_0^2 \frac{h^3}{12} , \tag{III.16}$$

such that $dE_{pot}/dt = (N_0^2 h^2/4) dh/dt$.

In the more general case of an entrainment layer with non-zero thickness (blue curve in Fig. III.2), we will still use Eq. (III.16) to define the mixed layer depth as

$$h = \left[\frac{12}{N_0^2} (E_{pot} - E_0) \right]^{1/3} . \tag{III.17}$$

As we will see later, this definition of h closely aligns with a more standard definition based on the position of the maximum density gradient. However, the position of the maximum gradient is sensitive to minor oscillations, while our definition, based on potential energy, is more robust.

In a more realistic profile, the entrainment layer is the buffer zone with a strong buoyancy gradient at the base of the mixed layer that connects the well-mixed profile with the stratified interior (see zoom in Fig. III.2). If we call N_e^2 the buoyancy gradient at the depth h, we estimate the thickness of this layer as $h_e = \Delta b / N_e^2$, which corresponds to the slope (in z, b space) times the buoyancy drop $\Delta b = N_0^2 h/2$. We get

$$h_e = \frac{N_0^2}{2N_e^2} h , \tag{III.18}$$

Note that for $t \to 0$, $N_e = N$ so that $h_e = h/2$. During the evolution, we shall see that h_e/h decreases rapidly during the first deepening phase and then decreases at a slower rate during the second deepening phase, as it will be specified by Eq. (III.28).

During this second deepening phase, the mixed layer can be considered as a uniform density fluid confined between a rigid lid and a depth h_c at which the density gradient begins to constrain turbulence. This depth h_c marks the upper edge of the entrainment layer while h marks its center. This definition of h_c also aligns with standard oceanographic practice, where mixed layer depth is defined as the level where density first deviates from its surface value (Treguier et al., 2023), corresponding precisely to the top of the entrainment layer. A precise definition of h_c will be given in section III.4.

III.2.3 The slab model of Pollard et al. (1973)

P73 considered no variation in z for the velocity in the mixed layer. In this context, the energy is referred to as 'slab energy' $E_{slab} = \left(\langle u \rangle^2 + \langle v \rangle^2 \right)/2$ expressed from (III.11) as

$$E_{slab}(t) = \frac{u_*^4}{f^2} (1 - \cos ft) . \tag{III.19}$$

The growth of the layer thickness is constrained by the variations of the total energy $E_{kin} + E_{pot}$ driven by the surface stress input $u_*^2\, u_{(z=0)}$. Assuming a uniform velocity in the layer, we have $u_{(z=0)} = \langle u \rangle / h$, so the production rate of the total energy $E_{kin} + E_{pot}$ is

$$\frac{dE_{kin}}{dt} + \frac{dE_{pot}}{dt} = u_*^2 \frac{\langle u \rangle}{h} \tag{III.20}$$

and there is no loss by internal friction. Since $E_{kin} = E_{slab}/h$ for a uniform velocity, we have

$$\frac{dE_{kin}}{dt} = \frac{1}{h}\frac{dE_{slab}}{dt} - \frac{1}{h^2}\frac{dh}{dt}\, E_{slab}\,. \tag{III.21}$$

Moreover, as a consequence of the integrated momentum equations (III.10), we have the exact result,

$$\frac{dE_{slab}}{dt} = u_*^2\, \langle u \rangle\,. \tag{III.22}$$

Then, introducing the expression (III.21) in (III.20) yields

$$-\frac{E_{slab}}{h^2}\frac{dh}{dt} + \frac{dE_{pot}}{dt} = 0 \tag{III.23}$$

Using (III.19) and (III.16), this yields

$$\left[-\frac{u_*^4}{h^2 f^2}(1-\cos ft) + N_0^2 \frac{h^2}{4}\right] \frac{dh}{dt} = 0 \tag{III.24}$$

which has two solutions,

$$\frac{dh}{dt} = 0 \qquad \text{or} \qquad h^4 = \frac{4u_*^4}{f^2 N_0^2}(1-\cos ft) \tag{III.25}$$

which demonstrates Eq. (III.2), as originally derived by P73. The thickness of the mixed layer h reaches a maximum $h = 8^{1/4} L_{P73}$ for $ft = \pi$, which corresponds to half the inertial period. After this time, P73 switched to $dh/dt = 0$, assuming that mixing is irreversible, so that h cannot decrease.

As mentioned in P73, four terms are neglected (assumed to sum to zero) in this derivation: (i) the energy input $u_* u_{(z=0)}$ is underestimated, as the surface velocity $u_{(z=0)}$ is actually larger than the depth-averaged velocity $\langle u \rangle / h$; (ii) P73 assumed that the neglected extra forcing and viscous losses cancel each other, so dissipation does not appear in equation (III.20); (iii) time variations of Turbulent Kinetic Energy (TKE) are neglected; (iv) the expression for the kinetic energy corresponds to a slab with uniform velocity and does not account for the actual vertical structure of the flow. The expression of these four terms is given in Appendix A, Eq. (III.71).

Taking into account point (iv) would lead to a modification of the kinetic energy term in Eq. (III.24). This would somewhat modify the coefficient for the initial growth Eq. (III.3), without much effect on the long term behavior. By contrast, hypothesis (ii) is most relevant for the deepening of the mixed layer after half an inertial period. Indeed, part of the TKE production is converted to potential energy of the background stratification, leading to the increase of h. This effect will be estimated by heuristic scaling arguments in next sub-section to motivate our proposed long-term scaling law for $h(t)$. A more rigorous derivation will be provided in Section III.4 through the complete analytical framework.

III.2.4 The effect of the entrainment layer

The effect of mixing beyond half an inertial period can be expressed by introducing a non-zero right hand side $\mathcal{R}$ in Eq. (III.24). This term must be positive to describe mixing layer deepening. Indeed $dh/dt > 0$, and the factor $\left[-\frac{u_*^4}{h^2 f^2}(1-\cos ft) + N_0^2 \frac{h^2}{4}\right]$ becomes positive after half an inertial period, as shown by the following argument. This factor remains close to 0 during the first half inertial period, with a balance between the positive potential energy term $N_0^2 h^2/4$ and the negative kinetic energy term. However as h^2 further increases, the potential energy term $N_0^2 h^2/4$ further increases and dominates the kinetic energy term which decreases as $\propto h^{-2}$. Since we consider a 1D model without surface heat flux, there is no mechanism able to decrease the potential energy term.

A first estimate of this term $\mathcal{R}$ has been provided by Niiler (1975), assuming that a given proportion of the TKE production is converted to potential energy. The TKE production is dominated by the shear stress in the log layer, whose TKE production rate scales like $\propto u_*^3$. This assumption therefore leads to an expression $\mathcal{R} = m_0 u_*^3$, with m_0 a constant related to the assumed 'mixing efficiency' (see section 5 of Niiler (1975), and Kundu (1980) for the full energy budget of the mixed layer). In this scenario, the right-hand side of Eq. (III.24) is no longer zero, and there is a non-trivial solution for long times, corresponding to $h \propto t^{1/3}$ (see also Cushman-Roisin, 1981).

This predicted growth rate is however stronger than what is observed in LES. Moreover it depends on the parameter N_0/f as it will be shown below, which is not confirmed by LES. In terms of physical mechanisms, this estimate by Niiler (1975) relies on TKE production in the upper shear layer. However this occurs in a well-mixed fluid with quasi-uniform density, where TKE is locally dissipated without significant mixing effect. The growth of the mixed layer is controlled instead by TKE produced in the entrainment layer as discussed next.

The TKE production term can be parameterized as (see Appendix III.6.2)

$$P = \nu_t \left| \frac{\partial \mathbf{u}}{\partial z} \right|^2 . \tag{III.26}$$

To give an order of magnitude of this term, we consider the dynamics of the entrainment layer at the base of the mixed layer (Fig. III.2). This layer of thickness h_e is strongly stratified, and we expect the shear flow to be in a state of marginal stability, a condition that is expressed in terms of the Richardson number

$$Ri = \frac{\partial b/\partial z}{|\partial \mathbf{u}/\partial z|^2} \tag{III.27}$$

Classical estimates of the Richardson number for marginal stability are $Ri = 1/4$. With the definition of the entrainment layer (Eq. III.18), we can estimate $\partial b/\partial z = N_e^2 \simeq N_0^2 h/(2h_e)$. The velocity drop can be estimated as $|\langle \mathbf{u} \rangle|/h$, which represents a first-order approximation that treats the velocity in the mixed layer as approximately uniform and close to its depth-averaged value. In reality, the velocity profile within the mixed layer is non-trivial and exhibits complex vertical structure, as we demonstrate through detailed analysis in Section III.4. This oversimplification is one of the key limitations of the present bulk scaling approach. From

(III.11), we have

$$\langle \mathbf{u} \rangle^2 = \frac{2u_*^4}{f^2}(1 - \cos ft),$$

Taking a time average over one oscillation, we thus estimate the velocity drop squared as $2u_*^4/(f^2h^2)$, so that $(\partial u/\partial z)^2 \simeq 2u_*^4/(f^2h^2h_e^2)$. With these estimates, the Richardson number condition (III.27) yields

$$\frac{h_e}{h} = 4\,Ri\frac{u_*^4}{h^4N_0^2f^2} \simeq \left(\frac{L_{P73}}{h}\right)^4 . \tag{III.28}$$

Hence, the entrainment layer thickness is considerably smaller than h within a factor 8 as early as the first half inertial period. From dimensional arguments, an eddy viscosity can be estimated in this entrainment layer as $\nu_t \propto u_*^2/N_e$ (see discussion near Eq. III.75). This parameterization, while commonly adopted in ocean models (Madec, 2008), represents another significant approximation that neglects the complex dependence of turbulent mixing on local shear and stratification. Nevertheless, proceeding with this approximation, we obtain

$$\nu_t \propto 2\sqrt{2}Ri^{1/2}\frac{u_*^4}{h^2N_0^2f} .$$

The resulting TKE production integrated over the entrainment layer is $\langle P \rangle_e \simeq \nu_t u^2/h_e$, which can be estimated from (III.28) and the velocity estimate $u^2 \simeq 2u_*^4/(f^2h^2)$, with integrals over the entrainment layer denoted by $\langle\cdot\rangle_e$. We then propose that the rhs $\mathcal{R}$ in Eq. (III.24) is a fraction m_e of the turbulent kinetic energy production in the entrainment layer

$$\mathcal{R} \simeq m_e\langle P \rangle_e = m_e\frac{u_*^4}{hf} , \tag{III.29}$$

where we have absorbed the prefactor $(2/Ri)^{1/2}$ in the constant m_e. Note that this scaling for the production of TKE is also consistent with the fit of Ushijima and Yoshikawa (2022) (see their Eq. 4). Introducing this expression of $\mathcal{R}$ in the slab model (III.24) yields

$$\left[-\frac{u_*^4}{f^2h^2}(1 - \cos(ft)) + N_0^2\frac{h^2}{4}\right]\frac{dh}{dt} = m_e\frac{u_*^4}{hf} . \tag{III.30}$$

After averaging the oscillations, the term in the left-hand side progressively approaches the value $N_0^2h^2/4$, so we get the asymptotic regime for long times

$$h^3\frac{dh}{dt} = 4m_e\frac{u_*^4}{N_0^2f} . \tag{III.31}$$

We can write Eq. (III.31) in non-dimensional form, introducing $\hat{t} = tf$, and $\hat{h} = h/L_{P73}$,

$$\hat{h}^3\frac{d\hat{h}}{d\hat{t}} = 4m_e . \tag{III.32}$$

Equation (III.32) integrates as

$$\hat{h} = 8^{1/4}\left[1 + 2m_e(\hat{t} - \pi)\right]^{1/4} , \tag{III.33}$$

where we can adjust the constant of integration to get P73's result $\hat{h} = 8^{1/4}$ at $\hat{t} = \pi$. This power law is consistent with the numerical results and will be shown later in Fig. III.6, with a fitted coefficient $m_e \simeq 0.04$.

This value of m_e is surprisingly small, suggesting that ν_t is only a small fraction of the estimate u_*^2/N_e in the entrainment layer. This point will be analysed in section III.4. Note also that we considered an averaged shear over one inertial period for the long-term evolution, while the shear intensity oscillates in time at the inertial frequency suggesting that the deepening occurs in pulses. Indeed, the evolution of the mixed layer depth in the LES (red curve in Fig. III.1) clearly shows these pulses in the deepening rate with enhanced activity when the mixed-layer velocity aligns with the wind stress (at $t/T_f = 0, 1, 2\ldots$). By focusing on a time-averaged evolution over an inertial period, we aim to capture the cumulative effect of these entrainment pulses.

We notice that the growth rate of $\hat{h}$ is independent of the parameter N_0/f. This is in good agreement with the LES result, whose dependency in N_0/f is small (see Eq. III.7). Equation (III.30) is similar to the one proposed by Niiler (1975) except that our expression for the residual is proportional to u_*^4/hf instead of u_*^3. With the expression of Niiler (1975), Eq. (III.32) would be replaced by $\hat{h}^2 d\hat{h}/d\hat{t} = 4m_0(N_0/f)^{-1/2}$. This leads to an excessive long-term growth in $h \propto (N_0/f)^{-1/6} t^{1/3}$, with a dependency in N_0/f inconsistent with the LES results.

In the next section, we will carry out several numerical integrations of a single column model with a k-ϵ closure and for various values of the parameters to assess the validity of this scaling law. As we will see at the end of this article, we can recover this scaling with a more precise derivation (see section III.4).

III.3 Results from the k-ϵ model

To better understand the vertical structure of the mixed layer and entrainment layer, we deploy a k-ϵ model in a single-column framework. This model allows for time integrations of the mean variables for various values of the non-dimensional stratification S. We compare this model with U20's results, and we analyse the vertical structure of the mixed layer.

III.3.1 Numerical simulations

For the k-ϵ calculations, we use the numerical implementation of the single column configuration of the open-source GOTM model[1] (General Ocean Turbulence Model). This model solves the momentum, salt and heat transport equations in a 1D water column. We recall the equations of this closure in Appendix III.6.2. Our configuration solves the k-ϵ equations (III.8, III.12, III.72,IV.42).

We perform calculations for a Coriolis parameter $f = 1.03 \times 10^{-4}$ s^{-1}, corresponding

[1] available at https://gotm.net/

to a latitude of 45°N, and consider four stratifications ranging from $N_0^2 = 8.9 \times 10^{-7}$ s^{-2} to $N_0^2 = 3.5 \times 10^{-3}$ s^{-2}, resulting in $S = \sqrt{N_0/f} = [3, 6, 12, 24]$. The friction velocity $u_* = 0.01$ m s^{-1} is fixed. The simulation duration is 6 days with a time step of 10 seconds. The vertical resolution is set to 0.1 m in a domain extending 100 m along the z-axis. We use the simulation with $N_0^2 = 2.2 \times 10^{-4}$ s^{-2} ($S = 12$) as the reference case.

III.3.2 Vertical structure of the flow

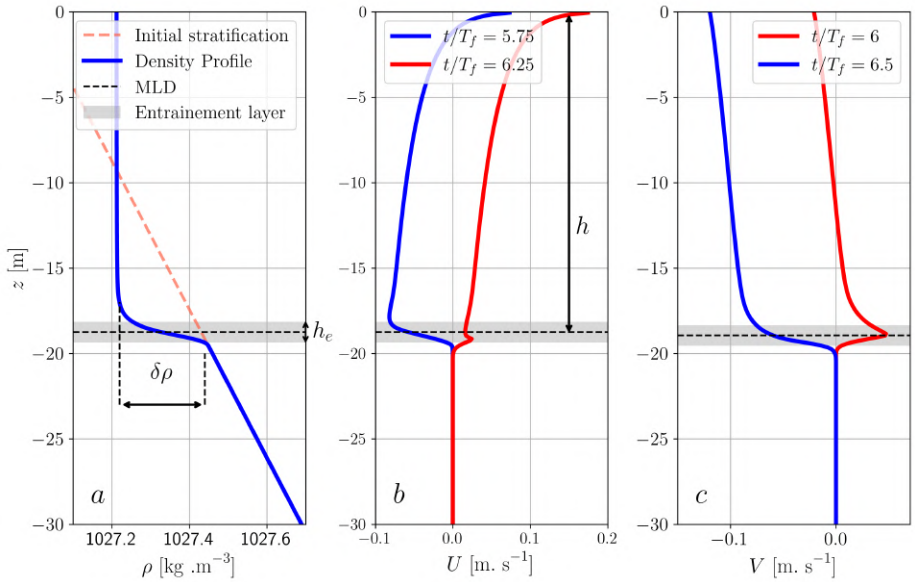

Figure III.3: Vertical profile of (a) density with the initial stratification profile in dashed line, (b) along-wind velocity u and (c) cross-wind velocity v. The velocity components are plotted at the moment of the crest (in blue) and the trough (in red) of the amplitude oscillation. Density profile is plotted at $t/T_f = 5.75$ The parameters of the simulation are : $f = 10^{-4}$ s^{-1}, $N_0^2 = 2.2 \times 10^{-4}$ s^{-2} ($S = 12$), and $u_* = 0.01$ m s $^{-1}$.

We plot in Fig. III.3 the vertical profiles of density and velocity for the reference case ($S = 12$). After 6 inertial periods, the density profile is quasi-uniform in a mixed layer. It is delimited by a thin and strongly stratified entrainment layer, marked by a grey band in Fig. III.3. A strong shear takes place in this active layer, as shown in the velocity profiles of each velocity component. For the along-wind and cross-wind components (u and v respectively), we plot two vertical profiles in antiphase of the inertial oscillation in Fig. III.3b,c.

At each instant, the u-profile shows a logarithmic profile near the surface, as expected from the law of the wall, and intense shear in the entrainment layer. The v-profile does not have this near-surface divergence, but again shows shear in the entrainment layer. We see that, if we exclude the entrainment layer, the shape of the velocity profile remains unchanged at different phases of the oscillation: the entire profile shifts uniformly, which indicates that the magnitude of the oscillation is independent of depth. The velocity profiles can then be expressed as the sum of a quasi-steady component and an oscillation at the inertial frequency, remarkably uniform in the layer and coherent in time. The quasi-steady component can be extracted by taking an

average over one inertial period, while the amplitude of the oscillating component is obtained by taking the difference between min and max. This decomposition between the amplitude of the steady and oscillatory components is plotted in Fig. III.4 and Fig. III.5 for the four values of the parameter S. The u-component is dominated by the log profile near the air-sea interface, while the v-component, produced by the Coriolis force, penetrates more deeply. The oscillating component is uniform down to the entrainment layer. These profiles are compared to those from an idealized model, which will be presented in section III.4. The amplitude of the inertial oscillation decays in time (not shown), which goes in concert with the deepening of the mixed layer described in the next section. Indeed, the exact integral relation (III.11) implies a constant value of the product $|\mathbf{u}|h$.

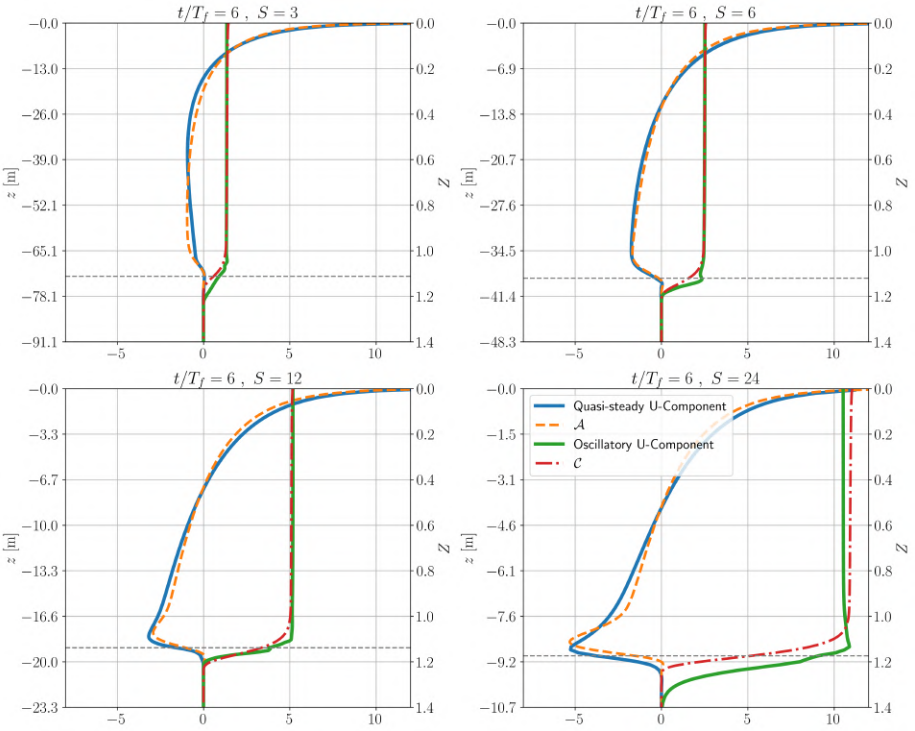

Figure III.4: Vertical profile of the quasi steady velocity and the amplitude of the inertial oscillation in the along-wind direction. The x–axis is the non-dimensional velocity (velocity normalized by u_*) Those components are obtained after filtering the oscillatory component by averaging over an inertial period. The dashed lines $\mathcal{A}$ and $\mathcal{C}$ are the quasi self-similar functions of Z, solution of Eq. (III.51) and Eq. III.59 resolved numerically. $\mathcal{A}$ is the solution for the along wind steady component, $\mathcal{C}$ is the solution for the oscillatory component. The parameters are $\delta = 0.035$, $h_c = h\ (0.9 - 0.002\ S)$, $\hat{c} = 0.1/(S\ h_c^3)$. The horizontal dashed black line marks the mixed layer depth.

III.3.3 Deepening of the mixed layer depth

Figure III.6 shows the time evolution of the mixed layer depth h for all values of S in log-log coordinates. These results align closely with the LES results of U20, indicated by the grey band. Note that while U20 observed slight oscillations within this band, they defined h as the position of the maximum density gradient. We also observe similar oscillations using the same criterion

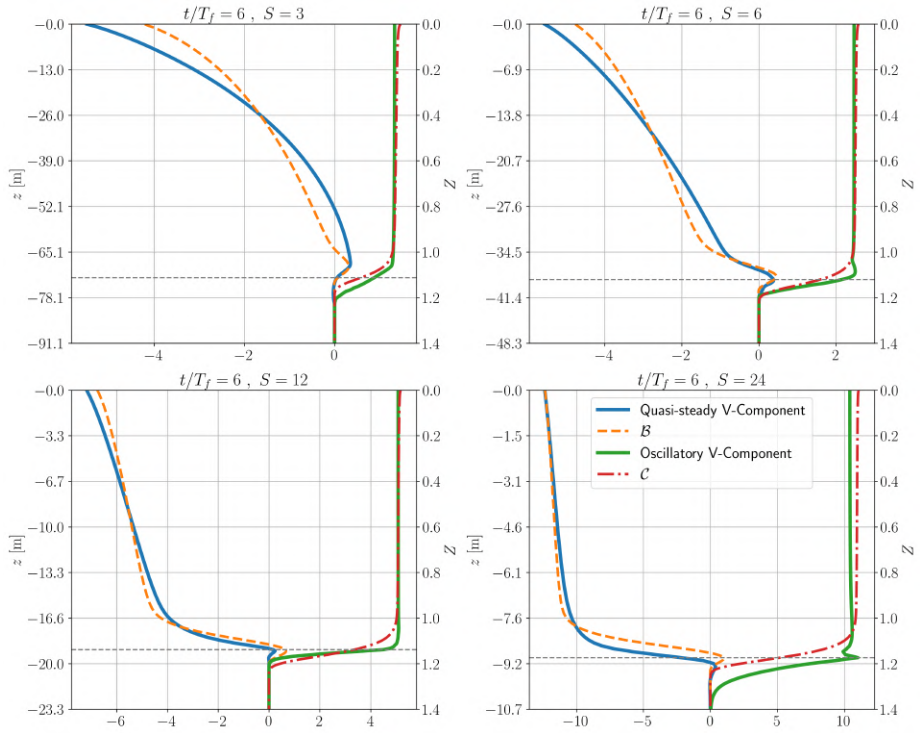

Figure III.5: Same as Fig. III.4 but for the quasi steady velocity and the amplitude of the inertial oscillation in the across-wind direction. $\mathcal{B}$ is the solution for the across wind steady component, $\mathcal{C}$ is the solution for the oscillatory component.

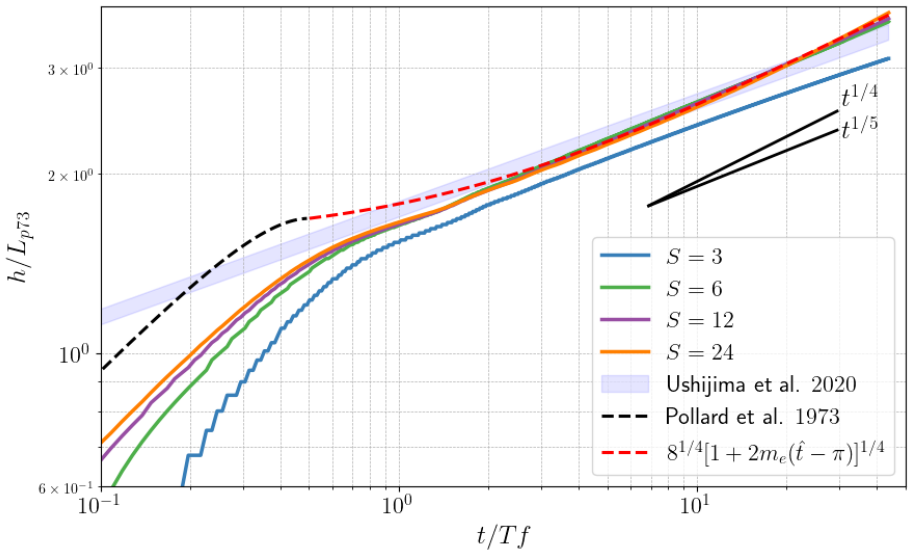

Figure III.6: Temporal variation of the mixed layer depth normalizes by L_{P73} in a log-log scale. Shading represent U20's law for a parameter $S = \sqrt{N_0/f}$ ranging from 3 to 24. The colours lines are k-ϵ simulations for different values of S. The dashed red line represent the scaling law Eq. (III.33) with a parameter $m_e = 0.04$. Slopes corresponding to the power $1/4$ and $1/5$ are given by the black lines. Note: The mixed layer depth h is computed by integrating potential energy over the water column excluding the near-bottom region, where the no-flux boundary condition creates small density variations that would otherwise affect the calculation.

but eliminate them in Fig. III.6 by defining h based on potential energy, ensuring it can only increase monotonically. We clearly distinguish the law $h \propto t^{1/2}$ before the first half inertial period, and a law close to $t^{1/4}$ on long times. Note, however, that the distinction between the exponents 1/4 and 1/5 (proposed by U20) is not really meaningful for durations limited to a few inertial periods. We also plot in Fig. III.6 the scaling law (Eq. III.33) which captures well the asymptotic behaviour. We emphasize that this scaling is independent of S, as it is nearly the case for U20's empirical fit (see Eq. III.7). Note that the case $S = 3$ corresponds to the transition between a pure Ekman layer with no stratification and a stratified regime where buoyancy effects become significant (see discussion in introduction). This regime transition may explain the different slope observed in Fig. III.6.

These results also provide a useful basis for evaluating turbulence closure schemes. In particular, we demonstrate in Appendix III.6.3 how the KPP model (Large et al., 1994) reproduces the late-stage entrainment regime shown in Fig. III.15. The KPP model effectively captures the regime change at the first inertial period, with a corresponding slowdown in mixed layer deepening. However, the KPP model exhibits stronger sensitivity to the parameter S and generally predicts a shallower mixed layer than both the k-ϵ model and the LES (see Fig. III.15). The KPP model configuration is described in Appendix III.6.3.

III.3.4 Energy budget

Another key feature is that after the first inertial period, the TKE is at equilibrium (see Appendix III.6.1). The vertical profiles of the main terms of the TKE equation are shown in Fig. III.7. The profile of the buoyancy flux is close to the linear profile expected for a fully mixed layer (see Eq. III.14). It reaches a maximum in the entrainment layer and drops to zero in the still unperturbed stratified fluid. The maximum of the buoyancy flux is related to the entrainment velocity by the expression $-\nu_t' \frac{\partial b}{\partial z} \simeq \frac{N_0^2}{2} h dh/dt$, obtained by extrapolating (III.14) to $z = -h$.

The limiting factor for this entrainment velocity is the availability of TKE, whose input in the entrainment layer is constrained by the balance

$$\langle P \rangle_e + \langle B \rangle_e - \langle \epsilon \rangle_e = T_k|_{z_{inf}}^{z_{sup}} \tag{III.34}$$

that we obtained by integrating the TKE equation (III.72) at equilibrium in a horizontal band, between altitudes $z_{inf} = h - h_e/2$ and $z_{sup} = h + h_e/2$ in the entrainment layer. With $B = \overline{w'b'} = -\nu_t' \frac{\partial b}{\partial z}$ the buoyancy production, ϵ the dissipation, and T_k, the TKE diffusive flux. The TKE is locally produced by the shear stress at rate P and also fed by incoming diffusive flux from the very active upper region as shown in Fig. III.7. It is partly dissipated at rate ϵ and partly converted to mixing, within a ratio $\Gamma \simeq 1/3$ expected from

$$\Gamma = \frac{-B}{\epsilon} \tag{III.35}$$

Many studies have been devoted to the determination of Γ (see Venaille et al. (2017) for a review). A value $\Gamma = 1/3$ is generally obtained in the case of strong stratification with uniform N, but it

obviously drops to 0 when the fluid is already well mixed, so that no potential energy is provided. We can see in Fig. III.7 that this ratio 1/3 approximately holds in the entrainment layer.

We also see in Fig. III.7, that the production P is less than the sum $\epsilon - B$, especially for low values of S. This means that TKE is partly fed by the diffusive flux coming from the actively sheared upper regions. For large values of S, diffusive fluxes play a minor role such that from (III.34) and (III.35) we get

$$-\langle B\rangle_e = \eta\langle P\rangle_e \tag{III.36}$$

with $\eta = \Gamma/(\Gamma+1) = 0.25$ if we use $\Gamma = 1/3$. Note that with a uniform shear and diffusivity laws (III.74) and (III.26), this relation takes the form of a Richardson number condition (III.27), with $Ri = (\nu_t/\nu_t')\eta$. In this section we showed that the k-ϵ model reproduces the initial deepening

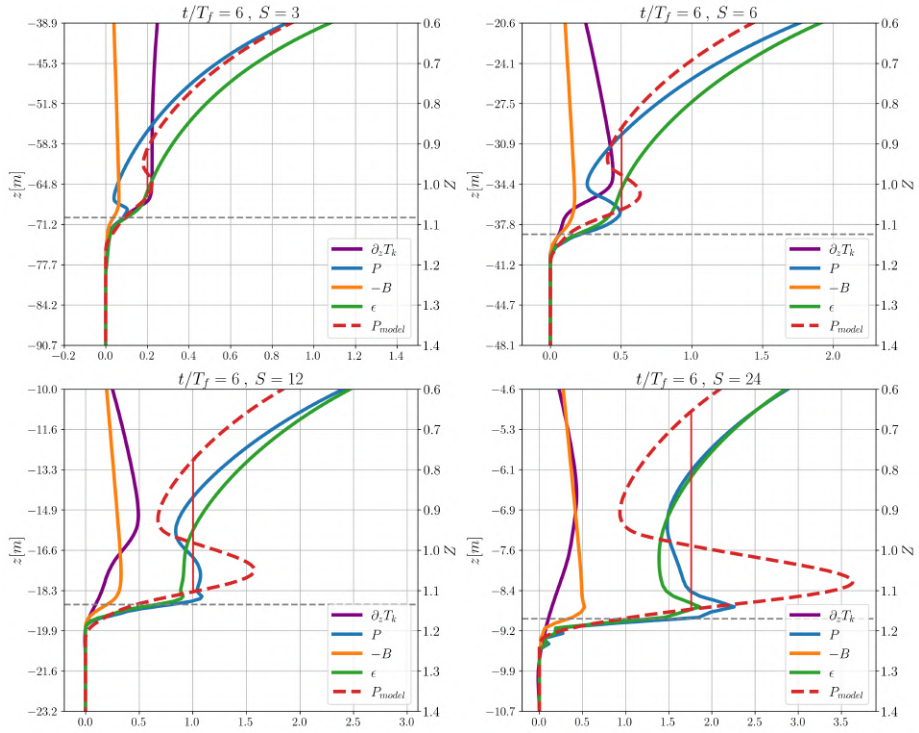

Figure III.7: Vertical turbulent flux representing the different terms of the TKE equation (Eq. III.72) averaged over an inertial period. The horizontal dashed black line represents the mixed layer depth (also averaged over the same inertial period). The dashed red line show the turbulent shear production for the theoretical model detailed in section III.4. The solids red lines show the integral mean over the maxwell construction. The parameters of the theoretical model are the same as in Fig. III.4. For each plot, we use both the dimensional depth and the non-dimensional depth $Z = z/h_c$ (see section III.4) The x-axis is rescale by a factor u_*^3/h_c.

and long-term tendency of the wind-driven mixed layer. P73 provided a correct scaling for the first half inertial period, but for longer times, we need to better describe the shear at the base of the mixed layer. For that purpose, we conduct an analytical development to describe the vertical profile of the horizontal velocity.

III.4 An idealized eddy viscosity model

Based on the k-ϵ model results, we propose that the velocity field can be decomposed into an oscillatory component, independent of z inside the mixed layer, and a stationary Ekman-log-layer. To confirm this, we first seek a self-similar solution and then propose simple solutions for the oscillatory and stationary components. These solutions are used to compute the vertical shear in the entrainment layer.

III.4.1 Quasi self-similar solutions

To find a self-similar solution for buoyancy and velocity, we assume that all dynamical variables depend on a reduced variable $Z = -z/h_c$, where h_c is the position of the top of the entrainment layer. It is close to the layer thickness h defined earlier from the potential energy, but the precise link will be provided when the potential energy will be calculated as an output of the model. We now introduce the following non-dimensional variables

$$(u, v, w) = u_*(\hat{u}, \hat{v}, \hat{w}) \,, \quad t = \hat{t}/f \,, \quad h_c = L_{P73}\hat{h}_c \,, \quad \nu_t = u_* h_c \hat{\nu} \,. \tag{III.37}$$

Near the upper boundary, the eddy viscosity follows the law of the wall, $\nu_t = -\kappa u_* z$, where $\kappa \simeq 0.4$ is the Von Karman constant. Using non-dimensional variables, this becomes $\hat{\nu} \simeq \kappa Z$. Eddy viscosity must also approach zero in the entrainment layer at $Z \simeq 1$, so we expect a maximum of $\hat{\nu}$ to occur near the middle of the mixed layer. These conditions can be approximated by the following model, which will serve as an input for our analysis. A symmetric law function of $\kappa Z(1-Z)$ is assumed in the core of the mixed layer, with its derivative equal to κ at $Z = 0$, consistent with the law of the wall. In the entrainment layer, we assume an exponential decay with a scale δ (relative to the layer thickness h_c) . The prefactor $\hat{\nu}_0$ of this exponential and the crossover position Z_0 are determined by the continuity conditions for both the eddy viscosity and its derivative

$$\begin{aligned} \hat{\nu} &= \kappa Z(1-Z) \,, \quad \text{for } Z < Z_0 \\ \hat{\nu} &= \hat{\nu}_0 e^{-(Z-1)/\delta} \,, \quad \text{for } Z \geq Z_0 \\ Z_0 &= 1 - \delta + \frac{1}{2}\left(\sqrt{1+4\delta^2} - 1\right) \simeq 1 - \delta \\ \hat{\nu}_0 &= \kappa Z_0(1-Z_0) e^{(Z_0-1)/\delta} \simeq \frac{\kappa}{e}\delta \end{aligned} \tag{III.38}$$

This model of the eddy viscosity profile is compared to the k-ϵ calculations in Fig. III.8, for $S = [3, 6, 12, 24]$. The agreement is reasonably good at large S, but significant discrepancy is observed for the lowest values of S, mainly because the magnitude of $\hat{\nu}$ is too strong compared to the k-ϵ turbulent viscosity in the middle of the mixed layer. However, we are mainly concerned with the behaviour in the lower part of the mixed layer, which controls the mixing rate. This behaviour depends on the decay rate δ, a free parameter at this stage. In anticipation of the result in section III.4.6.2, we set $\delta = 0.035$ for all values of S. By definition, h_c is the depth where $Z = 1$, the depth at which the symmetric viscosity profile $\kappa Z(1-Z)$ would vanish in

the absence of exponential decay. Hence, the values of h_c are determined, for each S, such that the value of the turbulent viscosity in the k-ϵ simulations at $Z = 1 - \delta$ is equal to the value of the theoretical viscosity profile at the same depth (Eq. III.38). This procedure yields four estimates of h_c, which are then linearly fitted as a function of S for simplicity, leading to the empirical relation $h_c = h\ (0.9 - 0.002\ S)$. Also, we assume for simplicity that the eddy diffusivity of buoyancy is equal to the eddy viscosity $\nu_t = \nu_t'$, which is in reasonable agreement with the k-ϵ calculations. Note that this profile of eddy diffusivity and viscosity resembles the form $\hat{\nu} = \kappa Z(1 - Z)^2$ used in the K-Profile Parameterization (KPP Large et al., 1994). However, the KPP model constructs its viscosity profile to satisfy specific boundary conditions, with turbulent viscosity dropping exactly to 0 beyond $Z = 1$. This creates numerical singularities for the present analytical development that can be resolved by adding a small non-zero value for the background viscosity. A discussion of the comparison between the KPP model and our model is provided in Appendix III.6.3. To obtain the non-dimensional dynamical equations from

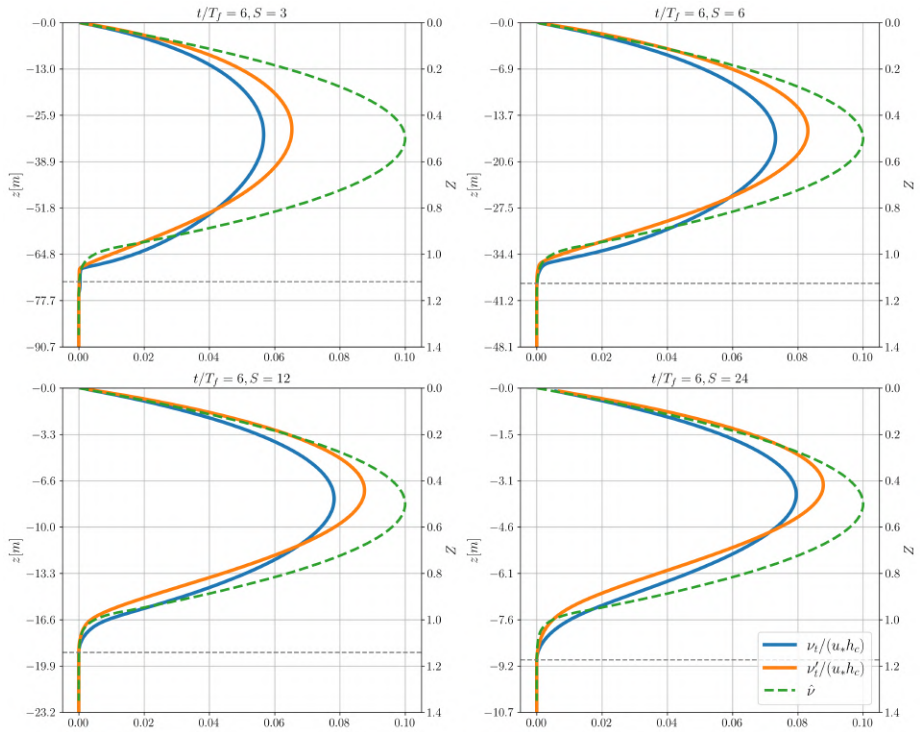

Figure III.8: Vertical profiles of eddy viscosity ν_t (blue lines) and eddy diffusivity ν_t' (orange lines) at $t/T_f = 6$, for different values of the parameter $S = \sqrt{N/f}$, as indicated in each panel. The depth of the mixed layer is plotted with a horizontal dashed line. The analytical model (Eq. III.38) is plotted with a dashed green line for each case. The parameters for this model are $\delta = 0.035$, and $h_c = h\ (0.9 - 0.002\ S)$.

the non-dimensional variables (Eq. III.37), we must account for the fact that the scale h_c depends on time. This leads to the change of coordinates

$$(z, t) \rightarrow (Z = -z/h_c, \hat{t})\,, \tag{III.39}$$

which gives the following derivatives

$$\frac{\partial}{\partial z} = -\frac{1}{h_c}\frac{\partial}{\partial Z}\,, \text{and} \quad \frac{\partial}{\partial t} = \frac{z}{h_c^2}\frac{dh_c}{dt}\frac{\partial}{\partial Z} + f\frac{\partial}{\partial \hat{t}}\,. \tag{III.40}$$

Let us introduce the non-dimensional entrainment velocity $\hat{c}$ defined as

$$\frac{dh_c}{dt} = u_* \hat{c}\,, \quad \text{or} \quad \hat{c} = S^{-1} d\hat{h}_c/d\hat{t} \tag{III.41}$$

so that the coordinate transform is expressed as

$$\frac{\partial}{\partial t} = -\frac{Z}{h_c} u_* \hat{c} \frac{\partial}{\partial Z} + f \frac{\partial}{\partial \hat{t}} \tag{III.42}$$

Note that the value of $\hat{c}$, introduced here as a parameter, should be determined as the end result of our derivation. However, we can estimate it from the k-ϵ model (see Fig. III.1), which shows a slope of $d\hat{h}/d\hat{t} \simeq 0.02$ (note that the abscissa must be multiplied by 2π to express it in terms of phase). Thus, we estimate that during the slow deepening phase, $\hat{c} \simeq 0.01$. We will systematically vary $\hat{c}$ between 0.001 and 0.016 to cover the appropriate range.

III.4.2 Equation for buoyancy

For the buoyancy equation, we first apply the change of variables to Eq. (III.12), defining a non-dimensional buoyancy $\hat{b}$ as follows

$$b = N_0^2 h_c \hat{b} \tag{III.43}$$

Then Eq. (III.12) becomes

$$\frac{\mathrm{d}}{\mathrm{d}Z}\left(\hat{\nu}\frac{\mathrm{d}\hat{b}}{\mathrm{d}Z}\right) = \hat{c}\left(-Z\frac{\mathrm{d}\hat{b}}{\mathrm{d}Z} + \hat{b}\right) \tag{III.44}$$

where we have dropped the term in $\partial\hat{b}/\partial\hat{t}$, as we are seeking self-similar solutions that depend only on the rescaled altitude Z. Therefore, we switch from partial to ordinary derivatives with respect to Z.

Note that the mixed layer depth $\hat{h}_c$ does not appear in Eq. (III.44) because the eddy diffusivity is assumed to scale with h_c. On the contrary, if viscosity were constant, such as the estimate $\nu_t' \sim u_*^2/N$ from (III.75), we would introduce a factor of $\hat{h}_c\hat{c}$ on the right-hand side. The self-similarity condition $\hat{h}_c\hat{c} = S^{-1}\hat{h}_c\frac{d\hat{h}_c}{d\hat{t}} = \text{const.}$ would imply $\hat{h}_c \propto t^{1/2}$. This represents the initial phase when the entrainment layer covers most of the mixed layer. In contrast, during the later phase, the mixed layer is mostly mixed, justifying the scaling $\nu_t \propto h_c$ used in Eq. (III.37). In this case, self-similarity imposes $\hat{c} = \text{const.}$ Self-similarity is not strictly achieved, but we expect it to be a good approximation since $\hat{c}$ evolves only slowly.

Assuming that the eddy diffusivity follows the law (III.38), we can numerically solve Eq. (III.44) in the domain $[0, Z_{\max}]$, where $Z_{\max}$ is an arbitrary upper bound (> 1) chosen for numerical resolution. The no-flux condition at $Z = 0$ implies $\hat{\nu}\frac{\partial\hat{b}}{\partial Z} = 0$. A similar no-flux condition holds at the boundary $Z = Z_{\max}$, but this does not provide any constraint, as $\hat{\nu}$ vanishes there. However, the integral (III.13) must remain equal to its initial value of $-Z_{\max}^2/2$ for the linear profile, so we require

$$\int_0^{Z_{max}} \hat{b} dZ = -\frac{Z_{max}^2}{2}\,. \tag{III.45}$$

We obtain the numerical solution of equation (III.44) by imposing the no-flux condition and setting an arbitrary value of $\hat{b} = 1$ at $Z = 0$. The solution is then renormalized by its integral to satisfy Eq. (III.45), as detailed in Appendix III.6.5. The results are shown in Fig. III.9, where we also indicate the normalized layer thickness h/h_c, obtained from the potential energy definition (III.16), which translates to

$$\left(\frac{h}{h_c}\right)^3 = 12\int_0^{Z_{max}} \hat{b} Z dZ + 4Z_{max}^3 \,. \tag{III.46}$$

This equation allows us to estimate h_c as function of h a posteriori. However, this requires an initial guess for h_c, for each value of S. Using the first estimate, detailed earlier (see Section III.4.1), we obtain new values of h_c for the four values of S with Eq. (III.46). As earlier, we perform a linear fit to get h_c as linear function of S. This procedure is applied iteratively and the linear fit converges to the relation $h_c = h\,(0.905 - 0.0022\,S)$, which is close to our initial guess.

We observe that the non-dimensional depth h/h_c corresponds well to the position of the maximum buoyancy gradient. The thickness of the entrainment layer increases with δ (see Fig. III.9a), while increasing $\hat{c}$ only shifts the vertical position of the entrainment layer without changing its thickness (see Fig. III.9b). To explain these tendencies, we note that the strong buoyancy gradient occurs in the region with exponential decay of diffusivity. In this region, the right-hand side of equation (III.44) is dominated by the first term, involving the derivative at $Z \simeq 1$, so equation (III.44) can be approximated as

$$\frac{\mathrm{d}}{\mathrm{d}Z}\left[\hat{\nu}_0 e^{-(Z-1)/\delta}\frac{\mathrm{d}\hat{b}}{\mathrm{d}Z}\right] = -\hat{c}\frac{\mathrm{d}\hat{b}}{\mathrm{d}Z} \tag{III.47}$$

Regarding the influence of δ, we obtain from (III.38) that for small δ, $\hat{\nu}_0 \simeq \kappa\delta/e$. Therefore, if we rescale δ by an arbitrary factor λ, and if we rescale $Z-1$ by the same factor λ, it would leaves equation (III.47) unchanged. As a result, the entrainment layer thickness $\hat{h}_e$ is proportional to δ, as shown in Fig. III.9a. A simple fit (not shown) of the non-dimensional version of Eq. III.18 ($\hat{h}_e = \hat{h}/(2d\hat{b}/dZ)$) gives $\hat{h}_e \simeq 3\delta$. This thickness is plotted with a vertical bar in Fig. III.9 along with the buoyancy profile. A more formal derivation of this scaling is provided in Appendix III.6.4. To explain the impact $\hat{c}$, we note that multiplying $\hat{c}$ by an arbitrary factor $\lambda > 1$ results in the same equation (III.47) if the variable Z is shifted by adding $-\delta\ln(\lambda) < 0$. This shift is visible in Fig. III.9b. For reference, we also plot in Fig. III.9c the non-dimensional buoyancy profiles for the k-ϵ model for $S = [3, 6, 12, 24]$. A visual comparison reveals that the thickness of the entrainment layer is almost constant while its depth decreases with S.

III.4.3 Momentum equations

We now seek self-similar solutions for the momentum equations in a manner similar to the approach used for the buoyancy equation. Before proceeding, it is convenient to combine the two equations (III.8) into a single equation using the complex variable

$$q = u + iv \,. \tag{III.48}$$

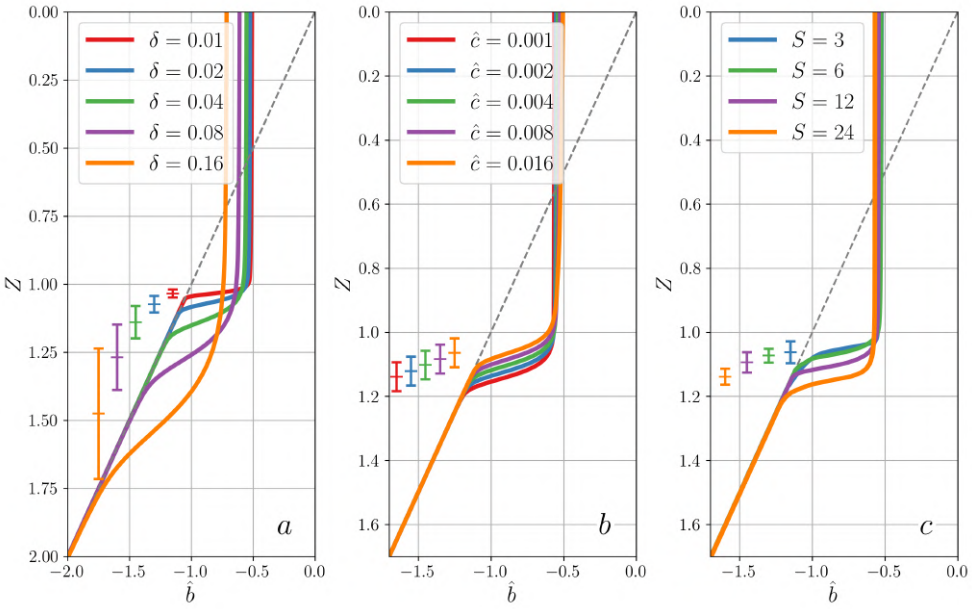

Figure III.9: Profiles of $\hat{b}$ solutions of Eq. (III.44), (a) influence of the parameter $\delta = 0.01 \times [1, 2, 4, 8, 16]$, with $\hat{c} = 0.004$ (curves shift downward for increasing δ). (b) influence of entrainment velocity $\hat{c} = 0.001 \times [1, 2, 4, 8, 16]$, with $\delta = 0.03$ (curves shift upward for increasing $\hat{c}$). The vertical bar correspond to the estimate of the entrainment layer thickness $h_e/h_c \sim 3\delta$. The tick in the middle of the vertical bar marks the position of the mixed layer depth h/h_c. (c) Profiles of $\hat{b}$ for the k-ϵ model for different values of S. The vertical bar correspond to $\hat{h}_e$ from Eq. (III.18), and the tick show the height $\hat{h}$. The initial buoyancy profile is given by the gray dashed line.

This is achieved by taking a linear combination of the two equations (III.8), with coefficients 1 and i respectively, leading to

$$\frac{\partial}{\partial z}\left(\nu_t \frac{\partial q}{\partial z}\right) = \frac{\partial q}{\partial t} + ifq\,. \tag{III.49}$$

Applying the transform (III.42) to the non-dimensional variable $\hat{q} = q/u_*$ leads without any approximation to the rescaled version

$$\frac{\partial}{\partial Z}\left(\hat{\nu}\frac{\partial \hat{q}}{\partial Z}\right) = -\hat{c}Z\frac{\partial \hat{q}}{\partial Z} + S^{-1}\hat{h}_c\left(\frac{\partial \hat{q}}{\partial \hat{t}} + i\hat{q}\right)\,. \tag{III.50}$$

For a given eddy viscosity profile and entrainment velocity $\hat{c}$, this is a linear equation in $\hat{q}$ whose general solution can be expressed as the sum of time periodic solutions. A whole spectrum of frequencies is excited as obtained from a Fourier transform of Heaviside function which represents the wind forcing starting at time $t = 0$. In the simplified case of a constant viscosity ν, and no entrainment velocity term, a perturbation in $\exp(i\omega t)$ would decay vertically in $\exp(-mZ)$ with $\nu m^2 = S^{-1}\hat{h}_c i(\omega+1)$, so that $m = h_c^{1/2}(2S\nu)^{-1/2}(\omega+1)^{1/2}(1+i)$. Therefore, for large S, the decay rate with depth is small in amplitude and phase shift (the imaginary component of m). The decay rate completely vanishes for the inertial frequency $\omega = -1$. This gives support to the slab model, so we expect the flow to be quickly dominated by a steady component and an inertial oscillation whose vertical integral behaves according to Eq. (III.11).

III.4.4 Steady solutions

For the steady component $\hat{q}_s$, Eq. (III.50) reduces to

$$\frac{\mathrm{d}}{\mathrm{d}Z}\left(\hat{\nu}\frac{\mathrm{d}\hat{q}_s}{\mathrm{d}Z}\right) = -\hat{c}Z\frac{\mathrm{d}\hat{q}_s}{\mathrm{d}Z} + (S/\hat{h}_c)^{-1}i\hat{q}_s\,, \tag{III.51}$$

with boundary conditions

$$\left(\hat{\nu}\frac{\mathrm{d}\hat{q}_s}{\mathrm{d}Z}\right)_{Z\to 0} = -1\,, \tag{III.52}$$

and $\hat{q}_s \to 0$ at large Z. Notice that this equation has the same mathematical structure as Eq. (III.44) for buoyancy (but with complex variables), and solutions can be numerically obtained in a similar way (see Appendix III.6.5).

The resulting $\hat{u}$ and $\hat{v}$ profiles, obtained by taking the real and imaginary parts respectively, are shown in Fig. III.10. They compare well with the k-ϵ results as shown in Fig. III.4 and Fig. III.5. These profiles can be viewed as Ekman spirals squeezed in the entrainment layer as the viscosity is dropping to 0. This is clearly visible in the hodographs of Fig. III.10c.

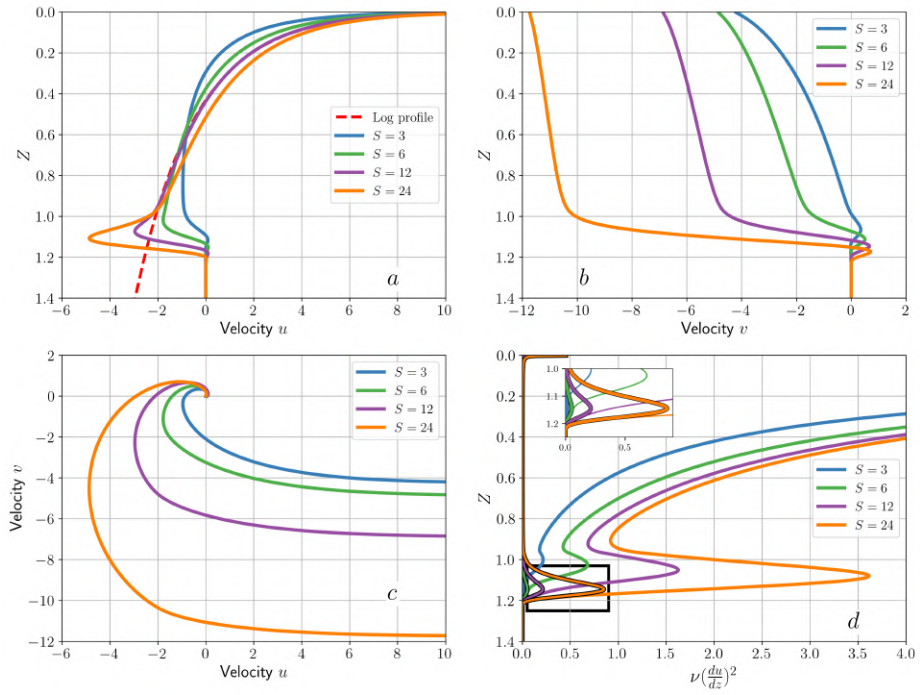

Figure III.10: (a): Profiles of $\hat{u}$ and (b): $\hat{v}$, respective real and imaginary parts of the solutions of steady momentum Eq. (III.51), (c) Hodograph of the $\hat{u}$, $\hat{v}$ velocities. (d) Vertical profile of the turbulent shear production for a constant parameter δ. The insert plot is a zoom of the main plot highlighted by the black square showing the TKE shear production due to the inertial component. The other curve are due to the steady components. The parameters for this model are $\delta = 0.035$, $\hat{h}_c = 2$, $\hat{c} = 0.001$ for $S = [3, 6, 12, 24]$.

We observe that the entrainment velocity term on the right-hand side of (III.51) has a negligible influence. Indeed $\hat{c}$ is typically of order 10^{-3}, while the second term scales like

$\hat{h}_c/S \sim 10^{-1}$. Neglecting this term in $\hat{c}$, and writing $\hat{q}_s = A(Z) - i(S/\hat{h}_c)B(Z)$, the complex Eq. (III.51) can be split as

$$\begin{aligned} \frac{\mathrm{d}}{\mathrm{d}Z}\left(\hat{\nu}\frac{\mathrm{d}A}{\mathrm{d}Z}\right) &= B \\ \frac{\mathrm{d}}{\mathrm{d}Z}\left(\hat{\nu}\frac{\mathrm{d}B}{\mathrm{d}Z}\right) &= -(S/\hat{h}_c)^{-2}A\,, \end{aligned} \tag{III.53}$$

with the boundary condition at the surface yields

$$\begin{aligned} \left(\hat{\nu}\frac{\mathrm{d}A}{\mathrm{d}Z}\right)_{Z\to 0} &= -1 \\ \left(\hat{\nu}\frac{\mathrm{d}B}{\mathrm{d}Z}\right)_{Z\to 0} &= 0\,. \end{aligned} \tag{III.54}$$

The functions A and B must drop to 0 for $Z \gtrsim 1$, and the momentum fluxes also vanish. The integral conditions (III.11), also verified by integrating Eq. (III.53) vertically, impose that

$$\begin{aligned} \int_0^\infty A(Z)\,dZ &= 0 \\ \int_0^\infty B(Z)\,dZ &= 1\,. \end{aligned} \tag{III.55}$$

Because of the vanishing viscosity, we have the logarithmic divergence $A = -\frac{1}{\kappa}\ln Z + \text{const}$. Extending that expression to the whole layer, and using the integral condition (III.55), we get the simple approximation expected for large S.

$$\begin{aligned} A(Z) &= -\frac{1}{\kappa}(\ln Z + 1) \\ B(Z) &= 1\,. \end{aligned} \tag{III.56}$$

We can see in Fig. III.4 and Fig. III.5 that the actual $\hat{u}$ profiles approach this logarithmic law for large values of $S/\hat{h}_c$, while the $\hat{v}$ profiles tend to approach the constant value $\hat{v} = -S/\hat{h}_c$, corresponding to $B = 1$. However, all the profiles smoothly drop to zero in the entrainment layer, whereas the simple estimates (III.56) drop to 0 discontinuously. We will use these results at the end of this analysis to determine the model parameters $\hat{c}$ and δ.

III.4.5 Inertial oscillations

For the oscillatory component at the inertial frequency, we can express the solution in the form

$$\hat{q}_i = i\,\frac{S}{\hat{h}_c}C(Z)\exp\left(-i\hat{t}\right)\,. \tag{III.57}$$

If $C(Z)$ is real, this corresponds to $\hat{u} = (S/\hat{h}_c)C\,\sin\hat{t}$ and $\hat{v} = (S/\hat{h}_c)C\,\cos\hat{t}$, so that the integral constraints (III.11) translate to

$$\int_0^\infty C dZ = 1\,. \tag{III.58}$$

The time derivative and Coriolis terms cancel each other in Eq. (III.50), leading to

$$\frac{\mathrm{d}}{\mathrm{d}Z}\left(\hat{\nu}\frac{\mathrm{d}C}{\mathrm{d}Z}\right) = -\hat{c}Z\frac{\mathrm{d}C}{\mathrm{d}Z}\,. \tag{III.59}$$

We notice that the coefficients of Eq. (III.59) are real, so that there is no phase shift within the layer. The choice (III.57) with $C(Z)$ real is therefore justified. The circular motion of fluid elements corresponds to the free trajectories of particles subject to the Coriolis force, so the surface forcing diffuses efficiently, similar to unidirectional motion in the absence of Coriolis effects. This contrasts with the steady component, whose diffusion is constrained by Coriolis effects, as expressed by the second term on the right-hand side of Eq. (III.51). Equation (III.59) is again mathematically similar to the buoyancy equation (III.44) and can be solved numerically by similar methods. It can also be solved analytically (see Appendix III.6.4). The vertical profiles of the oscillatory component are then similar to the buoyancy profiles (Fig. III.9), except that $C \to 0$ for $Z > 1$. The solution C is plotted with the oscillatory component of the solution of the k-ϵ model in Fig. III.4 and III.5. We confirm that the oscillatory component is almost uniform in the vertical with a sharp transition at the base of the mixed layer. As expected, the amplitude of this oscillating component is close to $S/2$.

III.4.6 Energy constraints

For a given value of S and $\hat{h}_c$, the results depend on two parameters, $\hat{c}$ and δ, which are arbitrary so far. They can be determined by using the fact that the entrainment layer is in a state of marginal stability, which corresponds to a constant Richardson number. This Richardson number constraint can be expressed in non-dimensional variables, using $|\partial\mathbf{u}/\partial z|^2 = (u_*/h_c)^2[(\partial\hat{u}/\partial Z)^2 + (\partial\hat{v}/\partial Z)^2]$ with $h_c^2 = \hat{h}_c^2 L_{P73}^2 = \hat{h}_c^2 u_*^2/(N_0 f)$, and $\partial b/\partial z = -N_0^2\partial\hat{b}/\partial Z$, so that the Richardson constraint (III.36) becomes

$$\frac{\langle|\partial\hat{\mathbf{u}}/\partial Z|^2\rangle_e}{\langle-\hat{h}_c^2 S^2\partial\hat{b}/\partial Z\rangle_e} = \frac{1}{\eta}\,. \tag{III.60}$$

We use here the inverse Richardson number, which can be conveniently expressed by adding the different contributions to the velocity. Indeed, the vertical shear can be expressed as the sum of the stationary and oscillating contributions,

$$\left|\frac{\partial\hat{\mathbf{u}}}{\partial Z}\right|^2 = \left[\frac{dA}{dZ} + \frac{S}{\hat{h}_c}\frac{dC}{dZ}\sin(ft)\right]^2 + \frac{S^2}{\hat{h}_c^2}\left[\frac{dB}{dZ} - \frac{dC}{dZ}\cos(ft)\right]^2\,, \tag{III.61}$$

expressed also as

$$\left|\frac{\partial\hat{\mathbf{u}}}{\partial Z}\right|^2 = \left(\frac{dA}{dZ}\right)^2 + \frac{S^2}{\hat{h}_c^2}\left(\frac{dB}{dZ}\right)^2 + \frac{S^2}{\hat{h}_c^2}\left(\frac{dC}{dZ}\right)^2 + 2\frac{S}{\hat{h}_c}\frac{dC}{dZ}\frac{dA}{dZ}\sin(ft) - 2\frac{S^2}{\hat{h}_c^2}\frac{dC}{dZ}\frac{dB}{dZ}\cos(ft)\,. \tag{III.62}$$

Taking the average over one inertial period, we may drop the last two terms, with zero mean. We now examine the contribution of the stationary component and then the impact of the inertial component. This energetic balance must be integrated in a band enclosing the entrainment layer, for which we can neglect the boundary flux of TKE, as stated in the next sub-section.

III.4.6.1 Determination of the entrainment velocity

The vertical profile of the normalised TKE production $\hat{P} = \hat{\nu}\,|\partial\hat{\mathbf{u}}/\partial Z|^2$ is plotted in Fig. III.10d. The production is maximum near $Z = 0$, due to the log profile of the u component. Then it reaches a minimum near $Z = 1$ and increases again in the strongly sheared entrainment layer. The buoyancy flux is still close to its maximum near $Z = 1$, so the minimum of $\hat{P}$ is the bottleneck region for the energetic constraint to mixing expressed by (III.60). Let us choose the test zone around this minimum, obtained by a 'Maxwell construction' as shown by the vertical segment. This zone covers the minimum and lower maximum, and the vertical segment in Fig. III.7 is positioned at the value where the production is equal to its integral over the zone. The Maxwell construction is motivated by two considerations. First, turbulent diffusion homogenizes TKE within the entrainment zone while preserving its integral, and the Maxwell construction effectively models this diffusion process. Second, although the magnitude of the production peak varies significantly depending on the choice of the vertical viscosity profile, the integral of production over the entrainment layer remains remarkably consistent across closures (see Appendix III.6.3). The results shown in Fig. III.7 for the k-ϵ model display a maximum production in the entrainment zone while ϵ, related to TKE, has a smoother profile. We expect that the 'Maxwell construction' provides a good proxy for the homogenisation process. It neglects the possibility of incoming diffusive flux from the very active upper regions, so it yields a lower estimate of the mixing process.

We notice that the TKE production is dominated by the quasi-stationary components u and v (see insert in Fig. III.10d). The shear associated with the inertial oscillation is of the same order, but its maximum is located at a lower position. It is in the exponentially decaying zone for viscosity, leading to a lower production. We neglect the stationary component in the TKE production term since the ratio of the stationary component to the oscillatory component (two terms in the right-hand side of Eq. (III.61)) is approximately 1% when integrated over the entrainment layer (not shown). The direct consequence is that mixing is primarily controlled by the stationary component and that inertial oscillations have little effect on entrainment. Since the profiles of the steady components are not sensitive to the value of $\hat{c}$, as it was shown in section III.4.4, the TKE production is independent of $\hat{c}$ to a good approximation.

We find that the TKE production obtained by the Maxwell construction is roughly proportional to $S/\hat{h}_c$, as seen in Fig. III.11. It can be fitted as

$$\langle \hat{\nu} \left| \frac{\partial \hat{\mathbf{u}}}{\partial Z} \right|^2 \rangle_m \simeq 0.16 \, \frac{S}{\hat{h}_c}\,, \tag{III.63}$$

where $\langle\cdot\rangle_m$ is the integral over the Maxwell construction normalized by the thickness of the layer. This figure compares results with different values of the parameter δ and little sensitivity is found. Therefore, we can use this fit although the parameter δ has not been set at this stage.

On the other hand, the buoyancy flux is given in the mixed layer by Eq. (III.14), which writes in non-dimensional form $\hat{\nu}\frac{\partial \hat{b}}{\partial Z} = \hat{c}Z/2$. Since our averaging zone is close to Z=1, we can estimate

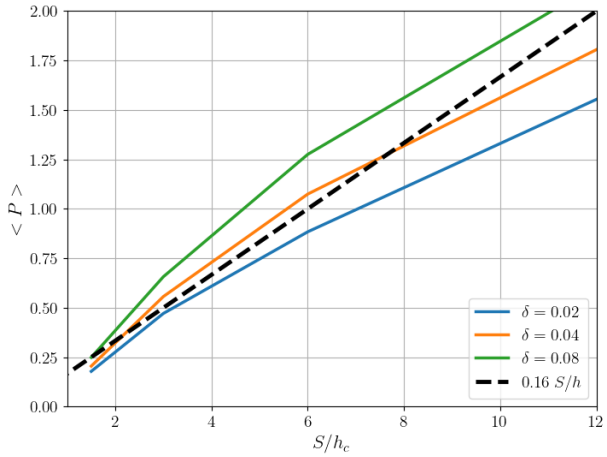

Figure III.11: TKE production averaged in the lower zone $\langle \hat{P} \rangle_m$ versus S/h_c for given values of $\delta = [0.02,\ 0.04,\ 0.08]$. The black dashed line represent an empirical fit (Eq. III.63).

$\langle \hat{\nu} \frac{\partial \hat{b}}{\partial Z} \rangle_m \simeq \hat{c}/2$, so the energetic balance (III.60) yields

$$\hat{c} = 0.32 \frac{\eta}{S \hat{h}_c^3} \,. \tag{III.64}$$

Since $\hat{c} = S^{-1} d\hat{h}_c/d\hat{t}$, this yields the law

$$\hat{h}_c^3 \frac{d\hat{h}_c}{d\hat{t}} = 0.32\, \eta \simeq 0.1 \,. \tag{III.65}$$

Considering that $\hat{h}_c$ is not far from $\hat{h}$, this equation is similar to Eq. (III.32) derived with scaling arguments. The numerical solution to this equation appears in Fig. III.6, and is consistent with the results of the LES and the k-ϵ model.

The production tends to drop for low values of $S/\hat{h}_c$. In this regime, the flow is confined by the Ekman spiral effect before reaching the stratified interface. However, diffusion of TKE, not taken into account here, must increase the rate of mixing. For high values of $S/\hat{h}_c$, we also observe a reduction of the entrainment velocity with respect to the linear law, as represented by (III.63). In that case, the entrainment layer occupies a significant part of the flow, so the distinction between $\hat{h}_c$ and $\hat{h}$ becomes significant.

III.4.6.2 Estimation of the entrainment layer thickness

The thickness δ is still a free parameter of our simplified model. We provide here a constraint from the profile of the Richardson number. The Richardson number must be sufficiently small in the entrainment layer to maintain some turbulence production, as required for mixing. The most critical region is the zone of strongest density gradient, near $z = -h$. At this height, the shear is dominated by the inertial component, whose shear modulus is well approximated by $|d\hat{u}/dZ| = (S/h_c)|dF_c/dZ|$, with a maximum of $|dF_c/dZ|$ equal to $0.35/\delta$ (see section III.4.5 and Appendix A). The buoyancy gradient at this level is well approximated by $d\hat{b}/dZ = (1/2)|dF_c/dZ|$. The

Richardson number is expressed in terms of the non-dimensional variables as $Ri = -\frac{\hat{h}_c^2 S^2}{|d\hat{\mathbf{u}}/dZ|^2}\frac{d\hat{b}}{dZ}$, which thus approximates as

$$Ri = \frac{\hat{h}_c^4}{2}\left|\frac{dF_c}{dZ}\right|^{-1} \tag{III.66}$$

With the maximum of $|dF_c/dZ|$ equal to $0.35/\delta$, reached at $z \simeq -h$, this yields $Ri \simeq 1.5\,\hat{h}_c^4\delta$. Assuming a critical value $Ri = Ri_c = 0.843$, as stated in Appendix III.6.2, this yields $\delta \simeq 0.67\,Ri_c/\hat{h}_c^4$. For $\hat{h}_c = 2$, we get $\delta = 0.035$. From the derivation of section III.4.2, this corresponds to a thickness of the entrainment layer $h_e/L_{P73} \simeq 3\delta$. Therefore, we get a result similar to the previous scaling (III.28) in section III.2.4,

$$h_e/L_{P73} \simeq 2.0\,Ri_c\left(\frac{L_{P73}}{h}\right)^4 \tag{III.67}$$

Note this result $\delta \simeq 0.035$ is independent of the parameter S while the fits of the eddy viscosity profile shown in Fig. III.8 suggest that it should increase with increasing parameter S. However, careful comparisons indicate that eddy viscosity decays more strongly in the lowest part of the entrainment layer, suggesting that the scale δ should not remain constant, but decrease with depth instead. Moreover, we have chosen for simplicity a constant turbulent Prandtl number ν_t/ν_t' while the k-ϵ model yields a value significantly larger than 1 for Richardson numbers approaching Ri_c.

Notice however that this difficulty to get a fully consistent determination of the parameter δ does not affect the entrainment velocity $\hat{c}$, which turns out to be insensitive to the value of δ. This entrainment velocity is indeed determined by the energy constraint (III.60) around the level of minimum TKE production. At this level the eddy viscosity is not affected by the exponential decay, so it does not depend on δ.

III.5 Conclusions

In this work, we revisited the long-term deepening of a wind-driven mixed layer under the combined effects of rotation and stratification. Using a one-dimensional column model with a k–ϵ turbulence closure, we showed that this model captures both the initial evolution and the long-term deepening of the mixed layer, in agreement with previous LES studies. Starting from the analysis of Pollard et al. (1973), we revisit some of their hypotheses. More precisely, since most of the mixing occurs in a thin entrainment layer at the base of the mixed layer, we propose a parameterization for the missing terms in the energy budget, proportional to the production of turbulent kinetic energy in that layer. We obtain an equation of evolution of the thickness of the mixed layer h (Eq. III.31) whose solution is $\hat{h} \propto \hat{t}^4$ (with non-dimensional variables).

We confirmed this scaling with the development of a simplified model for the mixed-layer depth evolution, based on an idealized eddy viscosity profile in the entrainment zone. By assuming an exponential decay of turbulent viscosity within the entrainment layer, we reproduced the vertical structure of the mixed layer observed in the k–ϵ simulations. We then isolated the

contribution of inertial oscillations from the near-surface logarithmic velocity profile, which enabled us to analytically derive the long-term asymptotic behavior as a scaling law that agrees well with the LES results. This approach provides a more physically grounded understanding of how energy is distributed and dissipated in the system.

In our approach, we neglected the pulsed nature of entrainment (visible in Fig. III.1) and considered the averaged response over one inertial period to capture the long-term evolution. However, these inertial-period pulses open intriguing research directions. Future studies could examine the detailed dynamics of these entrainment pulses to provide insights into short-term mixed layer variability. Investigating how these pulses interact with other oceanic processes, such as internal waves or submesoscale dynamics, offers promising opportunities for advancing our understanding of upper ocean mixing processes.

While our analysis provides new insights into rotation-modified entrainment, we acknowledge that surface wave effects – particularly Langmuir turbulence, and wave breaking – represent a crucial next step in developing a complete theory of mixed layer deepening (Deike, 2022). Langmuir circulation, driven by the interaction between surface waves and wind-driven currents, can significantly enhance vertical mixing and modify entrainment rates, especially during the weak late-stage deepening regime identified in our study. The incorporation of wave-driven processes into our rotational framework is a natural extension of this work.

Last, some studies have pointed out the limitations of one-dimensional models under strong stratification (Ezer, 2000). In future work, we aim to further assess the robustness of turbulence closure models with dedicated laboratory experiments conducted on the Coriolis rotating platform (LEGI, France). These experiments of turbulent stratified entrainment in rotation, are designed to build a dataset against which turbulence closures can be tested and parameterizations can be improved. We have already evaluated the performance of the k-ϵ model and found that it is able to accurately reproduce the entrainment dynamics and the vertical structure of the turbulent boundary layer. These results support the relevance of our 1D modelling approach and provide a basis for future model development and validation.

III.6 Appendices

III.6.1 Exact energy equation

The exact energy budget for the total energy $E = E_{kin} + E_{turb} + E_{pot}$ (the sum of the vertical integral of the mean kinetic energy, turbulent kinetic energy, and potential energy, respectively) is given by

$$\frac{d}{dt}E_{kin} + \frac{d}{dt}E_{turb} + \frac{d}{dt}E_{pot} = u_*^2 u_{(z=0,t)} - \mathcal{E}\,, \tag{III.68}$$

where the vertical integral of the local dissipation rate $\mathcal{E} = \langle\epsilon\rangle > 0$ represents the viscous energy dissipation rate controlled by the turbulent cascade. The wind forcing produces a shear layer near the surface, so that $u_{(z=0,t)} > \langle u\rangle/h$. The additional energy production $u_*^2\left(u_{(z=0)} - \langle u\rangle/h\right)$ serves as the source of turbulence. Turbulent kinetic energy remains small compared to the

mean kinetic and potential energy, as it cannot accumulate and is dissipated partly through viscous dissipation at the local rate ϵ, and partly through transfer to the mixing of the mean density profile. Therefore, equation (III.20) should be replaced by

$$\frac{d}{dt}E_{kin} + \frac{d}{dt}E_{pot} \geq u_*^2 \frac{\langle u \rangle}{h} ,$$

which means the right-hand side of equation (III.24) is not exactly zero, but instead should show a small positive residual. To find this residual, let us examine the processes occurring in the mixed layer. The shear stress is primarily concentrated near the surface, where the fluid is already well mixed, so turbulence is dissipated locally without contributing to further mixing. Additionally, the rate of transfer is constrained by the momentum equation and the related slab energy E_{slab}, which scales as hE_{kin}. This constraint implies that rapid mixing would lead to a strong decrease in $E_{kin} \sim E_{slab}/h$, reducing the shear at the lower interface and providing negative feedback to the mixing process. This justifies the hypothesis in equation (III.20) as a first approximation. However, slow mixing is expected to persist after half an inertial period, controlled by a small non-zero value of the right-hand term in equation (III.24).

A second simplification by P73 is the assumption of a uniform slab velocity, such that $E_{kin} = E_{slab}/h$. In reality, we have $E_{kin} = E_{slab}/h + \tilde{E}$, where $\tilde{E}$ represents the kinetic energy associated with the deviation of the velocity from the uniform slab velocity. Using equation (III.19), this can be expressed as

$$\tilde{E} = \frac{1}{2}\int (\mathbf{u} - \frac{\langle \mathbf{u} \rangle}{h})^2 dz = E_{kin} - \frac{u_*^4}{f^2 h}\left(1 - \cos(ft)\right) . \tag{III.69}$$

Thus Eq. (III.23) is replaced by

$$-E_{slab}\frac{dh}{h^2 dt} + \frac{d\tilde{E}}{dt} + \frac{d}{dt}E_{turb} + \frac{d}{dt}E_{pot} = u_*^2\left(\frac{\langle u \rangle}{h} - u_{(z=0,t)}\right) - \mathcal{E} , \tag{III.70}$$

so that, from (III.19) and (III.16),

$$\left[\underbrace{-\frac{u_*^4}{h^2 f^2}(1-\cos(ft))}_{\text{SLAB}} + \underbrace{N_0^2\frac{h^2}{4}}_{\text{POTENTIAL}}\right]\frac{dh}{dt} = \overbrace{\underbrace{u_*^2\left(u_{(z=0,t)} - \frac{\langle u \rangle}{h}\right)}_{\text{EXTRA PROD}} - \underbrace{\mathcal{E}}_{\text{DISSIPATION}} - \underbrace{\frac{d}{dt}\tilde{E}}_{\text{DEVIATION}} - \underbrace{\frac{d}{dt}E_{turb}}_{\text{IMBALANCE}}}^{=\mathcal{R}} . \tag{III.71}$$

The k-ϵ model gives us an opportunity to verify this energy budget. In Fig. III.12, we compare the four terms of the right-hand side of Eq. (III.71). Although $\tilde{E}$ is large due to the strongly sheared log layer near the surface, this shear flow component does not significantly vary in time, so that $d\tilde{E}/dt$ remains small compared to the time derivatives of the slab kinetic energy and the potential energy. This gives support for the slab model. We notice, however, that $d\tilde{E}/dt > 0$ during the first inertial period, which leads to a somewhat smaller growth rate of h and smaller value at half inertial period. Another element that supports P73's hypothesis is the balance between the extra production and dissipation (we plot $+\mathcal{E}$ in Fig. III.12 but it appears with a minus sign in Eq. (III.71)). The residual $\mathcal{R}$ (dashed line in Fig. III.12) is small as mentioned in P73 but it is not exactly zero as we can see in the insert. It is this term that is responsible for continued deepening after the first inertial period.

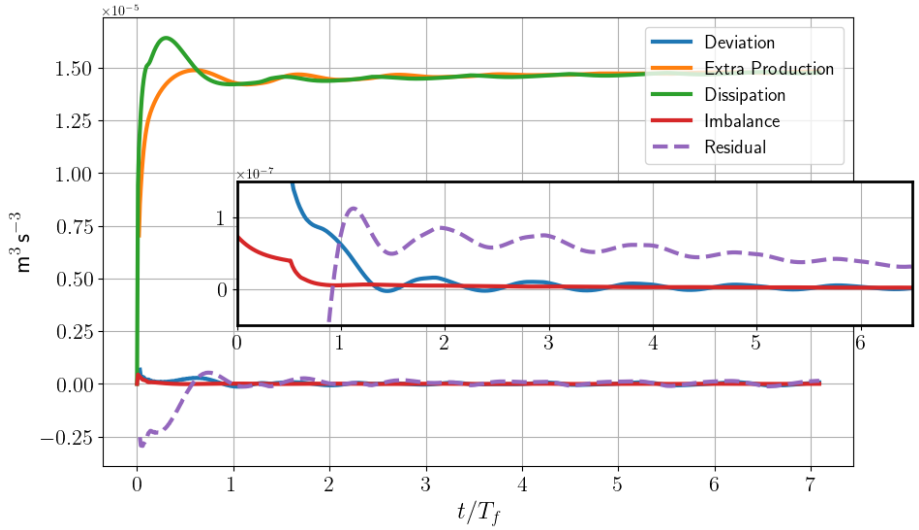

Figure III.12: Time evolution of the terms of the right-hand side in Eq. (III.71) for the reference case ($S = 12$): Extra-Production, Dissipation, Deviation from the slab model and the Imbalance term from the evolution of the turbulent kinetic energy.. The dashed purple line is the sum of those terms and corresponds to the "residual term" $\mathcal{R}$. In the main plot, the value are instantaneous. The insert plot is a zoom of the main plot with averaged value over an inertial period.

III.6.2 k-ϵ equations

To close the system of equations (III.8) and (III.12) we use the k-ϵ approach to compute the eddy viscosity ν_t and diffusivity ν_t'. Within this framework, we have two prognostic equations for turbulent kinetic energy (k) and dissipation (ϵ). The equation for the TKE $k \equiv \overline{\mathbf{u}'^2}/2$ can be written in the form

$$\frac{\partial k}{\partial t} + \frac{\partial T_k}{\partial z} = P + B - \epsilon \tag{III.72}$$

where the eddy flux T_k, the production rate P, the conversion rate to potential energy B, and the dissipation rate ϵ can be expressed exactly from correlations of turbulent fluctuations (the notation $\bar{\cdot}$ and $\cdot'$ denote the standard ensemble averaging and deviation from the ensemble mean respectively).

Within the eddy viscosity model, the production P is set by the shear according to

$$P = -\overline{u'w'}\frac{\partial u}{\partial z} - \overline{v'w'}\frac{\partial v}{\partial z} = \nu_t \left|\frac{\partial \mathbf{u}}{\partial z}\right|^2 . \tag{III.73}$$

The flux T_k tends to smooth the inhomogeneities of the production P while preserving the integral of k. It is modelled by a diffusion law $T_k = -\nu_t \partial k/\partial z$. Note that the TKE remains small compared to the energy of the mean flow, so that the term $\partial k/\partial t$ can be neglected in the slowly varying flows considered here. The diffusive flux T_k is also rather small as shown by Kundu (1980), so the dominant process is the balance between the three terms on the right-hand side of (III.72).

The conversion rate to potential energy B also represents the vertical flux of buoyancy.

Within the eddy diffusivity hypothesis, it is expressed as

$$B = \overline{w'b'} = -\nu'_t \frac{\partial b}{\partial z} \equiv -\nu'_t N^2 \,, \tag{III.74}$$

introducing the local buoyancy frequency $N_{(z,t)}$.

The dissipation rate ϵ is controlled by the turbulent energy cascade process and can be estimated by dimensional arguments as $\epsilon \sim u'^3/l$ for turbulence with a given scale l and velocity $u' \sim k^{1/2}$.

The eddy viscosity can be estimated as $\nu_t \sim \nu'_t \sim u'l$ from a mixing length argument. Then (III.72) can be closed if we know the turbulent scale l. In neutrally buoyant shear flows, l scales as the distance to the boundary or like the thickness of the shear zone in free flows. However, density stratification imposes a limitation to $l \sim u'/N$. Beyond this scale, the Froude number $u'/(Nl)$ is indeed smaller than 1, so that perturbations propagate as internal waves, with little mixing effects. With this constraint on l, we get for strongly stratified conditions

$$\nu_t \sim \nu'_t \sim \frac{u'^2}{N} \,. \tag{III.75}$$

This implies from (III.74) that $-\overline{w'b'} \sim u'^2 N$. We get a similar estimate for $\epsilon \sim u'^3/l \sim u'^2 N$, and the ratio of these two quantities is the mixing efficiency Γ.

The k-ϵ approach considers ϵ as the additional variable instead of the turbulence scale l, and a diffusion equation is introduced for ϵ to close the system. It takes a similar form as the TKE equation (III.72),

$$\frac{\partial \epsilon}{\partial t} + \frac{\partial}{\partial z}\left(\frac{\nu_t}{\sigma_\epsilon}\frac{\partial \epsilon}{\partial z}\right) = \frac{\epsilon}{k}\left(c_{\epsilon 1}\, P + c_{\epsilon 3}\, \overline{w'b'} - c_{\epsilon 2}\, \epsilon\right) \,. \tag{III.76}$$

The values chosen for the coefficients are $\sigma_\epsilon = 1.3$, $c_{\epsilon 1} = 1.44$ and $c_{\epsilon 2} = 1.92$. Those are the classical choices for neutrally buoyant fluids, resulting from fits to simple turbulent flow configurations (Rodi, 1987).

The parameter $c_{\epsilon 3}$ is less consensual. We use here $c_{\epsilon 3} = -0.621$, which has been adjusted to provide reasonable results in the case of 'sustainable uniform shear' (Burchard and Bolding, 2001). In this case, the left-hand side of (III.72) and (IV.42) are set to 0, so we are left with a pair of algebraic equations. This balance yields by linear combination of the two equations,

$$-\overline{w'b'} = \frac{c_{\epsilon 2} - c_{\epsilon 1}}{c_{\epsilon 2} - c_{\epsilon 3}} P = 0.189\, P \tag{III.77}$$

This is the model representation of the steady state Richardson criteria (Eq. III.27). Indeed, expressing B by (III.74) and P by (III.73), this condition (III.77) takes the form of the marginal stability condition (III.27), with $Ri \equiv Ri_{st} = 0.189\, \nu_t/\nu'_t$.

The previous scaling arguments give $\nu_t \sim \nu'_t \sim u'^4/\epsilon$, leading to the expressions

$$\nu_t = c_\mu \frac{k^2}{\epsilon} \qquad \nu'_t = c'_\mu \frac{k^2}{\epsilon} \,. \tag{III.78}$$

For homogeneous fluids, the standard values $c_\mu \simeq c'_\mu \simeq 0.09$ are used to reproduce data from simple shear flows. In the stratified case, they are assumed to depend on the local shear and stratification, expressed as functions of the respective non-dimensional parameters $\alpha_M = k^2 \left|\partial \mathbf{u}/\partial z\right|^2 / \epsilon^2$ and $\alpha_N = k^2 N^2/\epsilon^2$. These so-called 'stability functions' fulfil appropriate physical and mathematical constraints, as discussed by Burchard and Bolding (2001) and Umlauf and Burchard (2005). Note that $\sqrt{\alpha_N}$ can be viewed as the inverse of a turbulent Froude number from the scaling $\epsilon \sim k^{3/2}/l$, which yields $\sqrt{\alpha_N} = Nl/k^{1/2}$. Moreover, the Richardson number is the ratio $Ri = \alpha_N/\alpha_M$. Particular cases of interest are the 'quasi-equilibrium states', for which Eq. (III.72) reduce to the local balance $P = -B + \epsilon$. Expressing P and $-B$ respectively by the expressions (III.73) and (III.74), and using (III.78), this local balance writes $c_\mu \alpha_M - c'_\mu \alpha_N = 1$. This expression defines a relation between α_M and α_N, or equivalently between the turbulent Froude number $\alpha_N^{-1/2}$ and the Richardson number $Ri = \alpha_N/\alpha_M$. In these quasi-equilibrium relations, the Froude number, as well as the functions c_μ and c'_μ, decrease with increasing Richardson number. They reach zero at a critical Richardson number, denoted Ri_c, beyond which turbulence cannot be locally maintained by the shear. This threshold differs from Ri_{st}, representing the 'sustainable uniform shear'. In the latter case, the flux of ϵ also vanishes.

In the lower part of the mixed layer, the buoyancy flux varies slowly with z, on scale h, as well as the shear stress, so we may assume that it approaches the 'sustainable uniform shear', with $Ri \simeq Ri_{st}$. This contrasts with the entrainment layer, where the buoyancy flux and shear stress vary abruptly, on scale h_e. Therefore, we expect that $Ri = Ri_c$ at this level of maximum density gradient. Beyond this level, the Richardson number still increases further, as the shear rate decreases while stratification remains. There, turbulence is not locally sustained but it diffuses from the neighbouring level of strong shear.

In the present study, we use Canuto et al. (2001)'s formulation of the stability functions c_μ and c'_μ. It corresponds to the case denoted 'CA' by Burchard and Bolding (2001), and 'CHCD01A' by Umlauf and Burchard (2005). The reference Richardson numbers are $Ri_{st} = 0.25$ and $Ri_c = 0.843$.

III.6.3 Entrainment in the KPP Model

We can conduct a similar analysis as in section III.4 with the KPP eddy viscosity (diffusivity) profile. This profile is

$$\begin{aligned} \hat{\nu} &= \kappa Z (1-Z)^2 + \nu_b \,, \quad \text{for } Z < 1 \\ \hat{\nu} &= \nu_b \,, \quad \text{for } Z \geq 1 \,, \end{aligned} \tag{III.79}$$

with ν_b a non-zero background diffusivity, and other notations similar to section III.4. The main differences between Eq. III.38 and Eq. III.79 are the quadratic vs cubic profiles, and the exponential decay in the entrainment layer.

We can then repeat the analysis in section III.4 with this new viscosity profile: we discuss the main outcome here. We plot in Fig. III.13 the velocity profiles obtained via the resolution of

Eq. (III.50). Overall, there is good agreement between Fig. III.13 and Fig. III.10, with one notable distinction at the base of the mixed layer. Figure III.13a reveals a sharp transition in the along-wind velocity profile, particularly pronounced for large values of S. We conducted numerical simulations with the full KPP model in GOTM and verified that the profiles obtained here are similar to those from the complete KPP implementation (not shown). This sharp transition is internally consistent with the KPP framework. Indeed, in KPP, the maximum velocity shear is located at the same height as the maximum density gradient. With such collocation of the maximum gradients, we can expect stronger velocity gradients while still respecting the critical Richardson number constraint. This abrupt shear in KPP generates a highly peaked TKE production term (which can still be diagnosed in KPP even if TKE is not part of the numerical model) that appears less physical than the plateau observed in k-ϵ calculations. This production term is plotted in Fig. III.13d and Fig. III.14.

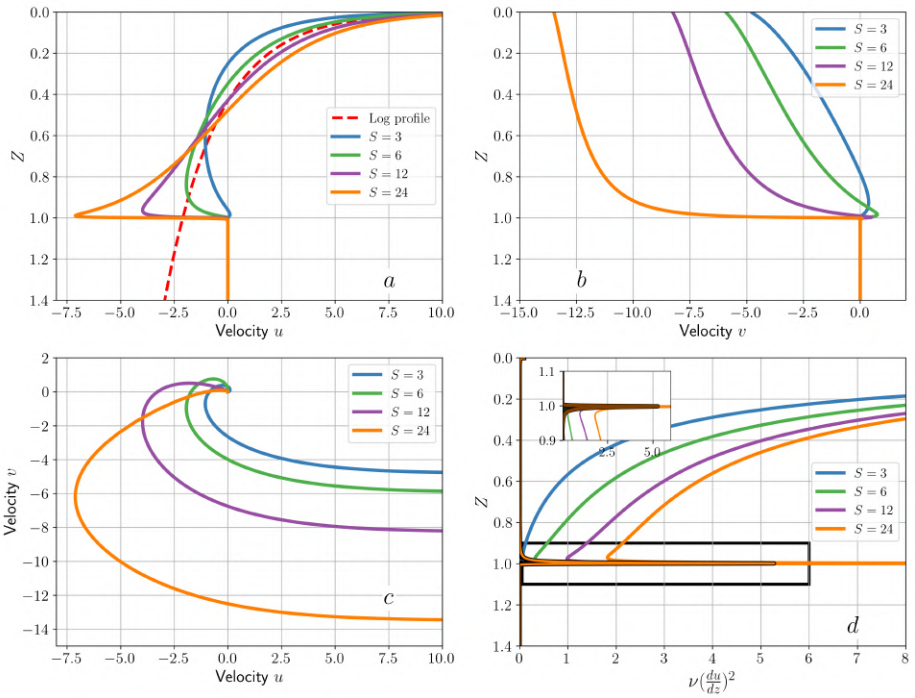

Figure III.13: Same figure as Fig. III.10 but with the KPP turbulent viscosity profile (Eq. III.79) (a): Profiles of $\hat{u}$ and (b): $\hat{v}$, respective real and imaginary parts of the solutions of steady momentum Eq. (III.51), (c) Hodograph of the $\hat{u}$, $\hat{v}$ velocities. (d) Vertical profile of the turbulent shear production for a constant parameter δ. The insert plot is a zoom of the main plot highlighted by the black square showing the TKE shear production due to the inertial component. The other curve are due to the steady components.

Figure III.14 compares the turbulent production terms between k-ϵ and the idealized eddy viscosity model with the KPP viscosity profile. As noted, the KPP production profile exhibits a sharper peak at the mixed layer base compared to k-ϵ. However, the Maxwell construction values remain remarkably similar to the plateau in the k-ϵ configuration. This similarity justifies our use of the Maxwell construction: while the peak intensity may vary between models, turbulent diffusion smooths these variations, making the Maxwell construction the physically meaningful quantity for determining entrainment rates.

We conclude this appendix with a brief analysis of the full KPP model (in the GOTM

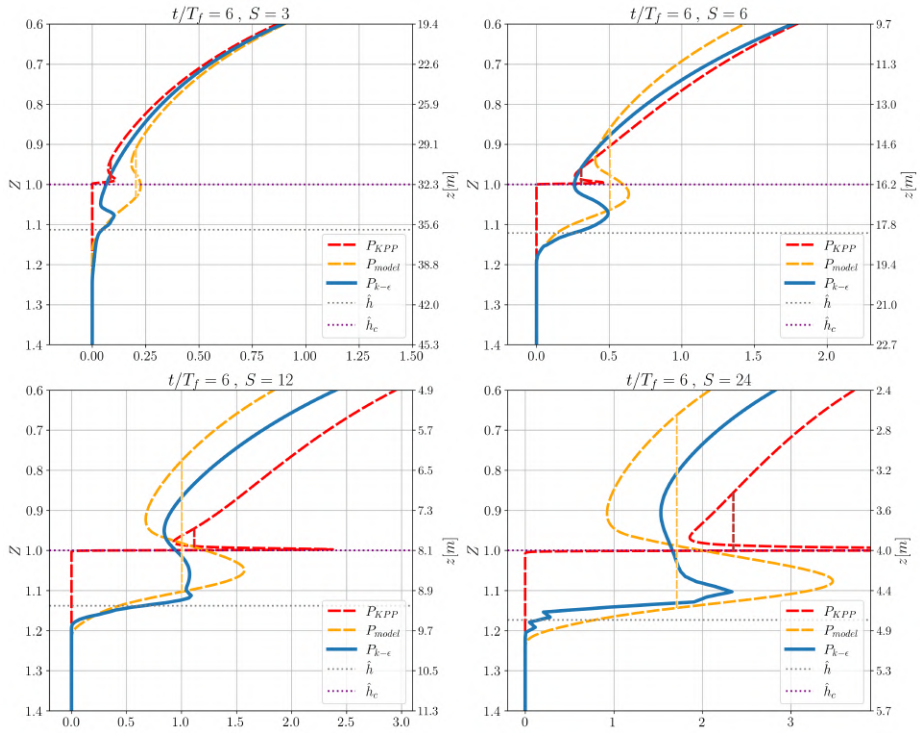

Figure III.14: Vertical profiles of the TKE production. Blue: computed from the $k-\epsilon$ model closure simulation. Orange: using the quadratic profile and exponential tail for the turbulent viscosity profile (Eq. III.38) and the theoretical model developped in section III.4. Red: using the cubic turbulent viscosity profile (Eq. III.79). The vertical lines show the integral mean over the maxwell construction for each model. The parameters of the theoretical model are identical to those in Fig. III.10 with $h_c = h\ (0.9 - 0.002\ S)$. For each plot, we use both the dimensional depth z and the non-dimensional depth $Z = z/h_c$ (see section III.4). The x-axis is rescaled by u_*^3/h_c .

implementation). We use the default parameters with quadratic interpolation for the bulk Richardson number and a critical Richardson number $Ri_c = 0.3$. We do not use any Langmuir parameterization. We plot in Fig. III.15 the time evolution of the mixed layer depth obtained with this full KPP model for the same values of S studied in the main text ($S = 3, 6, 12, 24$). We see in this figure that KPP captures well the transition between the initial deepening regime and the late-stage regime. However, compared to the k-ϵ model (Fig. III.6), we observe a stronger dependence of the mixed layer depth on the parameter S. Additional results obtained with different values of Ri_c show that fine tuning of the KPP parameters could also change the deepening rate (not shown). A detailed investigation of this model would be necessary to reach a firm conclusion about the ability of the KPP model to reproduce the late-stage deepening rate.

III.6.4 Analytical derivation of the entrainment layer thickness

Equation (III.59) (which is equivalent to its buoyancy counterpart Eq. III.47) can be solved analytically by introducing the variable $\phi = \nu dC/dZ$, so this equation becomes $d\phi/(\phi dZ) =$

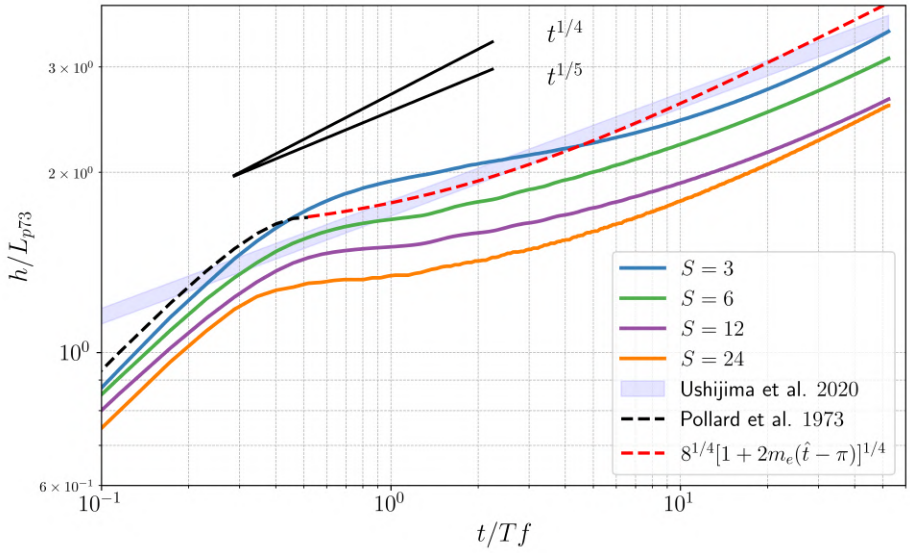

Figure III.15: Same figure as Fig. III.6 for the KPP turbulent model closure. Temporal variation of the mixed layer depth normalizes by L_{P73} in a log-log scale. Shading represent U20's law for a parameter $S = \sqrt{N_0/f}$ ranging from 3 to 24. The colours lines are KPP simulations for different values of S. The dashed red line represent the scaling law Eq. (III.33) with a parameter $m_e = 0.04$. Slopes corresponding to the power $1/4$ and $1/5$ are given by the black lines.

$-\hat{c}Z/\hat{\nu}$. This can be integrated by noting that $d\phi/(\phi dZ) = d\ln\phi/dZ$, leading to

$$\frac{\mathrm{d}C}{\mathrm{d}Z} = -D_0\hat{\nu}^{-1}\exp\left(-\hat{c}\int_0^Z \hat{\nu}^{-1}Z'dZ'\right). \tag{III.80}$$

The constant of integration D_0 can be determined by the surface flux at $Z = 0$: $D_0 = \nu\frac{dC}{dZ}\Big|_{Z=0}$. However, this cannot be determined from simple physical arguments, as it requires a full analysis using the Fourier transform of the Heaviside forcing function. Nevertheless, it can be obtained from the integral constraint (III.58). Thus, the profile $C(Z)$ can be computed with numerical integrating with $D_0 = 1$, then normalizing by its integral to satisfy the constraint (III.58). Results are shown in Fig. III.16 for different values of $\hat{c}$ and δ. The behaviour is similar to that of the buoyancy profiles, except that the velocity drops to 0 at large Z rather than reaching the linear profile $\hat{b} = Z$. The curves for different $\hat{c}$ are simply shifted with the same maximum slope, with a corresponding shift in amplitude due to the integral constraint. In fact, Eq. (III.59) is the same as Eq. (III.47), which is used as an idealized description of the buoyancy.

Interestingly, the profile $C(Z)$ can be well approximated by the analytical function $F_{c(Z)}$ defined by

$$F_c(Z) = \exp\left(-\hat{c}\int_0^Z \hat{\nu}^{-1}Z'dZ'\right). \tag{III.81}$$

The derivative of this function is $\frac{dF_c}{dZ} = -\hat{c}\hat{\nu}^{-1}ZF_c(Z)$. Since $\hat{c}$ is small, this function remains equal to 1 until $Z \simeq 1$, where it drops to 0 due to the divergence of ν^{-1}. An approximate solution

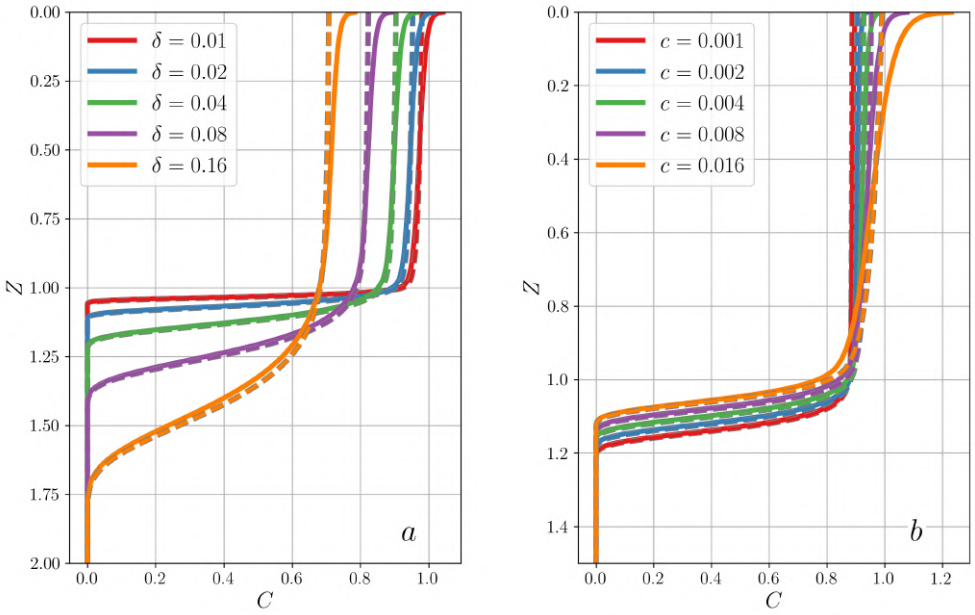

Figure III.16: Profiles of $C(Z)$ solution of Eq. (III.59) (solid lines) compared to the approximate solution Eq. (III.82) (dashed lines). (a) influence of the parameter $\delta = 0.01 \times [1, 2, 4, 8, 16]$, with $\hat{c} = 0.004$ (curves shift downward for increasing δ). (b) influence of entrainment velocity $\hat{c} = 0.001 \times [1, 2, 4, 8, 16]$, with $\delta = 0.03$ (curves shift upward for increasing $\hat{c}$).

is obtained by renormalising this function by its integral to satisfy Eq. (III.58),

$$C(Z) \simeq \frac{F_c(Z)}{\int_0^\infty F_c(Z)dZ}\,. \tag{III.82}$$

The agreement with the numerical integration is excellent, as shown in Fig. III.16. Note that this profile is independent of the stratification parameter S (which does not appear in Eq. (III.59).

The thickness of the shear layer is proportional to the thickness δ, while the position of this shear shifts as $-\delta \ln\hat{c}$, as discussed for the buoyancy profile. The maximum shear is $dF_c/dZ \simeq -0.35/\delta$, while the function F_c drops from 1 to 0. This defines a shear layer thickness equal to the inverse of the maximum derivative; hence $h_e \simeq 3\delta$.

III.6.5 Numerical method to solve the idealized model

We can solve Eq. (III.44), (III.51), and (III.59) with numerical methods. These equations have a similar structure, and we focus here on the buoyancy equation (III.44) for simplicity. We define a new variable $\hat{b}_f$ as

$$\hat{b}_f = \hat{\nu}\frac{\mathrm{d}\hat{b}}{\mathrm{d}Z}\,, \tag{III.83}$$

such that we can rewrite Eq. (III.44) as

$$\frac{\mathrm{d}}{\mathrm{d}Z}\hat{b}_f = \hat{c}\left(-\frac{Z}{\hat{\nu}}\hat{b}_f + \hat{b}\right)\,, \tag{III.84}$$

where both Eq. (III.83) and Eq. (III.84) form a system of coupled ordinary differential equations with unknown $\hat{b}$ and $\hat{b}_f$. For given values of δ, $S/\hat{h}_c$, and $\hat{c}$, we can compute the eddy viscosity $\hat{\nu}$, as given by Eq. (III.38). We then solve this system as a boundary value problem with the function `solve_bvp` from the `scipy.integrate` package. We specify the boundary conditions (cf. main text), solve the system, and then proceed to the normalization as mentioned in the main text. To compute the normalization constant, we use the `simpson` function from `scipy.integrate` to compute integrals.

III.7 Asymptotic regimes of wind-driven boundary layers in rotation

We identify a third asymptotic regime of wind-driven mixed-layer deepening, where Ekman dynamics saturate but inertial oscillations continue to drive vertical momentum transfer and entrainment.

III.7.1 Quasi Stationary vs Inertial component

To obtain the oscillating component, a simple high-pass filter is applied to the velocities for each z level. The filtered component is called quasi-stationary (QS) and the residue of the filtering is the inertial oscillation (IO) (see Fig. III.20). Most of the diagnostics performed are intended to study the long-term asymptotic regime and therefore the initial transient effects are ignored.

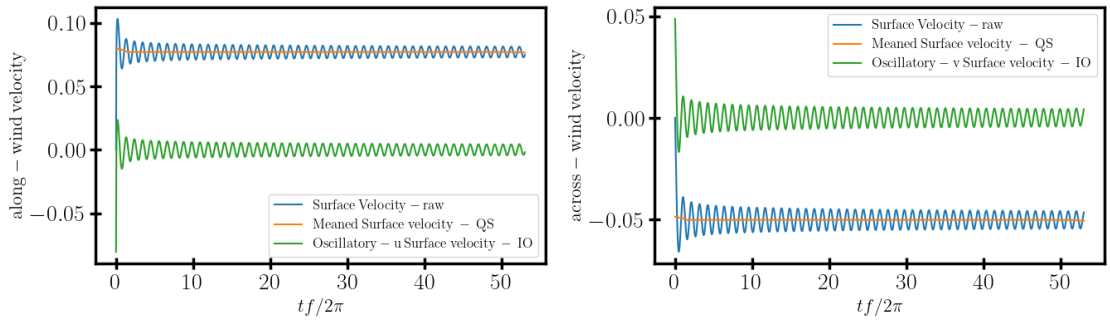

Figure III.17: Surface velocity decomposition into a quasi-steady and an oscillatory component

Hereinafter, we will refer to the 'Ekman layer' as the zone in which the quasi-stationary components are non-zero. As explained in Chap. III, in the Ekman layer, inertial oscillations are practically barotropic, i.e. uniform vertically. In this layer, it can be expressed as follows:

$$U_{IO}(t) = A_{IO}\sin(ft)\,; \qquad V_{IO}(t) = A_{IO}\sin\left(ft - \frac{\pi}{4}\right) \tag{III.85}$$

However, inertial oscillations penetrate beyond the Ekman layer and are no longer barotropic

(see Fig. III.19a.). Nevertheless, the phase difference between the U and V components remains the same (not shown here). We therefore have

$$U_{IO}(\hat{z},t) = A_{IO}\xi(\hat{z})\sin(ft)\,; \qquad V_{IO,}(t,\hat{z}) = A_{IO}\xi(\hat{z})\sin\left(ft-\frac{\pi}{4}\right) \tag{III.86}$$

with $\hat{z} = z/d_{IO}$, d_{IO} being the depth of penetration of the inertial oscillations (dependent on time) and ξ is a function such that:

$$\xi(\hat{z}) = 1, \quad \hat{z} < d_{Ek}/d_{IO} \tag{III.87}$$
$$\xi(\hat{z}) = 0, \quad \hat{z} = 1 \tag{III.88}$$

III.7.2 Singular case: neutral Ekman layer $N = 0$

III.7.2.1 Stationary Ekman Layer

To obtain an simulation of the equilibrium state Ekman layer without inertial oscillations, we initialised the forcing (absolute wind) with a gentle ramp $T_{ramp} \gg f^{-1}$s. There are still inertial oscillations, but their amplitude is two orders of magnitude lower than the quasi-equilibrium velocities.

For comparison, the other simulation is forced by a constant wind impulse.

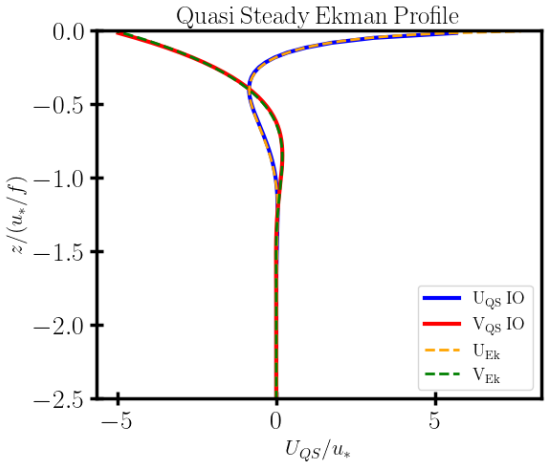

Figure III.18: Vertical profile of the turbulent viscosity anomaly from a confined Ekman Profile (taken at $t = 2\,T_f$).

We can see in Fig. III.18 that the quasi-stationary equilibrium components are identical both in the presence or absence of inertial oscillations. We can conclude that inertial waves do not alter the equilibrium state of the Ekman turbulent layer.

III.7.2.2 Oscillatory Ekman Layer

The Ekman veering spiral is fully developed and confined in the Ekman layer delimited by the Ekman depth d_{Ek} (Fig. III.18) but inertial oscillations continue to deepen, as can be seen in Fig. III.19.

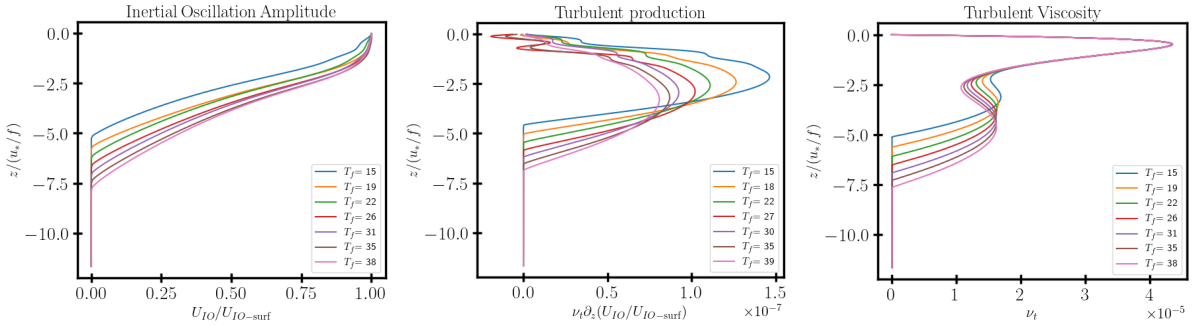

Figure III.19: Simulation of a Neutral Ekman Layer $N = 0$. Left: vertical profile of the $u-$inertial component of the velocity for different times of the simulation. The amplitude of the velocity is adimensionalized by the surface value. Center: vertical turbulent production due to the inertial oscillation for different times. For both, the vertical scale is adimensionalized by u_*/f. Right: vertical profile of the turbulent viscosity.

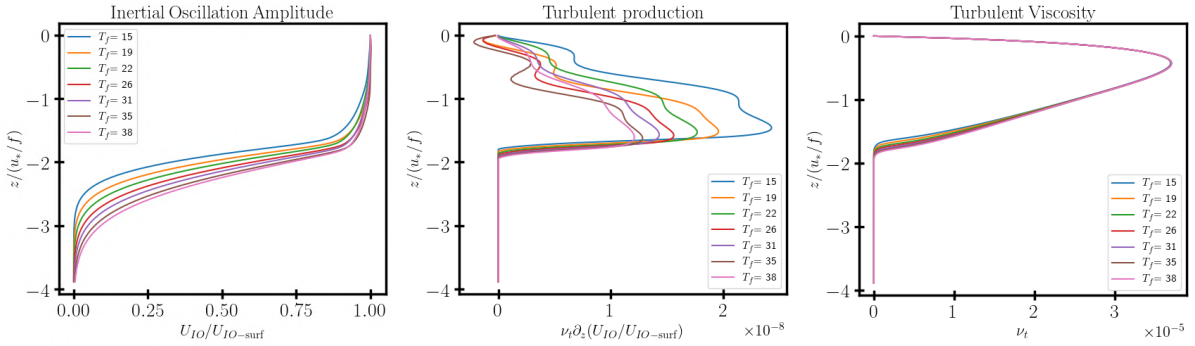

Figure III.20: Simulation of a Weakly stratified Ekman Layer $S = \sqrt{N/f} = 1$ Left: vertical profile of the $u-$inertial component of the velocity for different times of the simulation. The amplitude of the velocity is adimensionalized by the surface value. vertical turbulent production due to the inertial oscillation for different times. Right: Turbulent viscosity profile. For both, the vertical scale is adimensionalized by u_*/f.

III.7.3 Penetration of the Inertial Oscillation

Two methods are used to detect the penetration depth of the Inertial Oscillation d_{IO}

- $d_{IO} = z\left(\max(\partial_z(U_{IO}/U_{IO}^{surface})\right)$
- $d_{IO} = z\left(U_{IO} = U_{IO}^{surface}/10\right)$

For the first method, adimensioning by surface amplitude makes it possible to ignore the phase of the inertial oscillation and focus solely on the profile curve.
For the second method, the threshold $/10$ is arbitrary, and the shape of the curves in Fig. III.21 remains unchanged except in amplitude for thresholds ranging from $U_{IO}^{surface}/10$ and $U_{IO}^{surface}/2$. Fig. III.21 shows that the second method is more robust.

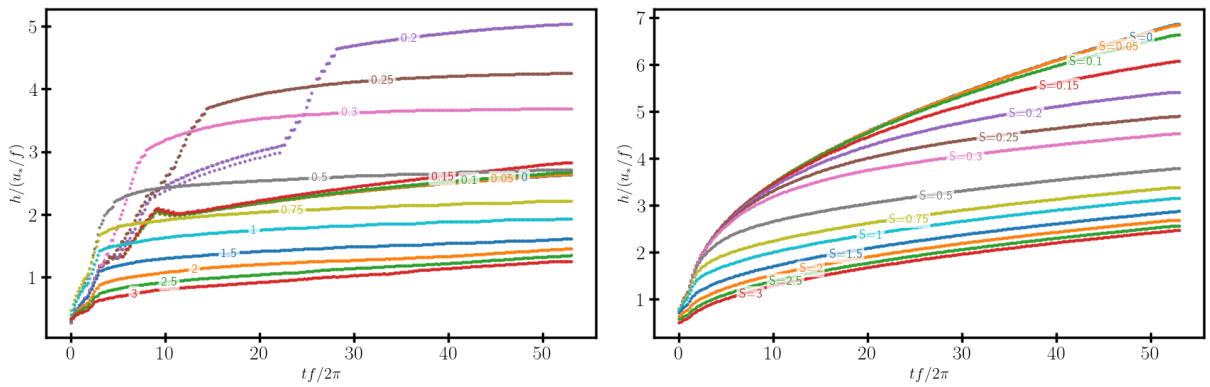

Figure III.21: Time evolution of the penetration depth of Inertial oscillation for different values of S indicated over the curves. Left: detection method for the penetration depth based on the maximum vertical shear of the inertial component. Right: detection method for the penetration depth based on the deeper height where the IO-amplitude is about $U_{IO}(d_{IO}) = U_{IO}(z=0)/10$.

From the fit performed in log, we can investigate the evolution of inertial oscillation penetration in the form of an (arbitrary) power law, in the form

$$d_{IO}(t) \sim A\, t^{\alpha} \tag{III.89}$$

This can be done for each simulation at a given S. This gives us a qualitative view of the penetration rate as a function of S. This is shown in Fig. III.22.

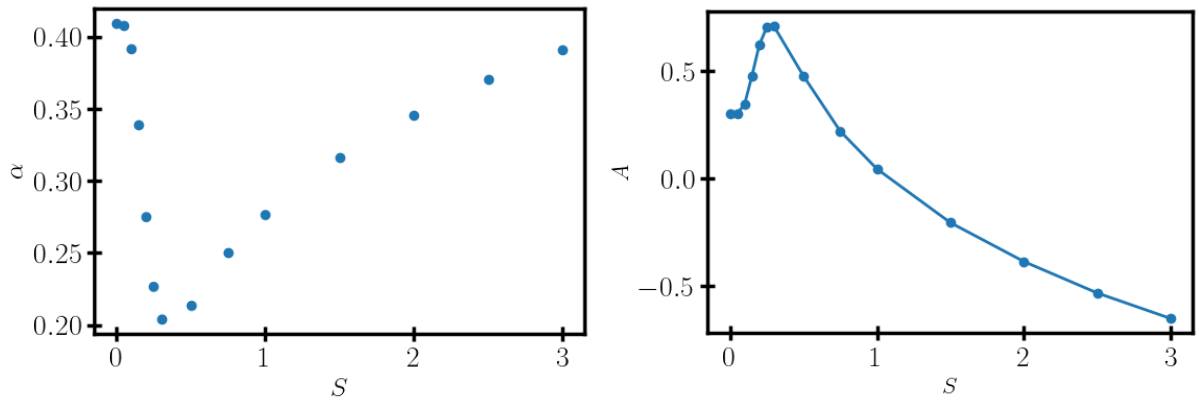

Figure III.22: Rate of penetration of the inertial Oscillation from a fit following the scaling law (see Equ:III.89). Left: power exponent α versus S. Right: prefactor $\log(A)$ versus S.

The coefficient α appears to vary between 0.2 and 0.4. We can see a change in regime towards $S = 0.1$, but it is difficult to draw any conclusions.
Ultimately, we do not observe a deepening in $\sqrt{t}$ as expected by pure turbulent diffusion.

III.7.3.1 Transition rotation-stratification regime

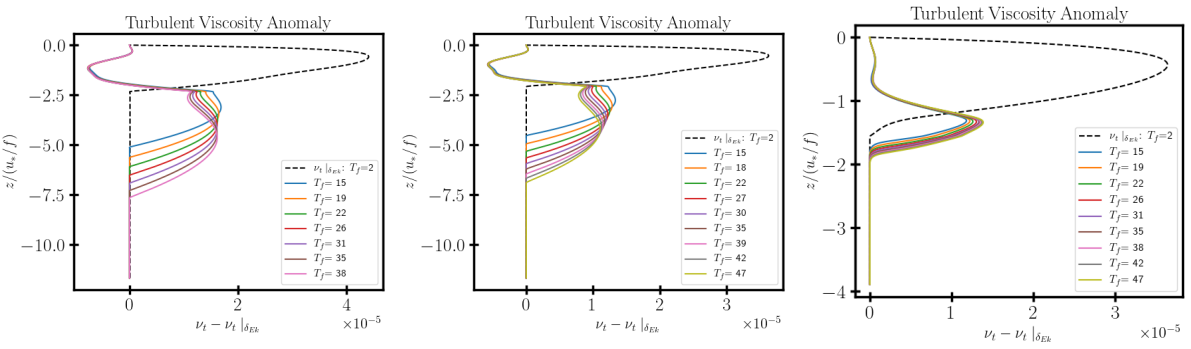

Figure III.23: Vertical profile of the turbulent viscosity anomaly from a confined Ekman Profile (taken at $t = 2\,T_f$).Left: Neutral Ekman Layer $S = 0$. Center: $S = 0.1$. Right: $S = 1$

We observe on Fig. (III.23 that the peak in the turbulent viscosity profile due to inertial oscillation saturates at a certain amplitude value but continues to deepen with time. For the neutral Ekman Boundary, this peak thickens with time, but the maximum value remains fairly constant. For weak stratified layer ($S = 0.1$), the maximum in turbulent viscosity decreases over time but continues to deepen. For a stronger stratification (but still weak, $S = 1$) there is very little change over time.

Fig. III.24 shows the time series of the turbulent viscosity integrated over the entire column. Although this metric does not provide any information about the dynamics of the boundary layer, we can still deduce information about the shape/geometry of the viscosity profile and when stratification as a passive parameter and the transition to active stratification occur. Indeed, we note that the viscosity profile is divided into a quasi-stationary part, well described in Chap. III by a quadratic profile with exponential decay, and a part with an extremum located beyond the stationary Ekman layer. This second part seems to evolve in a way that depends on stratification. For $S < 0.1$, the integral of ν_t increases significantly with time, which implies that the turbulent viscosity self-sustained by inertial oscillations remains at a relatively constant level while its penetration continues. For $S > 0.3$. The integral increases slightly. We can then obtain a first estimate of the threshold at which stratification becomes active: $S_{crit} \sim 0.1 - 0.15$.

This threshold is an order of magnitude smaller than that estimated by the ratio of the turbulent Ekman layer $d_{Ek} = 0.3\frac{u_*}{f}$ and the characteristic length of Pollard et al. (1973) $L_{P73} = \frac{u_*}{\sqrt{Nf}}$. This is due to the fact that inertial oscillations penetrate deeper than the classical scaling of the Ekman turbulent layer. If we scale relative to the penetration depth of the inertial oscillations $d_{IO} = A\frac{u_*}{f}$ we obtain $S_{crit} \sim 1/A$. Therefore, for $S_{crit} \sim 0.1 - 0.15$ we have $A \sim 6 - 7$. This is approximately the depth reached for a neutral Ekman layer.

Note that the penetration depth of inertial oscillations $d_{IO} = A\frac{u_*}{f}$ is not constant and depends on time, as shown in the curves. The coefficient $A = \Phi(N/t)$ is therefore a function of stratification and time.

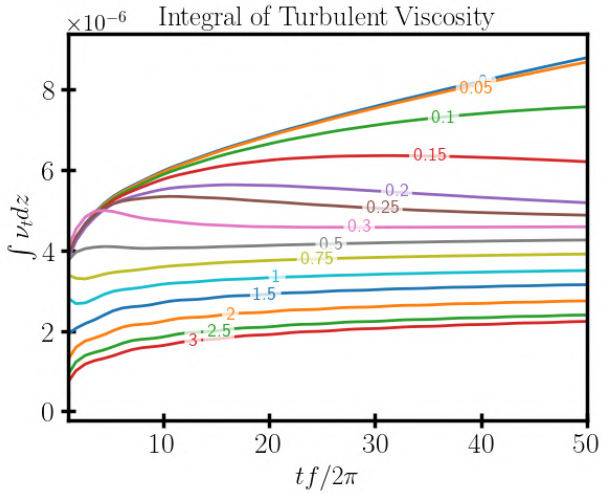

Figure III.24: Time evolution of the integral of Turbulent viscosity over the water column $\int \nu_t dz$ for different values of S indicated over the curves.

III.8 Conclusion

The regime we have examined in this chapter shows that the deepening of the mixed layer continues beyond an inertial period, but at a rate that is significantly reduced compared with the non-rotating case. It should, however, be noted that this deepening law remains valid only as long as stratification effects, and not rotation, limit the turbulence. Indeed, the quasi-stationary component identified in this chapter corresponds to an Ekman component squeezed at the depth of the mixed layer. However, as h increases, it is expected that the turbulence generated at the surface will, after a certain time, cease to be blocked by stratification and will instead be inhibited by rotation: the quasi-stationary component then no longer produces sufficient shear in the entrainment layer, and the system falls outside the regime of validity of the scaling law developed in this chapter.

As a preliminary observation, we also observe that the turbulence associated with inertial oscillations appears capable of sustaining itself, as the layer in which these oscillations develop continues to propagate vertically over time — it should be noted that this is not a vertical propagation of the inertial oscillations but rather the thickening of the layer in which these oscillations evolve. This raises the question of a distinct asymptotic regime dominated by inertial oscillations rather than by the stationary component; however, we have not yet been able to characterise this regime.

Alongside this theoretical and numerical approach, we sought to test experimentally, using the Coriolis platform, the existence of an entrainment law in the presence of rotation, following the approach of Kato and Phillips' experiments, but with an aspect ratio nine times greater than that of their original apparatus (this experimental configuration is detailed in Chap. II and its data are analysed in Chap. IV). Despite this geometric improvement, which was intended to minimise boundary effects, we encountered difficulties with secondary recirculation and associated lateral flows. Furthermore, the stratification established was too weak to achieve a

sufficiently stable regime over time, and thus to obtain data robust enough to converge to an entrainment law. A new experimental campaign, with stronger stratification (with salt) in order to slow the deepening, is currently underway and represents a short-term perspective of the work carried out here.

More broadly, this chapter has provided us with an insight into the mechanisms of turbulent entrainment under asymptotic regime and idealised conditions. Two limitations of this framework are worth noting in the context of this work. Firstly, wind stress is in reality never constant, as we mentioned in the introduction (Sec. I.2.1): the mixed layer is therefore constantly adjusting in response to an intermittent forcing. Secondly, as the rate of deepening is particularly low in the asymptotic regime, the mixed layer depth observed under real conditions is established, in the first order of magnitude, during the first inertial period — that is, precisely when the Ekman component is still in its transient regime. It is this transitional phase, about which little is known in the presence of turbulence, that we address in the following chapter through experiments conducted on the Coriolis rotating platform.

Chapter IV

Transient turbulent Ekman Layer

Summary of the Chapter

Spin-up experiments carried out on the Coriolis platform with time-resolved S-PIV measurements, allow for the direct observation of the transient dynamics of the turbulent Ekman boundary layer. The vertical profiles of velocity, turbulent kinetic energy and temperature are in good agreement with single-column simulations using the k-ε closure in the three configurations tested: non-rotating unstratified, non-rotating stratified, and rotating stratified.

In the rotating case, the boundary layer thickness stabilises at $\delta_{Ek} \sim 0.4\, u_*/f$ and the horizontal velocities organise into an Ekman spiral (the velocity vector rotates with depth) over one-half of the inertial period $T_f/2 = \pi/f$. This dynamics is superimposed with characteristic oscillations of frequency f which persist for approximately five periods before damping out. Thus, the mean structure of the boundary layer is established well before the transient oscillations disappear, showing that, in the turbulent regime, the stationary Ekman spiral and the inertial oscillations evolve largely independently and superimpose linearly.

These oscillations are clearly identified in both velocity at a fix depth and integrated transport. In, the latter, they appear as a fluctuation of the barotropic velocity at the inertial frequency. Their damping is controlled by the formulation of the bottom boundary condition: a quadratic friction coefficient C_f governs energy dissipation and determines the longevity of the oscillations, interpolating between the free-slip (almost no damping) and no-slip (strong damping rate) laminar limits. A value of $C_f = 5 \times 10^{-3}$, calibrated independently from the cross-isobaric angle obtained in the DNS simulations of Marlatt et al. (2012), accurately reproduces the experimentally observed damping rate. These results highlight the central importance of the parameterisation of bottom friction in describing the transient dynamics of turbulent Ekman boundary layers and confirm the ability of the k-ε closure to reproduce the dynamics in such regimes.

The results of this chapter are reproduced from :
Coppin, M., Deremble, B., Sommeria, J. S., Viboud, T., Valran & M.E., Negretti (2026). "Laboratory observations of a transient turbulent Ekman layer". submitted in *Geophysical & Astrophysical Fluid Dynamics*

Contents

———Article submitted in Geophysical and Astrophysical Fluid Dynamics———

Chapter (III) has demonstrated, through theoretical analysis and numerical simulations, the dynamics of mixed-layer deepening over long time scales in the presence of rotation. In particular, it has shown that inertial oscillations play a major role in the mechanisms of deepening and turbulent entrainment. However, this chapter focused primarily on the steady-state regime of the mixed layer. Yet, the ocean boundary layer is rarely in equilibrium and is mostly in a state of transient adjustment. Understanding the development of the turbulent Ekman layer and the evolution of inertial oscillations is therefore essential for characterizing the fundamental underlying dynamics of the surface ocean.

This issue raises two questions. The first concerns the ability of turbulence models to reproduce this transient dynamics. Whilst the k-ε model correctly reproduces the mean structure of a turbulent Ekman layer in steady-state conditions under idealised configurations (Braun et al., 2020), it was developed and calibrated for quasi-stationary flows. **Its validity in a transient regime, where turbulence evolves on a timescale comparable to that of the rotation and where the turbulent viscosity is itself evolving, remains largely open**. The second question concerns the evolution of inertial oscillations. The previous chapter highlighted their role in mixing dynamics, but without addressing their dissipation. However, ocean observations show that these oscillations dampen over time (Fig. I.4). **What are the mechanisms controlling this damping, and to what extent are they correctly reproduced by numerical models?**

To answer these questions, we present an article submitted to Geophysical and Astrophysical Fluid Dynamics. This study describes impulsive Spin-up experiments carried out on the Coriolis platform, recalls the exact analytical solutions to the transient Ekman problem in the laminar case, highlights the existence of inertial oscillations in a turbulent Ekman layer, and compares these observations with the predictions obtained using the k-ε model.

ARTICLE SUBMITTED IN *Geophysical and Astrophysical Fluid Dynamics*

Laboratory observation of a transient turbulent Ekman layer

Abstract: We investigate the transient dynamics of a turbulent Ekman boundary layer through large-scale spin-up experiments on the Coriolis rotating platform in Grenoble. An impulsive change in rotation rate generates a well-controlled bottom stress, exciting inertial oscillations that decay over several inertial periods, more slowly than laminar theory predicts. We show that this behaviour is controlled by the bottom stress formulation: a quadratic drag law $\tau_b = C_f|\mathbf{u}|\mathbf{u}$, with $C_f \approx 5 \times 10^{-3}$, correctly reproduces both the damping rate and the interior spin-up. Despite the slow attenuation, the steady Ekman spiral and the inertial oscillations superpose linearly, extending a result trivially expected in the laminar case to the turbulent regime. The k-ε closure appears to be in good agreement with the data.

IV.1 Introduction

Oceanic boundary layers at the surface and seafloor are key sites of energy injection and dissipation (Wunsch and Ferrari, 2004). At the surface, wind stress drives a turbulent mixed layer whose depth controls air–sea exchanges of heat, gases, and momentum. At the seafloor, bottom friction dissipates the kinetic energy of geostrophic currents and tidal flows, and sets the bottom boundary condition for the large-scale circulation (Pedlosky, 1996; Vallis, 2006). Yet, representing these layers in numerical models remains a challenge, as their turbulent structure depends sensitively on the choice of closure scheme and boundary conditions.

Observations of the bottom boundary layer over continental shelves and in the deep ocean have documented the Ekman spiral, the log-layer structure of the mean velocity, and the inhibition of turbulence by stable density stratification (Weatherly and Martin, 1978; Perlin et al., 2005, 2007). At the ocean surface, direct current measurements have also confirmed the Ekman spiral and the wind-driven mixed layer deepening (McPhaden et al., 2024; Price et al., 1978b). Laboratory experiments have played a complementary role in advancing our understanding of turbulent boundary layers. In particular, the spin-up experiment of Kato and Phillips (1969a), in which a stress is applied at the surface of a rotating, stratified fluid, has become a standard benchmark for testing turbulence parameterizations (Price et al., 1986; Umlauf and Burchard, 2003).

The dynamical regime in the boundary layer under the influence of constant surface stress has been described in the seminal work of Ekman (1905), who showed that the steady balance

between the Coriolis force and the divergence of the vertical momentum flux gives rise to a veering spiral confined within a depth $\delta_E = \sqrt{2\nu/f}$, where f denotes the Coriolis parameter and ν the kinematic viscosity.

In geophysical flows, molecular viscosity can be tentatively replaced by a turbulent eddy viscosity $\nu_t \sim u_* \delta_E$ (with u_* a friction velocity), yielding the turbulent scaling $\delta_E \propto u_*/f$ (Rossby and Montgomery, 1935; Zilitinkevich and Mironov, 1996). Unlike the laminar case, for which the momentum equations are linear and admit an exact analytical solution, turbulence introduces nonlinearities through the Reynolds stress terms, which couple the mean flow to the velocity fluctuations. The eddy viscosity $\nu_t(z,t)$ is no longer a known quantity but must be modeled, giving rise to the turbulence closure problem.

Several modelling approaches have been proposed to better understand this physical situation, as reviewed by Kim et al. (2014): slab models, which ignore the vertical structure entirely (Pollard and Millard, 1970; D'Asaro, 1985; Alford, 2001); imposed eddy-viscosity profiles $\nu_t(z)$, which prescribe the turbulent mixing without a dynamical equation for the turbulent kinetic energy (Faller and Kaylor, 1966; Madsen, 1977; Endoh and Nitta, 1971; Lewis and Belcher, 2004). Another approach is to use linear Rayleigh damping $-r\mathbf{u}$, where the empirical coefficient r aggregates unresolved mechanisms such as wave breaking and turbulent dissipation (Csanady and Shaw, 1980; Ashkenazy et al., 2015; Kim et al., 2014). In coarse-resolution ocean models, linear or quadratic friction coefficients are typically defined as a bulk drag coefficient relating the bottom stress to the depth-averaged or near-bottom velocity. Whether this bulk value is consistent with the local boundary drag coefficient inferred from the Law of the Wall remains an open question, particularly in the transient regimes where the logarithmic layer may not be fully established. More sophisticated two-equation closures, such as the k-ε model, have been applied to the steady turbulent Ekman layer and shown to agree well with high-resolution DNS (Braun et al., 2020; Marlatt et al., 2012).

The steady turbulent Ekman layer is only part of the picture. Wind stress is inherently unsteady. Impulsive or intermittent forcing excites inertial oscillations which carry a significant fraction of the near-surface kinetic energy and represent a major pathway for momentum transfer into the deep ocean (Pollard and Millard, 1970; D'Asaro, 1985; Alford, 2001). In the linear framework, the transient inertial response and the steady Ekman spiral simply superpose (Pollard and Millard, 1970): inertial oscillations produced by the onset of a constant stress decay through frictional dissipation, leaving eventually the steady Ekman balance. In the turbulent regime, however, this decoupling breaks down: the oscillating shear modulates the eddy viscosity $\nu_t(z,t)$, which in turn alters the vertical Ekman spiral profile (Coppin et al., 2025). This two-way coupling is a fundamentally nonlinear effect, and its consequences for the decay rate of inertial oscillations and the structure of the turbulent Ekman layer remain poorly documented.

The open questions that we aim to address in this study are the following: first, the decoupling between inertial oscillations and the Ekman spiral, exact in the laminar case, has not been verified in the turbulent regime. Second, the sensitivity of inertial oscillation decay to the boundary condition remains poorly explored. Third, the ability of turbulent closures to reproduce the transient turbulent Ekman layer has not been assessed against data. We consider the k-ε model (Burchard and Bolding, 2001), a two-equation scheme that solves prognostic equations for the

turbulent kinetic energy and its dissipation rate, widely used in ocean modelling but has rarely been tested in transient, rotation-dominated regimes.

To address these questions, we present large-scale spin-up experiments conducted on the Coriolis rotating platform in Grenoble (France). The spin-up process has been extensively studied since Greenspan and Howard (1963) (see the review by Duck and Foster (2001)), but few experiments have reached turbulent regimes (Caldwell et al., 1972; Sous et al., 2013), and none have documented the transient oscillating stage that immediately follows the impulsive forcing. The large Reynolds numbers achieved on the Coriolis platform allow the boundary layer to be fully turbulent while preserving a clear inertial signal. We focus on the weakly stratified limit, for which rotation rather than buoyancy constrains the vertical structure: in strongly stratified regimes the Ekman layer becomes buoyancy-limited to a depth $\delta_E\sqrt{f/N}$ (Pollard et al., 1973; Fernando, 1991; Kato and Phillips, 1969a). The threshold value of f/N at which this transition occurs remains poorly constrained (Zilitinkevich, 2012). We investigate the regime $f/N \sim \mathcal{O}(1)$, where rotation rather than buoyancy is expected to control the vertical structure of the flow.

The paper is organized as follows. The experimental setup and measurement techniques are described in Section IV.2. Section IV.3 develops the theoretical framework: the 1D axisymmetric model, the friction law, and inertial oscillations together with laminar analytical solutions for the no-slip and free-slip limits. Results are presented in Section IV.4 and Section IV.5, where mean flow profiles, turbulent statistics, and the transient inertial response are compared against the k-ε closure. Section IV.6 summarizes the findings and discusses their implications for the parameterization of oceanic boundary layers.

IV.2 Experimental Methods

To investigate the transient dynamics of a turbulent Ekman layer under controlled conditions, laboratory experiments were carried out in the Coriolis Platform at Grenoble (Fig. IV.1). The circular tank (13 m in diameter) is filled with water to a depth $H = 0.5$ m. The forcing is produced by an impulsive change in the platform rotation speed, which generates an azimuthal flow in the platform frame of reference. This procedure is referred to as *spin-up* when the rotation speed increases, and *spin-down* when it decreases. The platform reaches its nominal rotation speed after an acceleration phase of 20 s.

Throughout this paper, we use cylindrical coordinates (e_r, e_θ, e_z) when describing the flow in the tank. The vertical coordinate z is oriented upward, with origin $z = 0$ at the tank floor (where the forcing is applied). The three velocity components (u_r, u_θ, u_z) are measured by Stereoscopic Particle Image Velocimetry (S-PIV) in a vertical plane tangent to the azimuthal direction at the fixed radius $r_0 = 4.5$ m.

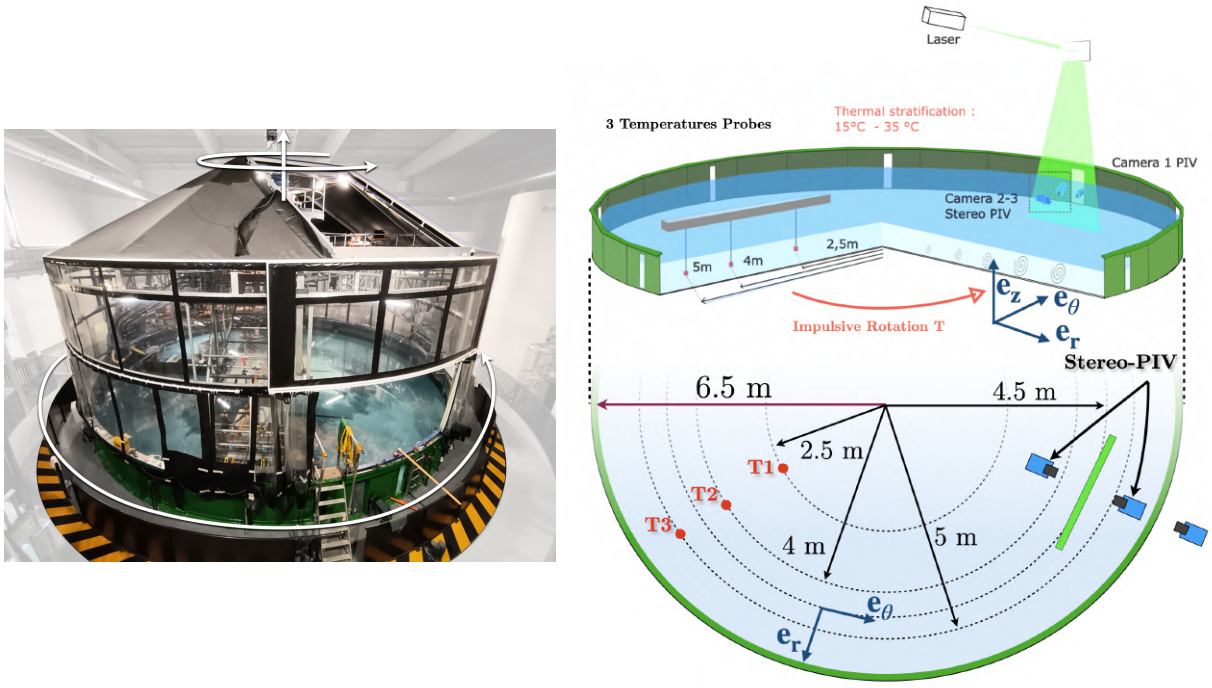

Figure IV.1: Illustration of the experimental apparatus. Left: Picture of the 13 m wide rotating Coriolis Platform. Right: Schematic side and top view of the experimental set-up. The water height in the tank is 50 cm.

IV.2.1 Experimental Configuration

The experiments are characterized by three main external control parameters: the Coriolis parameter $f = 2\Omega_i$, set by the initial background rotation rate Ω_i of the platform, the impulsive change in rotation speed $\Delta\Omega = \Omega_f - \Omega_i$, and the buoyancy frequency N, set by the initial density stratification.

IV.2.1.1 Background rotation

The platform rotates at an initial angular velocity Ω_i, which sets the background rotation of the fluid and defines the Coriolis parameter $f = 2\Omega_i$. In the rotating experiments, $\Omega_i = 0.05$ rad s^{-1}, corresponding to an inertial period $T_f = 2\pi/f \approx 63$ s. In the non-rotating reference case, $\Omega_i = 0$ and the relevant time scale is instead set by the impulsive forcing $\Delta\Omega$.

IV.2.1.2 Mechanical Forcing

The forcing is generated by an impulsive change in the platform rotation rate, which appears as a suddenly imposed bottom velocity in the initial reference frame, while the fluid far above remains at rest temporarily due to inertia. In all the experiments presented here, the same rotation rate increment $\Delta\Omega = 0.05$ rad s^{-1} is applied. At the measurement radius $r_0 = 4.5$ m,

it results in a given bottom velocity $v_0 = r_0\ \Delta\Omega = 23.5\ \mathrm{cm\,s^{-1}}$. The resulting bottom stress $\tau = \rho u_*^2$, where u_* is the friction velocity, drives the formation of the Ekman boundary layer and the subsequent spin-up of the fluid column. Due to the veering effect of the Coriolis force, the stress is tilted by an angle α_0 with respect to the azimuthal direction, so we must distinguish the azimuthal shear stress $\tau_\theta = \rho u_*^2 \cos\alpha_0$ and the radial shear stress $\tau_r = \rho u_*^2 \sin\alpha_0$.

The friction velocity will be estimated from the measurements of the total vertical flux of azimuthal momentum,

$$\tau_\theta = -\left\langle v'w'\right\rangle\big|_{z\to 0} + \nu \left.\frac{\partial\langle v\rangle}{\partial z}\right|_{z\to 0}, \tag{IV.1}$$

which remains approximately constant with z in the wall layer. Since the spatial resolution of the S-PIV does not allow us to resolve the viscous sublayer, u_* is estimated by extrapolating the measured momentum flux profile toward the wall. We can similarly estimate the radial stress τ_r from the radial velocity component u. Typical values obtained for the friction velocity are $u_* \simeq\ 0.8\ \mathrm{cm\,s^{-1}}$ (see section IV.4.2).

IV.2.1.3 Density stratification

We perform experiments with no stratification to study the canonical Ekman layer. Along with these experiments, we consider the weakly stratified limit to provide a comparison with the reference experiment of Kato and Phillips (1969a). This stable density stratification is due to a constant vertical temperature gradient established prior to each experiment by filling the tank progressively from the bottom. The injected water is a mixture of water preheated to 40^{o}C and cold tap water at approximately 17^{o}C, with the hot fraction decreasing continuously from 100% at the start to 0% at the end of the filling. To avoid turbulent mixing during filling while limiting heat loss to the atmosphere, the tank is filled over 4 h to reach a depth of H = 50 cm. The resulting density profile is characterized by the buoyancy frequency N defined by

$$N^2 = -\frac{g}{\rho_0}\frac{\partial\rho}{\partial z} = g\alpha_T\frac{\partial T}{\partial z}, \tag{IV.2}$$

where α_T is the thermal expansion coefficient and ρ_0 a mean reference density. The value of N is approximately uniform over the lower 30 cm of the water column. The upper layer ($\approx$ 20 cm) is mixed due to convection at the water–air interface; we do not consider this upper layer further in the analysis. The stratification obtained with temperature is weaker than those usually obtained with salinity, in order to explore the limit of weak stratification. The choice of a temperature stratification instead of the more usual salt stratification was motivated as part of a wider project involving thermal convection, not discussed here.

IV.2.1.4 Overview of the experiments

In this article, we analyse four main experiments defined by the presence or absence of background rotation and stable stratification, as summarized in Table IV.1.

Label	f (rad s^{-1})	N (s^{-1})
EXP-Ref	0	0
EXP-S	0	0.25
EXP-R	0.104	0
EXP-SR	0.104	0.32

Table IV.1: Experiment names with values of the control parameters. f is the Coriolis parameter, N the buoyancy frequency. In all the experiments, the water depth is $H = 50$ cm and $\Delta\Omega = 0.05$ rad s^{-1}, corresponding to a bottom velocity $v_0 = 23.5$ cm s^{-1} at the reference radius $r_0 = 4.5$ m, where velocity measurements are made.

IV.2.2 Measurement techniques

We use three complementary techniques to observe the flow: laser-induced fluorescence (LIF), which gives a qualitative picture of the flow structure; Stereoscopic PIV (S-PIV), which provides the three velocity components in a vertical plane; and vertically profiling thermistor probes, which resolve the temperature stratification.

IV.2.2.1 Laser-induced fluorescence

Figure IV.2 presents a snapshot of the flow during the transient growth of the boundary layer, visualised using fluorescent dye (rhodamine 6G) injected at the tank floor at the beginning of the experiment. The image is taken in the (e_θ, e_z) plane; the bottom stress drives the flow from left to right. Immediately above the floor lies the *viscous sublayer*, a thin region where viscous stresses dominate and the velocity profile is linear, which is too thin to be visible in the figure. Above it lies the *log layer*, a region where the flow is governed by the law of the wall, with a logarithmic mean velocity profile whose range increases with the Reynolds number.

Above this log layer, the *mixed layer* is characterised by an approximately uniform dye concentration, reflecting efficient scalar mixing by turbulent eddies. The velocity field within this layer, however, retains significant vertical structure: it decreases monotonically with height in the non-rotating case, and adopts an Ekman-like veering profile when background rotation is present. In the rotating case, the Coriolis force confines this active layer to a depth $\delta_E \sim u_*/f$, beyond which the flow decouples from the bottom stress.

At the top of the mixed layer, the *entrainment layer* marks the transition to the quiescent stratified interior above. It is visible in Fig. IV.2 as the bright, turbulent interface where overturning structures erode the stratification. The entrainment is driven by Kelvin–Helmholtz billows, which arise when the local Richardson number falls below $Ri_c \approx 0.25$ (Miles, 1961; Howard, 1961). Overturning intrusions and small-scale eddies then engulf pockets of stratified fluid.

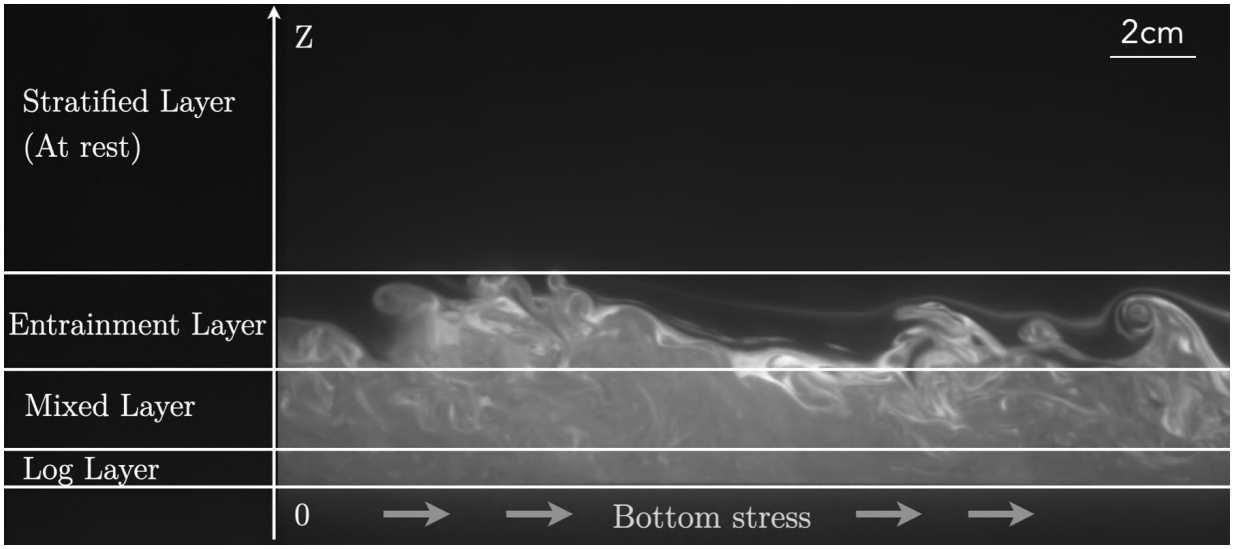

Figure IV.2: EXP-S: Snapshot of vertical view, at $r = 4.5$ m, of the boundary layer turbulence revealed by a fluorescent dye (in white) injected into the denser water at the bottom prior to the experiment. The horizontal lines qualitatively illustrate the vertical structure of the flow. The black region above is at rest.

IV.2.2.2 Stereoscopic Particle Image Velocimetry (S-PIV) and image processing

The velocity field is measured in a vertical plane located at $r_0 = 4.5$ m from the centre (2 m from the outer boundary) using Stereoscopic Particle Image Velocimetry (S-PIV), which provides the three components of the velocity field in a two-dimensional plane. The fluid is seeded with polyamide particles (Orgasol, 60 μm diameter), which are approximately neutrally buoyant. The particles are illuminated by a continuous 5 W YAG laser source operating at $\lambda = 532$ nm, shaped into a vertical light sheet by a Powell lens. Two cameras (PCO, 2048×2048 pixels, 14-bit monochrome) are mounted on both sides of the light sheet, observing the same plane from two different view angles. Each camera provides the particle displacement in the plane perpendicular to the line of sight, so the three velocity components can be deduced by geometric projection.

Images are acquired in short bursts of 3 frames at 100 Hz, repeated five times per second. All image processing is performed with the UVMAT software. The processed velocity fields have a spatial resolution of 1 mm in both the horizontal (e_θ) and vertical (e_z) directions, and a temporal resolution of 0.2 s. Further details on the S-PIV method are given in Sous et al. (2013).

The view field spans $L_{\text{laser}} = 32$ cm along the azimuth. The cartesian velocity components (u_x, u_y, u_z) in this tangential vertical plane can be treated as the cylindrical components (u_θ, u_z, u_r) to a good approximation. The velocity is measured in the platform reference frame which holds the cameras, but for a better connection with modelling, we convert them to the initial reference frame by subtracting the velocity increment $v_0 = r_0 \Delta\Omega$ to the azimuthal component.

IV.2.2.3 Temperature measurements

Temperature profiles are obtained using three vertically profiling thermistor probes mounted on a motor-driven gantry positioned along a tank radius. The probes are equally spaced at 1 m intervals, sampling at radial distances of 1.5 m, 2.5 m, and 4 m from the outer boundary. They are deliberately placed at the opposite azimuthal position with respect to the S-PIV measurement plane to minimise disturbance to the velocity field. Each probe traverses the water column at $5\ \mathrm{cm\,s^{-1}}$ with an acquisition frequency of 140 Hz. The raw profiles are interpolated onto a regular temporal–vertical grid with resolutions $\Delta t_{\mathrm{Temp}} = 0.01$ s and $\Delta z_{\mathrm{Temp}} = 1$ mm.

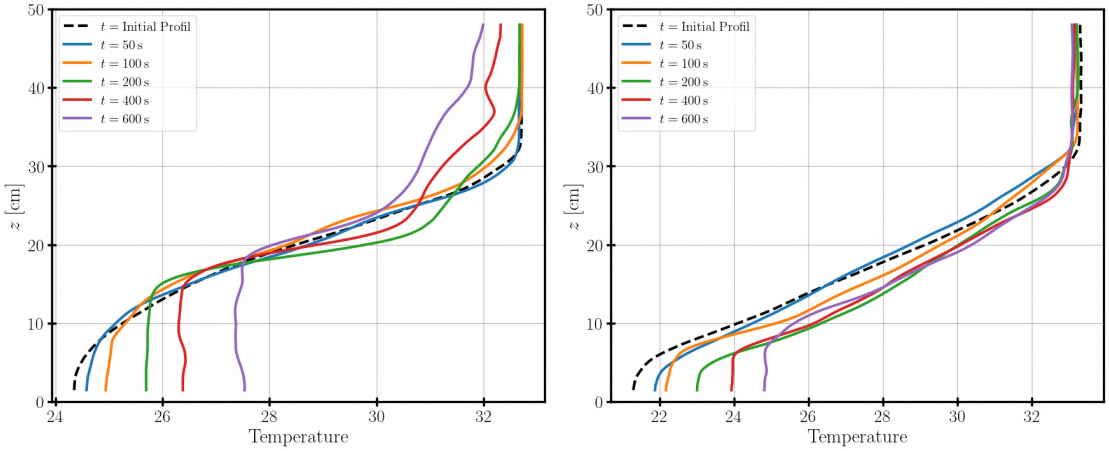

Figure IV.3: Vertical profiles of temperature for different time during the acquisition. Each color mark a different time of the experiment. The dark dashed line shows the initial profile of stratification prior to the experiment. For both figure, the temperature probe is at 4 m (resp. 2.5 m) from the center (resp. the lateral boundary) of the tank. Left: Experiment without initial rotation (EXP-S). Right: Experiment with initial rotation (EXP-SR).

Figure IV.3 shows representative temperature profiles at several times during EXP-S (no rotation) and EXP-SR (with rotation). In both cases, the initial profile (dashed) exhibits a nearly linear temperature gradient over the lower 25–30 cm, capped by a well-mixed upper layer resulting from convection at the water–air interface. As the experiment progresses, the bottom stress erodes the stratification from below: the temperature profiles develop a growing isothermal layer near the floor, whose upper boundary marks the base of the mixed layer. The deepening is markedly faster in the non-rotating case (EXP-S), where the mixed layer reaches approximately 20 cm after 600 s, than in the rotating case (EXP-SR), where the Coriolis force limits the vertical penetration of momentum and the mixed layer remains significantly shallower over the same duration. This contrast between the two experiments illustrates the controlling role of rotation on mixed-layer deepening and motivates the quantitative analysis presented in Section IV.4.

IV.2.3 Non-dimensional parameters

We consider the flow produced in a cylindrical tank of radius $R = 6.5$ m and depth $H = 0.5$ m by a sudden change of rotation rate from Ω_i to $\Omega_f = \Omega_i + \Delta\Omega$. The large aspect ratio $R/H = 13$

ensures that the dynamics are controlled by local vertical fluxes, with negligible influence of the lateral boundary, at least during the initial phases of the spin-up. It is natural to express all horizontal length scales in terms of the measurement radius $r_0 = 4.5$ m $= 0.69\,R$. The aspect ratio is then defined as

$$a = \frac{r_0}{H} = 9 \tag{IV.3}$$

In the initial state of solid-body rotation, the free surface is in equilibrium with the centrifugal force and takes the shape of a paraboloid, with elevation $z = H + \Omega_i^2 r^2/(2g)$. For the present value $\Omega_i = 0.05$ rad s^{-1}, the elevation difference between the center and the outer edge at $r = 6.5$ m is at most $\sim$5 mm, so the free surface can be treated as effectively flat.

The relevant physical parameters are the rotation rate increment $\Delta\Omega$, the Coriolis parameter $f = 2\Omega_i$, the kinematic viscosity of water, the depth H, the radius r_0, and the time t, the buoyancy frequency N, and the diffusivity of heat κ. We discuss here the relevant non-dimensional parameters that we can form with these quantities.

We define the Rossby number Ro based on the rotation rate increment

$$Ro = \frac{\Delta\Omega}{\Omega_i}\,. \tag{IV.4}$$

In our experiments, $Ro \approx 1$, which indicates that the impulsive forcing is of the same order as the background rotation. We define the Reynolds number Re_δ based on the wall velocity $v_0 = r_0\Delta\Omega$ and the laminar Ekman layer thickness $\sqrt{\nu/\Omega_i}$:

$$Re_\delta = \frac{r_0\Delta\Omega}{\sqrt{\nu\Omega_i}}\,. \tag{IV.5}$$

The Reynolds number based on the laminar Ekman layer thickness is $Re_\delta \approx 10^3$ (computed with $\nu = 10^{-6}$ m^2 s^{-1}), well above the threshold for the transition to turbulence in Ekman layers ($Re_\delta \gtrsim 150$, Lingwood 1996; Sous et al. 2013), confirming that the boundary layer is fully turbulent throughout the experiments. The same value $Re_\delta = 1000$ was used in the DNS of Marlatt et al. (2012), which provides evidence of a fully developed turbulent regime.

A more intrinsic Reynolds number can be formed from the friction velocity u_* and the turbulent Ekman layer thickness $\propto u_*/f$:

$$Re_* = \frac{u_*^2}{f\nu}. \tag{IV.6}$$

This quantity (also called 'friction Rossby number') is not directly controlled by the experimental parameters but is estimated a posteriori from the velocity measurements (by Eq. (IV.1)). The friction Reynolds number, estimated a posteriori is $Re_* \approx 10^3$, comparable to values reported in DNS studies of the turbulent Ekman layer (Marlatt et al., 2012; Braun et al., 2020).

The Ekman number $E_k = \nu/(fH^2)$ also characterises the effect of viscosity in rotating flows. In the laminar regime it sets the Ekman layer thickness as $\delta/H = E_k^{1/2}$ and the Ekman spin-up time as $\Omega_i\tau_E = E_k^{-1/2}$. Its relevance in the turbulent regime is less clear. For our experiment, we have $Ek \approx \mathcal{O}(10^{-5})$. The Ekman number is related to our parameters by $E_k = Ro^2 Re_\delta^{-2} a^{-2}$.

The time t is naturally expressed in units of the inertial period: $\Omega_i t$ when $\Omega_i \neq 0$, or $\Delta\Omega\, t$ otherwise. Three successive phases of the motion can be distinguished:

1. $\Delta\Omega\, t < \pi$: the influence of fluid trajectory curvature is small and the flow can be treated as rectilinear.
2. $\Omega_i t \sim 2\pi$ (or $\Delta\Omega\, t \sim 2\pi$ if $\Omega_i = 0$): an Ekman layer (or von Kármán layer) is established after the damping of a few inertial oscillations, while the bulk flow remains largely unchanged.
3. $\Omega_i t \gg 2\pi$ (or $\Delta\Omega\, t \gg 2\pi$ if $\Omega_i = 0$): the bulk flow progressively spins up under the effect of bottom friction.

The values of the non-dimensional numbers can be compared to typical oceanic conditions. In the ocean bottom boundary layer over continental shelves, the friction velocity is of order $u_* \sim 0.5$–2 cm s^{-1} (Perlin et al., 2005) and the Coriolis parameter is $f \sim 10^{-4}$ s^{-1}. The turbulent Ekman depth $\delta_E \sim u_*/f$ is thus of order 10–100 m in the ocean, compared to ~ 5–10 cm in our experiments. With the kinematic viscosity $\nu \sim 10^{-6}$ m^2 s^{-1} this yields $Re_* = u_*^2/(f\nu) \sim 10^7$–$10^8$ in the ocean, several orders of magnitude larger than in the laboratory. However, the transport properties are expected to become independent of the Reynolds number as long as the flow is fully turbulent. Similarly, the Ekman number is several orders of magnitude larger in the laboratory than in the ocean ($E_k \sim 10^{-8}$), both regimes are expected to lie within the fully turbulent asymptote, where transport properties become independent of E_k.

The influence of stable density stratification is quantified by the Richardson number based on the velocity $r_0\Delta\Omega$ and the fluid depth H:

$$Ri = \frac{N^2}{a^2\Delta\Omega^2}. \tag{IV.7}$$

The Richardson number ranges from 0 (EXP-REF) to ≈ 0.4 (EXP-SR), placing the stratified experiments in the weakly stratified limit where rotation rather than buoyancy controls the boundary layer depth. We can also define a Richardson number Ri_* based on the thickness u_*/f instead of H,

$$Ri_* = \left(\frac{N u_*}{f v_0}\right)^2. \tag{IV.8}$$

In our experiments $N/f \sim 3$ while $u_*/v_0 \sim 1/20$, so that $Ri_* \sim 0.02$. Therefore, stratification has little influence in the dynamics of the Ekman layer. We will use the temperature as a quasi-passive scalar field.

The Prandtl number, ratio of kinematic viscosity to thermal diffusivity, is $Pr \simeq 6$ for water, in contrast with $Pr \simeq 700$ for salinity. Since the present study focuses on momentum dynamics and the stratification remains weak ($Ri \lesssim 0.4$), the precise value of Pr has presumably a negligible influence on the results.

Alternative choices of non-dimensional parameters are possible. In particular, the final rotation rate Ω_f could be used instead of Ω_i. The general problem of a steady boundary layer

between a fluid rotating at Ω_i and a plate rotating at Ω_f has been analysed by Lingwood (1996), providing both the steady solutions and their instability properties. This general case, called BEK, encompasses as special cases the von Kármán layer ($\Omega_i = 0$), the Bödewald layer ($\Omega_f = 0$), and the Ekman layer recovered in the limit $\Omega_f \to \Omega_i$. Their analysis suggests using a weighted average of Ω_i and Ω_f, which reduces to $0.5(\Omega_i + \Omega_f)$ near the Ekman limit. However, the initial stage of spin-up studied here is more strongly influenced by Ω_i, which justifies our choice in Eqs. (IV.4)–(IV.5). This is further supported by Sous et al. (2013), who found experimentally that wall friction depends primarily on Ω_i in the turbulent regime.

IV.3 Theory of the transient Ekman layer in the rotating tank configuration

IV.3.1 Extended 1D model for axisymmetric cases

We can describe our experiments in terms of a one dimensional model along the vertical, starting from the Boussinesq equations for an axisymmetric flow in a rotating reference frame with Coriolis parameter f. In cylindrical coordinates, the incompressibility condition writes

$$\frac{1}{r}\frac{\partial (r u_r)}{\partial r} + \frac{\partial u_z}{\partial z} = 0 \,, \tag{IV.9}$$

and the dynamical equations for the velocity components (u_r, u_θ, u_z) and the buoyancy $b = -g(\rho - \rho_0)/\rho_0$ write

$$\frac{\partial u_r}{\partial t} + u_r \frac{\partial u_r}{\partial r} + u_z \frac{\partial u_r}{\partial z} - \frac{u_\theta^2}{r} - f u_\theta + \frac{1}{\rho_0}\frac{\partial p}{\partial r} = \frac{\partial}{\partial z}\left(\nu_t \frac{\partial u_r}{\partial z}\right) \tag{IV.10a}$$

$$\frac{\partial u_\theta}{\partial t} + u_r \frac{\partial u_\theta}{\partial r} + u_z \frac{\partial u_\theta}{\partial z} + \left(f + \frac{u_\theta}{r}\right) u_r = \frac{\partial}{\partial z}\left(\nu_t \frac{\partial u_\theta}{\partial z}\right) \tag{IV.10b}$$

$$\frac{\partial u_z}{\partial t} + u_r \frac{\partial u_z}{\partial r} + u_z \frac{\partial u_z}{\partial z} + \frac{1}{\rho_0}\frac{\partial p}{\partial z} - b = \frac{\partial}{\partial z}\left(\nu_t \frac{\partial u_z}{\partial z}\right) \tag{IV.10c}$$

$$\frac{\partial b}{\partial t} + u_r \frac{\partial b}{\partial r} + u_z \frac{\partial b}{\partial z} = \frac{\partial}{\partial z}\left(\kappa_t \frac{\partial b}{\partial z}\right) \,. \tag{IV.10d}$$

We have introduced an eddy viscosity ν_t, and diffusivity κ_t for the vertical turbulent transport, but neglected the corresponding horizontal turbulent flux because of the large aspect ratio condition $a \gg 1$. Note that in the rotating frame, the centrifugal force $\rho\Omega^2/r$ is exactly balanced by an additional radial pressure gradient; these two terms cancel and are therefore omitted in Eq. (IV.10a).

Initially, the fluid and bottom plate ($z = 0$) are at rest (or in solid-body rotation). Taking this state as the reference frame, the velocity is zero everywhere for $t < 0$. At $t = 0$, the bottom plate is impulsively set to rotate at an angular velocity $\Delta\Omega$, while the velocity remains zero far

from the boundary layer ($z \to \infty$). Since the geometry is axisymmetric, it is natural to seek solutions with u_r, u_θ proportional to r. Introducing a reference radius r_0, we write

$$u_r = \frac{r}{r_0}\, u(z,t) \;\;,\;\; u(0,t) = 0 \tag{IV.11a}$$

$$u_\theta = \frac{r}{r_0}\, v(z,t) \;\;,\;\; v(0,t) = r_0\, \Delta\Omega \;\; \text{for } t > 0 \tag{IV.11b}$$

$$u_z = w(z,t) \;\;,\;\; w(0,t) = 0 \tag{IV.11c}$$

$$b = b(z,t) \;\;,\;\; \frac{\partial b}{\partial z}(0,t) = 0 \tag{IV.11d}$$

Then Eq. (IV.9) and (IV.10) become

$$2\frac{u}{r_0} + \frac{\partial w}{\partial z} = 0 \tag{IV.12a}$$

$$\frac{\partial u}{\partial t} + w\frac{\partial u}{\partial z} + \frac{u^2 - v^2}{r_0} - fv + \frac{r_0}{r}\frac{1}{\rho_0}\frac{\partial p}{\partial r} = \frac{\partial}{\partial z}\left(\nu_t \frac{\partial u}{\partial z}\right) \tag{IV.12b}$$

$$\frac{\partial v}{\partial t} + w\frac{\partial v}{\partial z} + \left(f + \frac{2v}{r_0}\right) u = \frac{\partial}{\partial z}\left(\nu_t \frac{\partial v}{\partial z}\right) \tag{IV.12c}$$

$$\frac{p}{\rho_0} = \frac{p_\infty(r)}{\rho_0} + \int_z^\infty \left(\frac{\partial w}{\partial t} + w\frac{\partial w}{\partial z} - b\right) dz + \frac{w_\infty^2}{2} - \nu_t \left.\frac{\partial w}{\partial z}\right|_{z=0} \tag{IV.12d}$$

$$\frac{\partial b}{\partial t} + w\frac{\partial b}{\partial z} = \frac{\partial}{\partial z}\left(\kappa_t \frac{\partial b}{\partial z}\right) \tag{IV.12e}$$

For a viscosity ν_t and diffusivity κ_t depending only on z, this is a one-dimensional system of equations in terms of the coordinate z. The pressure is the sum of a term depending only on z (the hydrostatic pressure), and a term $p_\infty(r)$, equal to zero with our hypothesis of vanishing velocity away from the boundary layer. This columnar model represents an Ekman boundary layer in unsteady regime, modified by the radial acceleration and transport effects due to the fluid rotation rate. In this columnar model, the buoyancy has no direct action on the mean velocity. It acts only on the turbulent kinetic energy, which influences the mean flow through the eddy viscosity.

Three phases of motion can be distinguished as stated in section IV.2.3.

1. $\Delta\Omega\, t < \pi$: At short times, smaller than the half inertial period π/f, the radial velocity and non-linear terms in Eq. (IV.12c) are negligible. The azimuthal velocity is driven by the bottom friction like in a unidirectional flow. Then the momentum balance can be expressed in terms of the displacement thickness

$$\delta_1 = \frac{1}{v_0}\int_0^\infty v\; dz \tag{IV.13}$$

This thickness increases under the effect of wall stress ρu_*^2 as $d\delta_1/dt = u_*^2/v_0$. For a constant friction coefficient $C_\delta = u_*^2/v_0^2$, this results in the linear growth with time t,

$$\delta_1 = C_\delta\, v_0\, t \tag{IV.14}$$

2. $\Omega_i t \sim 2\pi$ (or $\Delta\Omega\, t \sim 2\pi$ if $\Omega_i = 0$): After a time approaching half an inertial period, a radial velocity u appears, and the momentum balance is modified by the Coriolis term fu. This leads to a steady Ekman layer, or to a more general Bodewald-Ekman-Karman layers if we include the local Coriolis effect associated with the angular velocity $\sim v_0/r_0$. This will be further discussed in section IV.3.2.

3. $\Omega_i t \gg 2\pi$ (or $\Delta\Omega\, t \gg 2\pi$ if $\Omega_i = 0$): At still later times the friction effect at the bottom is progressively transferred to the fluid column by Ekman pumping effects, as it will be discussed in section IV.3.3.

To close this 1D set of equations, turbulent viscosity and diffusivity will be computed with the k-ε model, implemented in the GOTM single-column framework (Umlauf and Burchard, 2005). Full details of the numerical setup are given in Appendix IV.7.2. Note that we do not solve Eq. (IV.12) in its full form. First we neglect the radial pressure term, which is valid at the early stage, before the buildup of a significant bulk flow by the spin-up process. We also neglect the vertical advection of momentum which turns out to be negligible in our calculations (see appendix IV.7.4). In consistency, the advection of TKE by the mean vertical velocity is also neglected.

IV.3.2 Theory of the transient Ekman layer

To build physical intuition, we solve analytically the onset of the Ekman layer in the laminar limit ($Ro \to 0$, $Re_\delta \to 0$, $\nu = const.$). Two boundary conditions are considered: an imposed stress, whose exact solution has been already published by Ekman (1905), and an imposed velocity, which is the relevant condition for our laboratory tank and whose solution is derived here to complement Ekman's solution. The comparison of the two reveals that the boundary condition controls the damping rate of inertial oscillations. In the aforementioned limit, the system (IV.12) reduces to

$$\frac{\partial u}{\partial t} - fv = \nu \frac{\partial^2 u}{\partial z^2}\,, \tag{IV.15a}$$

$$\frac{\partial v}{\partial t} + fu = \nu \frac{\partial^2 v}{\partial z^2}\,. \tag{IV.15b}$$

These two equations can be combined into a single equation by introducing the complex velocity $q = u + iv$, which satisfies

$$\frac{\partial q}{\partial t} + ifq = \nu \frac{\partial^2 q}{\partial z^2}. \tag{IV.16}$$

Let us introduce the normalized coordinate z/δ_E, where $\delta_E = \sqrt{2\nu/f}$ is the thickness of the steady Ekman layer. Looking for time oscillating solutions in the form $q = \hat{q}(z)\exp(-i\omega t)$, we get spatial oscillations decaying with z of the form

$$\hat{q}(z) \propto \exp\left[-\frac{(1+i)}{(1-\omega/f)^{1/2}}\frac{z}{\delta_E}\right] \tag{IV.17}$$

Note that the fluid is assumed at rest for large z since the flow is analysed in the rotating reference frame before spin-up, so that u, v exponentially decay for $z \to \infty$. In the alternative case of a uniform geostrophic velocity at large z, the same equation (IV.15) would hold for the velocity defect, obtained by subtracting the geostrophic velocity to the velocity field (see equ IV.35).

The general solution of (IV.16) can be expressed as an integral over frequencies of such elementary solutions. The weight of each frequency can be obtained as the Fourier transform of the step function representing the boundary condition at $z = 0$. After typically half an inertial period, this integral is quickly dominated by the frequency $\omega = 0$, dominant in the boundary condition, and by the inertial frequency $\omega = f$ which is resonant, as the penetration depth $\delta(\omega) = \delta_E(1 - \omega/f)^{-1/2}$ diverges for $\omega \to f$. Then the solution can be approximately expressed as the sum of the classical steady Ekman layer solution $q_{\rm Ekman}(z)$ and an inertial oscillation whose amplitude $q_{\rm IO}(z,t)$ slowly evolves with time,

$$q(z,t) \simeq q_{\rm Ekman}(z) + q_{\rm IO}(z,t)\ \exp(-ift), \tag{IV.18}$$

The quality of this approximation will be checked below by the exact solution (Fig. IV.4) and compared with the laboratory experiments in Section IV.5.

The first term in Eq. (IV.18) is the classical steady state Ekman solution given by (IV.17) for $\omega = 0$, $q_{\rm Ekman}(z) \propto \exp(-z/\delta_E)\ \exp(-iz/\delta_E)$. Equation (IV.17) diverges for $\omega = f$ but the inertial oscillation can be specified by introducing the form $q = q_{\rm IO}(z,t)\exp(-ift)$ in Eq. (IV.16). This eliminates the Coriolis term and yields the pure diffusion equation

$$\frac{\partial q_{\rm IO}}{\partial t} = \nu \frac{\partial^2 q_{\rm IO}}{\partial z^2}. \tag{IV.19}$$

It describes circular particle motion (in the anticyclonic direction) driven by the divergence of the diffusive flux. The amplitude of this circular motion diffuses by viscosity like the linear momentum in the absence of Coriolis effect. This contrasts with the steady component whose penetration is inhibited by Coriolis effects. Therefore the inertial oscillation will eventually penetrate deeper than the steady component, forming a slab of circular motion whose thickness spreads as $\delta_{IO} \propto (\nu t)^{1/2}$.

The behaviour then depends on the boundary condition at $z = 0$. We shall distinguish the case of an imposed velocity v_0 and the case of an imposed shear stress u_*^2, for $t > 0$,

$$\begin{aligned} \text{imposed stress}: &\quad \nu\frac{\partial v}{\partial z} = -u_*^2\,, \quad \nu\frac{\partial u}{\partial z} = 0 \\ \text{imposed velocity}: &\quad v = v_0\,, \quad u = 0\,. \end{aligned} \tag{IV.20}$$

The steady component for a given velocity $v = v_0$ is given by

$$q_{\rm Ekman}(z) = iv_0\ \exp\left[-(1+i)\frac{z}{\delta_E}\right]. \tag{IV.21}$$

The corresponding viscous stress $-\nu\partial q_{\rm Ekman}/\partial z$ has the same form but is tilted by an angle $\pi/4$.

$$-\frac{\partial q_{\rm Ekman}}{\partial z} = i\frac{v_0}{\delta_E}\,\sqrt{2}\,\exp\left(i\frac{\pi}{4}\right)\,\exp\left[-(1+i)\frac{z}{\delta_E}\right]. \tag{IV.22}$$

The value of this shear stress at the boundary is $u_*^2 = \nu v_0/(\delta_E\sqrt{2})$, tilted by $\pi/4$ with respect to the y axis. Therefore, Eq. (IV.21) is also the solution of the problem with this imposed shear stress.

However, the inertial oscillation behaves differently in each case. Indeed, by vertical integration of (IV.19), we get

$$\frac{d}{dt}\int_0^\infty q_{\rm IO}dz = -\nu\left.\frac{\partial q_{IO}}{\partial z}\right|_{z=0}. \tag{IV.23}$$

A boundary condition of given shear stress $-\nu\frac{\partial q}{\partial z}\Big|_{z=0}$ will result in a zero average of the oscillating component $\nu\partial q_{IO}/\partial z = \nu\frac{\partial q}{\partial z}\exp(ift)$. Therefore, the integral $\int_0^\infty q_{\rm IO}dz$ is conserved. Since the thickness of the inertial oscillation increases by diffusion as $\delta_{IO} \propto (\nu t)^{1/2}$, the amplitude of the oscillation also decreases in $\propto (\nu t)^{-1/2}$. There is no such clear argument for the no-slip solution: we need the exact solution to analyse the decay of inertial oscillations.

We turn now to the exact solution of (IV.16) for the stepwise surface forcing. The imposed stress solution has already been published in the seminal article of Ekman (1905) (the mathematical solution is acknowledged as a contribution of I. Fredholm). The approach relies on the Green's function of (IV.16), which describes the response to an impulsive forcing applied at time $t_i < t$ and takes the form

$$q(z,t) = \frac{q_0}{\sqrt{t'}}\exp(-ift')\,\exp\left(-\frac{z^2}{4\nu t'}\right), \tag{IV.24}$$

where $t' = t - t_i$ (this is the elementary solution of the diffusion equation (IV.19) for the variable $q\,\exp(ift)$).

Then the solution for the sudden shear stress set at $t > 0$ is obtained as an integral of this elementary solution over all time origins t_i in the range $[0\;\; t]$. It yields the following integral over the time delay, expressed in terms of the non-dimensional time $\tau' = ft'$,

$$q(z,t) = \frac{iu_*^2}{\sqrt{\pi}(\nu f)^{1/2}}\int_0^{ft}\frac{\exp(-i\tau')}{\tau'^{1/2}}\,\exp\left(-\frac{fz^2}{4\nu\tau'}\right)\,d\tau'. \tag{IV.25}$$

The prefactor has been adjusted to fit the shear stress condition at $z = 0$ as justified below. After taking the real and imaginary parts, it corresponds to Eq. (10) of Ekman (1905). This is the exact solution of the transient problem. It can be interpreted as a sum of inertial oscillations with amplitude and phase depending on ζ.

The shear stress $-\nu\partial q/\partial z$ is then expressed as

$$-\nu\frac{\partial q}{\partial z} = \frac{iu_*^2}{\sqrt{2\pi}}\int_0^{ft}\frac{\exp(-i\tau')}{\tau'^{3/2}}\,\frac{z}{\delta_E}\,\exp\left(-\frac{fz^2}{4\nu\tau'}\right)d\tau'. \tag{IV.26}$$

This expression should tend to the step function (Heaviside function) in the limit $z \to 0$. This limit is not obvious since the integrand diverges for $\tau' \to 0$. It can be obtained by making the change of variable $X = (z/\delta_E)\tau'^{-1/2}$, such that $d\tau' = -2(z/\delta_E)^2 X^{-3} dX$. Then (IV.25) becomes, reversing the bounds of the integral obtained with the new variable,

$$-\nu\frac{\partial q}{\partial z} = iu_*^2\sqrt{\frac{2}{\pi}}\int_{(z/\delta_E)(ft)^{-1/2}}^{\infty} \exp\left(-\frac{X^2}{2} - i\frac{z^2}{\delta_E^2 X^2}\right)\, dX\,. \tag{IV.27}$$

The integral now converges for any z, and for $z \to 0$, it tends to $\int_0^\infty \exp(-X^2/2)\, dX = \sqrt{\pi/2}$. Therefore, the imaginary part of $-\nu\partial q/\partial z$ is equal to u_*^2 for $t > 0$, while its real part is equal to 0, which fits with the boundary condition (IV.20) for imposed stress.

The case of imposed velocity can be deduced from Eq. (IV.25) by noticing that if $q(z,t)$ is a solution of (IV.16), then $\partial q/\partial z$ is also a solution, thanks to the commutation of the partial derivatives with respect to time and space. Thus, we switch from the case of imposed stress to the case of imposed velocity by the transform

$$q \;\to\; -\frac{v_0\nu}{u_*^2}\frac{\partial q}{\partial z}\,. \tag{IV.28}$$

Thus we immediately deduce from (IV.27) a solution for an imposed velocity v_0,

$$q(z,t) = \frac{iv_0}{\sqrt{2\pi}}\int_0^{ft} \frac{\exp(-i\tau')}{\tau'^{3/2}}\,\frac{z}{\delta_E}\,\exp\left(-\frac{fz^2}{4\nu\tau'}\right))d\tau'\,. \tag{IV.29}$$

The main difference with the original solution (Eq. IV.25) derived by Ekman is the exponent of the decay time ($\tau^{-1/2}$ for the free-slip solution and $\tau^{-3/2}$ for the no-slip solution), such that the damping rate is very different in the two cases.

We have numerically determined the solution (IV.25) for an imposed wall stress and the solution (IV.29) for the no-slip case. The reduced coordinate $\zeta = z/\delta_E$ is used. In the latter case, we choose a unit velocity $v_0 = 1$, and in the former case a wall condition $-\partial|q|/\partial\zeta = \sqrt{2}$ tilted by an angle $\pi/4$ so that the final steady state is the same in both cases. As anticipated, we observe a much faster decay of the inertial oscillations in the no-slip case. This is visualized in Fig. IV.4 by plotting the two velocity components at altitude $\zeta = 1$, for which the two velocity components are equal in the steady regime. Although we have not made any hypothesis about the separation of the steady regime and inertial oscillation, the exact solution appears as a clear superposition of the two solutions.

A key question is how these laminar results extend to the turbulent regime. In the limit of large Reynolds numbers, steady flow components are expected to be functions of the reduced vertical coordinate $\zeta = zf/u_*$. This reflects the hypothesis that the properties of turbulence are fully determined by the friction velocity u_* (the eddy viscosity hypothesis is not required). This yields a universal velocity profile, the turbulent counterpart of (IV.21), which must be matched with the log layer near the wall (see for instance Garratt, 1992).

Although the time-dependent eddy viscosity $\nu_t(z,t)$ couples the mean flow to the oscillating shear, the steady-state Ekman balance is independent of the transient excitation: provided any

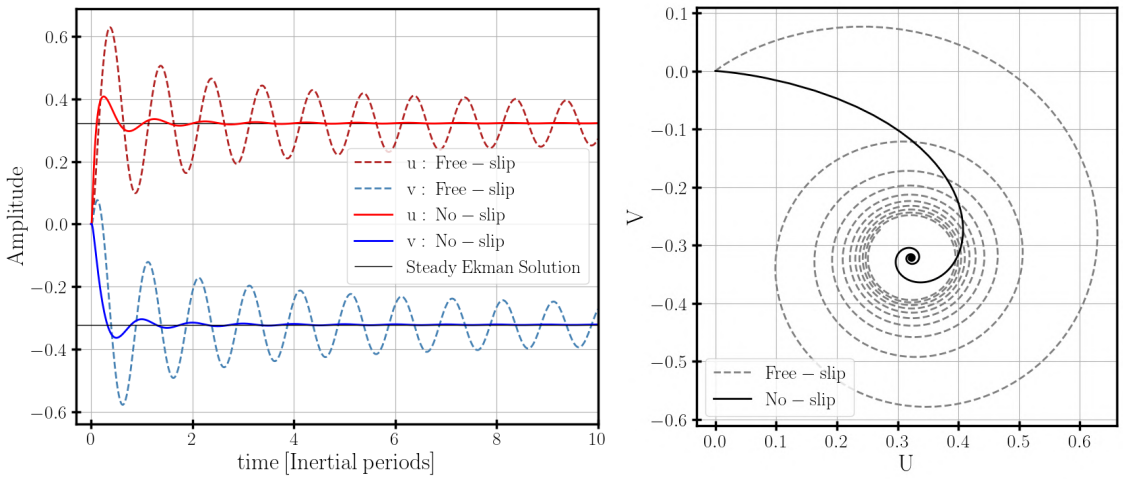

Figure IV.4: Damping of Inertial Oscillation for linear Oscillatory Ekman Layer. Left: resolution of Eq. (IV.29), in solid line, for a velocity impose at the boundary in the $x-$direction. In dashed line the resolution of Eq. (IV.25) for a shear stress impose (free-stress) at an angle $\pi/4$. For both the solution is computed at $\zeta = 1$. The thin black line display the steady Ekman solution (IV.21). Right: Hodograph for 10 successive inertial oscillations at $\zeta = 1$ for in solid (resp. dashed) line the no-slip (resp. free-slip) condition.

damping mechanism is present, the inertial oscillations decay and the flow converges to the same steady solution, regardless of the damping timescale. This will be investigated in Section IV.5 by decomposing the velocity field into a time-mean component and an oscillating residual, and comparing the k-ε simulations with the experimental results. We will show that, despite the slow attenuation of the oscillations, the two contributions remain statistically independent and the time-mean profile converges to the turbulent Ekman spiral.

In a turbulent boundary layer, the eddy viscosity ν_t vanishes as $\nu_t \sim \kappa u_* z$ in the log layer and drops to zero at $z = 0$, where the flow is locally laminar within the viscous sublayer. As a consequence, the effective stress transmitted to the fluid is neither the large no-slip viscous stress (which would require resolving the sublayer) nor zero (as in free-slip), but an intermediate value set by the quadratic drag law

$$\tau_b = C_f |\mathbf{u}_1| \mathbf{u}_1 \,, \tag{IV.30}$$

where $\mathbf{u}_1$ is the velocity within the log layer. This drag law encodes the integrated effect of the unresolved viscous sublayer through the empirical coefficient C_f.

The damping rate of the inertial oscillations is therefore controlled by C_f: a larger drag coefficient extracts momentum more efficiently from the oscillating flow and accelerates the decay, while a smaller one allows the oscillations to persist longer. In the no-slip laminar limit, the effective $C_f \to \infty$ (the velocity is pinned to zero at the wall), leading to rapid damping. In the free-slip limit, $C_f = 0$ and there is no damping from the boundary. The turbulent regime, with a finite C_f, naturally interpolates between these extremes.

It is worth noting that this mechanism is not specific to the laboratory setting: in the oceanic boundary layers, the same quadratic drag law governs the dissipation of near-inertial energy, and

the value of C_f directly controls the persistence of inertial oscillations generated by impulsive wind or tidal forcing.

The goal of our laboratory experiments is to extend the laminar picture to the turbulent regime, where the bottom boundary condition is no longer a strict no-slip but is governed by the quadratic drag law, as discussed in Section IV.5.

IV.3.3 Ekman pumping effects

In the absence of buoyancy effects, the resulting azimuthal velocity away from the wall $v_\infty(r,t)$ can be assumed independent of z. This results from the shallow water geometry, with height H smaller than the radius r, and the Taylor column effect due to rotation. Then the time evolution of the bulk azimuthal velocity v_∞ can be obtained by vertical integration of Eq. (IV.10b). In a first approximation the water column momentum $\int_0^H u_\theta dz \simeq H v_\infty$ is locally driven by wall friction

$$H\frac{\partial v_\infty}{\partial t} = -\nu_t \frac{\partial u_\theta}{\partial z}_{(z=0)} = u_*^2 \,. \tag{IV.31}$$

To refine this expression, we need to take into account additional terms due to advection by vertical and radial velocities. Assuming a fixed upper surface, the integral of u_r then vanishes by mass conservation. Furthermore, using (IV.9), we can express $u_z\partial u_\theta/\partial z = \partial(u_\theta u_z)/\partial z + (u_\theta/r)\partial(ru_r)/\partial r$. The vertical integral of the first term vanishes by the boundary conditions $u_z = 0$ at $z = 0$ and $z = H$, while the second term adds to $u_r\partial u_\theta/\partial r$. Then, the vertical integral of Eq. (IV.10b) can be expressed as

$$H\frac{\partial v_\infty}{\partial t} = u_*^2 - \frac{1}{r^2}\frac{\partial}{\partial r}\int r^2 u_r u_\theta \, dz \tag{IV.32}$$

The second term represents the divergence of the radial advection of angular momentum. With the scaling (IV.11), the latter is equal to $(4/r_0)\int uvdz$. Since $\int udz = 0$, this can be also written as $(4/r_0)\int u(v - v_\infty)dz$. For spin-up, the radial velocity within the boundary layer is outward ($u > 0$), while $v - v_\infty > 0$, so that it is opposed to the driving force[1]. This radial transport term is quadratic in velocity like the wall friction u_*^2. Therefore, the right hand term of (IV.32) can be empirically modeled as

$$H\frac{dv_\infty}{dt} = C_b(v_0 - v_\infty)^2 \,, \tag{IV.33}$$

where v_0 is the wall velocity. This integrates in time as

$$v_\infty = v_0\frac{(C_b v_0/H)\, t}{1 + (C_b v_0/H)\, t}, \tag{IV.34}$$

This introduces a characteristic turbulent spin-up time $\tau_{\rm turb} = H/(C_b v_0)$, which must be compared to the inertial time Ω_i^{-1} to assess the relative importance of rotation and friction in the long-time evolution. The coefficient C_b will be determined experimentally.

[1]For spin-down, $u < 0$, while $v - v_\infty < 0$, so it enhances the driving force (negative in this case).

IV.4 Mean flow and turbulent statistics

We now compare these analytical results with the observations on the Coriolis Platform.

IV.4.1 Coherent structures

Figure IV.5 shows dye visualisations of the boundary layer with and without background rotation, offering a qualitative picture of how rotation reorganises the turbulent boundary layer. In the absence of rotation (Fig. IV.5, top), large vigorous structures erupt from the bottom and penetrate deep into the interior, reaching heights of 10–12 cm. The dye interface is highly irregular, with mushroom-shaped tilted plumes and overturning billows across a broad range of scales, consistent with the absence of a rotational constraint. Similar patterns are visible in DNS computations of the temporally developing turbulent boundary layer by Kozul et al. (2016).

In the rotating case (Fig. IV.5, bottom), turbulent activity is confined to a layer of 6–8 cm, consistent with the rotational scaling $\delta_E \sim u_*/f$. The structures are markedly smaller and more regular, the interface sharper and more horizontal, indicative of the suppression of large vertical excursions by rotation and stratification. Kelvin–Helmholtz billows are visible at the interface. The structures in the rotating case hint at some horizontal organisation, possibly reflecting inertial effects reminiscent of the Ekman roll instability documented in DNS studies (Marlatt et al., 2012).

IV.4.2 Mean flow profiles

We now turn to a more quantitative analysis of the boundary layer structure, focusing on three configurations: EXP-REF, EXP-S and EXP-SR (cf. Table 1). Stereoscopic PIV measurements provide the three velocity components in a vertical plane aligned with the azimuthal direction. The velocity field has been decomposed into a mean component and a fluctuating component, taking average in the azimuthal direction and a sliding time window (see Appendix IV.7.1 for details). The resulting mean and variance can be interpreted as 1D profiles that allow the comparison with the 1D numerical simulation. We plot the vertical profiles at $t = 100$ s. It is worth stating that at $t = 100$ s the interior flow has already been partially spun up (Fig. IV.12). Since the interior velocity evolves in time due to the spin-up process, we define a defect velocity as the local velocity from which the interior velocity (measured sufficiently far from the bottom boundary) has been subtracted. Because the interior velocity is not directly accessible from the experimental measurements, we use, as a proxy, the azimuthal velocity averaged over the uppermost centimetre of the measured profile, denoted u_θ^{top}. This defect velocity is therefore defined as

$$\langle u_\theta \rangle - v_\infty \approx \langle u_\theta \rangle - u_\theta^{top}. \tag{IV.35}$$

The interior velocity has therefore been subtracted so that only the velocity anomaly is shown, with the region beyond the Ekman layer set to zero. Although the viscous sublayer is not

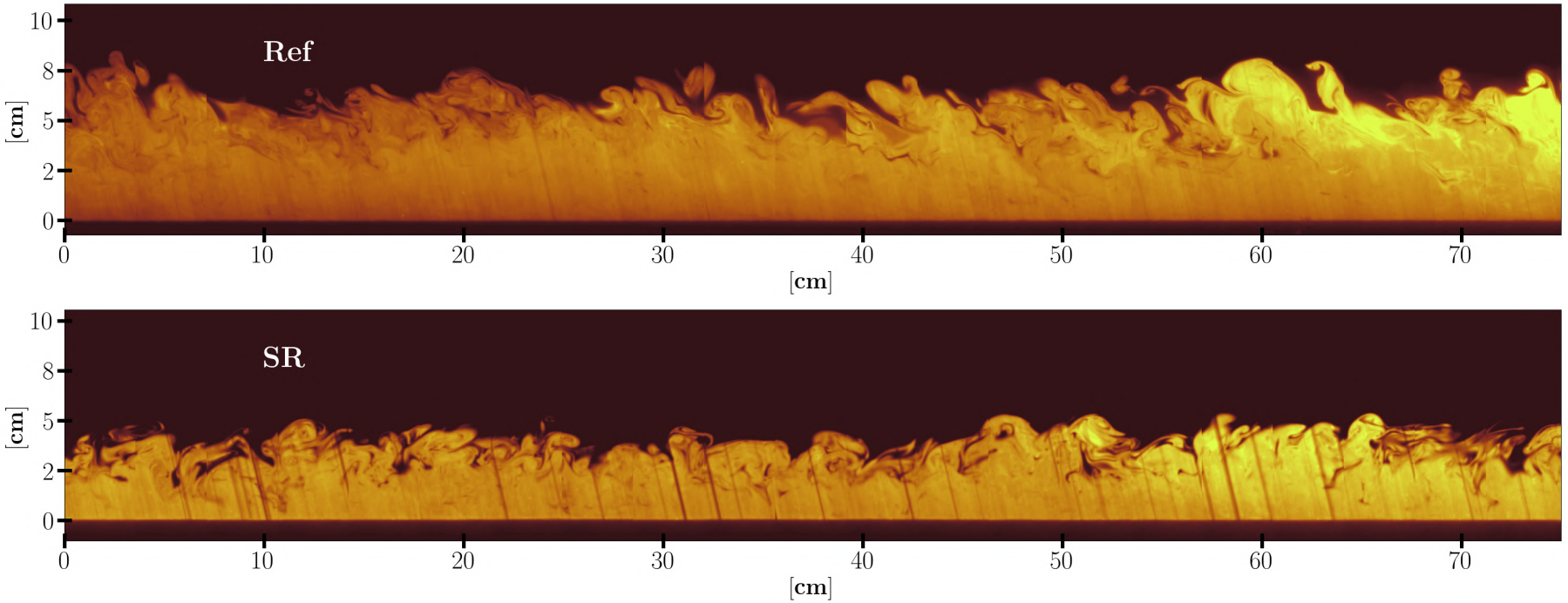

Figure IV.5: Panoramic reconstruction of the dye-visualised boundary layer over a horizontal extent of 0.75 m, obtained by compositing successive frames spanning $\Delta t = 5$ s. The first frame of each composite is taken at $t = 52$ s after the impulsive spin-up. Note that the contrast has been adjusted independently for each panel to enhance the visibility of the structures. Top: non-rotating, unstratified case (EXP-REF). Bottom: rotating, weakly stratified case (EXP-SR). For both picture, the saturation on the right comes from a brighter illumination of the right part of the laser sheet. Inclined black lines are shadows from clusters of particles on the surface.

resolved in the 1D simulation (see Appendix IV.7.2), the near-wall grid points agree well with the experimental data in both cases.

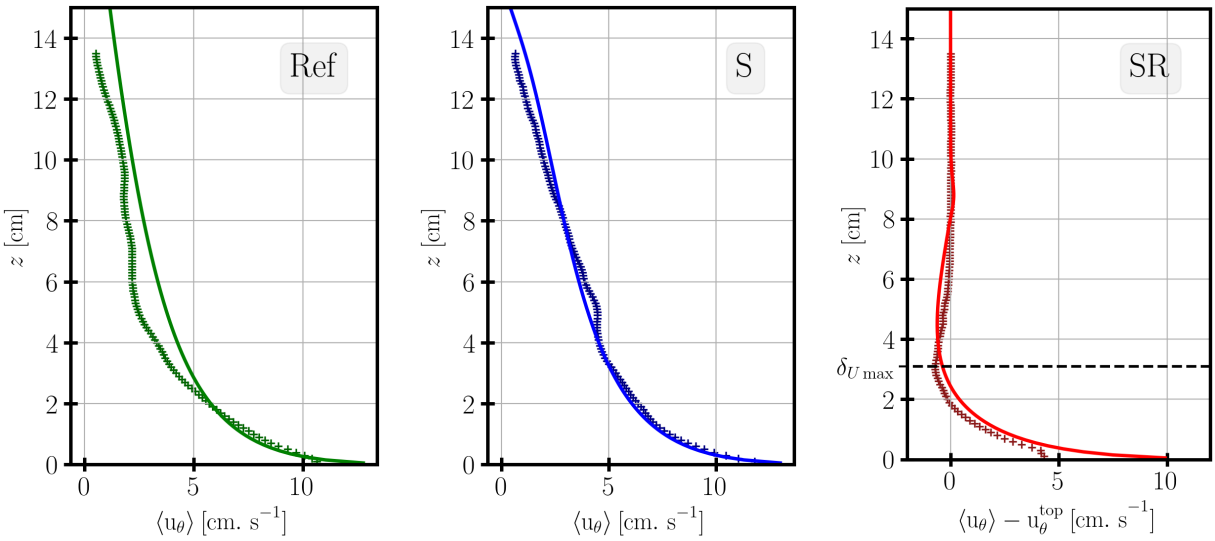

Figure IV.6: Vertical profiles of azimuthal mean velocity $\langle u_\theta \rangle$ at $t = 100$ s. Experimental data are marked by $+$. We plot with solid line, the vertical profile from k-ε simulation. Left: Experiment without rotation-without stratification (EXP-REF). Center: Experiment without rotation-with stratification (EXP-S) . Right: Experiment with rotation-with stratification (EXP-SR). For the experiment with rotation, the interior velocity (u_θ^{top}) has been subtracted in order to visualize the velocity anomaly. The horizontal dashed line in the right panel indicates the height of $\delta_{U\,\max}$ where the overshoot is at its maximum value.

We plot in Fig. IV.6 the azimuthal velocity for the three configurations. In the non-rotating cases, the near-bottom velocity is similar across experiments, reaching $\langle u_\theta \rangle \simeq 7$ cm s^{-1} at $z = 1$ cm. The shear is maximum near the wall, where the no-slip condition imposes $u_\theta = v_0$ at $z = 0$. A rough estimate of the friction velocity follows from $u_*^2 \simeq \nu\, \Delta\langle u_\theta \rangle / \Delta z \simeq 1.6 \times 10^{-4}$ m^2 s^{-2}, consistent with independent estimates from the turbulent momentum flux profile (section IV.4.4.2). With this estimate, we also recover the scaling $u_*/v_0 \simeq 1/20$ (Sous et al., 2013).

The main differences between the non-rotating and rotating boundary layers appear in the layer above the near-bottom region. Rotation constrains the vertical extent of the boundary layer, with the azimuthal velocity reaching zero near $z = 6$ cm and a super-geostrophic overshoot visible between 2 and 5 cm, whereas the non-rotating boundary layer extends beyond the observation window. The height at which this super-geostrophic velocity reaches its maximum amplitude is defined as $\delta_{U\,\max}$.

This observation is also apparent in the radial velocity profiles (Fig. IV.7). In the rotating case, the radial velocity is driven primarily by the deflection of the primary geostrophic circulation by the Coriolis force, and the shear is approximately constant throughout the layer, in contrast to the azimuthal component. In the non-rotating case, the agreement between the 1D k-ε model and the experiments is less accurate, which is likely due to the superposition of several dynamical processes contributing to the radial flow at this stage of the spin-up. In particular, the centrifugal acceleration associated with the azimuthal flow drives an outward radial buoyancy flux that depends on the horizontal density gradient between neighbouring columns, which is unavailable

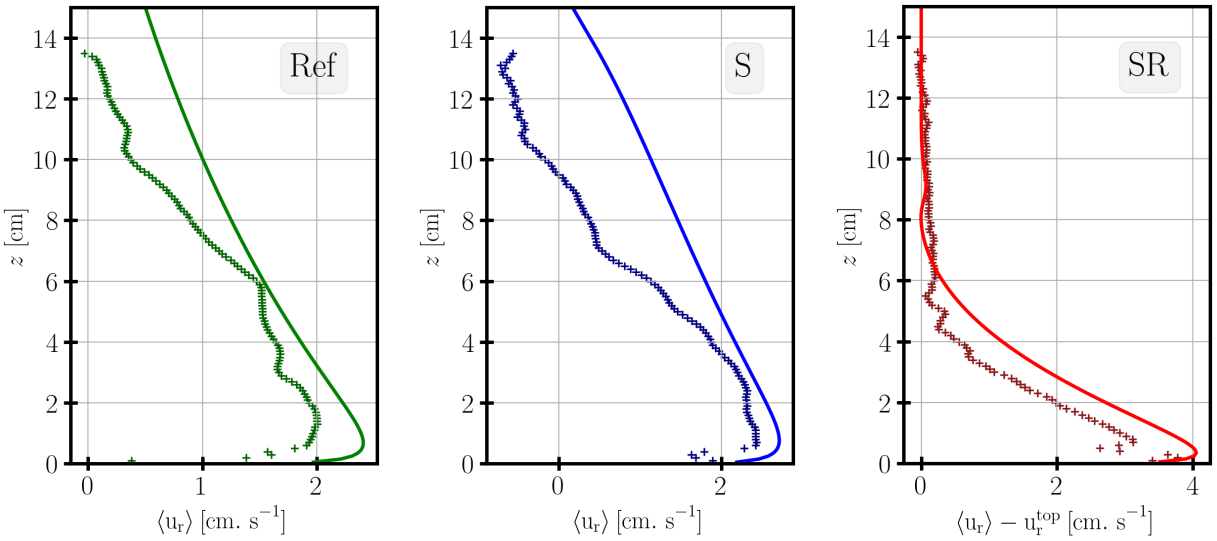

Figure IV.7: Same as figure IV.6 but for the radial velocity at $t = 100$ s

to a single-column model. Additionally, the absence of rotation means that there is no Coriolis restoring force to organize the radial flow, leaving it more sensitive to transient effects such as the initial filling of the tank and large-scale recirculation. As discussed in section IV.3, the centrifugal acceleration cannot be neglected in this configuration. Despite these limitations, the 1D model captures the amplitude and general shape of the vertical profile reasonably well. The similarity between the profiles in EXP-REF and EXP-S confirm that the chosen stratification does not exert a strong control on the dynamics.

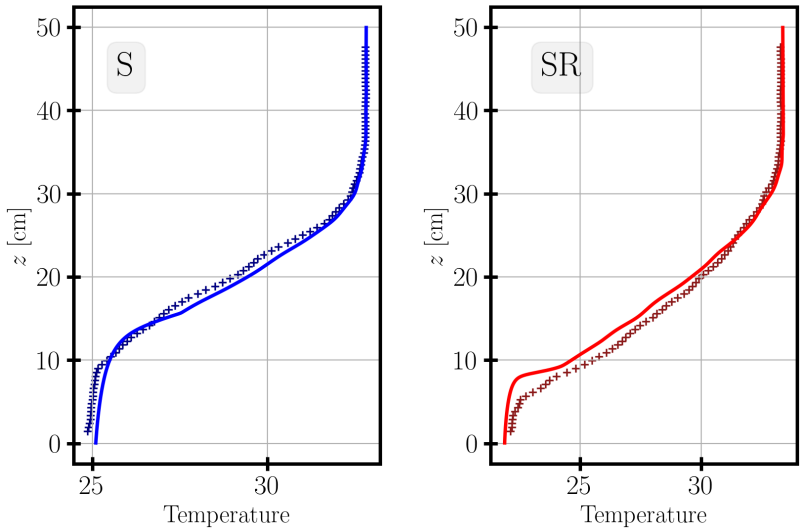

Figure IV.8: Same as figure IV.6 but for the temperature profile at $t = 100$ s. The vertical axis is greater than the one for the velocity data.

The vertical confinement by rotation is confirmed by the temperature profiles (Fig. IV.8). The mixed layer reaches only 6 cm in the rotating case against 13 cm in the non-rotating case despite similar initial stratification. The k-ε model also produces a sharper thermocline interface than observed in the experiments, an effect that is particularly pronounced in the rotating case.

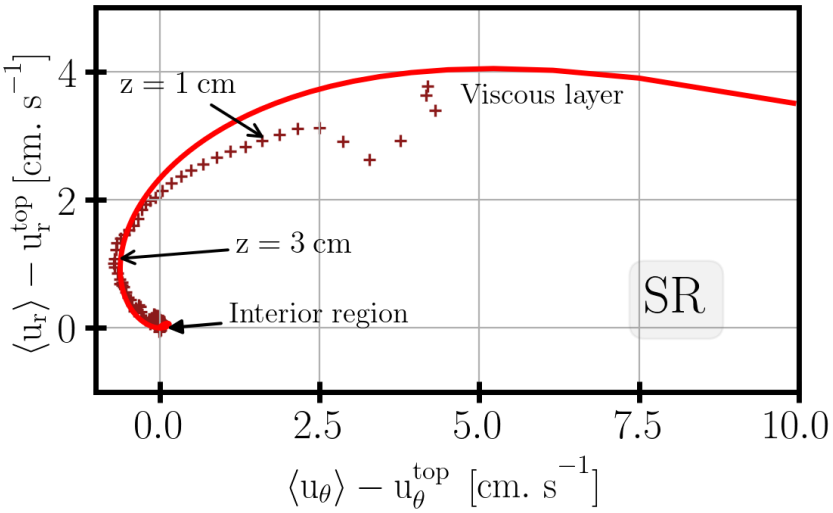

Figure IV.9: Hodograph of the defect velocity at $t = 100$ s showing the Ekman Spiral (radial vs azimuthal velocity components). Different height (in cm) are indicated by black arrow as the two characteristic region – the Interior region and the Viscous layer. In solid line, the vertical profile from k-ε simulation.Experimental data (SR) are plotted with crosses (+).

Figure IV.9 shows the hodograph of the horizontal velocity at $t = 100$ s, in which the Ekman spiral is clearly visible over the observed portion of the water column. The hodograph does not extend to the bottom boundary, so the viscous sublayer and the cross-isobaric angle cannot be directly determined from this plot alone; the missing endpoint corresponds to the no-slip condition at the tank bottom, where $u_r = 0$ and $u_\theta = v_0$. The k-ε model reproduces the overall spiral structure fairly accurately; even if we note that the agreement worsens near the viscous layer, which is neither correctly observed experimentally nor explicitly resolved by the 1D model and which depends, to a certain extent, on a drag coefficient that remains empirical.

IV.4.3 Calibration of the drag coefficient from the cross-isobaric angle

The k-ε model requires a value of the drag coefficient C_f appearing in the bottom boundary condition

$$u_*^2 = C_f |\mathbf{u}(z_1) - \mathbf{u}_{\mathbf{wall}}|^2 . \tag{IV.36}$$

Although C_f can in principle be estimated from the Law of the Wall as $C_f = [\kappa / \ln(z_1/z_0)]^2$ (see Appendix IV.7.2), its value depends logarithmically on the ratio z_1/z_0, which is not precisely known a priori because the roughness length z_0 is sensitive to the surface imperfections of the tank floor and to the Reynolds number. It is therefore preferable to calibrate C_f against an independent physical observable.

A natural calibration target is the cross-isobaric angle α_0, defined as the angle between the bottom wall stress $\boldsymbol{\tau}_b$ with respect to the azimuthal wall velocity (this would correspond to the angle of the wall stress to the geostrophic bulk velocity in a reference frame attached to the floor). In the turbulent Ekman layer, this angle is set by the vertical structure of the boundary layer and provides a sensitive integral measure of the eddy-viscosity distribution near the wall.

The DNS study of Marlatt et al. (2012), performed in Cartesian geometry at $Re_* = 1000$, reports a steady-state cross-isobaric angle $\alpha_0^{\mathrm{DNS}} = 18.6°$. This value constitutes a well-established reference against which the k-ε model can be calibrated. To obtain such a cross-isobaric flow, we find $C_f = 5 \times 10^{-3}$ (see Appendix C). This value of C_f is used in all k-ε simulations presented in this paper.

IV.4.4 Turbulent quantities

IV.4.4.1 Turbulent Kinetic Energy (TKE)

Figure IV.10 shows the vertical profiles of TKE at $t = 100$ s for the three configurations. In all cases, the TKE decreases monotonically with height, with maximum values near the bottom boundary of order 2–4 cm^2 s^{-2}, reflecting the dominance of bottom-generated shear turbulence. The k-ε model reproduces this near-bottom peak and the overall decay with height, though it predicts a sharper vertical gradient than observed experimentally. The experimental profiles exhibit a more gradual decay, with non-negligible TKE persisting throughout the mixed layer, likely due to the presence of large-scale turbulent structures not captured by the 1D closure.

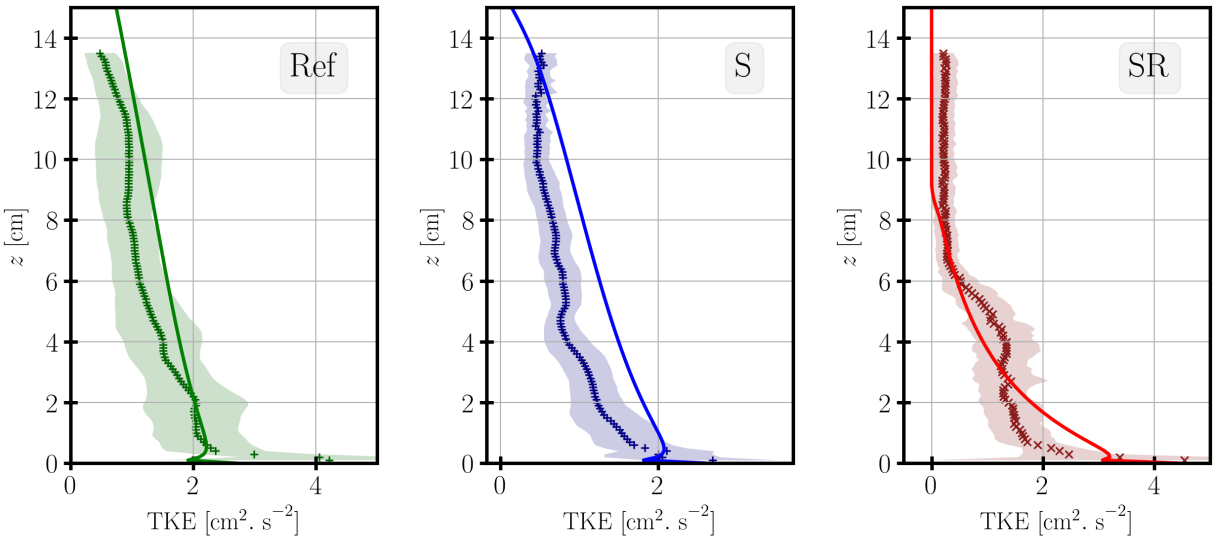

Figure IV.10: Vertical profiles of TKE at $t = 100$ s. Experimental data, marked by $\times$ are averaged, for each height, over a 10 s,temporal window. The shaded interval represent the variance regarding this averaging. In solid line, the vertical profile from k-ε simulation. Left: Experiment without rotation-without stratification (case REF). Center: Experiment without rotation-with stratification (case S). Right: Experiment with rotation-with stratification (case SR).

In the non-rotating unstratified case (EXP-REF, left panel), the TKE remains significant up to the top of the observation window, consistent with the absence of any mechanism limiting the vertical extent of turbulence. In the rotating stratified case (EXP-SR, right panel), the TKE drops more sharply above $z \approx 6$ cm, consistent with the rotational confinement of the boundary layer observed in the velocity profiles. The k-ε model captures this confinement with a slight overestimate but represents well the near-bottom TKE relative to the measurements.

Note that the shaded area indicates the associated standard deviation of the sliding mean over a 5 s interval. This deviation is calculated at each altitude and, as the observed field moves faster than the turbulence decorrelation time, this measurement is not the deviation of the turbulent fluctuation itself, but rather the estimate of the variance of the statistics. Our sliding time average lacks precision since the mean flow varies on similar time scale as the turbulent fluctuations. To improve the statistics, average on a wider azimuthal range would be needed, or an ensemble average on several experiments. Since EXP-REF and EXP-S are very similar, they provide a crude estimate of this ensemble average.

IV.4.4.2 Vertical Reynolds stress

Figure IV.11 shows the vertical profiles of the azimuthal turbulent momentum flux $\langle u'_\theta u'_z \rangle$ for the three configurations at $t = 100$ s.

In the non-rotating cases (left and middle panels), the flux increases from zero at the bottom boundary, reaches a broad maximum of approximately 0.4–0.5 cm^2 s^{-2} near the bottom of the observation window, and decays linearly throughout the mixed layer. This quasi-linear profile is consistent with the transient momentum balance $\partial_t \langle u_\theta \rangle \approx \partial_z \langle u'_\theta u'_z \rangle$: in the absence of a mean pressure gradient, the divergence of the turbulent flux drives the local acceleration of the mean flow. We use the extrapolation of this linear profile to get the value of $u_* = 0.7$ cm s^{-1}. The k-ε model reproduces both the amplitude and the shape of the profile well in both non-rotating cases, confirming that the eddy-viscosity closure correctly represents the vertical transport of azimuthal momentum in this regime.

In the rotating stratified case (right panel), the turbulent flux is confined below $z \approx 6$ cm, consistent with the rotational suppression of the boundary layer depth observed in the mean velocity profiles (Fig. IV.6) and the mixed-layer thickness (Fig. IV.8). The flux peaks close to the bottom boundary and decays rapidly with height, reflecting the concentration of shear production within the Ekman layer. Above the layer, the flux drops to near zero, indicating that turbulent momentum transport is effectively shut off by the combined effect of rotation and stratification. The k-ε model captures this confinement accurately.

The turbulent statistics presented above reflect the same physical picture as the mean profiles: in the non-rotating cases, turbulence fills the entire mixed layer and drives efficient momentum transport, while in the rotating case it is confined within the Ekman layer. This contrast between scalar homogenisation and persistent velocity gradients is physically meaningful: scalars are mixed down-gradient by turbulent diffusion alone, whereas momentum is subject to the additional constraints of rotation and the time-evolving bottom stress. The following section examines how these dynamics evolve in time.

IV.5 Transient evolution of the turbulent Ekman Layer

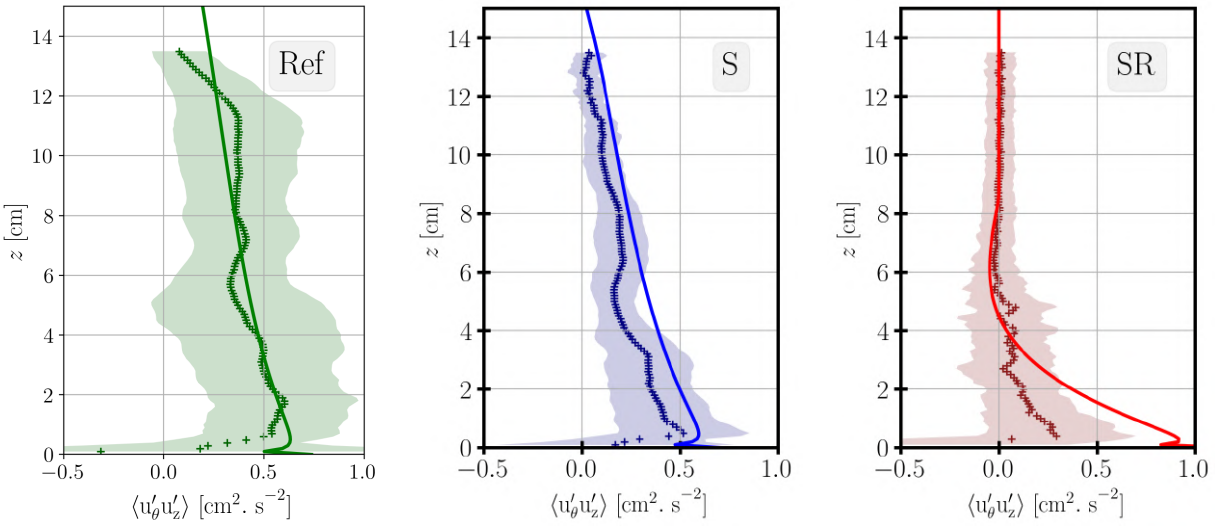

Figure IV.11: Same as figure IV.10 but for the vertical turbulent momentum flux $\langle u'_\theta u'_z \rangle$.

IV.5.1 Bulk Spin-up adjustment

Figure IV.12 shows a time series of the azimuthal velocity, averaged over the uppermost centimetre of the vertical profile u_θ^{top}. This quantity serves as a proxy for the interior geostrophic velocity noted v_∞ in section IV.4. In the fluid frame, it increases monotonically toward the platform velocity v_0 as bottom friction spins up the interior flow. The dashed line shows the friction law (Eq. IV.34), which provides a good fit to the observed decay, yielding $C_b \simeq 2.5 \times 10^{-3}$. Notably, both the rotating (EXP-SR) and non-rotating (EXP-S) cases follow the same friction law, indicating that the spin-up rate and hence C_b are insensitive to background rotation, consistent with the log-layer scaling of the bottom stress. The difference between C_f and C_b is expected: C_f is defined with respect to the near-wall velocity at z_1, which is smaller than the depth-averaged velocity used in the bulk formulation, so that $C_f > C_b$ is consistent with the Law of the Wall. The rotating case shows stronger low-frequency variability, likely due to large-scale structures generated during the filling process in rotation.

IV.5.2 Evolution of the vertical velocity profile

Figure IV.13a shows the temporal evolution of the displacement thickness δ_1 for two non-rotating cases: unstratified (EXP-REF) and weakly stratified (EXP-S). The growth is identical for both cases and follows a linear trend $\delta_1 \propto t$, as expected from momentum conservation in the absence of rotation (see Eq. IV.14). The fit of experimental data with this linear evolution yields $C_\delta = 10^{-3}$, which corresponds to a ratio $u_*/v_0 \sim 1/30$. This value is smaller than the friction coefficient $C_b \simeq 2.5\ 10^{-3}$ previously obtained for the bulk spin-up over longer times. The value of C_δ is also about twice smaller than the corresponding result of Kozul et al. (2016) from DNS of a temporally evolving turbulent boundary layer. This reflects the fact that both friction and turbulence require some time to become fully established after the impulsive forcing. Based on the experimental curves, this transition phase lasts approximately 20 s. By contrast an initial

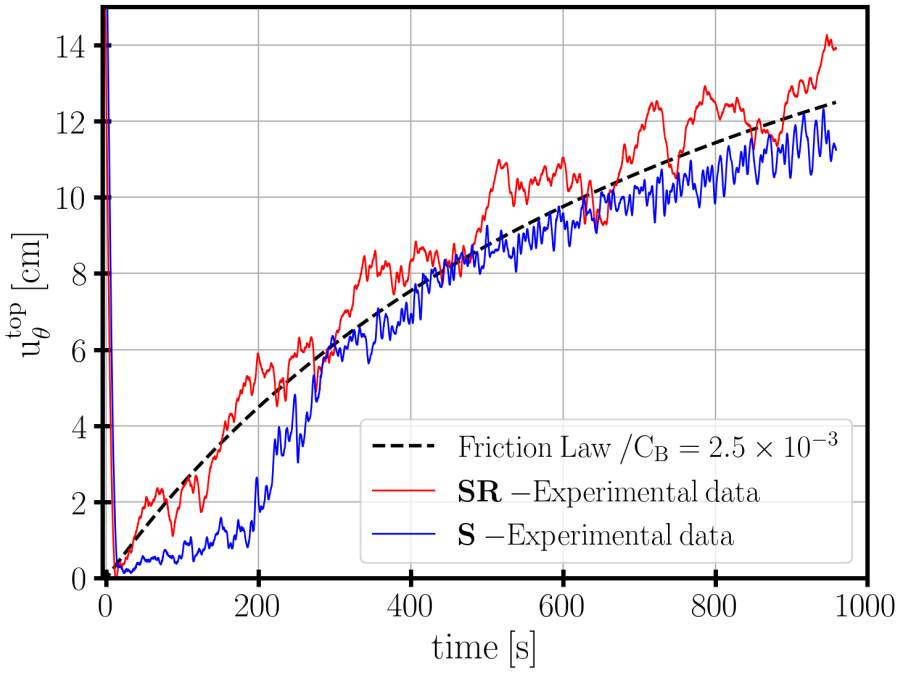

Figure IV.12: Time series of interior velocity for Spin-up case with (in red) and without (in blue) initial background rotation. The dashed black line correspond to the friction law given in Eq. (IV.34). The interior velocity $\langle u_\theta^{top} \rangle$ is defined by average between 13 and 14 cm above the bottom boundary – the last cm below the upper boundary of the observation window.

turbulence level is introduced in the DNS of Kozul et al. (2016), reproducing the effect of a trip wire often used to trigger turbulence in boundary layer studies.

The k-ε model closely follows the experimental measurements. The saturation observed at late times ($t \gtrsim 80$ s) occurs when the boundary layer extends beyond the PIV window, which is the upper limit of the integral. The other reason is also that at this time, the boundary layer begins to feel the effect of rotation and therefore its growth tends to be inhibited, as we will observe in Fig IV.14.

Note that δ_1 is a low indicator of the boundary layer thickness. An alternative indicator is the height δ_{99} at which the mean velocity reaches 99% of the outer velocity. This characterises roughly the layer with active turbulence. According to the DNS of Kozul et al. (2016), $\delta_1/\delta_{99} = C_1 u_*/v_0$ with $C_1 \simeq 4$, which would yield $\delta_{99} \simeq 6\delta_1$. We cannot reliably measure δ_{99} because of limited measurement precision, but we measure δ_{95} at which the mean velocity reaches 95% of the outer velocity. We find typically $\delta_{95} \simeq 5\delta_1$, in agreement with the experiments with a rotating disk of Imayama et al. (2014), who found $\delta_1 = 0.19\ \delta_{95}$.

We also determine the layer thickness by dye concentration, taking the boundary at the position with maximum gradient of the mean concentration in Fig. IV.5). This yields a thickness $\simeq 6\delta_1$, as visible in Fig. IV.13b. The dye is injected before the experiment through the tank floor as a thin layer of water at temperature 20^{o}C, in a warmer water above at temperature 22^{o}C. After some initial mixing it results in a ~ 5 cm thick layer of fluorescent fluid. The corresponding density stratification is wiped out by turbulence once the spin-up is started, so that mixing

occurs as a passive scalar. A virtually linear increase from 5 cm to 12.5 cm is observed within 110 s. Beyond this point, once again, the observation is limited by the height of the observation window.

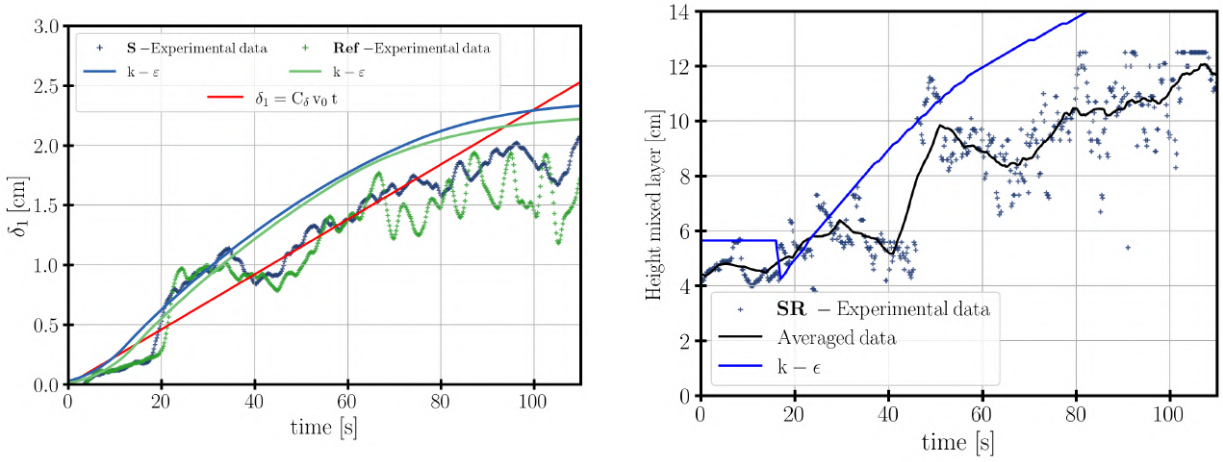

Figure IV.13: Left: Time evolution of the displacement thickness δ_1 (defined in Eq. IV.13). Two non-rotating configuration (case Ref and S) are display with + markers and compared with their associated k-ε simulations (in dashed line). The red solid line show the linear fit for $\delta_1 \propto t$ with $C_\delta = 10^{-3}$, and $v_0 = 23.5$ cm .s^{-1}. Right: Time evolution of the height of the mixed layer revealed by the maximum gradient of dye concentration for the Ref case. The thick black line is the average of the experimental data over a neighbour of 10 s.

IV.5.3 Rotation constraints on boundary layer depth

In the rotating case (EXP-SR) the azimuthal velocity profile is not monotonic, with a maximum at height denoted $\delta_{U\,\max}$ (see Fig. IV.6). This height $\delta_{U\,\max}$ then provides a convenient characterisation of the boundary layer thickness. Figure IV.14(a) shows the temporal evolution of this thickness.

Following the step change in rotation rate at $t = 0$, the boundary layer develops from rest and $\delta_{U\,\max}$ grows rapidly. Within the gray shaded area, we observe a linear growth of $\delta_{U\,\max}$ for $0 \lesssim t \lesssim 30$ s: during this early phase, the flow is dominated by turbulent friction and particle trajectories are not yet significantly deflected by the Coriolis force. The large initial values of $\delta_{U\,\max}$ should not be interpreted as a physical overshoot: at early times, before the Ekman veering spiral is established, the velocity maximum is very weak and the diagnostic is ill-defined. At $t \approx 30$ s ($\approx T_f/2$, i.e. half the inertial period) the Coriolis force becomes dynamically significant and the velocity profile develops a clear maximum, marking the onset of the Ekman veering spiral and the transition to a rotationally controlled regime. We see that $\delta_{U\,\max}$ then approaches the known Ekman depth $0.3\,u_*/f$. The result is in reasonable agreement with the k-ε model, which tends to a constant height $\delta_{U\,\max} = 0.4\,u_*/f$. This value is in agreement with the DNS of Marlatt et al. (2012).

At longer times, the experimental data show a gradual thinning of the boundary layer, unlike the model. This thinning is related to the spin-up process, which is not included in the model.

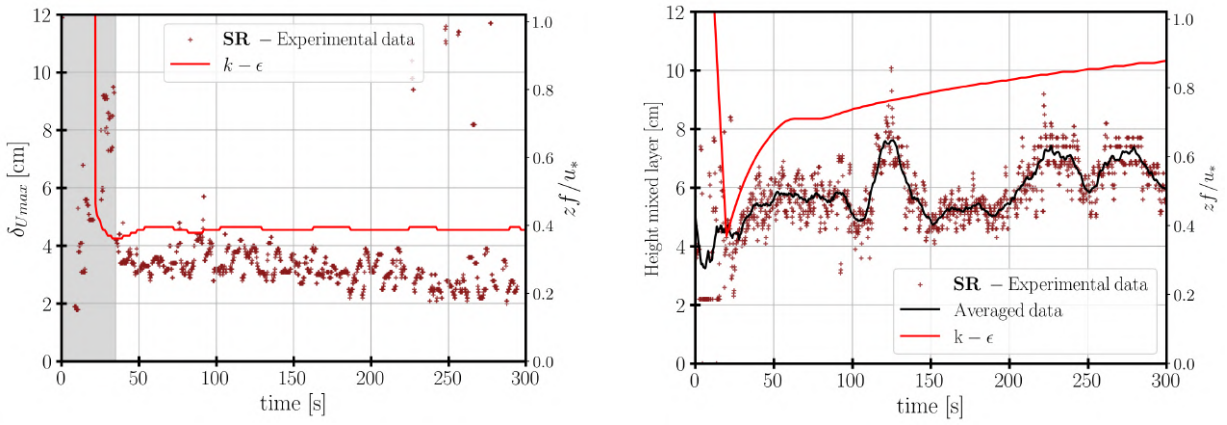

Figure IV.14: Left: Temporal evolution of the height of the maximum azimuthal velocity $\delta_{U_{max}}$. Right: same as figure IV.13b for experiment SR with rotation. For both figure, the experimental data marked with $+$ and from the $k-\varepsilon$ model (in solid line) and the adimensional scale on the right y-axis is given for a constant $u_* = v_0/20$ and a constant $f = 0.1\text{s}^{-1}$.

Two effects are involved. Firstly, the shear stress u_* decreases as the velocity difference between the floor and the bulk decreases. Secondly, the spin-up increases the effective rotation rate of the fluid, increasing the effective Coriolis parameter f.

Figure IV.14b shows the corresponding growth of the boundary layer thickness characterised by the dye concentration. This is the counterpart of Figure IV.13b for a case with rotation. The horizontally inhomogeneous dye injection process does not allow us to observe the very initial growth phase unaffected by rotation. Oscillations observed at later times are attributed to the crossing of large horizontal eddies possibly produced by detachment of the lateral boundary layers. Nevertheless, this figure enables us to demonstrate that the growth of the mixed layer is indeed limited by rotation (and not stratification). It initially stabilises to a value $h \simeq 0.5u_*/f$. The results from the k-ε model is somewhat larger, and a slow thickening persists on longer times. This is due to the diffusion of turbulence away from its shear driven production zone.

We do not observe the further decrease of the thickness observed for $\delta_{U\,\max}$. Indeed the layer of scalar concentration cannot 'un-mix'. Nevertheless, after 300 s, the height reached does not exceed 8 cm.

IV.5.4 Inertial oscillation in a turbulent regime

Due to large-scale turbulence, as well as additional motions not directly related to the Ekman adjustment (instabilities, radial transport, Poincaré waves), it is not feasible to perform a reliable strict quasi-stationary/oscillatory decomposition. However, we are able to characterize the inertial response of the Ekman layer using (i) time series at a fixed depth and (ii) depth-integrated transports, which are less sensitive to small-scale intermittency.

IV.5.4.1 Temporal signature at a given depth

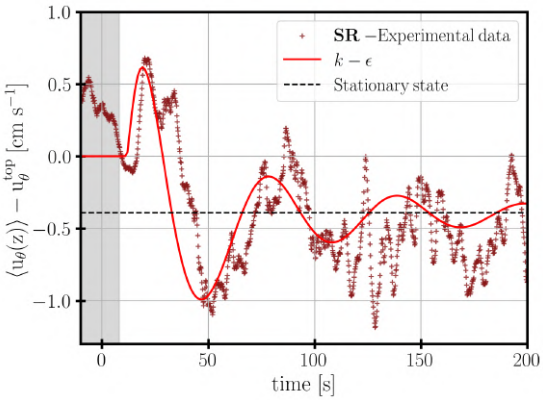

Figure IV.15: Dots: Temporal evolution of the defect velocity at $z = 3$ cm for EXP-SR. Solid line, same but for the k-ε model. The dashed black line indicates the stationary state after the damping of the oscillations in the k-ε model.

Figure IV.15 shows the evolution of the velocity defect ($\langle u_\theta \rangle - u_\theta^{\text{top}}$) at a given altitude ($z = 3$ cm). We observe the onset of an oscillation at the inertial frequency f. Because the observation is not at $z = 0$, the oscillation does not starts at $t = 0$, but start around $t \simeq 10$ s, suggesting that the active layer where the inertial response develops only reaches the observed altitude after a finite time. The shadow zone shows the initial state of the flow previous to the spin-up, we observe the azimuthal velocity is not zero meaning that residual velocities from the fill-up phase are present at the initial state. The progressive decrease of the velocity during this interval coincide with the duration of the incremental angular acceleration. These elements indicate that the structure is passing through the PIV observation window. Since the incremental acceleration is the same as the initial rotation rate ($\Delta\Omega = \Omega_i$), this structure (and possibly other) may be observed at this frequency. These disturbances also appear in figure IV.14b, between 15 s and 30 s, and then again between 110 s and 130 s, as evidenced by a temporary increase in the height of the mixing layer.

The 1D model reproduces the initial excitation mechanism well: both the amplitude and phase of the first oscillation are captured, aside from a systematic phase shift of approximately 10 s. Agreement deteriorates beyond $t \approx 100$ s, where the experimental signal shows intermittent bursts at a frequency close to f, suggesting that additional processes modulate and phase-shift the inertial response. Most strikingly, while the 1D model predicts a clear monotonic decay, the experimental amplitude does not diminish and even tends to grow with time. This amplification rules out instrumental noise and points to a genuine physical mechanism, possibly a resonance with the inertial frequency.

The value of the drag coefficient $C_f = 5 \times 10^{-3}$ controls the damping rate of the inertial oscillations: a larger C_f would extract momentum more efficiently from the oscillating flow and shorten the decay timescale. The agreement between the experimental data and the 1D model is an independent confirmation of the value of C_f.

IV.5.4.2 Temporal signature on horizontal transport

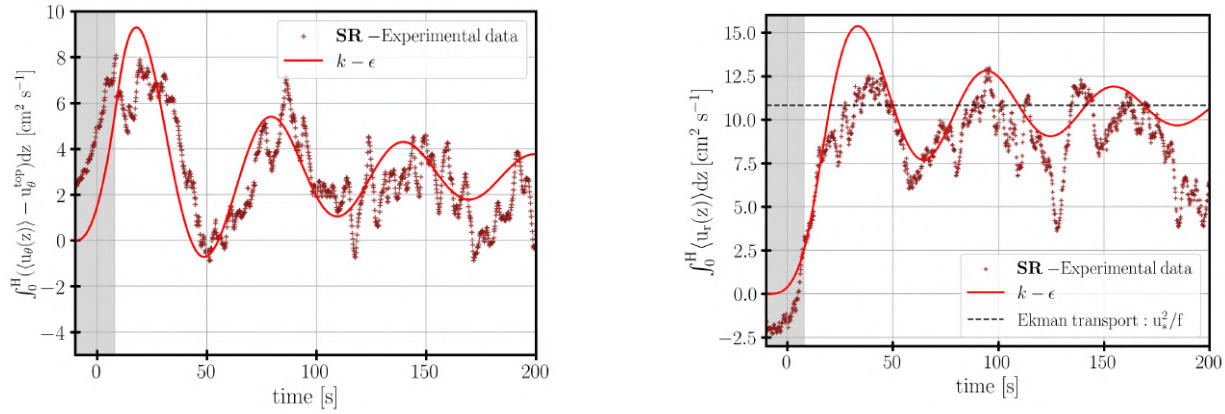

Figure IV.16: The temporal evolution of the transport between the bottom and $z = 6$ cm for the defect azimuthal velocity (left panel) and for the radial velocity (right panel). In both panel , the solid line show the k-ε model. The dashed black line show the theoretical Ekman transport u_*^2/f.

A more robust evaluation of this transient state can be obtained by considering the vertically integrated transport over the height of the boundary layer (Fig. IV.16). This height, estimated at 6 cm in Fig. IV.7 and Fig. IV.6, remains relatively constant over the first 300 seconds in the case EXP-SR. Figure IV.16a (resp. IV.16b) shows the integrated transport between the wall and $z = 6$ cm for the defect azimuthal component (resp. for the radial component).

For the azimuthal defect transport (Figure IV.16a), the inertial oscillation appears more clearly than at a fixed height. We observe an oscillation close to the frequency f, with a decreasing amplitude. Once again, there is good agreement with the 1D model in terms of both amplitude and phase, although the same phase shift of the order of 10 s is observed.

The radial transport (Fig. IV.16b) is more difficult to interpret. Oscillations at the inertial frequency are clearly visible, but other oscillations persist. They appear to be uniform across the full height of the PIV window, rather than confined to the Ekman layer as for the azimuthal component. This contrast is physically meaningful: the azimuthal defect velocity directly reflects the inertial deviation relative to the interior flow, whereas the radial velocity receives significant contributions from non-axisymmetric motions of comparable amplitude, making it more sensitive to large-scale structures that may pre-exist the spin-up.

We can however conclude that the main time scale of the damping is globally well reproduced, even though the experimental envelope remains less regular than in the simulation. The transient response of the flow to an impulsive friction is therefore characterised by the damping of inertial oscillations. This decay controls the duration of the transient regime, the phase relation between radial and azimuthal component and the characteristic time of the steady Ekman layer to be fully developed.

IV.6 Conclusions

In this study, we have investigated the transient dynamics of a fully turbulent Ekman boundary layer through large-scale spin-up experiments conducted on the 13 m Coriolis rotating platform in Grenoble.

An important result is the reliable estimation of the friction velocity in a transient regime through several independent methods: extrapolation of the turbulent momentum flux profile toward the wall, fitting the interior velocity decay to the quadratic friction law (IV.34), and direct comparison with the 1D model. This multi-method approach complements the work of Sous et al. (2013), who estimated the friction velocity under the assumption of a fully established regime, and confirms that $C_b \approx 2.5 \times 10^{-3}$ holds robustly throughout the transient phase.

We also show that unlike the laminar case, where the attenuation rate is set analytically by the viscous Ekman layer, the turbulent experiments show that oscillations persist over several inertial periods, with an amplitude decay slower than predicted by laminar theory. The turbulent experimental case lies between the laminar no-slip and free-slip limits, a behaviour that is directly controlled by the nature of the bottom stress formulation. We show that the physically consistent representation of the bottom stress in a turbulent regime, where the viscous sublayer is not resolved, is neither a strict no-slip nor a free-slip condition, but rather a quadratic drag law of the form $\tau_b = C_f|\mathbf{u}|\mathbf{u}$, with $C_f \approx 5 \times 10^{-3}$. This formulation, in which the stress depends on the velocity of the fluid relative to the moving boundary, proves essential for correctly reproducing both the damping rate of the inertial oscillations and the spin-up rate of the interior flow. Furthermore, despite the slow attenuation of the oscillations, we verified that the steady Ekman spiral and the transient inertial oscillations superpose linearly to a good approximation, even in the turbulent regime.

The k-ε closure is shown to faithfully reproduce the mean velocity profiles, the turbulent kinetic energy, and the Reynolds stress profiles of the turbulent Ekman layer. In particular, the model correctly captures the vertical confinement of the boundary layer by rotation, the amplitude and phase of the inertial oscillations during the first few periods, and the deepening of the mixed layer in the stratified cases. Estimates of the mixing length derived from the measured turbulent correlations, both with and without background rotation, are consistent with the k-ε scaling.

The k-ε closure relies on the Boussinesq eddy-viscosity hypothesis, which assumes that the Reynolds stress tensor is proportional to the mean strain-rate tensor through a single scalar isotropic eddy viscosity ν_t. In a standard shear-driven boundary layer, this assumption is a reasonable first approximation, and the k-ε model has been shown to reproduce mean velocity profiles and TKE budgets with acceptable accuracy (Pope, 2000). However, in a rotating boundary layer such as the Ekman layer, the Coriolis force introduces a preferred direction that breaks the symmetry between the streamwise and cross-stream components of the Reynolds stress tensor (Svensson, 1979). In particular, Direct Numerical Simulations (DNS) studies of the turbulent Ekman layer (Marlatt et al., 2012) have shown that the off-diagonal component $\langle u'v' \rangle$ makes a non-negligible contribution to the turbulent energy budget, a direct consequence

of the rotation-induced coupling between the two horizontal velocity components (Wirth, 2010). This anisotropy is not captured by the standard k-ε model, which uses a single eddy viscosity for all stress components. More sophisticated closures, such as Reynolds Stress Models (RSM), transport individual components of the Reynolds stress tensor and can, in principle, represent this directional asymmetry (see e.g. Launder et al., 1975). In the present study, the good agreement between the k-ε model and the experimental data suggests that, at the Reynolds numbers considered, the isotropic approximation remains adequate for the mean flow and TKE, even if it may underestimate the cross-stream stress.

The present results have direct implications for the parameterization of oceanic boundary layers in numerical models. In coarse-resolution models, the grid spacing far exceeds the thickness of the turbulent boundary layer, so that the bottom boundary condition is not merely a numerical detail but a physical one with large-scale consequences. The choice of bottom friction parameterization directly controls the energy dissipation rate of the large-scale flow (Gallet and Ferrari, 2020; Thompson and Young, 2006). This sensitivity underscores the importance of using a physically motivated drag law rather than an ad hoc boundary condition. Imposing a classical no-slip condition directly on the resolved velocity field is inconsistent with the Law of the Wall at coarse resolution: the molecular processes responsible for arresting the flow at the wall are not represented by the eddy-viscosity parameterizations used in such models, and the resulting dissipation is dominated by the artificial shear imposed to meet the no-slip condition (Deremble et al., 2011). Conversely, a free-slip condition sets the tangential stress to zero, which is equally unphysical for a solid boundary. The physically consistent approach is therefore to supplement a free-slip condition with a drag parameterization of the form $\tau_b = C_f|\mathbf{u}|\mathbf{u}$, in the spirit of the Law of the Wall, with $C_f \approx \mathcal{O}(10^{-3})$ as inferred from this study. Future work should extend these results to strongly stratified regimes, where buoyancy limits the vertical penetration of momentum and the interaction between the Ekman layer and the pycnocline becomes the dominant control on mixed-layer deepening.

IV.7 Appendices

IV.7.1 Statistics of the mean and the turbulent fluctuation field

We consider the 2D ($x - z$) vertical-plane of the laser sheet, which is perpendicular to the radius at its middle section.

The instantaneous velocity field is of dimension $u(x, z, t)$. The average mean flow is obtained with a spatial average (over $N_x = 321$ grid points in the $x-$axis) and a temporal average (3 s, which corresponds to $N_t = 15$ snapshots)

$$\langle u(z,t)\rangle = \int_{x_{min}}^{x_{max}} \int_{t-1.5s}^{t+1.5s} u(z,t)\ dt\ dx.$$

This spatio-temporal average represents the mean flow over $N_x \times N_t = 4815$ profiles.

The turbulent fluctuations are obtained by subtraction, for each time t_i and each $x-$position x_i, the instantaneous velocity field by the spatio-temporal average

$$u'(x_i, z, t_i) = u\,(x_i, z, t_i) - \langle u(z, t_i)\rangle$$

And finally the cross correlation are averaged following the same method than for the mean flow but for a temporal neighbourhood of 10 s ($N_t = 50$ snapshots).

$$\langle\, u'w'(z,t)\,\rangle = \int_{t-5s}^{t+5s}\int_{x_{min}}^{x_{max}} \left(u\,(x_i, z, t_i) - \langle u(z, t_i)\rangle\right) \times \left(w\,(x_i, z, t_i) - \langle w(z, t_i)\rangle\right)\, dx\, dt \tag{IV.37}$$

IV.7.2 Single-column model setting: k-ε closure

We use the open-source GOTM model (General Ocean Turbulence Model) in the single column configuration to numerically solve Equations (IV.12). This model solves the momentum, salt and heat transport equations in a 1D water column, using the k-ε model of turbulence. In this model, the eddy viscosity ν_t and eddy diffusivity of buoyancy ν'_t are locally expressed from the turbulent kinetic energy (TKE) k and the TKE dissipation rate ε as

$$\nu_t = c_\mu \frac{k^2}{\varepsilon} \qquad \nu'_t = c'_\mu \frac{k^2}{\varepsilon}\,. \tag{IV.38}$$

The coefficients c_μ and c'_μ depend on the local stratification and vertical shear. We use Canuto et al. (2001)'s formulation corresponding to the case denoted 'CA' by Burchard and Bolding (2001), and 'CHCD01A' by Umlauf and Burchard (2005). However the stratification effects remain small in our study, so the coefficients c_μ and c'_μ remain close to the value 0.09 classically used in shear flows with uniform density.

The equation for the TKE $k \equiv \overline{\mathbf{u}'^2}/2$ is written as a transport equation

$$\frac{\partial k}{\partial t} + \frac{\partial T_k}{\partial z} = P + B - \varepsilon \tag{IV.39}$$

involving an eddy flux T_k, a production rate P, a conversion rate to potential energy B, and the dissipation rate ε. The eddy flux is modelled by a diffusion law $T_k = -\nu_t \partial k/\partial z$, while P and B can be exactly expressed from the correlations of turbulent fluctuations.

The production P is set by the shear according to

$$P = -\overline{u'w'}\frac{\partial u}{\partial z} - \overline{v'w'}\frac{\partial v}{\partial z} = \nu_t \left|\frac{\partial \mathbf{u}}{\partial z}\right|^2 \tag{IV.40}$$

(the notation $\bar{\cdot}$ and $\cdot'$ denote the standard ensemble averaging and deviation from the ensemble mean respectively).

The conversion rate to potential energy B also represents the vertical flux of buoyancy. Within the eddy diffusivity hypothesis, it is expressed as

$$B = \overline{w'b'} = -\nu'_t \frac{\partial b}{\partial z} \equiv -\nu'_t N^2\,, \tag{IV.41}$$

introducing the local buoyancy frequency $N(z,t)$.

A transport equation with similar form is empirically introduced for ε to close the system,

$$\frac{\partial \varepsilon}{\partial t} + \frac{\partial}{\partial z}\left(\frac{\nu_t}{\sigma_\varepsilon}\frac{\partial \varepsilon}{\partial z}\right) = \frac{\varepsilon}{k}\left(c_{\varepsilon 1}\, P + c_{\varepsilon 3}\, \overline{w'b'} - c_{\varepsilon 2}\, \varepsilon\right) . \tag{IV.42}$$

We use the classical values $\sigma_\varepsilon = 1.3$, $c_{\varepsilon 1} = 1.44$, and $c_{\varepsilon 2} = 1.92$ (Rodi, 1987). The parameter $c_{\varepsilon 3}$ is less consensual, but it is of weak relevance in our case of weak stratification. We use here $c_{\varepsilon 3} = -0.621$ (Burchard and Bolding, 2001).

The boundary condition at $z = 0$ is a key difficulty. At the air-sea interface, the boundary condition is generally set as a given wind stress u_*^2 at the free surface. By contrast the wall velocity is imposed in our experiments, a common situation in the engineering context. Then the turbulent region must be matched with the viscous sub-layer, which requires appropriate modification of the k-ε or the related k-ω model (Speziale et al., 1992).

We here use a simplified approach by considering that our first grid point, at $z = z_1$ is in a log layer. This log-layer is characterized by a constant shear stress u_*^2 with an angle α_0 with respect to the azimuthal direction. In this log layer, the fluid is well mixed, so that $B = 0$ in Eq. (IV.39), and the TKE production locally balances dissipation. Considering that $\nu_t = \kappa u_* z$ (where $\kappa \simeq 0.41$ is the von Karman constant), we get for $z \to 0$,

$$\kappa z \frac{\partial u}{\partial z} \to u_* \sin\alpha_0 \tag{IV.43a}$$

$$\kappa z \frac{\partial v}{\partial z} \to u_* \cos\alpha_0 \tag{IV.43b}$$

$$k = c_\mu^{-1/2} u_*^2 \tag{IV.43c}$$

$$\varepsilon = P = u_*^3/(\kappa z) \tag{IV.43d}$$

This provides an appropriate set of boundary conditions for the k-ε equations if the wall stress is imposed. The velocity then diverges logarithmically,

$$u(z) = \frac{u_*}{\kappa}\sin\alpha_0 \ \ln\left(\frac{z}{z_0}\right) \tag{IV.44a}$$

$$v(z) - v_0 = \frac{u_*}{\kappa}\cos\alpha_0 \ \ln\left(\frac{z}{z_0}\right) \tag{IV.44b}$$

In the case of a smooth wall, the expression $u/u_* = \kappa^{-1}\ln(z u_*/\nu) + 5.2$ is generally used instead (see for instance Pope, 2000). This is recovered from (IV.44) with the expression $z_0 \simeq (\nu/u_*)\ \exp(-5.2\,\kappa) \simeq\ 0.12\,\nu/u_*$.

Let us assume that the first grid point z_1 is in the log layer, so that $z_1 \gg z_0$. There is a velocity shift $\mathbf{u}(z_1) - \mathbf{u_b}$ with respect to the boundary velocity $\mathbf{u_b}$ which is aligned with the shear stress. The square of modulus of this velocity shift is proportional to the shear stress u_*^2,

$$u_*^2 = C_f |\mathbf{u}(z_1) - \mathbf{u_{wall}}|^2 \tag{IV.45}$$

where $C_f = [\kappa/\ln(z_1/z_0)]^2$ according to Eq. (IV.44). This coefficient depends only logarithmically on the shear stress u_* and the grid mesh z_1. In our calculations $z_1 = 0.1$ cm and u_* remains of the order of 1 cm s^{-1}, leading to $C_f = 8.6 \times 10^{-3}$. The value of C_f obtained here is somewhat greater than the reference value of 5×10^{-3} found in this study. This discrepancy may be attributed to the moderate Reynolds number of the present experiments, for which the turbulent boundary layer is not yet fully developed and the logarithmic layer is not firmly established. We find that the results are not sensitive to this choice, thanks to the logarithmic dependency.

The roughness length z_0 depends strongly on the surface type and flow regime. For a smooth wall, the viscous scaling $z_0 \simeq 0.12\,\nu/u_*$ applies, giving $z_0 \sim \mathcal{O}(10^{-5})$ m for typical oceanic friction velocities. In the ocean, the situation is more complex. At the sea surface, the wind-roughened interface introduces an aerodynamic roughness; under moderate winds and in the absence of surface waves, values of $z_0 \approx 0.02$ m are commonly reported (e.g. Charnock, 1955), and wave breaking can significantly enhance z_0 above this baseline (Carlsson et al., 2010). At the seafloor, the roughness is set by sediment grain size and bedform geometry, and is on the order of $z_0 \sim 10^{-3} - 10^{-4}$ m (Weatherly and Martin, 1978). Through the expression $C_f = [\kappa/\ln(z_1/z_0)]^2$, this spread of z_0 values translates into a relatively modest uncertainty in C_f, owing to the logarithmic dependence, consistent with the range $C_f \sim \mathcal{O}(10^{-3})$ inferred from the present study.

Equations (IV.45) and (IV.43c-d) can be used in principle to solve the k-ε equations. However, it has been shown by Burchard and Baumert (1998) that Neumann conditions are numerically more stable. These follow directly by differentiating Eqs. (IV.43c-d) with respect to z:

$$\frac{\partial k}{\partial z} = 0, \tag{IV.46a}$$

$$\frac{\partial \varepsilon}{\partial z} = -\frac{u_*^3}{\kappa (z_1)^2}\,. \tag{IV.46b}$$

The no-flux condition is also used for the temperature.

The simulations are configured to match the laboratory experiments at radius $r_0 = 4.5$ m (the PIV measurement location). The vertical grid spacing is 0.1 cm over a domain extending 50 cm along the z-axis. Simulations run for 600 s with a time step of 0.1 s. The surface stress is imposed as a linear ramp rather than an impulsive condition, in order to reproduce the finite spin-up time of the rotating platform. The origin $t = 0$ is defined as the midpoint of the ramp, where the velocity reaches half its nominal value. We set the Coriolis parameter to $f = 0.1$ s^{-1}, corresponding to the initial rotation rate of the laboratory experiments, and set $f = 0$ in the non-rotating cases. The initial temperature profile used in the 1D simulations are interpolated on the vertical grid of the model from experimental measurement.

IV.7.3 Calibration of the Drag coefficient for the 1D model

The drag coefficient C_f is calibrated by matching the steady-state cross-isobaric angle α_0 predicted by the k-ε model to the DNS reference value of Marlatt et al. (2012). Simulations are

run in Cartesian geometry (without centrifugal acceleration terms) to reproduce the planar configuration of the DNS, and are integrated until inertial oscillations are fully damped so that α_0 reflects only the mean boundary-layer structure. Figure IV.17 shows α_0 as a function of C_f for two vertical grid resolutions. For the fine grid ($z_1 = 0.1$ cm), the DNS reference value $\alpha_0^{\mathrm{DNS}} = 18.56°$ is matched at $C_f \approx 5 \times 10^{-3}$, which is therefore adopted in all k-ε simulations presented in this study. The coarse grid ($z_1 = 0.5$ cm) systematically overestimates α_0 regardless of C_f, confirming that adequate near-wall resolution is required for a reliable calibration.

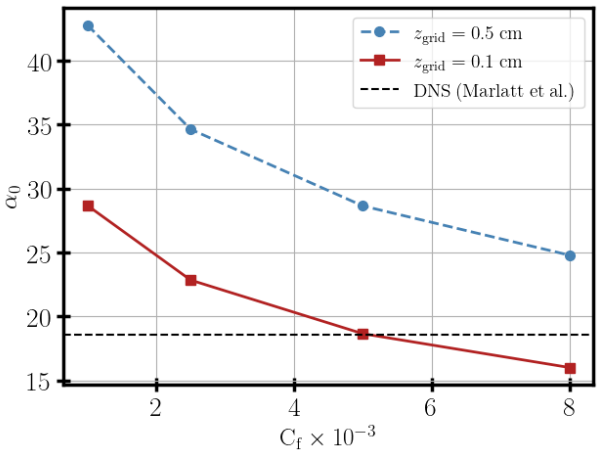

Figure IV.17: Cross-isobar angle measured a the first grid point as a function of the bottom drag coefficient C_f, computed at steady state (inertial oscillation are fully damped) for two vertical grid resolutions: $z_1 = 0.5$ cm (circles, dashed) and $z_1 = 0.1$ cm (squares, solid). Horizontal lines indicate the DNS reference values of reported by Marlatt et al. (2012) (18.56, dashed) for a steady Ekman layer at $Re = 1000$. Centrifugal acceleration terms are excluded from all simulation shown

IV.7.4 Assessment of the single-column approximation

The validity of the single-column framework for axisymmetric geometry, particularly when the Rossby number $Ro \approx 1$, is based on the assumption that the vertical momentum advection terms, associated with Ekman pumping, remain small compared to the centrifugal acceleration terms retained in the model. In order to evaluate this assumption, we compare, based on experimental data (EXP-REF and EXP-SR) at a given height $z = 4$ cm, the amplitudes of the various non-linear terms appearing in equations (IV.12)b and (IV.12)c (Figures IV.18 and IV.19).

In the non-rotating case (EXP-REF), the vertical advection term $w\partial u/\partial z$ is negligible compared to the dominant contribution v^2/r_0, which is several orders of magnitude larger (see the inset in Fig: IV.18). The contribution u^2/r_0, although weaker than v^2/r_0, remains significantly greater than the vertical advection. The same observation applies to the azimuthal equation, where $w\partial v/\partial z$ remains much smaller than $2uv/r_0$

The presence of rotation does not modify this scaling, the vertical advective terms $w\partial u/\partial z$ and $w\partial v/\partial z$ are still several order weaker than the dominant terms v^2/r_0 and the Coriolis terms ($fv,\ fu$). Nevertheless, it should be noted that u^2/r_0 and $w\partial u/\partial z$ become comparable in amplitude here, but in order to maintain consistency with the cases modelled without rotation,

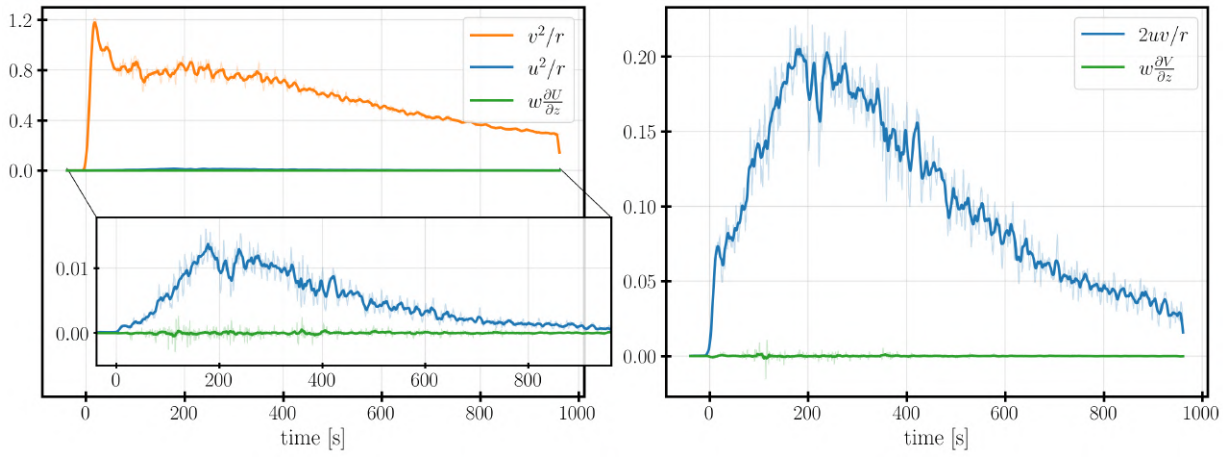

Figure IV.18: Time series of the non-linear terms entering Eq. IV.12, evaluated from the experimental data (EXP-REF) at $z = 4$ cm. Left: radial momentum equation (v^2/r_0, u^2/r_0, and $w\,\partial u/\partial z$). Right: azimuthal momentum equation ($2uv/r_0$ and $w\,\partial v/\partial z$). The inset in the left panel highlights the weaker contributions u^2/r_0 and $w\,\partial u/\partial z$.

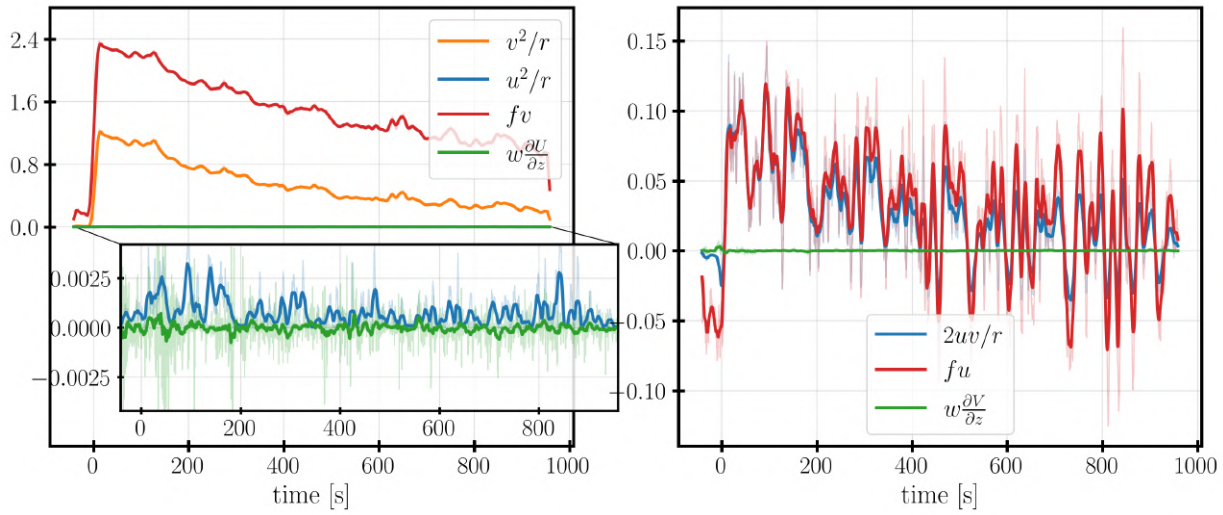

Figure IV.19: Same as Fig:IV.18 but for case SR

we have chosen to retain all the centrifugal acceleration terms in the cases involving initial rotation

Chapter V

Horizontal convection Experiment

Summary of the Chapter

This chapter presents a set of horizontal convection experiments carried out at the Geophysical Fluid Dynamics Laboratory in the Atmospheric, Oceanic and Planetary Physics Department of the University of Oxford in collaboration with P. Read. This work was carried out as part of a two-month academic visit funded by the University of Grenoble Alpes. The aim of this project was to study the onset of turbulence in a horizontal convection configuration, and try new thermistor probes as prototypes on a small tank in order to use it on the Coriolis platform.

Highlights

- Without rotation, the mean circulation is steady and reproduces the laminar solution of Rossby (1965)
- Rotation sets up a geostrophic circulation and triggers an unsteady mesoscale eddy field at the deformation scale
- The domain-integrated kinetic energy grows with the imposed thermal contrast and is redistributed by rotation, enhanced at moderate rotation ($f = 1\ \mathrm{s}^{-1}$), reduced at stronger rotation ($f = 3\ \mathrm{s}^{-1}$).

Contents

V.1 Introduction

The two previous chapters have characterised the wind-driven ocean surface layer. In both chapters, the surface buoyancy flux was zero ($B_0 = 0$), with the dynamics driven exclusively by mechanical shear. In the real ocean, this purely frictional regime is highly idealized. Wind-driven mixing and convective mixing coexist, interact, and compete across a wide range of conditions (as described by Legay et al. (2024)).

In the horizontally uniform forcing configuration, heavy fluid is introduced by the cooling at the surface and drives turbulence as it sinks. This configuration was investigated experimentally in Sec. II.3, through the classical rotating Rayleigh–Bénard problem in an upside-down configuration. Instead of cooling the surface, a uniformly heated bottom boundary drives convective plumes that progressively erode the background stratification.

However, this buoyancy-driven mechanism has important limitations when considered at a global scale. As first recognized by Sandström, understanding thermally driven circulations requires considering spatially non-uniform buoyancy forcing. The present chapter investigates such a configuration experimentally, as represented in Fig. V.1, with a radial temperature gradient imposed at the bottom of a cylindrical tank. We investigate how a non-uniform buoyancy forcing sets a rotating fluid in motion, and how rotation modifies the resulting circulation, from a steady laminar state to an unsteady eddying regime.

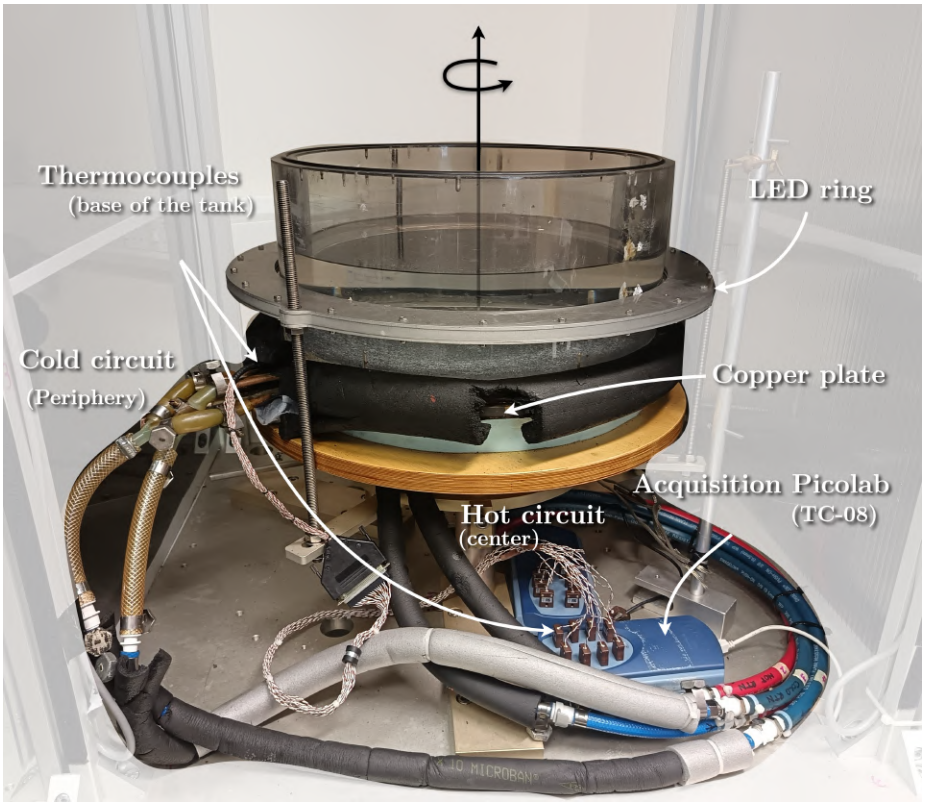

Figure V.1: Picture of the tank mounted on the copper plate differentially heated form a cold and a hot circuit. The imposed temperature is measured using Picolab thermocouples. The illumination, in a horizontal plane is produced by LED embedded in an aluminium ring.

Horizontal convection[1] refers to the flow resulting from a non-uniform buoyancy forcing applied at a single geopotential level within a closed domain. In the ocean, the thermal forcing occurs mostly at the surface (with the exception of geothermal heating), where temperature contrasts between the equator and the poles generate horizontal density gradients (Stommel, 1962; Rossby, 1965; Hughes and Griffiths, 2008). Similar mechanisms also operate at smaller scales, such as in subglacial flows, where pressure contrasts due to the ice cover sustain circulation along the base of ice shelves Couston et al. (2022), as well as in estuaries Burchard (2009). More generally, any system in which a horizontal buoyancy gradient is maintained is likely to develop horizontal convective circulation.

Although they are similar from a conceptual point of view, a distinction must be made between horizontal convection and lateral convection. The latter involves forced heating and cooling applied to opposing vertical walls; experimentally, this configuration is favoured for the study of atmospheric circulation and baroclinic instability (Hide, 1958; Scolan and Read, 2017; Read et al., 2014). The main difference between the two lies in the energy aspect; to sustain circulation, it is necessary to supply potential energy to the system, which will be converted into kinetic energy; therefore, fundamentally, the heating source must be located lower than the

[1]In the oceanographic context, we also refer to "Sideways convection" (see Vallis (2017) for a full description). Given that a distinction is made between experimental set-ups involving horizontal convection and lateral convection, we prefer the term 'horizontal convection'

cooling source. However, whilst in lateral convection the forcing extends over the entire height of the walls—allowing the buoyancy flow to supply potential energy—horizontal convection does not permit this, as the buoyancy source and sink are at the same level. This energetic constraint is known as Sandström's postulate[2].

Paparella and Young (2002) have formalised this postulate by bounding the volume-averaged kinetic-energy dissipation,

$$\varepsilon = \langle w\, b \rangle \leq \frac{\kappa\, \Delta b}{H}, \tag{V.1}$$

where Δb is the maximum buoyancy difference at the boundary and H the fluid depth. The power injected by buoyancy is thus bounded by to the diffusivity κ and vanishes in the limit $(\nu, \kappa) \to 0$ at fixed Prandtl number ($Pr \equiv \nu/\kappa$). This means that for a vanishing viscosity, the dissipation also goes to zero. This goes against a fundamental property of turbulent flow, namely that energy dissipation at high Reynolds numbers is not a function of viscosity Miller et al. (2024). This bound concerns the volume-averaged energetics only, and does not exclude, at large Rayleigh number, turbulence confined to the boundary layer (Gayen et al., 2014). The role of the boundary layer is of primary importance in this problem. Although the energetic constrain V.1 is unchanged and the singular limit is the same, we expect that with rotation this dynamics may be different.

In fact, (i) the structure of the boundary layer is affected by rotation, (ii) outside the Ekman layers, the flow becomes geostrophic: the horizontal pressure gradient induced by the buoyancy field is balanced by the Coriolis force, and the thermal wind,

$$\frac{\partial \mathbf{u_h}}{\partial z} = \frac{g\alpha}{f} \mathbf{e_z} \times \nabla_\mathbf{h} T\,, \tag{V.2}$$

describes the formation of a jet transverse to the temperature gradient. $\mathbf{u_h}$ stands for horizontal velocity, $\mathbf{e_z}$ the vertical axis and $\nabla_\mathbf{h}$ for horizontal gradient. In particular, the inclination of the isopycnals forms a reservoir of potential energy (APE) (Vreugdenhil et al., 2017; Gayen and Griffiths, 2022). Under certain conditions, this APE is subsequently released by baroclinic instability, which creates a mesoscale eddy field and renders the flow unsteady. This transition to an unsteady, eddying regime was demonstrated experimentally by Park and Whitehead (1999), who observed the development of baroclinic eddies in a rotating horizontal convection configuration.

Building on these observations, we use particle image velocimetry (PIV) to resolve the horizontal velocity field quantitatively, in a rotating cylindrical tank with a radial temperature gradient imposed at the base. This is the same configuration as the rotating annulus of Hignett et al. (1981), at moderate Rayleigh number ($Ra \sim 10^8$). We thereby address the central question of this chapter: **How does rotation affect the onset of mesoscale turbulence in horizontal convection, as the imposed bottom temperature difference increases?** After introducing

[2]The reader may be more familiar with the term Sandström "theorem", however this terminology is somewhat misleading. As pointed out by Coman et al. (2006), Sandström originally formulated it as a postulate rather than a theorem, and the later interpretation as a theorem relied on an incorrect analogy with the thermodynamics of a Carnot cycle.

the set-up, control parameters and flow regimes, the results first describe the multi-scale structure of the flow, namely the mean circulation, the synoptic eddies field and the high-frequency fluctuations, then turn to the role of rotation in the kinetic-energy budget.

V.2 Theory of the horizontal convection

We consider a tank of diameter L where a non uniform thermal forcing, characterised by the temperature difference $\Delta T = T_{hot} - T_{cold}$, is applied at the bottom. With α the thermal expansion coefficient, ν the kinematic viscosity and κ the thermal diffusivity, the governing parameters of horizontal convection are

$$Ra = \frac{g\alpha\Delta T L^3}{\nu\kappa}, \qquad Pr = \frac{\nu}{\kappa}, \qquad Ek = \frac{\nu}{fL^2}, \tag{V.3}$$

respectively the temperature-based Rayleigh, Prandtl and the Ekman numbers.

V.2.1 No rotation limit

Horizontal convection is characterised by an asymmetry between the cold and warm regions The seminal work of Rossby (1965) established, through the study of experimental circulation in non-rotating horizontal convection, the essentials of laminar phenomenology. Using a scale analysis, Rossby (1965) showed that the thermal boundary layer has a characteristic thickness

$$\delta_{th} \sim LRa^{-1/5}. \tag{V.4}$$

Heat transport is conveniently characterised by the Nusselt number, based on the imposed buoyancy flux B, which measures the ratio of convective to conductive heat transfer.

$$Nu = \frac{BL}{\kappa g\alpha\Delta T}. \tag{V.5}$$

In this viscous laminar regime, Rossby (1965) found the classical scaling $Nu \sim Ra^{1/5}$, indicating that the overall heat transfer is controlled by the thermal boundary layers: as they become thinner, the conductive heat flux through it increases. It is also convenient to express the forcing in terms of the imposed buoyancy flux through the flux Rayleigh number,

$$Ra_F = Nu\, Ra = \frac{BL^4}{\nu\kappa^2}, \tag{V.6}$$

which is used below to classify the rotating regimes. Although the $1/5$ exponent is robust over a wide range of Rayleigh numbers, it is not universal: transitions to three-dimensional and then turbulent regimes can lead to different scaling laws (Sheard and King, 2011; Shishkina et al., 2016).

V.2.2 Rotating regime

Rotation produces two outcomes. On the one hand, it produces structures aligned with the axis of rotation (Taylors column) and to inhibit vertical motion which tends to maintain the flow in a 2D state. On the other hand, the tilt of the isopycnals constitutes a reservoir of available potential energy (APE). Above a certain threshold, this energy is released by baroclinic instability, which is a 3D mechanism, generating a field of mesoscale vortices and rendering the flow unsteady. It is the combination of these two effects, controlled by the rotation rate and the intensity of the forcing (ΔT), that determines the flow regime.

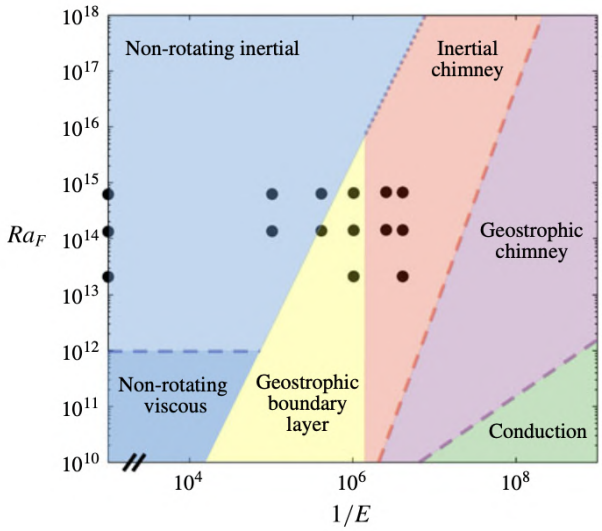

Figure V.2: Regime diagram for rotating horizontal convection, Figure from Vreugdenhil et al. (2017). $E = E_k$ with our notation.

To classify these regimes, we draw on the analysis in Vreugdenhil et al. (2017), which uses the convective Rossby number $Ro_* = B^{1/2}/(f^{3/2}L)$ as a control parameter. Three main regimes emerge depending on the rotation[3]:

- Non-rotating regime: rotation is negligible and the flow follows Rossby phenomenology ($Nu \sim Ra^{1/5}$);
- Geostrophic boundary layer: the Coriolis force constrains cross-isotherm motion in the boundary layer, reducing the overturning circulation and the associated heat transport. For $Ro_* \leq 0.1$, the mean circulation organises itself into gyres on a basin-wide scale.
- Chimney regime: convection is concentrated in vertical plumes (analogous to deep-ocean convection chimneys), and heat transport becomes essentially independent of rotation.

Note that this classification is a refinement of that proposed by Hignett et al. (1981), who were the first to characterise these regimes in a rotating annulus. By considering the ratio

[3]A more complete picture of these regimes can be drawn within the $(Ra - Ek)$ plane; see Fig. V.2

(squared) of the thicknesses of the thermal boundary layer $\delta_{th} \sim L\, Ra^{-1/5}$ and the Ekman layer $\delta_{Ek} \sim L\, Ek^{1/2}$, Hignett et al. (1981) proposed a dimensionless number

$$Q = \left(\frac{\delta_{th}}{\delta_{Ek}}\right)^2 = Ra^{-2/5}\, Ek^{-1}, \tag{V.7}$$

which measures the competition between the effects of rotation and horizontal convection. For their experiments, they identified a critical threshold $Q \simeq 3.4$ beyond which the axisymmetric flow yields to baroclinic waves and vortices. The convective Rossby number is expressed in terms of Q as $Ro_* = Nu^{1/2}\, Pr^{-1}\, Ra^{-1/10}\, Q^{-3/2}$.

This chapter focuses on the unsteady regime triggered by rotation, which lies at the lower edge of the 'geostrophic boundary layer' region in the diagram V.2.

V.3 Experimental Methods

V.3.1 Experimental configuration

We use a cylindrical tank, with a radius of $R = 20$ cm and a height of $H_{max} = 20$ cm (see Fig. V.1 and Fig. V.3). The tank walls are made of transparent Plexiglas, which allows for slice illumination provided by LEDs arranged in an aluminium ring.

The tank is mounted on a turntable that allows the rotation to be adjusted with a precision of ± 0.01 rad·s^{-1} and a maximum rotation of 2 rad·s^{-1}. Rotation is possible in both directions, but throughout the experiments we rotated the device counter-clockwise ($f > 0$).

V.3.1.1 Heating device

The bottom of the tank consists of a 1.3 cm thick copper plate, tinted black, in which we have two pipe circuits. Each of these pipes is supplied by heated or cooled refrigerant controlled by a Huber Unichiller unit, allowing for distinct temperatures with a stability of ± 0.1 °C. The first circuit is positioned at the periphery of the tank, while the second is arranged in a spiral at the centre of the copper plate. This arrangement allows for the creation of two distinct zones: the annular periphery and the core at the centre. When a cold command is applied to one circuit and a hot command to the other, this setup allows for heating in the form of a radial temperature gradient on the bottom of the tank. Two thermal configurations are studied:

- **CC** (cold-core, Fig. V.4, upper right): cold centre, warm periphery. Cold downwelling convection is localised at the centre; warm upwelling is peripheral. Most of the analysis in this chapter will adopt this configuration.
- **WC** (Warm-core, Fig. V.4, upper left): warm centre, cold periphery. Reversed situation.

The bottom temperature is measured using Type T thermocouples connected to a Picolog TC-08 data logger (accuracy of ±0.2°C). Using observations with an infrared camera, we verified that the setpoint temperature imposed on the heating units was consistent with the surface temperature at the bottom of the tank. The images captured by the infrared camera for both configurations are shown in Fig. V.4. The temperature plot as a function of radius also allows us to determine the shape of the imposed radial temperature gradient. We observe that the central region is temperature-homogeneous over the first 5 cm, and then the gradient is linear, regardless of the configuration.

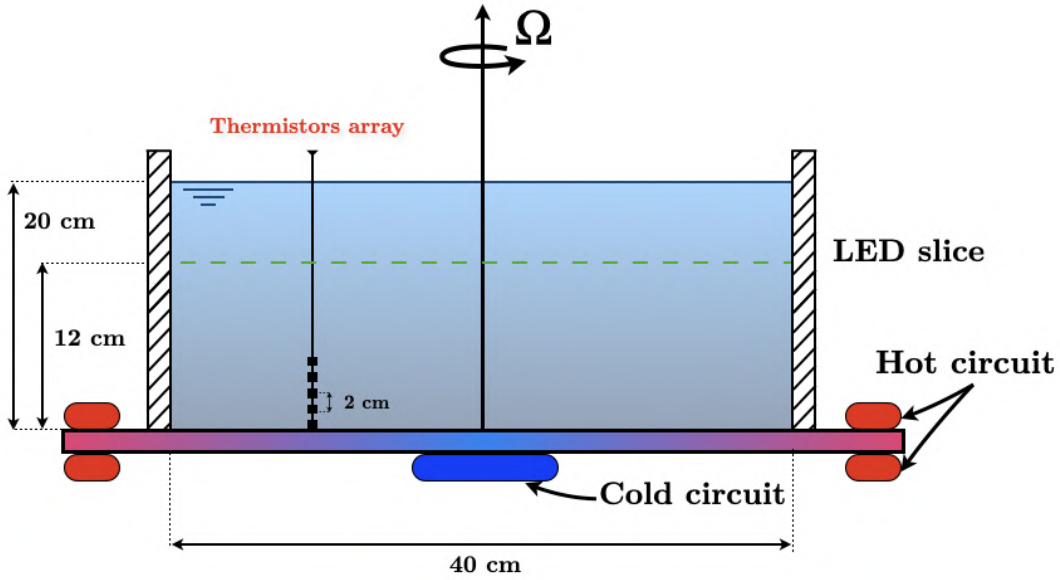

Figure V.3: Scheme of the differential bottom heating tank

In addition, a temperature-measuring device based on thermistors immersed in the fluid was tested, but the results were inconclusive[4] The objective was to measure local temperature fluctuations within a PIV slice. Thermistors were preferred for this application because temperature fluctuations measured by thermocouples result in particularly small voltage variations. This limitation is exacerbated when the cables connecting the thermocouples to the acquisition card are long, as is the case on the Coriolis platform. Thermocouples remain, however, well-suited for measuring average temperature over long periods. The areas occupied by the thermistor mounts appear as missing data in the various figures presented.

V.3.1.2 Measurement techniques

Velocity is measured using PIV in the horizontal plane illuminated by the LED ring positioned at $z = 20$ cm for all experiments, the total depth of water is set at $H = 18$ cm. The LED slice

[4]These probes were originally designed to operate in air. Their use in an aqueous environment therefore required the insulation of the conductive parts. This insulation proved to be incomplete, leading to corrosion and eventually the failure of the probes. Later, for the second campaign conducted on Coriolis, the application of an insulating varnish resolved this issue. The device could then be used to measure local temperature fluctuations within a PIV slice.

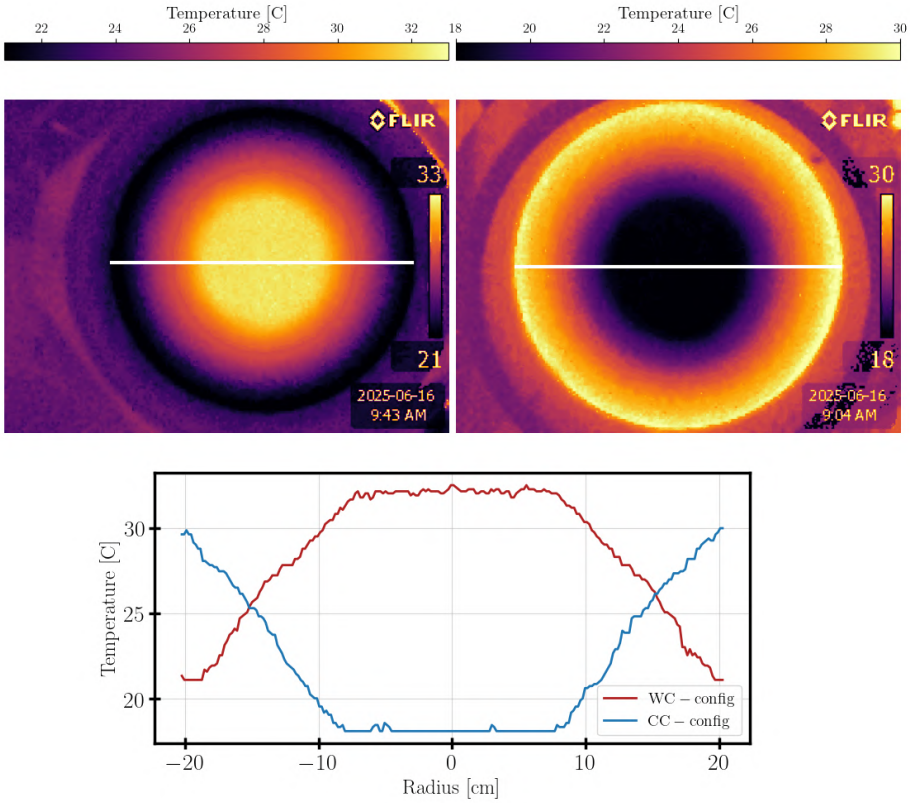

Figure V.4: Infrared top view image of the bottom of the plate WC configuration (left) and the CC configuration (right), the colorbars show the temperature. In the lower panel is plotted the temperature of the transect represented by the white line on the IR images.

illuminates particles similar to those used on the Coriolis platform. The observation was performed with an IDS camera (color - 12-bit - 3864×2176 pixels) equipped with a lens (10 mm, $f/1.9$) mounted on the turntable structure. The post-processing and PIV algorithms used are the same as those used for Coriolis data processing using the UVMAT software (LEGI, Grenoble).

From the raw fields $u(x, y, t)$ and $v(x, y, t)$, we define several dynamic scales (see Sec. V.4.1) depending on the temporal window used for the average.

V.3.2 Description of the experiments

The fluid used in the experiments is saline solution adjusted to a density of 1048 g/L (to match the buoyancy of the particles used for PIV). Two control parameters are considered: the rotation f and the temperature difference ΔT imposed at the bottom (from 1.2 to 7.9 °C). For each rotation, ΔT is varied across this range. The **CC** (cold core) configuration is the reference case analysed in this chapter; the **WC** (warm core) configuration, which is the inverse, is only carried out for a few cases (EXP14–EXP15 at $f = 0$, EXP22 at $f = 1$) in order to verify the symmetry of the forcing. Three groups are thus distinguished in Table V.1, indexed by f: the non-rotating cases (EXP08–EXP15), which provide the laminar reference; the cases with moderate rotation (EXP17–EXP22); and the cases with strong rotation (EXP23–EXP26). Within each group, varying

EXP	Designation	ΔT [°C]	T_{cold} [°C]	T_{Warm} [°C]	f [s^{-1}]
EXP08	$CC.f0.\Delta T2$	1.8	20.6	22.2	0
EXP09	$CC.f0.\Delta T3$	3.1	20.4	23.5	0
EXP10	$CC.f0.\Delta T4$	3.8	20.6	24.2	0
EXP12	$CC.f0.\Delta T6$	5.8	19.7	25.5	0
EXP13	$CC.f0.\Delta T8$	7.9	18.7	26.6	0
EXP14	$WC.f0.\Delta T2$	1.7	20.6	22.3	0
EXP15	$WC.f0.\Delta T3$	3.5	20.2	23.7	0
EXP17	$CC.f1.\Delta T2$	1.7	20.7	22.4	1
EXP18	$CC.f1.\Delta T3$	3.3	20.4	23.7	1
EXP19	$CC.f1.\Delta T4$	4.0	20.5	24.5	1
EXP20	$CC.f1.\Delta T5$	5.7	19.9	25.6	1
EXP21	$CC.f1.\Delta T7$	7.8	19.0	26.8	1
EXP22	$WC.f1.\Delta T7$	7.8	18.7	26.5	1
EXP23	$CC.f3.\Delta T2$	1.2	20.8	22.2	3
EXP24	$CC.f3.\Delta T3$	3.3	20.5	23.8	3
EXP25	$CC.f3.\Delta T5$	5.6	20.0	25.6	3
EXP26	$CC.f3.\Delta T8$	7.7	19.3	27.0	3

Table V.1: List of experiments and their control parameters: temperature contrast ΔT , warm- and cold-bottom temperatures T_{warm}, T_{cold}, and the Coriolis parameter f.

Parameter	Pr	ΔT	Ra	Ra_F	$1/Ek$	Ro_*
range	9	$1.7 - 7.8$	2×10^8 -10^9	10^{10} - 7×10^{10}	4×10^4 - 10^5	10^{-3} -7×10^{-4}

Table V.2: Ranges of the control and derived parameters spanned by the experiments.

ΔT allows us to observe the flow's response to an increasing thermal forcing.

The parameters for our experiments, expressed in the notation of Vreugdenhil et al. (2017), are summarised in Table V.2. The convective Rossby number is of order $Ro_* \sim 10^{-3}$, whilst the flux Rayleigh number remains moderate ($Ra_F \sim 10^{10}$). With regard to the classification established in Sec. V.2 (Fig. V.2), our experiments therefore fall within the geostrophic boundary layer regime, at the edge of the diagram, precisely the region where the stabilising or destabilising nature of the rotation remains most uncertain.

V.4 Results

V.4.1 Temporal analysis and scale decomposition

Data acquisition was performed once the temperatures at the bottom of the tank had stabilized in the steady regime. This is achieved in average in $t \approx 20$ min. The velocity fields were then recorded for a total duration of 600 s with a time interval of 1 s. Under these conditions, the thermal boundary condition can be considered as steady during the acquisition. However, we do

not have measurements that allow us to directly verify that the temperature gradients within the water column, in both the vertical and radial directions, have themselves reached a steady state. Before presenting the diagnostics based on the average fields, it is therefore useful to examine the temporal variation of the flow using a local velocity signal. Fig. V.5 presents a typical time series of the velocity components u and v, averaged over a surface area of approximately $1\ \mathrm{cm}^2$, at the tank centre and $z = 12$ cm.

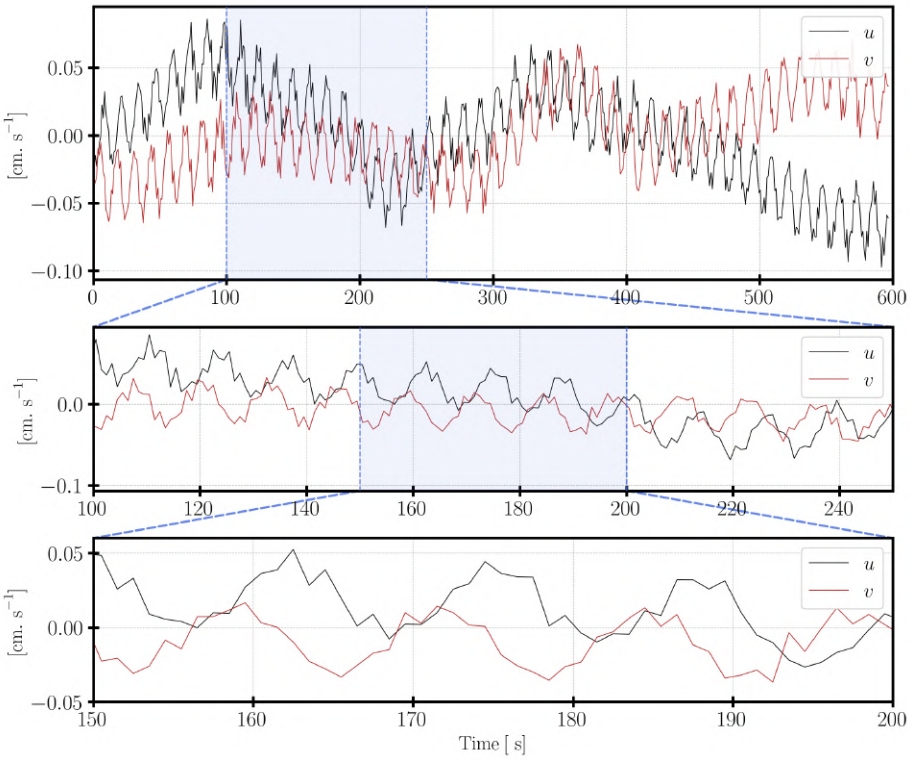

Figure V.5: Time series of the horizontal velocity components u (black) and v (red) measured at the centre of the tank (PIV plane at mid-depth) for experiment EXP18 ($f = 1$ rad s^{-1}; $\Delta T = 3.3$ ° C; CC configuration). Each panel shows a successive zoom into the time series: the full 600 s record (top), an intermediate window of 130 s (middle), and a 20 s window resolving the high-frequency fluctuations (bottom). Dashed blue lines and shaded rectangles indicate the zoomed region in the parent panel.

The signal highlights the simultaneous presence of several time scales. On a long-term scale, slow variations are observed, with a characteristic period of between 200 and 300 s, associated with changes in the large-scale structures of the geostrophic circulation. These slow variations are superimposed on faster fluctuations, with a typical amplitude of the order of $0.05\ \mathrm{cm\ s}^{-1}$. The gradual drift of the u component towards negative values reflects the slow evolution of an apparent coherent structure with a characteristic time of the order of 10^2 s. As we shall show in Sec. V.4.2, this evolution is linked to the dynamics of the mean circulation. Furthermore, an enlargement of the time window between 150 and 170 s reveals the presence of higher-frequency oscillations, with a characteristic period $T_{\mathrm{obs}} \approx 13$ s. The components u and v then appear in phase quadrature, with the v component ahead: when u reaches a maximum, v crosses zero. This property is a characteristic signature of an anticyclonic inertial motions in a rotating fluid. Note that these oscillations are exactly at the natural frequency of the platform so they can also be experimental artefacts due to, for example, precession phenomena on the platform.

These observations naturally lead to the identification of three time scales within the system. The first corresponds to the inertial scale, $\tau_f \sim 10$ s, associated with rapid oscillations. The second is an intermediate scale, referred to as synoptic, $\tau_s \sim 100$ s, characteristic of the evolution of large-scale coherent structures. Finally, the third corresponds to the total duration of the experiment, $\tau_{\text{exp}} = 600$ s, over which slow drifts in the mean state may occur. This separation of timescales will serve as a framework for interpreting all the analyses presented in the rest of this chapter.

V.4.1.1 Definition of the components of the velocity field

Based on the scale separation discussed above, we propose several definitions of the velocity field calculated from the instantaneous data $\mathbf{u}(x, y, t)$:

- The mean circulation, defined as the time-averaged flow over the entire experiment

$$\mathbf{U}(x, y) = \frac{1}{\tau_{exp}} \int_0^{\tau_{exp}} \mathbf{u}(x, y, t) dt \tag{V.8}$$

- The synoptic anomaly is defined as the difference between a moving average over a time window of duration τ_s and the time-averaged value of the experiment.

$$\mathbf{U_s}(x, y)|_{t_i} = \underbrace{\left(\frac{1}{\tau_s} \int_{t_i}^{t_i+\tau_s} \mathbf{u}(x, y, t) dt \right)}_{\text{sliding average over a synoptic period}} - \mathbf{U}(x, y) \tag{V.9}$$

  This field is defined over a time window τ_s centred on a time t_i. This allows us to isolate structures whose temporal coherence is on the synoptic scale: mesoscale vortices and persistent coherent structures. It is obtained by subtracting the background thermal circulation and smoothing out the high-frequency components.

It is worth noting the limitations of the definition of the synoptic field. Firstly, the global average $\mathbf{U}(x, y)$ is not strictly identical to the 'pure thermal circulation': if vortical structures persist for a significant portion of the experiment's duration, their contribution is partially absorbed into $\mathbf{U}(x, y)$. Secondly, the result depends on the choice of t_i: two offset windows may capture different instantaneous states of the mesoscale. Finally, the temporal averaging in the definition of $\mathbf{U_s}(x, y)|_{t_i}$ means that these two components do not constitute a Reynolds decomposition of the velocity field in the classical sense. The field $\mathbf{U_s}$ is obtained by a finite moving average and represents a synoptic anomaly, without guaranteeing the statistical properties of a zero-mean fluctuation.

Despite these limitations, this definition provides a diagnostic tool for characterising the mesoscale state in our experiments. It allows a qualitative distinction to be made between regimes with dominant axisymmetric circulation (low ΔT , $f = 0$) and regimes where coherent structures emerge (high ΔT , $f > 0$), and as such it will be used as a diagnostic of the mesoscale turbulent state throughout this chapter. From now on, we will use the term 'mean velocity' to refer to $\mathbf{U}(x, y)$ and 'synoptic velocity' to denote $\mathbf{U_s}(x, y)|_{t_i}$.

V.4.2 Mean Flow

V.4.2.1 Horizontal circulation without rotation

Fig. V.6 shows the mean horizontal circulation captured by PIV for the four experiments without rotation (EXP08, EXP09, EXP12, EXP13). The observed circulation is qualitatively consistent with the analytical solution of Rossby (1965), with convergence towards the centre (CC configuration, central downwelling) and divergence at the periphery (warm peripheral upwelling). Furthermore, the circulation is qualitatively similar regardless of ΔT (and depending on the averaging time, the result remains the same if averaged over the experiment period τ_{exp}). It can, however, be noted that the presence of the probe array in the central zone creates a visible wake in the form of a vorticity dipole for EXP08 ($\Delta T = 1.8$°C).

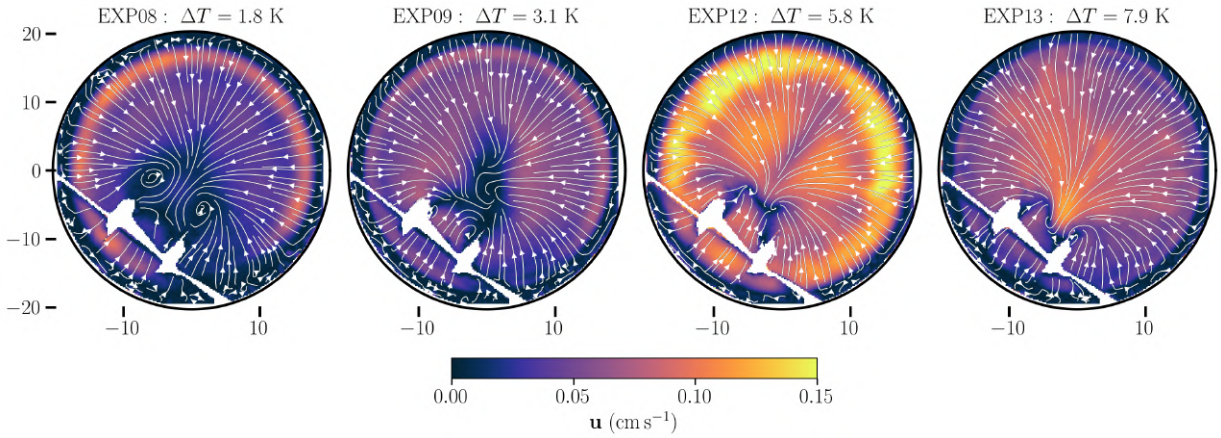

Figure V.6: Stream flow of the horizontal plane of the tank, the arrows shows the trajectories of the particles of fluid of the mean flow computed from the function "streamplot" form matplotlib on the Velocity averaged over 600 s. Different experiments are shown, all with no rotation, from left to right(EXP08 - EXP09 - EXP12 - EXP13) with for each a different ΔT. The colors show the intensity of the mean velocity field.

The transition threshold to the turbulent regime is expected to occur at $Ra_c \sim 10^{10}$ for $Pr = 7$ according to Gayen et al. (2014), beyond our range - $Ra \sim 10^8 - 10^9$. The absence of a transition in the structure of the mean flow for $\Delta T \in [1.8 - 7.9]$ K is therefore theoretically expected. However, in the divergence fields (Fig. V.7), we observe a slight fragmentation in the coherence of the region of high (positive) divergence with high ΔT values; this suggests the existence of developing coherent convective plumes at the warm periphery. This transition is consistent with the local stability analysis of Gayen et al. (2014), which predicts that the primary instability is a transverse convective instability localised within the warm forcing layer.

As for the synoptic field, it is practically zero, regardless of the value of ΔT . This indicates that, unlike the case shown in Fig. V.5, cases without rotation do not exhibit temporal variability on a scale smaller than that of the experiment τ_{exp}.

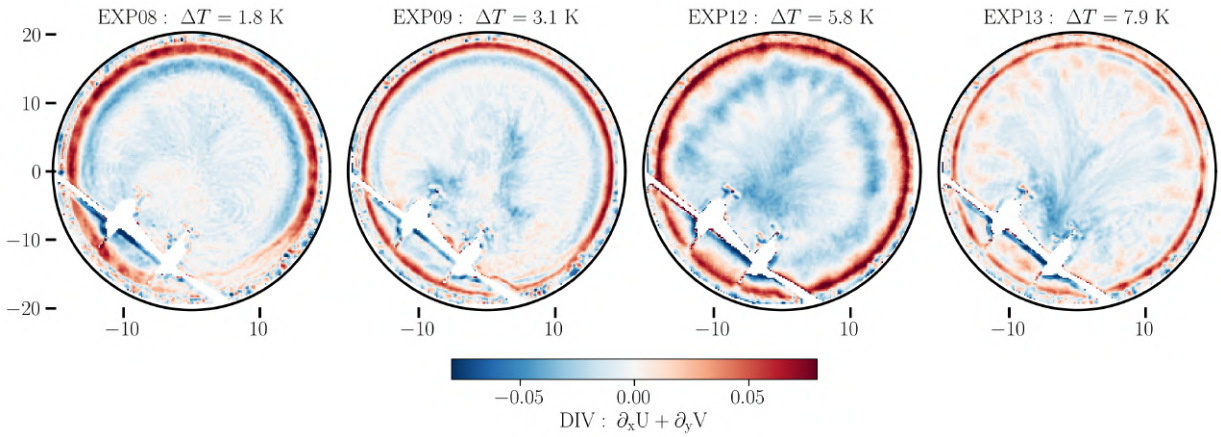

Figure V.7: Horizontal divergence computed from the mean velocity. Different experiments are shown, all with no rotation, from left to right (EXP08 - EXP09 - EXP12 - EXP13) with for each a different ΔT

V.4.2.2 Horizontal circulation with rotation

Rotation profoundly alters the flow structure. In this case, it becomes necessary to distinguish between coherent structures evolving on the synoptic timescale ($\tau_s \sim 100$ s) and the circulation obtained by averaging over the entire acquisition period ($\tau_{\text{exp}} = 600$ s). Fig. V.8 thus shows the velocity fields averaged over the entire duration of the experiment for the rotating cases at $f = 1$ (EXP17–EXP21). The qualitative difference from the non-rotating experiments is immediately apparent: regardless of the value of ΔT, the mean flow exhibits a cyclonic circulation (anti-clockwise).

This pattern is consistent with the establishment of an equilibrium close to geostrophic conditions within the fluid, where the horizontal pressure gradients induced by the thermal gradient are mainly balanced by the Coriolis force. It should be noted, nevertheless, that our configuration is inherently three-dimensional and convective. The vertical motions associated with convection locally break the assumptions of the geostrophic and hydrostatic approximations; the thermal wind relationship must therefore be regarded as a tool for the qualitative interpretation of the mean circulation rather than as a quantitative description of the flow.

In this context, the thermal wind relationship (Eq. V.2) relates the vertical shear of the horizontal velocity to the horizontal temperature gradient. In the CC configuration, the horizontal temperature gradient is directed radially outwards, from the cold region towards the warm region.

The order of magnitude of the associated velocity can be estimated by the characteristic velocity of the thermally driven flow

$$U_{th} = \frac{g\alpha\Delta T H}{fL} \simeq 1.6 \times 10^{-3}\Delta T \quad \text{m s}^{-1}. \tag{V.10}$$

For ΔT of 1.7 ° C to 7.8 ° C this estimate yields a characteristic velocity of the order of 1 to 12 mm s^{-1}, comparable to the velocities measured in the mean fields shown on Fig. V.8. This good agreement suggests that the mean circulation is controlled, in the first order, by a

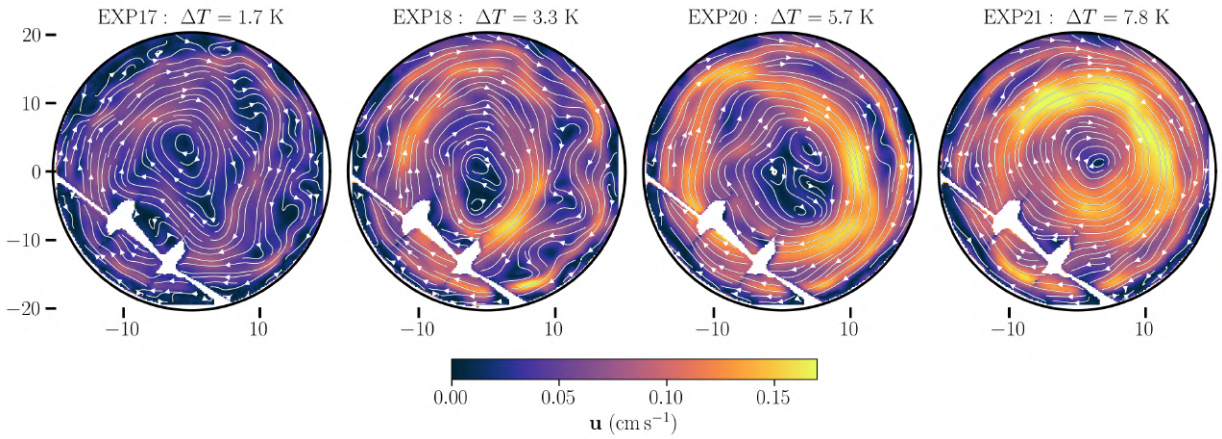

Figure V.8: Same as Fig. V.6 for the experiment with rotation ($f = 1$)

geostrophic-type balance, although three-dimensional contributions associated with convection remain present.

At the synoptic scale as well, the presence of rotation alters the circulation. Whereas in the previous case (not shown) the synoptic field is virtually zero for the experiments without rotation, Fig. V.9 (velocity fields) and Fig. V.10 (vorticity field) show the presence of vortex structures characteristic of rotating flows.

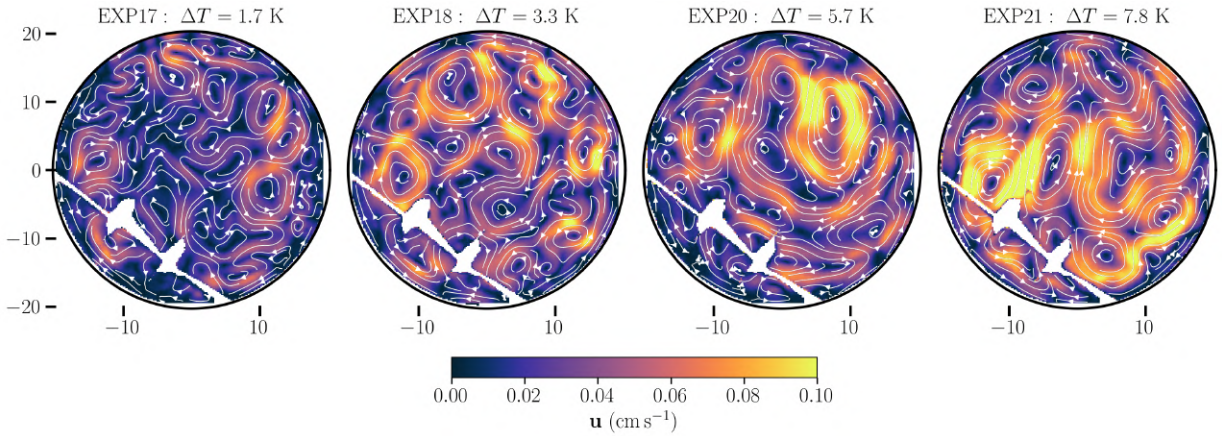

Figure V.9: Same as Fig. V.8 but for the synoptic field, for the experiment with rotation ($f = 1$). The colors show the velocity speed.

It may also be noted that the size of these structures seems to vary with ΔT . In general, the size of mesoscale structures is typically characterised by the Rossby deformation radius $R_d = (NH/f)$, where N is the vertical stratification. However, in our case of horizontal convection, the density gradient is radial; we can therefore set $N \sim \sqrt{g\alpha\Delta T/R}$ as an estimate of the buoyancy frequency, which implicitly assumes that the internal stratification scales with the temperature contrast imposed at the bottom. This assumption is not directly verified in our experiments (we do not measure the vertical stratification). So we obtain:

$$R_d = \frac{\sqrt{g\alpha\Delta TR}}{f}. \tag{V.11}$$

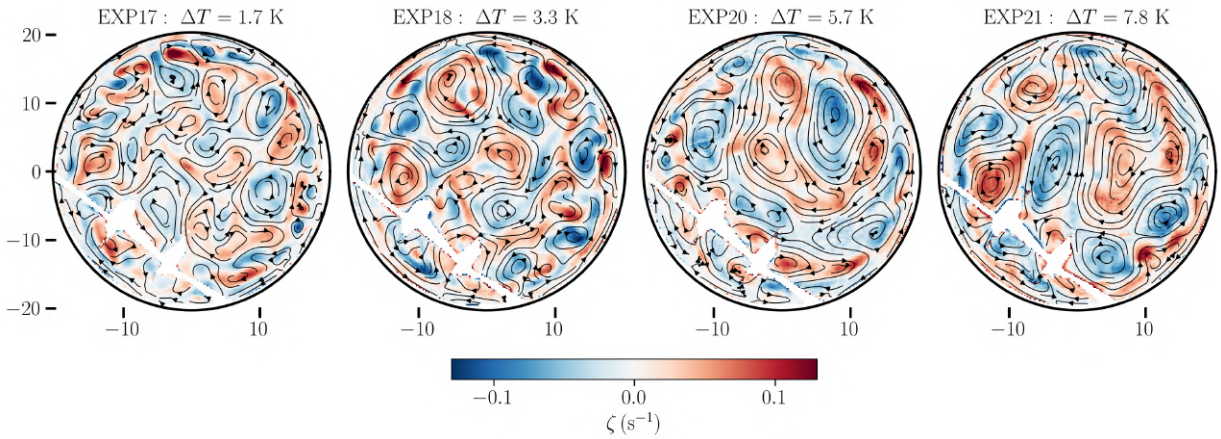

Figure V.10: Same as Fig. V.9 (synoptic circulation for the rotating experiment) but the colors show the vorticity field.

For $f = 1$ s^{-1} and $\Delta T = [1.7,\ 3.3,\ 5.7,\ 7.8]^\circ$ C, this corresponds respectively to $R_d = [3,\ 4.2,\ 5.5,\ 6.4]$cm. The size of the vortices visible on synoptic fields is consistent with this estimate. This result confirms that, even if the forcing is purely horizontal and not vertical, the horizontal temperature gradient is sufficient to define a baroclinic deformation scale relevant to mesoscale structures, in accordance with the discussion by Hide and Mason (1975) on the relationship between baroclinic instability and the radius of deformation in horizontal convection systems.

The probability density function (PDF) of vorticity, shown in Fig. V.11, allows us to assess whether there is any asymmetry between cyclonic and anticyclonic structures in the horizontal convection configuration. In rotating thermal convection, plumes tend to organise themselves into helicoidal columns aligned with the axis of rotation. In our configuration, the updraft region is spatially more localised than the downdraft region, which is more diffuse. One might therefore expect the upward and downward motion to be preferentially associated with vorticities of opposite signs, leading to an asymmetric distribution of vorticity and a predominance of one sign over the other. However, Fig. V.11 shows that the vorticity distribution remains broadly symmetric and is well described by a Gaussian distribution. This observation suggests that no mechanism significantly favours the production of cyclonic structures over anticyclonic structures under the experimental conditions studied.

V.4.3 Signature convection from horizontal velocity convergence

In order to compensate for the lack of data on vertical velocity, we use the horizontal divergence of the velocity field as a proxy for vertical convective dynamics. Fig. V.12 shows the PDF of the horizontal divergence for two sets of experiments (with and without rotation). The first observation is that in both case, the distribution shape seems to be fairly unaffected by ΔT . For non-rotating experiment we observe a positive skewness in the distribution with an apparent plateau for the positives value above the Gaussian distribution. This is consistent with the plots shown on Fig. V.7, the positive area (which represents the vertical velocity of the convective

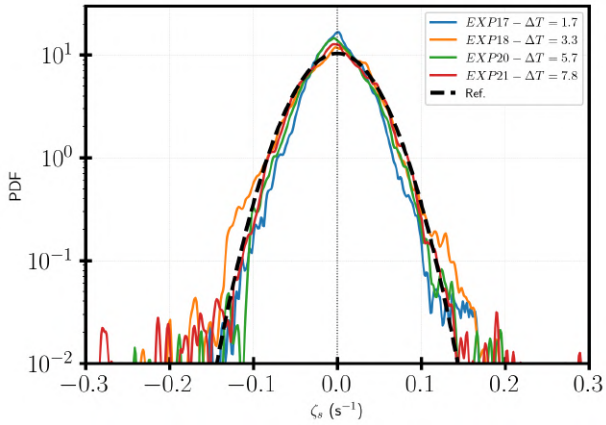

Figure V.11: PDF of the vorticity (displayed in Fig. V.10) for different experiments.

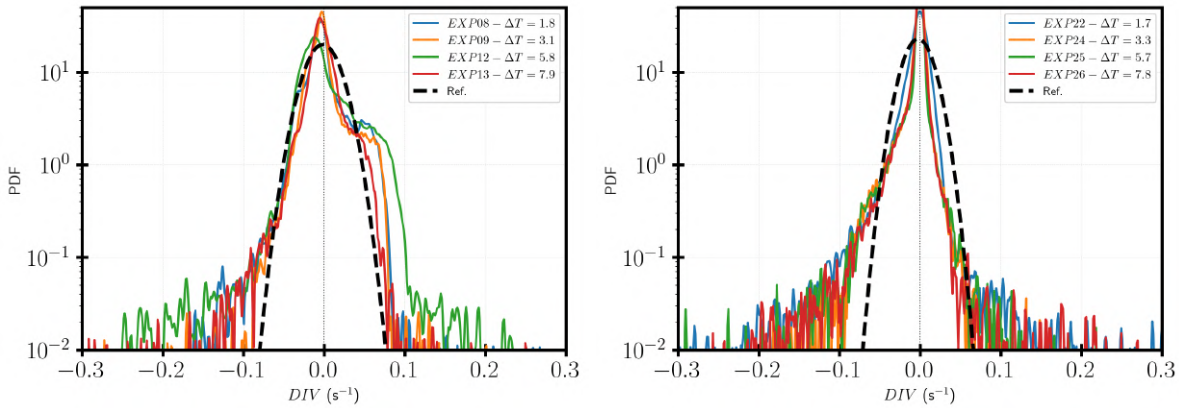

Figure V.12: PDF of the horizontal divergence for different ΔT . Left: experiment without rotation ($f = 0$); Right: Experiment with $f = 1$.

event) is concentrated in the outer region with some strong value. This step is not visible for the case with rotation. There, the distribution is more skewed toward the negative values, which suggests that the region of vertical acceleration is dominant. Furthermore, the distribution is much more sharply peaked, implying that the convective dynamics are concentrated on small scales compared to the case without rotation.

V.4.4 Kinetic Energy

V.4.4.1 Thermal gradient effect

Fig. V.13 shows the integrated kinetic energy over the domain $KE = \langle \frac{1}{2}(U^2 + V^2) \rangle_{x,y,t}$ as a function of ΔT for the different rotation rates $f = 0, 1, 3$ s^{-1}. It can be seen that the kinetic energy increases monotonically with ΔT (with one exeption) for each configuration, regardless of the rotation. This correlation seems intuitive. Two limiting regimes can be considered to interpret it:

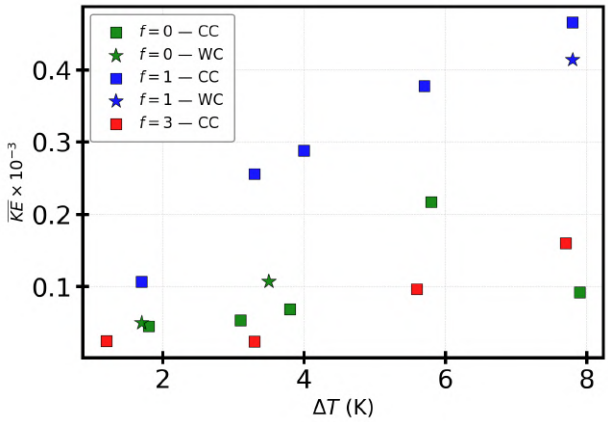

Figure V.13: Total Kinetic energy computed at each time stamp by spatial integration over the tank then average on the τ_{exp}

The first – so-called geostrophic regime – for ($f \neq 0$) is driven, at the first order, by the balance between the thermal gradient and Coriolis, giving a characteristic velocity that depends linearly on ΔT (see Eq. V.10). We then have

$$KE \sim U_{th}^2 \sim \Delta T^2. \tag{V.12}$$

The second regime – the convective regime – for $(f = 0)$. If we consider the characteristic scale to be the size of the boundary layer $\delta_{th} \sim LRa^{-1/5}$ (see Eq. V.4). Dimensionally, we can define the characteristic advection velocity in the boundary layer

$$U \sim \frac{\kappa}{\delta_{th}} \sim \frac{\kappa}{L} Ra_L^{1/5}. \tag{V.13}$$

And thus

$$KE \sim (\frac{\kappa}{L})^2 Ra_L^{-2/5} \sim \Delta T^{2/5}. \tag{V.14}$$

In both regimes, kinetic energy is therefore expected to be an increasing function of ΔT , although the predicted exponents differ significantly. The measurements presented here do not allow for a quantitative distinction between the scaling laws, but rather highlight the general trend of the $KE(\Delta T)$ relationship.

The first regime is based on a thermal wind equilibrium between the horizontal pressure gradient and the Coriolis force. This equilibrium, which is geostrophic, provides a simplified approximation that is, by its very nature, limited in a convective flow. The second scaling provides an estimate of the characteristic velocity within the thermal boundary layer, where the equilibrium between advection and diffusion is established (Hazewinkel et al., 2012). As the measurements presented here were taken at a distance from the bottom, this reasoning can only be used as a qualitative indication of the expected evolution of kinetic energy with ΔT . This distinction is all the more important given that velocity profiles can vary significantly between the boundary layer and the interior of the flow.

V.4.4.2 Rotation effect

For a fixed ΔT, KE is consistently higher at $f = 1\ \mathrm{s}^{-1}$ than at $f = 0\ \mathrm{s}^{-1}$. This result suggests a redistribution of energy towards horizontal modes: the Taylor–Proudman constraint inhibits vertical motion ($w \to 0$ in the geostrophic limit), so that the available convective energy is preferentially channelled into geostrophic horizontal velocities.
For $f = 3\ \mathrm{s}^{-1}$, however, the energy levels converge with or even fall below those of $f = 0\ \mathrm{s}^{-1}$. This decrease suggests that, at high rotation, the dynamic constraints associated with rotation become dominant and limit the development of large-scale convective circulation. It should be noted, however, that this interpretation is limited by the experimental setup, in particular by the position of the PIV plane and the absence of direct measurements of vertical velocity gradients. The analysis presented is a first step towards a precise quantification of the energy redistribution between vertical and horizontal components

V.5 Conclusion

This chapter presents an exploratory study of the rotating horizontal convection generated by a radial temperature gradient imposed at the bottom of a cylindrical tank. In the absence of rotation, the mean flow reproduces the laminar circulation described in Rossby (1965). Under rotation, a geostrophic circulation develops and an unsteady mesoscale eddy field emerges, the scale of which is consistent with the deformation radius. Kinetic energy is redistributed by Rotation—increasing at moderate rotation and decreasing at higher rotation. Thus, rotation appears to be the factor that transitions horizontal convection from a quiescent state to a unsteady state, providing a dynamical extension of Sandström's constraint in which rotation enables vigorous time-dependent circulation despite global energetic constraints. Furthermore, the testing of the thermistor-based temperature measurement system has enabled its later implementation in convection experiments on the Coriolis platform [5] These observations, whilst still preliminary, raise questions that could be resolved by vertically and thermally resolved measurements, and they provide the basis for a more rigorous study of the transition to mesoscale turbulence in rotating horizontal convection.

[5] these new measurements are now being applied to experiments conducted as part of the STAIRWAY project (see presentation Sec. VI.2)

Chapter VI

Conclusion and perspectives

VI.1 Main results

This thesis is devoted to the development of analytical and experimental models of free and forced oceanic convection, the analysis of the wind-driven oceanic mixed layer dynamics, and the validity of turbulence models within a single-column framework. Let us response to the questions raised in the introduction.

Deepening of the mixing layer

> What is the influence of inertial oscillations on the dynamics of the ocean surface boundary layer? What is the deepening regime of the wind-driven mixed layer in rotation?

In Chap. III, we addressed this question by revisiting the slab model of Pollard et al. (1973). We analysed the entrainment layer, which we considered to be in a state of marginal stability. We were thus able to show that the deepening of the oceanic mixed layer, in a rotating frame, was not halted beyond half an inertial period. We proposed a scaling law

$$h(t) \propto \frac{u_*}{\sqrt{N_0 f}}(ft)^{1/4}$$

which we subsequently validated using the k-ε model. Finally, we showed that the contribution of the inertial oscillations proved to be negligible relative to the contribution of the quasi-stationary component of the velocity.

Transient regime of turbulent Ekman Layer

> What is the transient dynamics of the turbulent Ekman layer? To what extent do the oscillations generated by wind forcing interact with the steady-state solution of the Ekman layer?

In Chap. IV, we presented laboratory experiment carried out on the Coriolis platform driven by a bottom shear (spin-up). These experiments enabled us to describe the settling of the turbulent

Ekman layer within half an inertial period, as well as the excitation of inertial waves, which are damped over a longer timescale (~ 5 inertial periods). We have shown that the transient state of the Ekman layer is characterised by the existence of a velocity spiral with these oscillations, and we observed no interaction between these two components, suggesting a linear superposition between them. Furthermore, we observed that the damping of the inertial oscillations is governed by the boundary friction condition. We have shown that a parameterisation of the friction such as

$$\tau_b = C_f |\mathbf{u}| \mathbf{u},$$

with $C_f \approx 5 \times 10^{-3}$, correctly reproduces both the damping rate and the interior spin-up. This result is an extension of the study conducted by Sous et al. (2013), which investigated the friction law in a fully developed turbulent Ekman Layer.

Validity of the k-ε model

To what extent do turbulence closure models – in particular the k-ε model – remain valid in rotating flows? Do the underlying assumptions of isotropic eddy viscosity apply to the study of rotating boundary layers?

In Chap. III, we used the k-ε model to represent the deepening of the mixed layer, and we showed that this rate was consistent with the LES data from Ushijima and Yoshikawa (2020) and De Abreu and Timmermans (2026). In Chap. IV, we compared this model against experimental data for the three configurations (neutral, stratified and rotating stratified). Our comparison criteria were based on the mean dynamic vertical profiles (velocity profiles) and turbulent vertical profiles (turbulent flux profiles), as well as on the temporal evolution of the boundary layers and the damping of inertial oscillations. We have shown that the k-ε model consistently describes the dynamics of a rotating shear flow despite the assumption of isotropic eddy viscosity.

Horizontal Convection

In addition to these questions, in Chap. V we carried out exploratory work on the onset of turbulence in a horizontal convection experiment and tested its sensitivity to rotation. We have shown that, in principle, rotation acts as a trigger for turbulence at moderate rotation rates but inhibits it at high rotation rates. This work requires further investigation and offers interesting new insights into the conditions governing horizontal convection and its turbulent regime.

VI.2 Perspectives

Based on the work developed in this thesis, there are several perspectives and research avenues

Extension of Kato and Phillips (1969a) entrainment law

A second experimental campaign with stronger stratification, using salt, was carried out in 2026 with the aim to refine an entrainment law and attempt to experimentally test the scaling law proposed in Chap. III. With these new data, the PIV observation is no longer limited vertically (observation from the bottom up to 40 cm in height, compared with 14 cm in the previous experiments), and this observation of vertical dynamics is complemented by a horizontal laser sheet, which also allows us to measure radial flows.

Horizontal characterisation of inertial oscillations

The new observations in the horizontal plane allow us to further characterise the inertial oscillations discussed in Chap. IV. We have seen that these oscillations behave barotropically within the Ekman layer, but we have not described their horizontal signatures. The presence of lateral boundaries forces these oscillations to have zero amplitude at the boundaries; furthermore, the azimuthal velocity increases with the radius of the tank. Under these conditions, what will be the horizontal profile of the inertial oscillations? Moreover, at the boundary layer, friction is not constant but rather fluctuating; how does this affect the organisation of these oscillations?

Figure VI.1: Picture of Ekman instability highlighted by dye during spin up experiment.

Limitations of the 1D view of the mixed layer

In addition to the horizontal measurements mentioned above, we also have access to LES data from a numerical twin of the Coriolis platform, providing the full three-dimensional flow field. These datasets offer the opportunity to investigate the limits of the one-dimensional framework adopted throughout this thesis. While the single-column description successfully captures the early evolution of the boundary layer, it is expected to break down as horizontal

motions progressively develop. Several mechanisms may contribute to this transition, including (i) the establishment of an axisymmetric circulation (Fig. VI.2), (ii) Ekman-layer instabilities (Lilly, 1966; Lingwood, 1997), which have already been observed in dye visualisations (Fig. VI.1), (iii) baroclinic instability under sufficiently strong horizontal density gradients (Walin, 1969), and (iv) frontogenesis within the tank (Linden and Heijst, 1984; Blumen and Lundquist, 2001). An avenues of the present work would therefore be to map these processes in the parameter space covered by the experimental the LES dataset, characterise the time scales for each of these processes and to quantify the associated lateral transports.

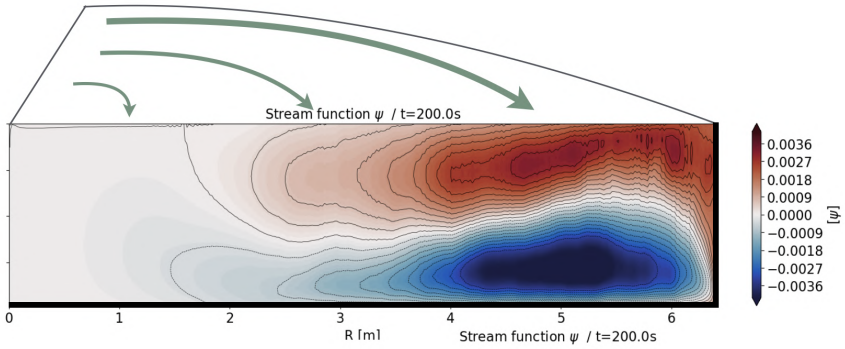

Figure VI.2: Radial section of the stream function Ψ in the (r, z)-plane, using LES twin of the coriolis platform for a stratified spin up without initial rotation.

Shear coupled with free convection and double-diffusive convection

In this thesis, we have focused on the study of free and forced convection processes individually. Two new sets of experiments cover the coupling of various convective processes.

A first series of experiments, which have not yet been analysed, was carried out as part of the PLUME project and aimed to study mixed convection processes; that is, experiments in which the water column is driven both mechanically by shear and by a buoyancy flux. This framework enables us to investigate how shear affects convective plumes, influences the growth of the mixing layer, and how, overall, the two processes interact in both rotating and non-rotating systems.

A second laboratory experimental campaign, carried out in 2026, introduced double-diffusive convection using the same heating system as in the PLUME project. Thermal stratification was replaced by a stable salinity gradient, whilst the heat flux was injected at the base of the column of fluid. The diffusive differences between temperature and salinity produce instabilities that gradually organise themselves into a succession of homogeneous layers. The density profile is then characterised by staircases visible in Fig. VI.3. Furthermore, thermistor probes (described in Chap. V) have been used successfully and currently enable the measurement of fluctuations in the temperature field within a vertical PIV slice, thereby allowing the measurement of vertical turbulent heat fluxes. These new experiments enable us to study, on the one hand, the impact of rotation on the formation and maintenance of the double-diffusive staircases. On the other hand, we can investigate the impact of shear on these structures and the associated heat fluxes.

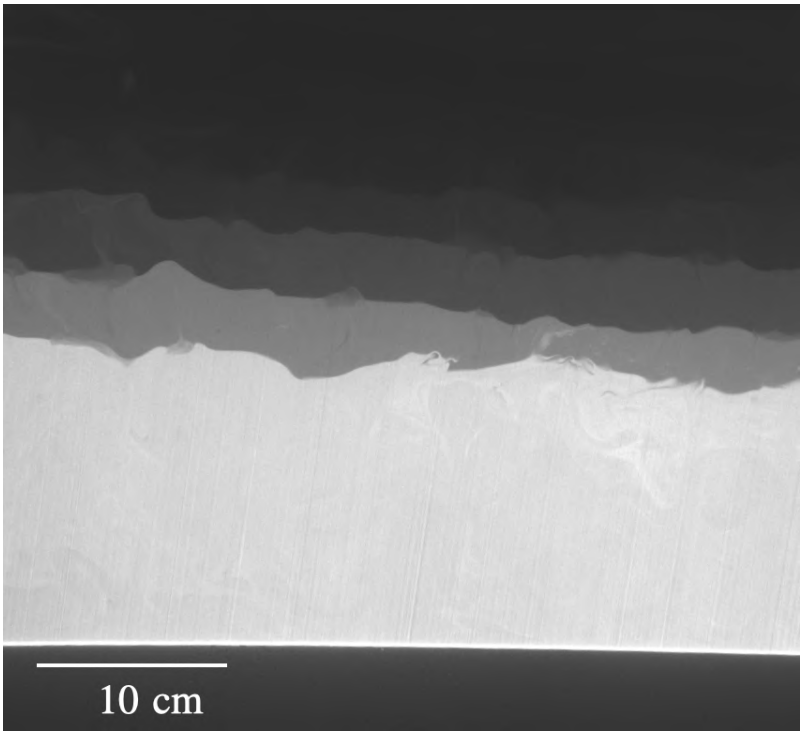

Figure VI.3: Vertical view of a double-diffusive convection experiment. A constant heat flux is applied at the bottom of a water column that is stably stratified in salinity. The resulting thermohaline staircases are revealed by the different dye concentrations. Courtesy of Olivier Marchand.

Publication of an experimental database

The final task, currently underway, involves aggregating the experimental data in the form of 1D profiles, in the same way as was done in Chap. IV, in order to create a database that is accessible and comparable with more common LES data. This will enable the parameterisations of turbulent closure models to be tested on controlled cases. This involves describing the validity periods of the 1D assumptions, the global dynamics within the platform, and the precise determination of the boundary conditions.

VI.3 Broader Context

The work presented in this thesis addresses a classic problematic in geophysical fluid mechanics: understanding how turbulent boundary layers drive interactions between the forced boundary and the fluid interior. These processes govern the transfer of momentum, heat and mass, and thus play a central role in the dynamics of the mixed layer and ocean circulation.

Since the pioneering work of Ekman (1905), followed by that of Pollard et al. (1973), Price et al. (1978a), Kato and Phillips (1969a) and many others, the description of the mixed layer has largely been based on a one-dimensional approach and on turbulence parameterisations. Whilst this framework has made it possible to describe many regimes, it generally treats the

response of the boundary layer as a succession of near-equilibrium states. The results of this thesis show that, in the presence of rotation, this assumption needs to be nuanced. Transient adjustment forms an intrinsic part of the dynamics: the formation of the turbulent Ekman layer, the evolution of the mixed layer and inertial oscillations develop on timescales comparable to those of atmospheric forcing. The response of the boundary layer therefore depends not only on the imposed conditions, but also on its own transient evolution.

This approach leads more to complementing existing approaches. The theoretical developments, numerical simulations and experiments carried out on the Coriolis platform provide reference cases for testing turbulence models under transient and rotating conditions, which are still relatively poorly documented. The scaling laws proposed in this manuscript, together with the experimental database currently being compiled, thus constitute tools for the development and validation of future parameterisations.

Finally, whilst this thesis has focused primarily on ocean mixed layer, several of the mechanisms studied extend beyond this context alone. The interactions between rotation, stratification, turbulence and convection play a role in many natural systems, ranging from the polar oceans to the oceans of icy moons, giant planets and stars, Earth liquid metal core and the accretion disc in astrophysical flows. The approaches developed and the datasets obtained may also serve as a reference for the study of other rotating stratified fluids. This work contributes to a broader effort to better understand the dynamics of rotating stratified fluids.

Appendix A

Appendices

A.1 Exploratory test of measurement technique

In this section, we present a method that we have tested, without success, to measure temperature non-invasive by observing a layer of water containing a thermoreactives dye illuminated by a laser.

A.1.1 Thermo-reactive dye observation measurement technique

This method consists of mixing a specific concentration of a thermoreactive dye (we use Rhodamine B) in a layer of water. The total concentration in the fluid must be perfectly homogeneous (4.8×10^{-5} g/L, for the Rhodamine B (Caudwell et al., 2016)). The principle behind this technique is that the absorption of light (emanating from a laser source) by the dye depends on its temperature; thus, by observing the intensity of light emitted by a portion of fluid illuminated by a laser, and using a properly established calibration, one is able to deduce its temperature. This method has been successfully implemented by Caudwell et al. (2016).[1]

The major challenge of this technique, therefore, lies in its ability to observe fluctuations in light intensity. Firstly, laser illumination must be as uniform as possible (using for example a Powell lens). The laser illumination must also be powerful enough to ensure that the fluctuation is not of the order of magnitude of the camera noise. Secondly, it is necessary to filter the laser light, the intensity of which masks the fluorescence emitted by the dye. The preferred method relies on the use of an interference filter. It is, however, at this stage that the main limitations of the technique become apparent. Indeed, an interference filter requires the optical path to pass through it at an angle as close as possible to the normal. Any angular deviation alters the filtered wavelengths and thus compromises the validity of the measurement. This constraint imposes a reduced field of view as well as a camera positioned at a great distance from the observed area. Such a restriction makes the implementation of this method across the Coriolis platform practically impossible.

The approach we have sought to develop involves overcoming the use of the interference filter by performing digital filtering of the signal on an image captured by a color camera. In fact, the image captured by CMOS cameras is an RGB image, i.e. a composition of three channels

[1] The reader is referred to Tobit Caudwell's PhD thesis (see Chapter 2, written in French) for a detailed description of laser-induced fluorescence temperature measurement

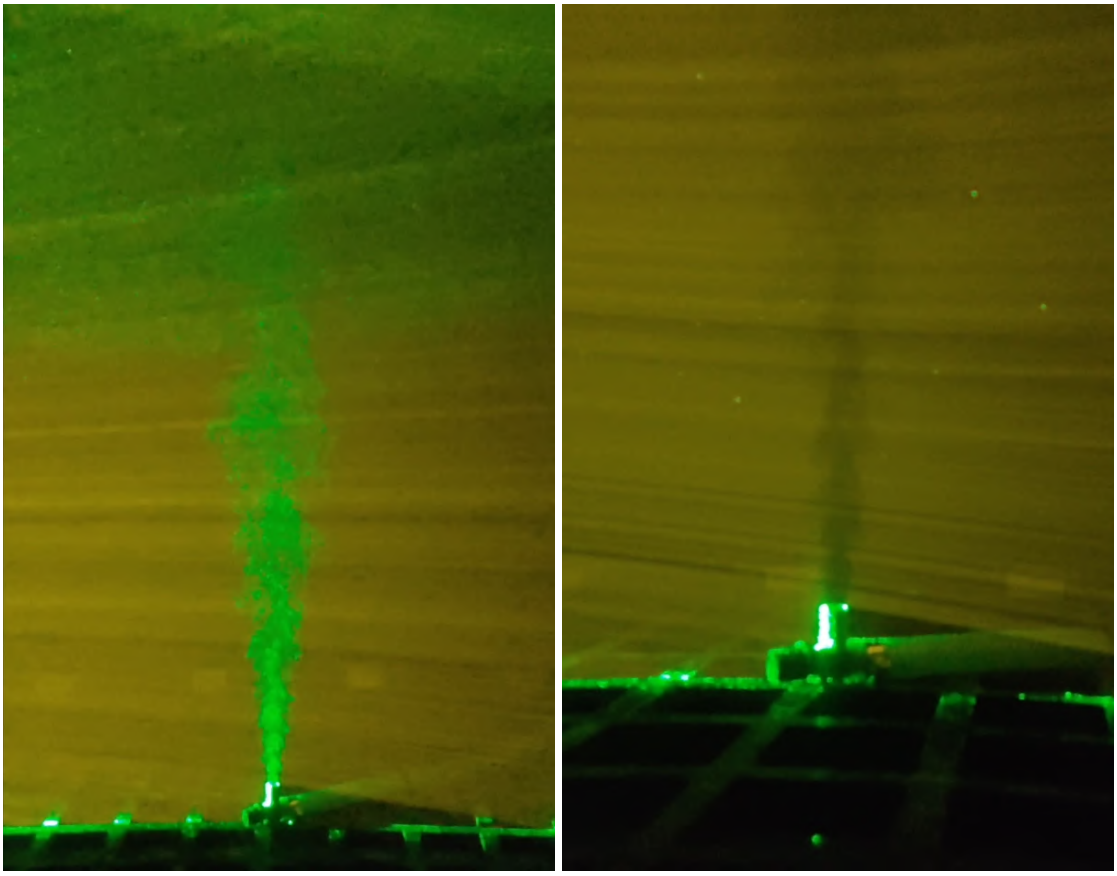

Figure A.1: Image single thermal turbulent plume. Left: PIV particles are injected in the hot water source. Right: the entire tank (and the hot water supply) has a uniform concentration of Rhodamine B.

(red, blue and green). It is therefore possible to find a linear combination of these three channels in order to numerically recreate an interference filter whilst avoiding its limitations. However, although for some experiment the plume (with an anomaly of around 50°C) was visible to naked-eye (as shown in figure A.1), all fluctuations measured were found to be of the same order of magnitude as the camera error.

A team in Switzerland has succeeded in implementing this technique (Shah et al. (2023)) with a different dye from the one we use. The temperature gradients they use are still very large and the field of view small, but this shows that the method is possible.

Bibliography

Alford, M. H. (2001). Internal Swell Generation: The Spatial Distribution of Energy Flux from the Wind to Mixed Layer Near-Inertial Motions. *Journal of Physical Oceanography*, 31(8):2359–2368. (Cited on pp. 9 and 87.)

Alford, M. H. (2020). Revisiting Near-Inertial Wind Work: Slab Models, Relative Stress, and Mixed Layer Deepening. *Journal of Physical Oceanography*, 50(11):3141–3156. (Cited on p. 15.)

Alford, M. H., MacKinnon, J. A., Simmons, H. L., and Nash, J. D. (2016). Near-inertial internal gravity waves in the ocean. *Annual review of marine science*, 8:95–123. (Cited on p. 6.)

Ashkenazy, Y., Gildor, H., and Bel, G. (2015). The effect of stochastic wind on the infinite depth Ekman layer model. *Europhysics Letters*, 111(3):39001. (Cited on pp. 15 and 87.)

Aurnou, J. M. (2025). Conference presentation: An overview of the overviews. *Institute for Pure and Applied Mathematics (IPAM), UCLA*. (Cited on p. 10.)

Blumen, W. and Lundquist, J. K. (2001). Spin-up and spin-down in rotating fluid exhibiting inertial oscillations and frontogenesis. *Dynamics of atmospheres and oceans*, 33(3):219–237. (Cited on pp. 8 and 148.)

Brainerd, K. E. and Gregg, M. C. (1995). Surface mixed and mixing layer depths. *Deep Sea Research Part I: Oceanographic Research Papers*, 42(9):1521–1543. (Cited on p. 2.)

Braun, L., Younis, B. A., and Weigand, B. (2020). A Turbulence Closure Study of the Flow and Thermal Fields in the Ekman Layer. *Boundary-Layer Meteorology*, 175(1):25–55. (Cited on pp. 85, 87 and 94.)

Burchard, H. (2002). *Applied Turbulence Modelling in Marine Waters*. Springer Science & Business Media. (Cited on pp. 12 and 15.)

Burchard, H. (2009). Combined effects of wind, tide, and horizontal density gradients on stratification in estuaries and coastal seas. *Journal of Physical Oceanography*, 39(9):2117–2136. (Cited on p. 127.)

Burchard, H. and Baumert, H. (1998). The formation of estuarine turbidity maxima due to density effects in the salt wedge. a hydrodynamic process study. *Journal of Physical Oceanography*, 28(2):309–321. (Cited on p. 121.)

Burchard, H. and Bolding, K. (2001). Comparative Analysis of Four Second-Moment Turbulence Closure Models for the Oceanic Mixed Layer. *Journal of Physical Oceanography*, 31(8):1943–1968. (Cited on pp. 35, 36, 70, 71, 87, 119 and 120.)

Caldwell, D. R., Van Atta, C. W., and Helland, K. N. (1972). A laboratory study of the turbulent ekman layer. *Geophysical Fluid Dynamics*, 3(2):125–160. (Cited on pp. 41 and 88.)

Canuto, V. M., Howard, A., Cheng, Y., and Dubovikov, M. S. (2001). Ocean Turbulence. Part I: One-Point Closure Model—Momentum and Heat Vertical Diffusivities. *Journal of Physical Oceanography*, 31(6):1413–1426. (Cited on pp. 36, 71 and 119.)

Carlsson, B., Papadimitrakis, Y., and Rutgersson, A. (2010). Evaluation of a roughness length model and sea surface properties with data from the baltic sea. *J. Phys. Oceanogr.*, 40(9):2007–2024. (Cited on p. 121.)

Caudwell, T., Flór, J.-B., and Negretti, M.-E. (2016). Convection at an isothermal wall in an enclosure and establishment of stratification. *Journal of Fluid Mechanics*, 799:448–475. (Cited on p. 151.)

Charnock, H. (1955). Wind stress on a water surface. *Quart. J. Roy. Meteor. Soc.*, 81(350):639–640. (Cited on p. 121.)

Chelton, D. B., DeSzoeke, R. A., Schlax, M. G., El Naggar, K., and Siwertz, N. (1998). Geographical variability of the first baroclinic rossby radius of deformation. *Journal of Physical Oceanography*, 28(3):433–460. (Cited on p. 5.)

Coman, M. A., Griffiths, R. W., and Hughes, G. O. (2006). Sandström's experiments revisited. *Journal of Marine Research*, 64:783–796. (Cited on p. 128.)

Coppin, M., Deremble, B., and Sommeria, J. (2025). Wind-mixed layer deepening in a rotating frame. *Geophysical & Astrophysical Fluid Dynamics*, 119(5):646–684. (Cited on p. 87.)

Couston, L.-A., Nandaha, J., and Favier, B. (2022). Competition between rayleigh–bénard and horizontal convection. *Journal of Fluid Mechanics*, 947:A13. (Cited on p. 127.)

Csanady, G. and Shaw, P. (1980). The Evolution of a Turbulent Ekman Layer. *Journal of Geophysical Research-Oceans*, 85:1537–1547. (Cited on pp. 15 and 87.)

Cushman-Roisin, B. (1981). Deepening of the wind-mixed layer: A model of the vertical structure. *Dynamic Meteorology and Oceanography*, 33(6):564–582. (Cited on pp. 42 and 48.)

Cushman-Roisin, B. and Beckers, J.-M. (2011). *Introduction to geophysical fluid dynamics: physical and numerical aspects*, volume 101. Academic press. (Cited on p. 5.)

D'Asaro, E. A. (1985). The Energy Flux from the Wind to Near-Inertial Motions in the Surface Mixed Layer. *Journal of Physical Oceanography*, 15:1043–1059. (Cited on pp. 6, 42 and 87.)

Davis, R. E., deSzoeke, R., and Niiler, P. (1981). Variability in the upper ocean during MILE. Part II: Modeling the mixed layer response. *Deep Sea Research Part A. Oceanographic Research Papers*, 28(12):1453–1475. (Cited on p. 42.)

De Abreu, S. and Timmermans, M.-L. (2026). Mixed layer deepening and internal wave generation under sea ice in free drift. *Journal of Physical Oceanography*, 56(4):823–837. (Cited on p. 146.)

de Boyer Montégut, C., Madec, G., Fischer, A. S., Lazar, A., and Iudicone, D. (2004). Mixed layer depth over the global ocean: An examination of profile data and a profile-based climatology. *Journal of Geophysical Research: Oceans*, 109(C12). (Cited on p. 2.)

de Szoeke, R. and Rhines, P. (1976). Asymptotic regimes in mixed-layer deepening. *Journal of Marine Research*, 34(1). (Cited on p. 42.)

Deike, L. (2022). Mass transfer at the ocean–atmosphere interface: The role of wave breaking, droplets, and bubbles. *Annu. Rev. Fluid Mech.*, 54(1):191–224. (Cited on p. 67.)

Deremble, B., Hogg, A. M., Berloff, P., and Dewar, W. K. (2011). On the application of no-slip lateral boundary conditions to 'coarsely' resolved ocean models. *Ocean Model.*, 39(3-4):411–415. (Cited on p. 118.)

Dewar, W. K. and Flierl, G. R. (1987). Some effects of the wind on rings. *Journal of physical oceanography*, 17(10):1653–1667. (Cited on p. 7.)

Dohan, K. and Davis, R. E. (2011). Mixing in the Transition Layer during Two Storm Events. (Cited on p. 42.)

Duan, J., Li, Y., Lyu, Y., Jing, Z., and Wang, F. (2025). Emergence of the north pacific heat storage pattern delayed by decadal wind-driven redistribution. *Nature Communications*, 16(1):668. (Cited on p. 4.)

Duck, P. W. and Foster, M. R. (2001). Spin-up of homogeneous and stratified fluids. *Annual Review of Fluid Mechanics*, 33(Volume 33, 2001):231–263. (Cited on p. 88.)

Ekman, V. W. (1905). On the influence of the earth's rotation on ocean-currents. *Arkiv för Matematik,, Astronomy Och Fysik*, 2,:1–53. (Cited on pp. 8, 40, 86, 98, 100 and 149.)

Endoh, M. and Nitta, T. (1971). A Theory of Non-Stationary Oceanic Ekman Layer. *Journal of the Meteorological Society of Japan. Ser. II*, 49(4):261–266. (Cited on p. 87.)

Ezer, T. (2000). On the Seasonal Mixed Layer Simulated by a Basin-Scale Ocean Model and the Mellor-Yamada Turbulence Scheme. *Journal of Geophysical Research: Oceans*, 105(C7). (Cited on p. 67.)

Fairall, C. W., Bradley, E. F., Hare, J., Grachev, A. A., and Edson, J. B. (2003). Bulk parameterization of air–sea fluxes: Updates and verification for the coare algorithm. *Journal of climate*, 16(4):571–591. (Cited on p. 6.)

Faller, A. J. and Kaylor, R. (1966). Oscillatory and transitory Ekman boundary layers. Technical Report BN-461. (Cited on p. 87.)

Fernando, H. J. S. (1991). Turbulen mixing in stratified fluids. *Annual Review of Fluid Mechanics*, 23:455–493. (Cited on p. 88.)

Flór, J. and Bush, J. M. (2002). Spin-up from rest in a stratified fluid. fluxes and structures in fluids. *Journal of Fluid Mechanics*, 472:51 – 82. (Cited on p. 22.)

Gallet, B. and Ferrari, R. (2020). The vortex gas scaling regime of baroclinic turbulence. *Proc. Natl. Acad. Sci. U.S.A.*, 117(9):4491–4497. (Cited on p. 118.)

Gardner, W. D., Gundersen, J. S., Richardson, M. J., and Walsh, I. D. (1999). The role of seasonal and diel changes in mixed-layer depth on carbon and chlorophyll distributions in the Arabian Sea. *Deep Sea Research Part II: Topical Studies in Oceanography*, 46(8):1833–1858. (Cited on p. 40.)

Garratt, J. R. (1992). *The atmospheric boundary layer*. New York, NY (United States); Cambridge University Press. (Cited on p. 101.)

Gayen, B. and Griffiths, R. W. (2022). Rotating horizontal convection. *Annual Review of Fluid Mechanics*, 54(1):105–132. (Cited on p. 128.)

Gayen, B., Griffiths, R. W., and Hughes, G. O. (2014). Stability transitions and turbulence in horizontal convection. *Journal of Fluid Mechanics*, 751:698–724. (Cited on pp. 128 and 137.)

Greenspan, H. P. and Howard, L. N. (1963). On a time-dependent motion of a rotating fluid. *Journal of Fluid Mechanics*, 17(3):385–404. (Cited on p. 88.)

Hazewinkel, J., Paparella, F., and Young, W. R. (2012). Stressed horizontal convection. *Journal of fluid mechanics*, 692:317–331. (Cited on p. 142.)

Hide, R. (1958). An experimental study of thermal convection in a rotating liquid. *Philosophical Transactions of the Royal Society of London. Series A, Mathematical and Physical Sciences*, 250(983):441–478. (Cited on p. 127.)

Hide, R. and Mason, P. (1975). Sloping convection in a rotating fluid. *Advances in Physics*, 24(1):47–100. (Cited on p. 140.)

Hignett, P., Ibbetson, A., and Killworth, P. D. (1981). On rotating thermal convection driven by non-uniform heating from below. *Journal of Fluid Mechanics*, 109:161–187. (Cited on pp. 128, 130 and 131.)

Howard, L. N. (1961). Note on a paper of john w. miles. *Journal of Fluid Mechanics*, 10(4):509–512. (Cited on p. 91.)

Huang, R. X. (2004). Ocean, energy flows in. *Encyclopedia of Energy*, 4:497–509. (Cited on p. 4.)

Hughes, G. O. and Griffiths, R. W. (2008). Horizontal convection. *Annual Review Fluid Mechanics*, 40(1):185–208. (Cited on p. 127.)

Imayama, S., Lingwood, R. J., and Alfredsson, P. H. (2014). The turbulent rotating-disk boundary layer. *European Journal of Mechanics-B/Fluids*, 48:245–253. (Cited on p. 112.)

Johnson, G., Lyman, J., Willis, J., Levitus, S., Boyer, T., Antonov, J., Good, S., Domingues, C., Wijffels, S., and Bindoff, N. (2012). Global oceans: Ocean heat content. *State of the Climate in 2011*, 93:S62–S65. (Cited on p. 2.)

Johnston, T. M. S. and Rudnick, D. L. (2009). Observations of the Transition Layer. *Journal of Physical Oceanography*, 39(3):780–797. (Cited on p. 42.)

Jonker, H. J., Van Reeuwijk, M., Sullivan, P. P., and Patton, E. G. (2013). On the scaling of shear-driven entrainment: a dns study. *Journal of Fluid Mechanics*, 732:150–165. (Cited on p. 41.)

Kantha, L. H., Phillips, O. M., and Azad, R. S. (1977). On turbulent entrainment at a stable density interface. *Journal of Fluid Mechanics*, 79:753–768. (Cited on p. 19.)

Kara, A. B., Rochford, P. A., and Hurlburt, H. E. (2000). An optimal definition for ocean mixed layer depth. *Journal of Geophysical Research: Oceans*, 105(C7):16803–16821. (Cited on p. 2.)

Kataoka, T., Kimoto, M., Watanabe, M., and Tatebe, H. (2019). Wind–Mixed Layer–SST Feedbacks in a Tropical Air–Sea Coupled System: Application to the Atlantic. *Journal of Climate*, 32(13):3865–3881. (Cited on p. 40.)

Kato, H. and Phillips, O. M. (1969a). On the penetration of a turbulent layer into stratified fluid. *Journal of Fluid Mechanics*, 37:643–655. (Cited on pp. 17, 86, 88, 90, 147 and 149.)

Kato, H. and Phillips, O. M. (1969b). On the penetration of a turbulent layer into stratified fluid. *Journal of Fluid Mechanics*, 37(4):643–655. (Cited on pp. 19 and 41.)

Keppler, L. and Landschützer, P. (2019). Regional wind variability modulates the southern ocean carbon sink. *Scientific reports*, 9(1):7384. (Cited on p. 4.)

Kim, S. Y., Kosro, P. M., and Kurapov, A. L. (2014). Evaluation of directly wind-coherent near-inertial surface currents off Oregon using a statistical parameterization and analytical and numerical models. *Journal of Geophysical Research: Oceans*, 119(10):6631–6654. (Cited on pp. 15 and 87.)

Kozul, M., Chung, D., and Monty, J. (2016). Direct numerical simulation of the incompressible temporally developing turbulent boundary layer. *Journal of Fluid Mechanics*, 796:437–472. (Cited on pp. 104, 111 and 112.)

Kraus, E. B. (1977). *Modelling and Prediction of the Upper Layers of the Ocean: Proceedings of a NATO Advanced Study Institute*. Elsevier Science & Technology. (Cited on p. 42.)

Kraus, E. B. and Turner, J. S. (1967). A one-dimensional model of the seasonal thermocline II. The general theory and its consequences. *Tellus*, 19(1):98–106. (Cited on p. 42.)

Kundu, P. K. (1980). A Numerical Investigation of Mixed-Layer Dynamics. *Journal of Physical Oceanography*, 10(2):220–236. (Cited on pp. 40, 42, 43, 48 and 69.)

Kundu, P. K. (1981). Self-similarity in stress-driven entrainment experiments. *Journal of Geophysical Research: Oceans*, 86(C3):1979–1988. (Cited on p. 43.)

Large, W. G., McWilliams, J. C., and Doney, S. C. (1994). Oceanic vertical mixing: A review and a model with a nonlocal boundary layer parameterization. *Reviews of Geophysics*, 32(4):363–403. (Cited on pp. 12, 15, 36, 54 and 57.)

Large, W. G. and Pond, S. (1981). Open ocean momentum flux measurements in moderate to strong winds. *Journal of physical oceanography*, 11(3):324–336. (Cited on p. 7.)

Launder, B. E., Reece, G. J., and Rodi, W. (1975). Progress in the development of a reynolds-stress turbulence closure. *Journal of Fluid Mechanics*, 68(3):537–566. (Cited on p. 118.)

Le Quéré, C., Moriarty, R., Andrew, R. M., Canadell, J. G., Sitch, S., Korsbakken, J. I., Friedlingstein, P., Peters, G. P., Andres, R. J., Boden, T. A., et al. (2015). Global carbon budget 2015. *Earth System Science Data*, 7(2):349–396. (Cited on p. 2.)

Legay, A., Deremble, B., Penduff, T., Brasseur, P., and Molines, J.-M. (2024). A Framework for Assessing Ocean Mixed Layer Depth Evolution. *Journal of Advances in Modeling Earth Systems*, 16(10):e2023MS004198. (Cited on pp. 40 and 126.)

Lenn, Y.-D. and Chereskin, T. K. (2009). Observations of Ekman Currents in the Southern Ocean. (Cited on p. 41.)

Lewis, D. M. and Belcher, S. E. (2004). Time-dependent, coupled, Ekman boundary layer solutions incorporating Stokes drift. *Dynamics of Atmospheres and Oceans*, 37(4):313–351. (Cited on p. 87.)

Lilly, D. K. (1966). On the instability of ekman boundary flow. *Journal of Atmospheric Sciences*, 23(5):481–494. (Cited on p. 148.)

Linden, P. F. and Heijst, G. J. F. V. (1984). Two-layer spin-up and frontogenesis. *Journal of Fluid Mechanics*, 143:69–94. (Cited on p. 148.)

Lingwood, R. J. (1996). An experimental study of absolute instability of the rotating-disk boundary-layer flow. *Journal of Fluid Mechanics*, 314:373–405. (Cited on pp. 94 and 96.)

Lingwood, R. J. (1997). Absolute instability of the ekman layer and related rotating flows. *Journal of Fluid Mechanics*, 331:405–428. (Cited on p. 148.)

Liu, Y., Jing, Z., and Wu, L. (2019). Wind power on oceanic near-inertial oscillations in the global ocean estimated from surface drifters. *Geophysical Research Letters*, 46(5):2647–2653. (Cited on p. 5.)

Lueck, R. and Reid, R. (1984). On the production and dissipation of mechanical energy in the ocean. *Journal of Geophysical Research: Oceans*, 89(C3):3439–3445. (Cited on p. 4.)

Madec, G. (2008). Nemo ocean engine. Technical Report 27. (Cited on p. 49.)

Madsen, O. S. (1977). A Realistic Model of the Wind-Induced Ekman Boundary Layer. *Journal of Physical Oceanography*, 7(2):248–255. (Cited on p. 87.)

Marlatt, S., Waggy, S., and Biringen, S. (2012). Direct Numerical Simulation of the Turbulent Ekman Layer: Evaluation of Closure Models. *Journal of the Atmospheric Sciences*, 69(3):1106–1117. (Cited on pp. xii, 83, 87, 94, 104, 109, 113, 117, 121 and 122.)

Marshall, J. and Schott, F. (1999). Open-ocean convection: Observations, theory, and models. *Reviews of geophysics*, 37(1):1–64. (Cited on p. 3.)

McMonigal, K., Larson, S., Hu, S., and Kramer, R. (2023). Historical changes in wind-driven ocean circulation can accelerate global warming. *Geophysical Research Letters*, 50(4):e2023GL102846. (Cited on p. 4.)

McPhaden, M. J., Athulya, K., Girishkumar, M. S., and Orlić, M. (2024). Ekman revisited: Surface currents to the left of the winds in the northern hemisphere. *Sci. Adv.*, 10(46). (Cited on p. 86.)

Miles, J. W. (1961). On the stability of heterogeneous shear flows. *Journal of Fluid Mechanics*, 10(4):496–508. (Cited on p. 91.)

Miller, L., Deremble, B., and Venaille, A. (2024). Gyre turbulence: Anomalous dissipation in a two-dimensional ocean model. *Physical Review Fluids*, 9(5):L051801. (Cited on p. 128.)

Moen (1981). A Review of One-Dimensional Oceanic Mixed-Layer Models,. Technical report, Defense Technical Information Center. (Cited on p. 42.)

Monterey, G. I. and Levitus, S. (1997). Seasonal variability of mixed layer depth for the world ocean. Technical report, United States. National Environmental Satellite, Data, and Information. (Cited on p. 2.)

Müller, P. and Frankignoul, C. (1981). Direct atmospheric forcing of geostrophic eddies. *Journal of Physical Oceanography*, 11(3):287–308. (Cited on p. 5.)

Niiler, P. P. (1975). Deepening of the wind-mixed layer. *Journal of Marine Research*, 33:405 – 422. (Cited on pp. 12, 42, 48 and 50.)

Paparella, F. and Young, W. (2002). Horizontal convection is non-turbulent. *Journal of Fluid Mechanics*, 466:205–214. (Cited on pp. xiii and 128.)

Park, Y.-G. and Whitehead, J. (1999). Rotating convection driven by differential bottom heating. *Journal of physical oceanography*, 29(6):1208–1220. (Cited on p. 128.)

Pedlosky, J. (1996). *Ocean Circulation Theory*. Springer. (Cited on pp. 5 and 86.)

Perlin, A., Moum, J. N., Klymak, J. M., Levine, M. D., Boyd, T., and Kosro, P. M. (2005). A modified law-of-the-wall applied to oceanic bottom boundary layers. *Journal of Geophysical Research: Oceans*, 110(C10). (Cited on pp. 86 and 95.)

Perlin, A., Moum, J. N., Klymak, J. M., Levine, M. D., Boyd, T., and Kosro, P. M. (2007). Organization of stratification, turbulence, and veering in bottom ekman layers. *Journal of Geophysical Research: Oceans*, 112(C5). (Cited on p. 86.)

Pollard, R. and Millard, R. (1970). Comparison between observed and simulated wind-generated inertial oscillations. *Deep Sea Research and Oceanographic Abstracts*, 17(4):813–821. (Cited on pp. 9 and 87.)

Pollard, R. T., Rhines, P. B., and Thompson, R. (1973). The deepening of the wind-Mixed layer. *Geophysical Fluid Dynamics*, 4(4):381–404. (Cited on pp. ix, x, 9, 12, 15, 37, 41, 43, 66, 80, 88, 145 and 149.)

Pope, S. B. (2000). *Turbulent Flows*. Cambridge University Press. (Cited on pp. 7, 117 and 120.)

Prandtl, L. (1925). Bericht über untersuchungen zur ausgebildeten turbulenz. *ZAMM - Journal of Applied Mathematics and Mechanics / Zeitschrift für Angewandte Mathematik und Mechanik*, 5(2):136–139. (Cited on p. 34.)

Price, J. F., Mooers, C. N. K., and Leer, J. C. V. (1978a). Observation and Simulation of Storm-Induced Mixed-Layer Deepening. 8(4):582–599. (Cited on pp. 41 and 149.)

Price, J. F., Mooers, C. N. K., and Van Leer, J. C. (1978b). Observation and simulation of storm-induced mixed-layer deepening. *Journal of Physical Oceanography*, 8(4):582–599. (Cited on p. 86.)

Price, J. F., Weller, R. A., and Pinkel, R. (1986). Diurnal cycling: Observations and models of the upper ocean response to diurnal heating, cooling, and wind mixing. *Journal of Geophysical Research: Oceans*, 91:8411–8427. (Cited on p. 86.)

Read, P. L., Jacoby, T., Rogberg, P., Wordsworth, R. D., Yamazaki, Y., Miki-Yamazaki, K., Young, R. M., Sommeria, J., Didelle, H., and Viboud, S. (2015). An experimental study of multiple zonal jet formation in rotating, thermally driven convective flows on a topographic beta-plane. *Physics of Fluids*, 27(8). (Cited on p. 18.)

Read, P. L., Pérez, E. P., Moroz, I. M., and Young, R. M. (2014). General circulation of planetary atmospheres: insights from rotating annulus and related experiments. *Modeling atmospheric and oceanic flows: Insights from laboratory experiments and numerical simulations*, pages 7–44. (Cited on p. 127.)

Rétif, S., Negretti, M. E., and Wirth, A. (2024). Predicting the vertical density structure of oceanic gravity current intrusions. *Scientific Reports*, 14(1):10274. (Cited on p. 18.)

Rodi, W. (1987). Examples of calculation methods for flow and mixing in stratified fluids. *Journal of Geophysical Research: Oceans*, 92(C5):5305–5328. (Cited on pp. 35, 70 and 120.)

Rossby, C.-G. and Montgomery, R. B. (1935). The layer of frictional influence in wind and ocean currents. (Cited on p. 87.)

Rossby, H. (1965). On thermal convection driven by non-uniform heating from below: an experimental study. *Deep Sea Research and Oceanographic Abstracts*, 12(1):9–16. (Cited on pp. xii, 125, 127, 129, 137 and 143.)

Sallée, J.-B., Pellichero, V., Akhoudas, C., Pauthenet, E., Vignes, L., Schmidtko, S., Garabato, A. N., Sutherland, P., and Kuusela, M. (2021). Summertime increases in upper-ocean stratification and mixed-layer depth. *Nature*, 591(7851):592–598. (Cited on p. 40.)

Scolan, H. and Read, P. L. (2017). A rotating annulus driven by localized convective forcing: a new atmosphere-like experiment. *Experiments in Fluids*, 58(6):75. (Cited on p. 127.)

Senapati, B., O'Reilly, C. H., and Robson, J. (2024). Pivotal Role of Mixed-Layer Depth in Tropical Atlantic Multidecadal Variability. *Geophysical Research Letters*, 51(15):e2024GL110057. (Cited on p. 40.)

Shah, J., Mucignat, C., Lunati, I., and Rösgen, T. (2023). Simultaneous PIV–LIF measurements using RuPhen and a color camera. *Experiments in Fluids*, 65(1):3. (Cited on p. 152.)

Sheard, G. J. and King, M. P. (2011). Horizontal convection: effect of aspect ratio on rayleigh number scaling and stability. *Applied Mathematical Modelling*, 35(4):1647–1655. (Cited on p. 129.)

Shi, H., Negretti, M.-E., Chauchat, J., Blanckaert, K., Lemmin, U., and Barry, D. A. (2022). Unconfined plunging of a hyperpycnal river plume over a sloping bed and its lateral spreading: Laboratory experiments and numerical modeling. *Water Resources Research*, 58(8):e2022WR032633. (Cited on p. 18.)

Shishkina, O., Grossmann, S., and Lohse, D. (2016). Heat and momentum transport scalings in horizontal convection. *Geophysical research letters*, 43(3):1219–1225. (Cited on p. 129.)

Sous, D. and Sommeria, J. (2012). A tsai's model based s-piv method for velocity measurements in a turbulent ekman layer. *Flow Measurement and Instrumentation*, 26:102–110. (Cited on p. 27.)

Sous, D., Sommeria, J., and Boyer, D. (2013). Friction law and turbulent properties in a laboratory Ekman boundary layer. *Physics of Fluids*, 25(4):046602. (Cited on pp. 20, 88, 92, 94, 96, 106, 117 and 146.)

Speziale, C. G., Abid, R., and Anderson, E. C. (1992). Critical evaluation of two-equation models for near-wall turbulence. *AIAA journal*, 30(2):324–331. (Cited on pp. 35 and 120.)

Stammer, D., Böning, C., and Dieterich, C. (2001). The role of variable wind forcing in generating eddy energy in the north atlantic. *Progress in Oceanography*, 48(2-3):289–311. (Cited on p. 5.)

Stommel, H. (1962). On the smallness of sinking regions in the ocean. *Proceedings of the National Academy of Sciences*, 48(5):766–772. (Cited on p. 127.)

Sun, W.-Y. and Sun, O. M. (2020). Inertia and diurnal oscillations of ekman layers in atmosphere and ocean. *Dyn. Atmos. Oceans*, 90:101144. (Cited on p. 41.)

Svensson, U. (1979). Structure of the Turbulent Ekman Layer. *Tellus*, 31(4):340–350. (Cited on p. 117.)

Sverdrup, H. U. (1947). Wind-driven currents in a baroclinic ocean; with application to the equatorial currents of the eastern pacific. *Proceedings of the National Academy of Sciences*, 33(11):318–326. (Cited on p. 4.)

Tassigny, A., Bardoel, S. L., Valran, T., Viboud, S., Gostiaux, L., Sommeria, J., Bordois, L., Carton, X., and Negretti, M. E. (2026). A realistic physical model of the gibraltar strait. *Ocean Science*, 22(1):459–500. (Cited on pp. 18 and 22.)

Tassigny, A., Negretti, M. E., and Wirth, A. (2024). Dynamics of intrusion in downslope gravity currents in a rotating frame. *Physical Review Fluids*, 9(7):074605. (Cited on p. 18.)

Thompson, A. F. and Young, W. R. (2006). Scaling baroclinic eddy fluxes: Vortices and energy balance. *Journal of Physical Oceanography*, 36(4):720–738. (Cited on p. 118.)

Thorpe, S. A. (2005). *The turbulent ocean*. Cambridge university press. (Cited on p. 6.)

Treguier, A. M., de Boyer Montégut, C., Bozec, A., Chassignet, E. P., Fox-Kemper, B., McC. Hogg, A., Iovino, D., Kiss, A. E., Le Sommer, J., Li, Y., Lin, P., Lique, C., Liu, H., Serazin, G., Sidorenko, D., Wang, Q., Xu, X., and Yeager, S. (2023). The mixed-layer depth in the Ocean Model Intercomparison Project (OMIP): impact of resolving mesoscale eddies. *Geoscientific Model Development*, 16(13):3849–3872. (Cited on pp. 40 and 46.)

Umlauf, L. and Burchard, H. (2003). A generic length-scale equation for geophysical turbulence models. *Journal of Marine Research*, 61(2):235–265. (Cited on pp. 12, 15 and 86.)

Umlauf, L. and Burchard, H. (2005). Second-order turbulence closure models for geophysical boundary layers. a review of recent work. *Continental Shelf Research*, 25(7-8):795–827. (Cited on pp. 36, 43, 71, 98 and 119.)

Ushijima, Y. and Yoshikawa, Y. (2020). Mixed layer deepening due to wind-induced shear-driven turbulence and scaling of the deepening rate in the stratified ocean. *Ocean Dynamics*, 70(4):505–512. (Cited on pp. ix, x, 37, 42, 43 and 146.)

Ushijima, Y. and Yoshikawa, Y. (2022). Nonlinearly interacting entrainment due to shear and convection in the surface ocean. *Scientific Reports*, 12(1):9899. (Cited on p. 49.)

Vallis, G. (2006). *Atmospheric and Oceanic Fluid Dynamics*. (Cited on p. 86.)

Vallis, G. K. (2017). *Atmospheric and Oceanic Fluid Dynamics: Fundamentals and Large-Scale Circulation*. Cambridge University Press, 2nd edition. (Cited on pp. 5 and 127.)

Van Roekel, L., Adcroft, A. J., Danabasoglu, G., Griffies, S. M., Kauffman, B., Large, W., Levy, M., Reichl, B. G., Ringler, T., and Schmidt, M. (2018). The KPP boundary layer scheme for the ocean: Revisiting its formulation and benchmarking one-dimensional simulations relative to LES. *J. Adv. Model. Earth Syst.*, 10(11):2647–2685. (Cited on p. 36.)

Venaille, A., Gostiaux, L., and Sommeria, J. (2017). A statistical mechanics approach to mixing in stratified fluids. *Journal of Fluid Mechanics*, 810:554–583. (Cited on p. 54.)

Villas Bôas, A. B., Ardhuin, F., Ayet, A., Bourassa, M. A., Brandt, P., Chapron, B., Cornuelle, B. D., Farrar, J. T., Fewings, M. R., Fox-Kemper, B., et al. (2019). Integrated observations of global surface winds, currents, and waves: requirements and challenges for the next decade. *Frontiers in Marine Science*, 6:434339. (Cited on p. 9.)

Von Storch, H. and Zwiers, F. W. (2002). *Statistical analysis in climate research*. Cambridge university press. (Cited on p. 5.)

Vreugdenhil, C. A., Griffiths, R. W., and Gayen, B. (2017). Geostrophic and chimney regimes in rotating horizontal convection with imposed heat flux. *Journal of Fluid Mechanics*, 823:57–99. (Cited on pp. 128, 130 and 134.)

Walin, G. (1969). Some aspects of time-dependent motion of a stratified rotating fluid. *Journal of Fluid Mechanics*, 36:289–307. (Cited on p. 148.)

Wanninkhof, R., Park, G.-H., Takahashi, T., Sweeney, C., Feely, R., Nojiri, Y., Gruber, N., Doney, S. C., McKinley, G. A., Lenton, A., et al. (2013). Global ocean carbon uptake: magnitude, variability and trends. *Biogeosciences*, 10(3):1983–2000. (Cited on p. 2.)

Watanabe, M. and Hibiya, T. (2002). Global estimates of the wind-induced energy flux to inertial motions in the surface mixed layer. *Geophysical research letters*, 29(8):64–1. (Cited on pp. 5 and 9.)

Watson, A. J., Schuster, U., Shutler, J. D., Holding, T., Ashton, I. G., Landschützer, P., Woolf, D. K., and Goddijn-Murphy, L. (2020). Revised estimates of ocean-atmosphere co2 flux are consistent with ocean carbon inventory. *Nature communications*, 11(1):4422. (Cited on p. 2.)

Weatherly, G. L. and Martin, P. J. (1978). On the structure and dynamics of the oceanic bottom boundary layer. *Journal of Physical Oceanography*, 8(4):557–570. (Cited on pp. 41, 86 and 121.)

Wirth, A. (2010). On the Ekman Spiral with an Anisotropic Eddy Viscosity. *Boundary-Layer Meteorology*, 137(2):327–331. (Cited on p. 118.)

Wunsch, C. and Ferrari, R. (2004). Vertical mixing, energy, and the general circulation of the oceans. *Annual Review Fluid Mechanics*, 36(1):281–314. (Cited on p. 4.)

Wunsch, C. and Ferrari, R. (2004). Vertical mixing, energy, and the general circulation of the oceans. *Annual Review Fluid Mechanics*, 36:281–314. (Cited on p. 86.)

Zhai, X., Johnson, H. L., Marshall, D. P., and Wunsch, C. (2012). On the wind power input to the ocean general circulation. *Journal of Physical Oceanography*, 42(8):1357–1365. (Cited on p. 7.)

Zilitinkevich, S., Chalikov, D., and Resnyansky, Y. (1979). Modeling the oceanic upper layer. *Oceanologica Acta*. (Cited on pp. 8 and 42.)

Zilitinkevich, S. and Mironov, D. V. (1996). A multi-limit formulation for the equilibrium depth of a stably stratified boundary layer. *Boundary-Layer Meteorology*, 81(3):325–351. (Cited on p. 87.)

Zilitinkevich, S. S. (2012). The Height of the Atmospheric Planetary Boundary layer: State of the Art and New Development. In Fernando, H. J. S., Klaić, Z., and McCulley, J., editors, *National Security and Human Health Implications of Climate Change*, pages 147–161, Dordrecht. Springer Netherlands. (Cited on p. 88.)

Zilitinkevich, S. S. and Esau, I. N. (2003). The effect of baroclinicity on the equilibrium depth of neutral and stable planetary boundary layers. *Quarterly Journal of the Royal Meteorological Society*, 129(595):3339–3356. (Cited on p. 41.)

Résumé — Le mélange induit par le vent à la surface de l'océan est un processus fondamental qui gouverne les échanges entre l'atmosphère et l'océan profond. Lorsqu'une contrainte de vent est appliquée, elle injecte de la quantité de mouvement qui érode la stratification existante, formant une couche de mélange turbulente qui s'approfondit par entraînement à sa base. Cette couche de mélange contrôle le transport vertical de chaleur, de sel, de quantité de mouvement et de traceurs biogéochimiques. Parallèlement, la force de Coriolis génère des oscillations inertielles, qui constituent un réservoir majeur d'énergie cinétique dont le rôle dans la dynamique de la couche de mélange et le transfert de quantité de mouvement vers l'océan profond reste encore mal compris.

Malgré des décennies d'études, plusieurs questions clés demeurent. L'hypothèse largement admise selon laquelle les oscillations inertielles limitent l'approfondissement de la couche de mélange repose sur des arguments globaux intégrés en profondeur qui n'ont jamais été testés de manière rigoureuse. Les schémas de fermeture turbulente utilisés dans les modèles océaniques ont été calibrés sur des écoulements non tournant, ce qui soulève des interrogations quant à leur validité en présence de rotation, notamment en ce qui concerne l'isotropie de la turbulence. De plus, l'amortissement des oscillations inertielles est mal contraint par les observations, et le régime transitoire de la couche d'Ekman turbulente n'a jamais été étudié expérimentalement, alors qu'il constitue le régime dominant dans l'océan réel.

Ce travail porte sur ces problematiques en combinant théorie analytique, expériences en laboratoire et modélisation numérique. Nous dérivons une loi d'échelle pour l'approfondissement de la couche de mélange en rotation et caractérisons sa structure verticale ainsi que son bilan énergétique à l'aide de simulations 1D utilisant une fermeture k-ε. Nous exploitons ensuite des données issues d'expériences en laboratoire à grande échelle (plateforme Coriolis, 13 m) afin d'étudier l'entraînement turbulent en milieu stratifié et la couche d'Ekman transitoire dans des conditions contrôlées. Ces expériences permettent de mesurer directement le taux d'amortissement des oscillations inertielles et d'évaluer le modèle k-ε en le confrontant à des observations dans une configuration en rotation et stratifié. Enfin, nous examinons les limites de l'approche en colonne unique en analysant la circulation dans des expériences de convection thermique horizontale en rotation.

Dans leur ensemble, ces résultats apportent un éclairage nouveau sur le rôle de la rotation dans la dynamique de la couche de mélange et proposent une évaluation critique des schémas de fermeture turbulente actuellement utilisés dans les modèles de circulation océanique.

Mots clés :
Couche de mélange, Entrainement turbulent, Fermeture turbulente, Couche d'Ekman, Régime transitoire, Oscillations inertielles.

Abstract — Wind-driven mixing at the ocean surface is a fundamental process governing exchanges between the atmosphere and the deep ocean. When wind stress is applied, it injects momentum that erodes the existing stratification, forming a turbulent mixed layer that deepens through entrainment. This mixed layer controls the vertical transport of heat, salt, momentum, and biogeochemical tracers. Simultaneously, the Coriolis force generates inertial oscillations, which represent a major reservoir of kinetic energy whose role in mixed layer dynamics and momentum transfer to the deep ocean remains poorly understood.

Despite decades of study, several key questions persist. The widely held assumption that inertial oscillations arrest mixed layer deepening rests on bulk, depth-integrated arguments that have never been rigorously tested. Turbulent closure schemes used in ocean models were calibrated on non-rotating flows, raising concerns about their validity under rotation, particularly regarding turbulence isotropy. Moreover, the damping of inertial oscillations is poorly constrained observationally, and the transient regime of the turbulent Ekman layer has never been studied experimentally, even though it represents the dominant regime in the real ocean.

This thesis addresses these gaps through a combination of analytical theory, laboratory experiments, and numerical modelling. We derive a scaling law for the deepening of the rotating mixed layer and characterise its vertical structure and energy balance using 1D simulations with the k-ε closure. We then exploit data from large-scale rotating platform experiments (Coriolis platform, 13 m) to study stratified turbulent entrainment and the transient Ekman layer under controlled conditions. These experiments allow us to directly measure the damping rate of inertial oscillations and benchmark the k-ε model against observations in a rotating, stratified setting. Finally, we examine the limitations of the single-column framework by analysing the circulation in experiments of rotating horizontal thermal convection.

Together, these results provide new physical insight into the rotational control of mixed layer dynamics and offer a critical assessment of the turbulent closures currently used in ocean circulation models.

Keywords:
Wind-driven Mixing, Mixed-Layer, Turbulent entrainment, Turbulent closure, Ekman layer, Transient regime, Inertial oscillation.